COMPUTATIONAL AND MODELING APPROACHES TO MULTI-SCALE ANATOMICAL DESCRIPTION OF NEURONAL CIRCUITRY

Linus Manubens-Gil

TESI DOCTORAL UPF / ANY 2017

DIRECTOR DE LA TESI

Dra. Mara Dierssen i Dr. Jordi Garcia-Ojalvo

Biologia de sistemes - Centre de Regulació Genòmica.

DEPARTAMENT CEXS-UPF-PHD PROGRAMME IN BIOMEDICINE

A qui dorm en CIEs, a la família, a les amistats, al laboratori i a l'Irene

"Intellectual work is an act of creation. It is as if the mental image that is studied over a period of time were to sprout appendages like an ameba—outgrowths that extend in all directions while avoiding one obstacle after another—before interdigitating with related ideas. "

Santiago Ramón y Cajal, Recuerdos de mi vida

Linus Manubens-Gil has been funded by a personal fellowship from La Fundació Privada del Centre de Regulació Genòmica (CRG; NIF **G62426937**) during the period 2013-2017.

The work has received financial help from the Spanish Ministry of Innovation and Economy (SAF2013-49129-C2-1-R), Jerome Lejeune Foundation, FRAXA Foundation, Spanish Ministry of Health, PI11/00744 and the Spanish Ministry of Economy and Compeitiveness, Centro de Excelencia Severo Ochoa 2013-2017', SEV-2012-0208.

ABSTRACT / RESUM

Abstract

During the last century the nervous system has been mainly studied from a reductionistic approach, based on the hypothesis that understanding in depth single neurons or limited neuronal populations would lead to general conclusions on brain function. However, to what extent anatomical details of single neurons can affect the wiring of the networks they form is a largely overlooked question. Intellectual disability provides an excellent opportunity to explore the relevance of fine structural details, because many disorders show specific architectural alterations that correlate with cognitive performance.

In this Thesis, I aimed to study how the network topology of neuronal circuits is affected by dendritic architectural features in a mouse model of intellectual disability, namely Down's syndrome, and upon the rewiring effect of pro-cognitive treatment. I did so from three points of view:

1. The exploration of a 2D minimal computational model of cortical layer II/III parameterized by experimental data on dendritic tree architecture of healthy mice and two Down syndrome mouse models
2. The study of within-region morphological variations of hippocampal CA1 pyramidal neurons and their dependency of spatial embedding and cellularity in healthy mice and a Down syndrome mouse model.
3. The development of an experimental and computational framework for whole brain multiscale assessment and reconstruction.

My work revealed that the dendritic tree architecture and the distribution of synaptic contacts have significant implications on how optimal single neurons are for information processing efficiency and storage capacity, and that those single-neuron features permeate to the network level, determining the computational capacities of neural ensembles.

Also, I found position-dependent neuromorphological inhomogeneities in CA1 pyramids along with variations of neuronal cell density, suggesting that intrinsic properties of CA1 can vary across its extension. Those inhomogeneities were different in healthy and TgDyrk1A mice, possibly affecting emergent functional aspects.

In my Thesis I faced challenges to bridge structure and function and to study morphological inhomogeneities at different scale (single cell and cell population). To solve those challenges, I developed computational methods for 3D mapping cellular population and dendritic density and assessed their validity. I also developed a computational modeling framework that allows the instantiation of multi-scale biologically realistic networks. Finally, I optimized the CLARITY whole-brain clearing technique and developed a pipeline to apply our population-based analysis and multi-scale modeling methods to the structural interrogation of whole brains, and to study the implications of the neuronal morphospace on the topology of neuronal circuitry.

Resum

Durant l'últim segle, el sistema nerviós s'ha estudiat des d'un punt de vista reduccionista, basant-se en la hipòtesi que entendre en profunditat neurones individuals o fraccions petites de poblacions neuronals portaria a conclusions generals sobre la funció del cervell. De totes maneres, fins a quin punt detalls anatòmics de neurones individuals poden afectar la connectivitat de les xarxes que formen, és una qüestió que en gran part s'ha passat per alt. Les discapacitats intel·lectuals proporcionen una oportunitat excel·lent per explorar la rellevància de detalls estructurals, perquè molts trastorns cognitius mostren alteracions arquitectòniques específiques que correlacionen amb habilitats cognitives.

En aquesta Tesi, pretenia estudiar com la topologia dels circuits neuronals és afectada per característiques arquitectòniques en un model murí de discapacitat intel·lectual, en concret de síndrome de Down, i per tractaments pro-cognitius amb efectes de remodel·lació de la xarxa. Ho he fet des de tres punts de vista:
1. L'exploració d'un model computacional 2D mínim de la capa cortical II/III parametritzat amb dades experimentals d'arquitectura dendrítica ens els nostres models de síndrome de Down.

2. L'estudi de neurones individuals, la seva diversitat i propietats morfològiques d'escala mesoscòpica en el model murí TgDyrk1A de síndrome de Down.
3. El desenvolupament d'un marc experimental i computacional per a l'estudi del problema des d'una perspectiva multi-escala.

La meva feina ha mostrat que l'arquitectura dendrítica i la distribució de contactes sinàptics tenen implicacions significatives en l'optimalitat de neurones individuals per a l'eficiència en el processat d'informació i per a la capacitat d'emmagatzemar memòries, i que aquestes dues quantitats permeen al nivell de xarxa, determinant les capacitats computacionals de conjunts de neurones.
També, he trobat variacions neuromorfològiques a CA1 dependents de la posició en neurones piramidals, acompanyades per variacions en densitat cel·lular, apuntat que propietats intrínseques de CA1 poden variar al llarg de la seva extensió. Aquestes

inhomogeneitats eren diferents en ratolins sans i TgDyrk1A, possiblement tenint efectes en aspectes funcionals emergents concrets.

En la meva Tesi he afrontat reptes en lligar estructura i funció i en l'estudi de les inhomogeneïtats morfològiques en múltiples escales (de cèl·lula individual i de poblacions). Per a assolir aquests reptes, he desenvolupat mètodes computacionals per al mapejat 3D de poblacions cel·lulars i de densitats dendrítiques i he avaluat la seva validesa. També he desenvolupat un marc de modelització que permet l'instanciació multi-escala de xarxes neuronals biològicament realistes. Finalment, he optimitzat la tècnica de clarejat de cervell sencer CLARITY i he desenvolupat un pipeline per a aplicar les nostres eines d'anàlisi de poblacions i els mètodes multi-escala de model·lització per a l'anàlisi estructural de cervells sencers, i per a l'estudi de les implicacions del morfoespai neuronal en la topologia de la circuiteria neuronal.

PREFACE

Preface

Despite being far from a complete description of the nervous system, the cellular architecture of neurons has an important role in determining the function of neuronal networks that gives rise to neural functions or dysfunctions. However, how anatomical details of single neurons affects the wiring of the networks they form, and consequently their function, is a largely overlooked question. Given that many pathological conditions, such as Alzheimer's disease, intellectual disability, epilepsy or chronic stress present aberrant dendritic morphologies, those scenarios provide an excellent opportunity to explore fine structural alterations that correlate with cognitive performance.

This Thesis originates from the interest of the Cellular and Systems Neurobiology group at the Center for Genomic Regulation in further understanding the mechanisms underlying the neuropathology of intellectual disability. Pioneering studies in our lab showed microstructural alterations in Down syndrome (DS) dendritic trees that could be partially rescued upon pro-cognitive treatments that correct the overdosage of a DS candidate gene, *DYRK1A*, which encodes for a member of the Dual-specificity tyrosine phosphorylation-regulated kinase (DYRK) family and is sufficient and necessary to recapitulate some of the DS phenotypes.

A key concept behind my Thesis is that dendritic architecture changes in intellectual disability may have a strong impact on complex network topologies. Consequently, I aimed at gaining a broader view by profiling dendritic trees in different mouse strains and Down syndrome models, gather a comprehensive view of the possible strain-dependent variation in the normal dendritic phenotypes, and their pathological deviations in intellectual disability.

During my Thesis I have implemented a variety of analytic frameworks and theoretical perspectives keeping in mind the challenge of using brain samples and datasets of different spatial scales (microscopic to mesoscopic), and of developing theoretical frameworks to test my hypothesis. The outcomes of my Thesis have set the basis for further research lines in Dierssen lab involving new computational modeling to interrogate the structure-function relationship. This theoretical and Systems Neuroscience approach was also supervised by Prof. Jordi García-Ojalvo (University Pompeu Fabra), co-director of my work. I used

computational models to explore how alterations in single-neuron morphostructural features in mouse models of intellectual disability, and neuronal reformatting and network rewiring upon pro-cognitive treatments known to rescue the cognitive phenotypes in DS impact local network topology.

I also applied graph theoretical analysis of organizational principles in neuronal connectivity at the cellular scale and experimentally explored within-class variability in a well-defined canonical neuronal population, such as CA1 pyramidal neurons as a function of their spatial location. These experiments provided initial population level descriptions that revealed an unexpected position-dependent level of variability that suggests continuous heterogeneity as an important feature of neural circuits.

In the final part of my Thesis, I made some steps to obtain whole brain structural information with microscopic resolution using state-of-the-art brain clearing techniques, to explore how micro-connectomic disturbances in local networks may impact on large-scale connectivity and imply specific topology alterations and suboptimal computational capacities at the systems level. Charting cellular localizations, projections, and network activity throughout the whole brain is a mandatory step to understand network properties, but the tools for combining these levels of description are not available yet. I started filling this gap by providing suite of unified software to construct multiscale structural maps from brain-clearing experiments, with specific subworkflows for understanding topological structure-function dependencies on a brain-wide scale. The set of tools I propose are a first step towards a systems perspective description of neuronal circuits' microscopic structural and population-based properties.

During the present Doctoral Thesis, I had the opportunity to be part of several international and national scientific collaborations with renowned research groups in the systems neuroscience. For applying the concept of optimality, I had the opportunity to discuss directly with Prof Hermann Cuntz. For the study of cortical basal trees, I had the opportunity to discuss directly with Prof. Inma Ballesteros. To perform whole-brain imaging I have established a long-term collaboration with James Sharpe's lab. For the implementation of the 2D model I had the opportunity to discuss directly with Jordi Soriano and Javier Orlandi. For the molecular dynamics study of fluorescent protein quenching I had the opportunity to assess my work with Gianni De Fabritiis.

During this Doctoral Thesis, I had the opportunity to present my work in four national and two international meetings, and I have participated also in other outreach activities of the laboratory.

INDEX

Index

List of Figures

List of Tables

GENERAL INTRODUCTION

GENERAL INTRODUCTION

Last century's Neuroscience was founded on the seminal studies of Ramón y Cajal. Guided by the neuron doctrine, neuroscientists deepened in the understanding of the nervous system focusing on the study of the individual cells forming it. Detailed molecular, cellular and electrophysiological studies have identified an increasing number of cell types that can be broadly grouped in neuronal cell types. During those years, a tendency towards excessive classification and reductionism has governed Neuroscience. But over the last decades, the community has noticed that, to understand the emergence of cognition, an important building block is missing: the complex connectivity patterns of the individual cells forming the brain are crucial to understand the emergence of neural activity dynamics that ultimately leads to cognitive function. In this sense, cognitive impairments are particularly revealing in two aspects. First, studies of neuromorphological alterations show that a precise interplay between dendritic architecture and axonal projections is necessary for proper function. And second, the fact that seemingly opposite morphological alterations can have the same implications at the behavioral level (e.g. increased or reduced spine densities in Fragile X and Down syndrome, respectively) reflects that emergent properties of the system are not well understood. I think that the study of relatively subtle neuromorphological alterations constitute a largely unexplored scenario that can be useful to identify fundamental structural properties of the nervous system, and to understand how these properties relate to cognitive function.

Systems neuroscience, both through the study of groups of neurons involved in a specific neural computation and through whole-brain neuroimaging techniques, has performed important steps in the direction of understanding the emergence of cognition. However, on the one hand the study of neuronal circuits at the cellular scale has been limited to highly specific questions and is still missing the description of fundamental properties of neuronal networks. And on the other hand, while whole-brain systems neuroscience is paving the way to theoretical frameworks that can well be used to identify such fundamental properties, it is still missing a wealth of important details at the microscopic scale. One of the concepts that seems to permeate through multiple scales of description of neuronal networks is wiring optimality. It has been proposed that dendritic trees grow to fill optimally a target space. A power law relating the total length and the number of dendritic branches in single neurons

has been derived from Cajal's principle for conservation of cytoplasm and conduction time. I interpret single-neuron wiring optimality studies as a first step towards a generic framework for understanding fundamental properties of the nervous system, and propose that graph-theoretical analyses of neuronal circuits at the cellular scale will allow (1) to identify neuronal subcircuits involved in specific functions, (2) to disentangle the implications of multi-scale morphological properties on neuronal wiring, and ultimately, (3) to identify the rules governing it.

To explore those concepts, I compared the brain of wild-type mice with those of mice with suboptimal cognitive function. Since in most cases the experimental tools to link microstructural properties with network topology do not exist, I first took a computational modeling approach and developed a framework that allows to quantitatively explore the neuromorphological space and assess its implications on the optimality for signal processing and storage capacity, linking single cell architecture with network contact topology. Subsequently, I obtained single neuron morphology experimental data in a brain region responsible of specific cognitive functions and analyzed how morphological alterations relate to cognitive impairment in intellectual disability. And, finally, I gathered multi-scale experimental data and developed an extensible computational modelling framework that allows a systems perspective analysis of the link between neuromorphology and network connectivity.

In the scope of this Thesis I hypothesize that dendritic neuromorphological alterations in intellectual disability lead to suboptimal connectivity and signal integration that (1) have significant implications on the network topology, leading to suboptimal computational capacities in intellectual disability, and (2) can explain specific cognitive impairments at the single cell level.

From the network perspective, I use a minimal computational model in order to explore the impact of dendritic architectural features on graph theoretical representations of the connectivity in neuronal layers. The rather abstract perspective taken is only generally linked to cognitive function, and circuit-specific details are missing. However, this perspective allows to disentangle, in a simplified context, the contribution of various architectural properties on neural connectivity, assessing the fundamental goal of this Thesis. Specifically

I hypothesize, using a minimal model of a stereotypical computing unit in the cortex (layer II/III), that healthy neuronal networks lay on a close-to-optimal organization for multiple objectives (Pareto optimality) including information processing, storage capacity and material cost, and that intellectual disability mouse models of Down's syndrome (Ts65Dn, TgDyrk1A and Dyrk1A+/-) deviate from this optimality.

To study the implications of detailed architectural properties on cognitive function, I focus on the well-studied hippocampal circuit and its percept contextualization function. The existing evidence points that layer CA1 is involved on the comparison of memories stored in CA3 and on the perceived experience encoded in the sensory cortex. Given that the inputs of the Medial Entorhinal Cortex (mainly encoding spatial information) innervate preferentially the stratum lacunosum of medial subiculum and lateral CA1 pyramidal neurons, I hypothesize that TgDyrk1A mice will show dendritic abnormalities accounting for imbalanced connectivity mainly in those regions.

Additionally, I also hypothesize that (1) a graph theoretical analysis of the hippocampal circuit at the cellular scale will underline the existence of subcircuits involved in specific functions (such as the lamellar organization of the hippocampus or subregional specific functionalities), (2) neuromorphological alterations throughout the hippocampal trisynaptic circuit associated with intellectual disability exhibit a Pareto suboptimal organization with specific effects on spatial memory formation, retrieval and contextualization, and (3) deviations from optimality will reveal network topological properties necessary for proper cognitive function. Even though testing these hypotheses is beyond the scope of this Thesis, I have developed computational tools that will allow such a validation in the near future.

HYPOTHESIS AND OBJECTIVES

HYPOTHESIS AND OBJECTIVES

During the last century the nervous system has been studied from a reductionistic approach based on the conviction that understanding in depth single neurons or limited neuronal populations would lead to general conclusions on brain function. However, to what extent anatomical details of single neurons can be affecting the wiring of the networks they form is a largely overlooked question. This is especially challenging when acknowledging for the unexpected morphological variety, and the structural inhomogeneities along each brain region, and most importantly along the cerebral cortex. A prevailing alternative approach has been to statistically characterize subpopulations of a canonical cell type, which has already uncovered traces of complex network topologies. Considering that dendritic morphology can undergo significant changes in many pathological conditions, such as Alzheimer's disease, intellectual disability, epilepsy, schizophrenia or chronic stress, those scenarios provide an excellent opportunity to explore the relevance of fine structural details. Pioneering studies in our lab indicate that Down syndrome, the most frequent genetic cause of intellectual disability is characterized by specific architectural alterations in pyramidal neurons that correlate with defective cognitive performance. In some cases, the neuronal structure and connectivity damage characteristic of this disorder may potentially be reversed by treatments with pro-cognitive effects. Specifically, we found that structural deficits can be partially rescued upon pro-cognitive treatment in Down syndrome (DS), which corrects the overdosage of a candidate gene, DYRK1A. We conjecture that both the dendritic tree architecture and distribution of synaptic contacts have significant implications on how optimal single neurons are for information processing efficiency and storage capacity, and to what extent that those single-neuron features permeate to the network level, determining the computational capacities of neural ensembles.

Hypothesis

We hypothesize that dendritic neuromorphological alterations of single neurons in intellectual disability lead to suboptimal signal integration and connectivity that (1) have significant implications on the network topology resulting in suboptimal computational capacities in intellectual disability, and (2) can explain specific pathological impairments.

Objectives

To prove the hypothesis above, the specific aims of this Thesis are:

Objective #1/ To investigate how alterations in single-neuron morphostructural features in mouse models of intellectual disability sculpt local network topology, through in silico exploration of the resulting morphospace.

Objective #2/ To assess the neuronal reformatting and network rewiring effect of proven pro-cognitive treatments known to rescue the cognitive phenotypes in DS.

Objective #3/ To develop new tools that will allow us to (1) explore how micro-connectomic disturbances in local networks may impact on large-scale connectivity, and (2) determne whether micro-connectomic aberrations imply specific topology alterations and suboptimal computational capacities at the systems level.

1. CHAPTER I. NEUROMORPHOLOGY IMPLICATIONS ON LOCAL NETWORK CONNECTIVITY IN A MINIMAL MODEL OF CORTICAL LAYER II/III

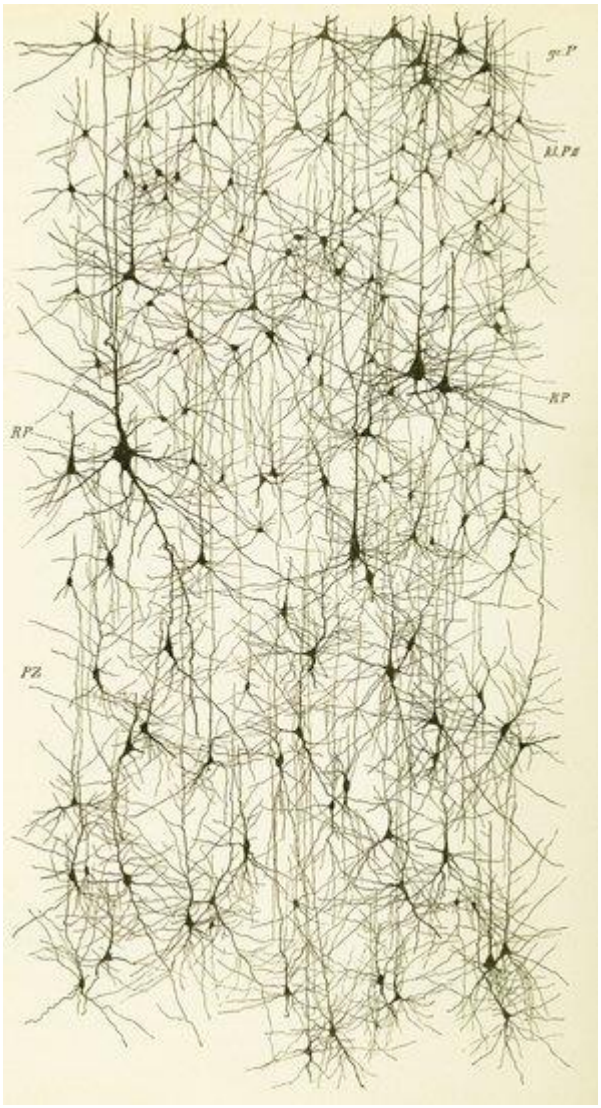

Cortical pyramids reconstructions and drawings by Cajal. From. Cajal's Butterflies of the Soul. Science and Art. Javier DeFelipe

"To know the brain—we said to ourselves in our idealistic enthusiasm—is equivalent to discover the material course of thought and will. [. . .] Like the entlogist hunting for brightly coloured butterflies, my attention was drawn to the flower garden of the grey matter, which contained cells with delicate and elegant forms, the mysterious butterflies of the soul, the beating of whose wings may some day (who knows?) clarify the secret of mental life. "

Santiago Ramón y Cajal, Recuerdos de mi vida

1.1. Introduction

There is consensus among neuroscientists that the cellular architecture of neurons, despite being far from a complete description of the nervous system, has an important role determining the function of neuronal networks. The spatial organization of synaptic connections in individual cells constrains the dynamics of a neural circuit, shaping the repertoire of collective activities that gives rise to neural functions or dysfunctions. This is studied by a new discipline called micro-connectomics, which deals with the graph theoretical analysis of organizational principles in neuronal connectivity at the cellular scale. A growing body of data on the anatomical microcircuitry at the cellular and synaptic level, in the form of 'microconnectomes', has shed light on information processing in specific neural systems. For complex structures such as the mammalian neocortex, which is related to many high-level computational processes such as sensory processing, planning, motor control, perception and language, detailed microconnectomes may still be years away. An alternative approach has been to statistically characterize connectivity patterns between different pairs of cell types(Hill, Wang, Riachi, Schürmann, & Markram, 2012), but few studies have been devoted to analyze connectivity patterns that could uncover complex network topologies.

Basics elements of neuronal architecture and their role in neuronal computation

Cellular anatomy has been the focus of intense investigation since the early days of neuroscience. A typical neuron may be divided into three distinct parts (**Figure 1**): a cell body or soma, an axon, and dendrites. The latter two are specialized extensions of membrane that constitute the neuron's communication interfaces. Dendrites are membranous protoplasmatic projections branching from the body of a neuron. They are usually subdivided extensively, forming a dense arborization surrounding the neuron, called a dendritic tree. The area occupied by the dendritic tree is larger than the soma, and consequently the dendritic membrane covers a much greater surface. The main objective described of the dendrites is to get information from other cells and deliver that information to the cell body. Moreover, dendritic spines are the membranous protrusions of the dendrites that actually synapse with the axon's terminal bulbs. A single dendrite has tens of thousands of dendritic spines, and they represent the excitatory inputs of information.

Most neurons also have an axon, which carries information from the soma to other cells. Axons terminate in terminal boutons (buttons), or endfeet, which transmit information to the receiving cell. The influence of the axonal morphology on activity was also demonstrated in experimental studies. Already in the 1970s, Ramon et al. showed action potential modifications at sites of abrupt increase in axonal diameter (Ramón, Moore, Joyner, & Westerfield, 1976)(Ramón et al., 1976). Branching is also an important factor. For example, high frequency current modulations in unbranched axons lead to abnormal patterns such as fragmented trains, quasi-periodic, and chaotic responses (Smith, 1977). Measurements along axonal branching points with two different radii exhibited different temporal responses in the two daughter branches (Sasaki, Matsuki, & Ikegaya, 2012). Stockbridge showed that if branching consisted of short and long daughter branches, only the first of adjacent spike pair invades the long branch, while the two spikes propagate along the short one (Stockbridge & Stockbridge, 1988). Sasaki et al. examined changes in action potential width caused by modulations of axonal length and branching order (Sasaki, Matsuki, & Ikegaya, 2011).

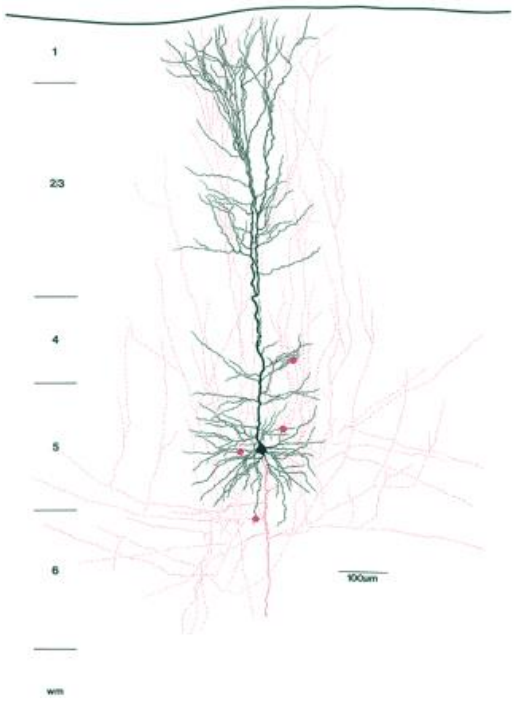

Figure 1. Camera lucida reconstruction of a pyramidal neuron from a rat neocortex. The reconstruction shows thick-tufted layer 5 pyramidal neuron. Dendritic morphology of the neuron is drawn in black, and axonal arborization in red. The red dots indicate contacts established onto basal and oblique dendrites by the axon. Note the extensive vertical axonal collaterals, some of which could be followed up to layer 1 (2.5 mm from the soma). (Lübke, Markram, Frotscher, & Sakmann, 1996)

In this Thesis I have focused in the study of the dendrites. This is in part because their microanatomical details are accessible, which is not the case for the axon, but also because of their prominent role in information acquisition and processing. Mammalian dendrites have a rich repertoire of electrical and chemical dynamics, making individual neurons capable of very sophisticated information processing (Yuste & Tank, 1996). Experimental and computational studies have shown a strong interdependence (Segev and Rall 1998; Van Elburg and van Ooyen 2010; Eyal et al. 2014), although the underlying mechanisms are poorly understood, and the impact of morphology on electrical activity remains elusive.

Dendritic geometry appears to be an important factor modulating the pattern of neuronal firings (action potentials) (Mainen, Sejnowski, & Others, 1996). In addition, the size of dendritic arbors modulates the shape of the action potential onset, which determines the capability of the axonal spikes to encode rapid changes in synaptic inputs (Ilin, Malyshev, Wolf, & Volgushev, 2013) being accelerated in neurons with larger dendritic surface area (Eyal et al., 2014). Interestingly, dendritic morphology is dynamic and can undergo significant changes in many pathological conditions. Using computational models of neocortical pyramidal cells (van Elburg & van Ooyen, 2010), it has been shown that not only the total length of the apical dendrite but also the topological structure of its branching pattern markedly influences inter- and intra-burst spike intervals and even determines whether or not a cell exhibits burst firing. In fact, there is only a range of dendritic sizes that supports burst firing, and that this range is modulated by dendritic topology. Either reducing or enlarging the dendritic tree, or merely modifying its topological structure without changing total dendritic length, can transform a cell's firing pattern from bursting to tonic firing.

The concept of optimality

At the end of the 19th century, Ramón y Cajal proposed the idea that dendrites optimize connectivity by minimizing conduction time in a tradeoff with total cable length cost[1]. During the last decades, the interest for the concept of optimality in neuronal cells and networks has

[1] "The laws of time, space, and material conservation, which must be considered the final cause of all variations in the shape of neurons... All that remains is to substantiate the influence of these laws on the conformation of particular neurons." *(Ramón y Cajal, 1909)*

been growing (Chen, Hall, & Chklovskii, 2006; Chklovskii, 2004; Chklovskii, Schikorski, & Stevens, 2002; Cuntz, Mathy, & Häusser, 2012). It has been proposed that dendritic trees grow to fill optimally a target space. A power law relating the total length and the number of dendritic branches in single neurons has been derived from Cajal's principle for conservation of cytoplasm and conduction time (Cuntz et al., 2012). Since Cuntz et al. proposed this optimal wiring scaling law for single neurons, some studies have used the concept to describe specific neuronal populations(Iyer et al., 2013; Polavaram, Gillette, Parekh, & Ascoli, 2014), and neuronal diversity in specific layers or regions (Leguey et al., 2016) or throughout development (Lefebvre, Sanes, & Kay, 2015). There is a wide variety of different neuronal morphologies in the brains of different animal species (Bullock & Horridge, 1965; Nieuwenhuys & Nicholson, 1998; Strausfeld, 2012), in different brain regions of the same species (Shepherd et al., 1998), or even in the same brain region (Markram et al., 2004), but all follow this optimal wiring. Even so, the high structural variability among neuronal classes, and the brain region and genetics for the same cell type makes it difficult to define an optimal range of variance. This may be achieved by capitalizing on the scenario provided by neuropathological models, using comparative analysis of micro-connectomics (Schröter, Paulsen, & Bullmore, 2017).

Linking single-neuron neuromorphological properties with network architecture and computational capacities

As highlighted above, research on neuronal morphology is essential both for the investigation of the basic structure–activity relationship in the brain, and in connection with studies on development, ageing, pathology and pharmacology. One approach is to linking the local properties of neuronal arborizations to network computation could be attained by embodying morphological reconstructions in computational simulations. Still, most computational models have commonly disregarded fine morphological features involved in network connectivity (Orlandi, Soriano, Alvarez-Lacalle, Teller, & Casademunt, 2013; Vegue, Perin, & Roxin, 2017; Voges, Schüz, Aertsen, & Rotter, 2010), and only some have simulated connectivity based on neuronal reconstructions with micrometric detail in specific layers or regions (Markram, 2006; Reimann et al., 2017), or whole organisms (Szigeti et al., 2014). A relevant example is the Blue Brain Project, that simulated cell to cell connectivity in a portion of rat cortex taking into account a wealth of multi-scale biological features(Markram, 2006).

While those examples have increased the level of detail used to parameterize the simulations, a systematic exploration of the relevance of microscopic neuromorphological architecture for the network connectivity is missing.

To link the single-neuron and network scales of description, I have applied the graph theory conceptual framework used in the neuroimaging field, has been applied to micro-connectome topology, often informed by economic principles that conceptually originated with Ramón y Cajal's conservation laws (see above). Neuronal networks are studied as graphs formed by the neurons (nodes) and the connections among them (directed edge) (Artzy-Randrup, Fleishman, Ben-Tal, & Stone, 2004). Mixed theoretical and experimental studies have found fundamental properties in neuronal networks (such as their clustered, hierarchical organization (Bullmore & Sporns, 2009; Sporns, Chialvo, Kaiser, & Hilgetag, 2004) that have been observed across organisms and along evolution.

More specifically, I used the concept of Pareto optimality, which is built on the idea that a system devoted to various functions, in order to be globally optimal, must obey tradeoffs between the performances in the diverse functions. One single study has applied this concept to human tractography data, and explored how genetic algorithms can modulate the capacities of whole-brain networks and displace them towards Pareto-optimal configurations (Griffa et al., 2014). Here, I aimed to use this concept in order to test whether neuronal networks are Pareto-optimal and, if they deviate in brain pathology, to dissect how differential neuromorphological properties contribute to such deviations.

Our model system: basal dendritic trees of neocortical pyramidal cells

Even though studying the wiring of circuits involved in specific functions will ultimately provide novel insights into network connectivity fundamental laws, it is reasonable to first assess the question in a simplified context and explore the relationship between diverse neuromorphological features and network connectivity in a manageable framework. Here I specifically selected the pyramidal cells of layers II and III of the motor cortex.

The cerebral cortex

The cerebral cortex is the brain zone (2-3 mm thick) that consists of an outer region of neural tissue (gray matter) and covers the two hemispheres. The primary cortices are defined as the cortical regions that present somewhat simpler functions. These include areas that directly receive the sensory input (vision, hearing, somatic sensation) or that are involved in the display of limb or eye movements. The association cortices perform more complex functions (**Figure 2**).

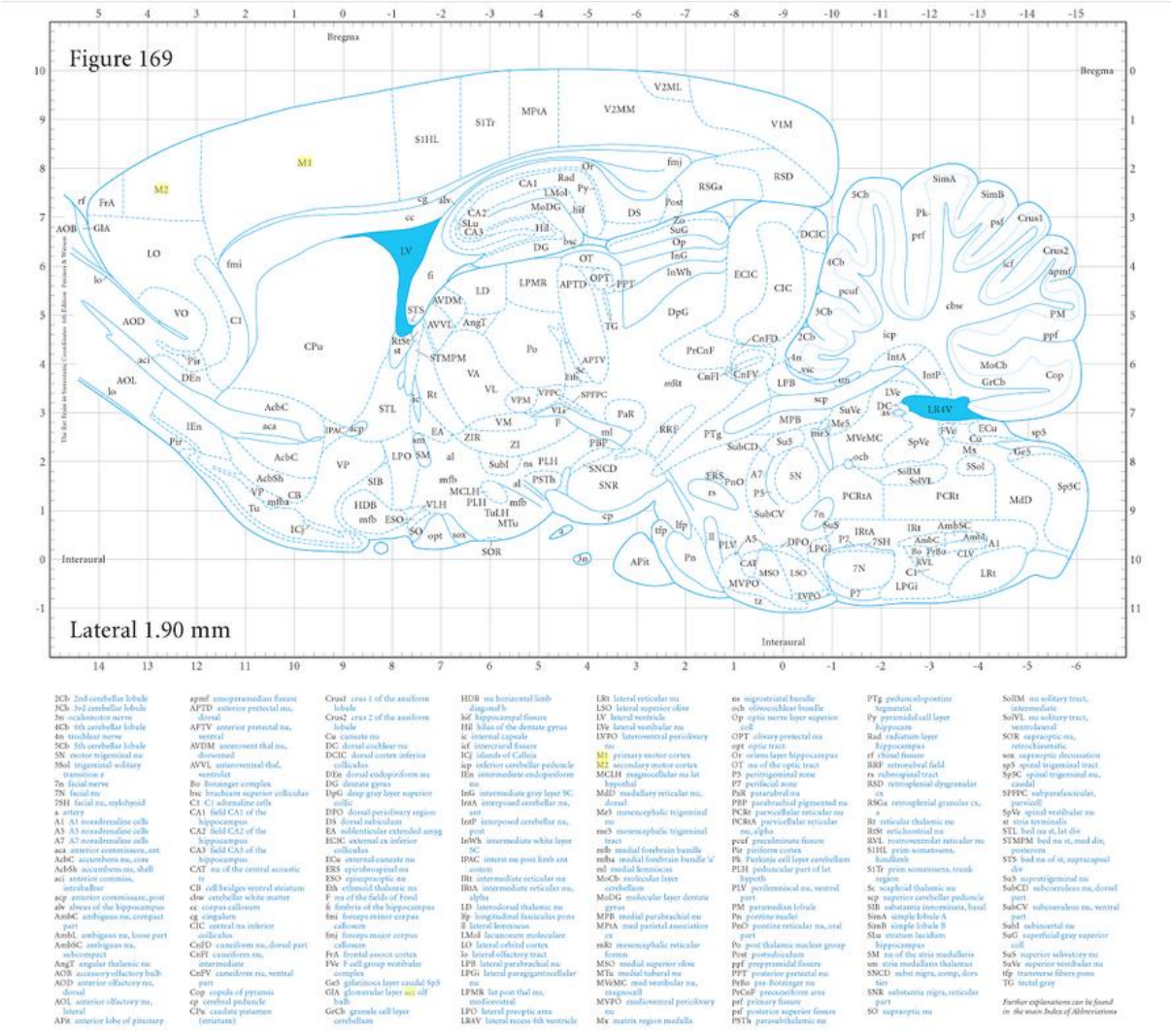

Figure 2. **Sagital view of the rat brain indicating the different brain areas**. Motor cortices (M1 and M2) are highlighted in yellow. From The Rat Brain in Stereotaxic Coordinates. (Paxinos, Watson, Pennisi, & Topple, 1985)

The great majority of the cerebral cortex is represented by the neocortex. It is morphologically divided in six layers and holds from 10 to 14 billion neurons of the human brain. These six layers are numbered with Roman numbers from the surfice to the inner part. The molecular layer (layer I) contains very few neurons; layer II is the external granular; layer III the external pyramidal; layer IV the internal granular; layer V the internal pyramidal; and layer VI the multiform, or fusiform layer. Each cortical layer involves different neuronal shapes, sizes and densities as well as different distributions of nerve fibers.

Functionally, the layers of the cerebral cortex can be divided into three parts. The supragranular layers involve layers I to III. The supragranular layers are the starting and ending point (?) of intracortical connections, which can be either associational (i.e., with other areas of the same hemisphere), or commissural (i.e., connections to the opposite hemisphere, through the corpus callosum). The supragranular region of the cortex is highly developed in humans and allows communication between one portion of the cortex and the other regions.

The internal granular layer receives thalamocortical connections, especifically from the specific thalamic nuclei and it is the most prominent in the primary sensory cortices. The infragranular layers (layers V and VI) primarily connect the cerebral cortex with subcortical regions. These layers are mainly developed in motor cortical regions. The motor areas present significantly small or non-existent granular layers and are often called "agranular cortex". Layer V provides all of the principal cortical efferent projections to basal ganglia, brainstem and spinal cord. Layer VI, the multiform or fusiform layer, projects primarily to the thalamus.

Here, I focused on the supplementary motor area (MII, superiomedial part of area 6), is a part of the premotor cortex that extends onto the medial side of hemisphere. This area shows projections to the primary motor cortex, basal ganglia, thalamus, brainstem and also to the contralateral supplementary motor area. This area is active before movement and is thought to be involved in initiation of motion. It consists of local circuit neurons, with short axons that exert their effects in the local region of their cell bodies and dendrites. They are located in brain areas served by the long-axoned principal neurons and act to affect the activity in these pathways. Local circuit neurons perform integrative and modulating functions in local brain regions (Paxinos & Franklin, 2004)

The pyramidal neuron

There are several identifiable cell types in the cerebral cortex. Pyramidal neurons are the most abundant cell type in the cerebral cortex of mammals, birds, fish and reptiles, indicating an adaptive value for the organism, and are found in most mammalian forebrain structures associated with cognitive functions, including the cerebral cortex, the hippocampus and the amygdala. The lone axon of each pyramidal neuron typically emanates from the base of the soma and branches profusely, making many excitatory glutamatergic synaptic contacts along its length. Of interest to my work, current research demonstrates that in the case of cortical neurons, about 98% of the synapses are axodendritic and only 2% synapse with the soma(Barrett & Others, 2010).

The dendritic tree of a pyramidal neuron has two distinct domains: the basal and the apical dendrites, which descend from the base and the apex of the soma, respectively. Usually, one large apical dendrite connects the soma to a tuft of dendrites. This main apical dendrite bifurcates before giving rise to the tuft at a variable distance from the soma. In some cases the resulting 'twin' apical dendrites each bifurcate again. Oblique apical dendrites emanate from the main apical dendrite at various angles. All pyramidal neurons have several relatively short basal dendrites. Pyramidal neurons are covered with thousands of dendritic spines that constitute the postsynaptic site for most excitatory glutamatergic synapses. The number of spines represents thus a minimum estimate of connectivity of a neuron.

In my work, I chose to study local horizontal connections of cortical layer II/III. The reasons for this choice are: (1) The abundance of horizontal recurrent connectivity in this layer (Voges et al., 2010), which justifies the simplification of the layer to a 2D homogeneous neuronal mosaic, (2) the stereotypical connectivity patterns found in the neocortex, which are conserved among cortical areas devoted to very diverse processing roles[2], and (3) the fact that Down-syndrome-related intellectual disability mouse models show dendritic alterations in cortical layers II/III in the M2 cortex implies that our computational modelling results can be contextualized by experimental data providing a link between our computational study and the biological reality.

[2] Understanding the role of subtle neuromorphological properties on the network connectivity and its computational capacities in a subsampled cortical area can be reasonably extrapolable to other areas in the neocortex

Intellectual disability as a model of suboptimal networks

Abnormalities in dendritic structure are a characteristic feature of many brain disorders. One clear example are individuals with intellectual disability that presents reduced dendritic branching patterns, shortened dendritic lengths, loss of spines and changes in spine shape and size (Kulkarni & Firestein, 2012). These alterations may most probably have strong implications on single-neuron wiring and its optimality. However, while in healthy phenotypes the studies assessing optimality questions are still limited (Schröter et al., 2017), the analysis of intellectual disability models has not even been used. Thus, our study constitutes a first step towards the identification of fundamental properties for optimal wiring through the comparative analysis of intellectual disability (P R Huttenlocher, 1970; Peter R Huttenlocher, 1974; Purpura, 1974).

Since the discovery in the 1970s that dendritic abnormalities in cortical pyramidal neurons are the most consistent pathologic correlate of intellectual disability, research has focused on how dendritic alterations are related to reduced intellectual ability. The recent identification of the genetic bases of some mental retardation associated alterations, and the introduction of powerful sophisticated tools in the field of microanatomy, has led to a growth in the studies of the alterations of pyramidal cell morphology in these disorders. Specifically, studies in Down syndrome, allow the analysis of the relationships between cognition, genotype and brain microanatomy.

Our laboratory has extensively studied Down syndrome mouse models to understand the microanatomical changes driven by specific genetic perturbations. The varied approaches used to study the consequences of increased gene dosage in DS and to investigate phenotype/genotype relationships of HSA21 genes in mice (see Cairns 2001; Galdzicki and J Siarey 2003 for review) are: (1) transgenic animals overexpressing single or combinations of genes, (2) mouse models that carry all or part of MMU16, which has regions of conserved homology with HSA21 and (3) chimaeric mice that carry a fragment of human chromosome 21 (Tomizuka et al., 1997).
In this Thesis I focused in a well validated model of partial trisomy and two models with dosage changes of a candidate gene for Down syndrome. The Ts65Dn mouse model (Davisson, Schmidt, & Akeson, 1990) contains three copies of mouse chromosome 16 (MMU16 from *App* to *Mx1*). Using intracellular injections with Lucifer Yellow to visualize

the whole basal dendritic tree, I found that pyramidal cells are smaller, less branched and 24% less spinous in Ts65Dn mice than those in controls. These effects on pyramidal cell structure parallel those obtained in humans. The structural changes in the Ts65Dn mice are paralleled with slight changes by the single overexpression of *DYRK1A* (Dual specificity tyrosine phosphorylation-regulated kinase 1A) possibly the most extensively studied chromosome 21 gene during the last decade, due to the remarkable correlation of its functions in the brain with important DS neuropathologies, such as neuronal deficits, dendrite atrophy, spine dysgenesis, and cognitive and behavioral deficits.

Environmental enrichment as a model of dendritic rewiring

The morphological and physiological characteristics of the central nervous system are the result of a combination of genetic and environmental factors(Bartoletti, Medini, Berardi, & Maffei, 2004).Several studies report anatomical and physiological consequences of exposure to a sensory enriched environment (EE)(Diamond, Krech, & Rosenzweig, 1964; Volkmar & Greenough, 1972). Many studies report the effects of EE on synaptic transmission in the hippocampus (Artola et al., 2006; Duffy, Craddock, Abel, & Nguyen, 2001; Foster & Dumas, 2001; Irvine & Abraham, 2005) as well as in the prefrontal cortex (Kolb & Gibb, 1991; Seib & Wellman, 2003) and in the parietal cortex (Leggio et al., 2005).

EE has been reported to increase synaptic plasticity that has been proposed as the cellular substrate of information processing and memory formation, consolidation, retrieval and extinction. These processes are probably dependent on structural modification of synaptic connectivity, with long-term potentiation (LTP) and long-term depression (LTD) initiating structural modifications in dendritic spines.

This is specially interesting in Down syndrome, since abnormalities in synaptic plasticity (that is, LTP) are seen in Down syndrome mice (see Mara Dierssen, Herault, and Estivill 2009 for review). A key finding in Down syndrome mouse models has been the imbalance of the excitation–inhibition at the network level (Belichenko et al., 2009; Kurt, Davies, Kidd, Dierssen, & Flórez, 2000; Kurt, Kafa, Dierssen, & Davies, 2004), over inhibition being observed that may explain the LTP and LTD disturbances (R J Siarey, Stoll, Rapoport, & Galdzicki, 1997; Richard J Siarey et al., 1999). In adult trisomic mice, treatment with a $GABA_A$ receptor antagonist normalized NMDA-type glutamate receptor-mediated currents

and induction of LTP was restored (Nambu, Lewis, Wharton, & Crews, 1991). Regarding *in vivo* studies, experience-dependent neural plasticity is of time-critical nature (Escorihuela, Fernandezteruel, et al., 1995). The main problem in DS is the lack of stability of the effects, probably due to alterations in the translation of transient synaptic changes into stable structural modifications.

1.2. Methods

In this first part of the Thesis I took a mixed experimental and computational modeling approach for analyzing the repercussion of single-cell neuromorphological properties on the neuronal network. Computational models allow the exploration of theoretical relationships between morphology and connectivity; however, the physiological relevance of the findings is not always clear. In this regard, mouse models showing different alterations of the dendritic morphospace along with cognitive impairment provide a convenient scenario for testing those findings.

First I extracted functional properties (dendritic wiring optimality) from specific neuromorphological metrics that I obtained from neuronal reconstructions of two mouse models (Ts65Dn and a Dyrk1A heterozygous) showing Down syndrome-like neuronal structure abnormalities and cognitive deficits. In order to explore the impact of dendritic architectural properties on the horizontal connectivity of cortical layer II/III, I implemented a computational model to explore and instantiate 2D homogeneous neuronal networks based on an existing model (Orlandi et al., 2013). I used this model to explore how the modification of dendritic tree size, its complexity and the density of synaptic contacts modulates the network topology and computational capacities. Finally, using published experimental data from our lab, I instantiated networks recapitulating the neuromorphological alterations found in Down syndrome mouse models.

1.2.1. Optimal dendritic wiring of cortical pyramidal neurons of Ts65Dn and Dyrk1A+/-

To identify how neuromorphological changes may affect dendritic wiring optimality , I used published neuronal reconstructions of single pyramidal neurons manually selected and injected with Lucifer Yellow (LY) (G N Elston & Rosa, 1997; Guy N Elston, Benavides-Piccione, & DeFelipe, 2001). Briefly, pyramidal neurons of layers II/III of motor cortices (M2) in 150 μm vibratome sections tangential to the cortical surface that contain whole basal dendritic trees are filled with LY by continuous current injection. A camera lucida

microscope attachment was used to draw the basal dendritic arbor, and those drawings are the actual information I used.

I used reconstructions of mouse models that show relevant genotype-specific dendritic arbor abnormalities along with cognitive deficits:
(1) The first dataset (M Dierssen et al., 2003) were neuronal reconstructions of Ts(1716)65Dn (Ts65Dn) a Down's syndrome (DS) and wild-type (wild-type) mice. The chromosomal rearrangement in B6EiC3Sn a/A-Ts (1716)65Dn (Ts65Dn) female was originally generated by radiation inducing a spontaneous reciprocal translocation of the telomere proximal region of Mmu16 to the centromere and pericentromeric region of Mmu17 (1716) and mice derive crossings of a B6EiC3Sn a/A-Ts (1716)65Dn (Ts65Dn) female to B6C3F1/J males (The Jackson Laboratory). Euploid littermates were used as controls.
(2) For the second dataset (Benavides-Piccione et al., 2005) neuronal reconstructions were obtained from heterozygous *Dyrk1A* mice (C57BL/6J-129Ola mixed genetic background, Harlan Ibérica, S.L.), a candidate gene for DS. Wild-type littermates were used as controls.

Of note, the controls of these two strains have different genetic backgrounds, and thus the study was separated in four different experimental groups, so that I could also compare non-pathological variations in dendritic structure.

Neuromorphological analysis

From the 82 neuronal reconstructions published in (M Dierssen et al., 2003)(Ts65Dn) and (Benavides-Piccione et al., 2005)(Dyrk1A+/-), I selected six pyramidal neurons from two mice per genotype. In the published work, metrics obtained included dendritic length and dendritic complexity obtained by the Sholl analysis. Even though the original datasets also include spine density measurements, I have focused here on the dendritic branching phenotype. These measures were obtained manually for the Ts65Dn experiment and using the Neurolucida package for the heterozygous mice. However, Neurolucida morphology files (*.asc; http://www.mbfbioscience.com/neurolucida) were not available. I re-analyzed the original data to obtain measurements that were comparable across models and that are needed for estimating dendritic wiring optimality.

I used the Simple Neurite Tracer plugin (Longair, Baker, & Armstrong, 2011) (available via http://fiji.sc/Simple_Neurite_Tracer as part of the package Fiji) to obtain *.swc format morphology files from the original camera lucida dendritic tree drawings. The software semi-automates the reconstruction procedure by finding the highest intensity path between manually selected points in an image. The obtained paths can be saved in standard neuronal reconstruction formats and subsequently analyzed. **Figure 3** shows a schematic overview of this procedure.

Simple Neurite Tracer morphological files for Ts65Dn, Dyrk1A+/- and their wild-type littermates were then exported to Trees Toolbox in *.swc format to obtain morphological metric statistics using the *stats_tree* function (Cuntz, Forstner, Borst, & Häusser, 2010). Briefly, the function provides a set of measurements that describe in detail the (1) dendritic tree size: total length, maximum and mean path length, mean branch length and dendritic spanning area; (2) dendritic complexity: number of branch points, maximum and mean branching order and dendritic area (surface occupied by dendrite); and (3) other morphological aspects: mean straightness of dendritic branches, mean branching angle, mean asymmetry, center of mass in different directions and the ratio between width and height (see **Table 1**).

Table 1: Neuromorphological metrics. Summary of the studied neuromorphological metrics used in this Thesis, with their units and a short description.

Name	Unit	Description
Total length	µm	Total length of dendrite, including all the branches of the dendritic tree
Path length	µm	Length from a terminal point to the root of the tree
Branch length	µm	Length of a single branch, including dendritic segments between branch points
Spanning area	µm²	Area covered by the tree
Number of branch points	-	Number of branches in a tree
Branch order	-	Property of every branch. Starts from value 0 at the root of the tree and increases by 1 after every branch point
Dendritic area (density)	µm²	Area occupied by dendritic segments

Straightness	-	Ratio between the path length and the euclidean distance between a terminal point and the root of the tree
Branching angle	rad	Angle between two daughter branches at any branch point
Asymmetry	-	At any branch point, the ratio between the number of terminal points of the less complex and the more complex daughter branch
Center of mass	µm	Center of mass of the tree in a single dimension
Width vs Height ratio	-	Ratio between the width of a tree (size in x) and its height (size in y)

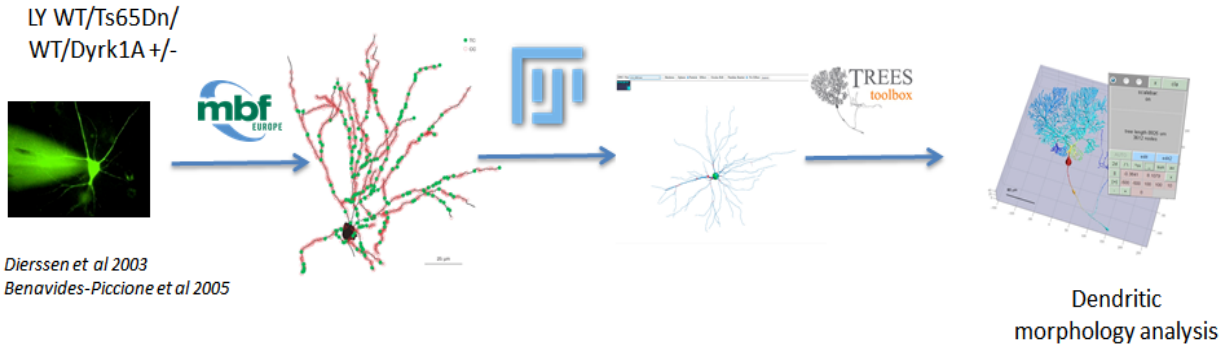

Figure 3: Schematic representation of the workflow for single neuron reconstruction and morphometric analysis. LY injections were performed and camera lucida drawings obtained as part of previous studies in our lab. 2D reconstructions were obtained using Simple Neurite Tracer in Fiji. A statistical analysis of the morphological metrics summarized in Table 1 was done using the Trees Toolbox.

Sholl analyses were done in the mutant models by quantifying the number of branches intersecting circles at equispaced radii from the soma with a radius step = 25 µm (dendritic branches smaller than 25 µm might not be counted) in the camera lucida drawings (M Dierssen et al., 2003). High magnification imaging (x100 Zeiss immersion lens) was used to quantify spine densities by counting the number of spines per 10 µm increments of 20 randomly selected dendritic segments (M Dierssen et al., 2003).

Principal Component Analysis

To identify the metrics that better separate the Ts65Dn, Dyrk1A +/- and their respective controls, I performed a Scaled Principal Component Analysis (Wold, Esbensen, & Geladi,

1987) (PCA) of dendritic tree architectural metrics using the PCA function of R. Plots were constructed in R (version 3.4.1) using ggplot2 (version 2.2.1) to reduce the number of variables into a smaller number of principal components (artificial variables) that account for most of the variance.

The purpose of this analysis was to identify which morphological variables explain most of the variance in the analyzed neurons, and to what extent combinations of those variables explain the differences between genotypes. All metrics were statistically tested for their variance among groups using ANOVA (ggpubr implementation, version 0.1.5). Pairwise comparisons were performed using two-way unpaired t-tests. Shapiro-Wilk tests were used to check whether the distributions are normal.

Optimal dendritic wiring

Cuntz found that dendritic trees optimally wired to connect to sets of points (synapses) in space follow a power law between the total tree length and the amount of branch points(Cuntz et al., 2012) . The power law was derived mathematically based on Cajal's law for conservation of cytoplasm and conduction time (Ramón y Cajal 1995). Here I explored whether trisomic and heterozygous neurons were optimally wired, and also if the differences in morphological metrics between the controls of the trisomic and heterozygous strains detected in the PCA, affected optimality. This is important since there is a strain-dependent motor behavior difference.

Optimality was assessed by fitting a power law to the relation between total tree length and amount of branch points (described in detail in Cuntz, Mathy, and Häusser 2012). The code used for the analysis, including reconstruction datasets, the morphological metric statistical analysis and the power law fit to the reconstructed trees can be found at https://bitbucket.org/linusmg/2d_model_bitbucket.

1.2.2. A 2D minimal model to determine the impact of dendritic wiring features on network properties

The next question was if single cell neuromorphological properties (namely dendritic tree size, its variability, dendritic complexity and synaptic density) had an effect on network connectivity. To this aim I used a 2D minimal computational model, that allowed us an in silico exploration of the most important neuromorphological variables and an instantiation of the DS networks.

The model mimics the growth process of a homogeneous network (Orlandi et al., 2013) providing a synthetic instantiation of a 2-dimensional homogeneous neuronal population. The assumption of a bi-dimensional homogeneous local cortical network (Orlandi et al., 2013) is justified given that our experimental data derive from "mosaic-like" basal dendritic trees. This computational model allows to explore the changes in the morphospace driven by the dendritic properties (in this case of different mouse models), and determine the topological properties of the instantiated "mutant" networks, relating them to computational capacities of neuronal networks.

I used the numerical values derived from the neuromorphological analysis performed in datasets of the previously described models (Ts65Dn and Dyrk1A +/-) and a transgenic mouse model (Altafaj et al., 2001), over-expressing *DYRK1A* (TgDyrk1A, Altafaj et al., 2001). In this model the full-length rat *DYRK1A* sequence is under the control of an inducible sheep metallothionein-Ia promoter in a C57BL6/SJL background. Littermates not expressing the transgene were used as controls. This third dataset was obtained from (de Lagran et al., 2012).

Finally, to test dendritic rewiring effects I used environmental enrichment (See Chapter I). Briefly, after weaning (21 days of age), TgDyrk1A and wild-type mice were randomly reared under non-enriched (NE) or enriched (EE) conditions. The NE mice were reared in conventional Plexiglas cages (20 x 12 x 12 cm height) in groups of two to three animals. EE mice were reared in spacious (55 x 80 x 50 cm height) Plexiglas cages with toys, small houses, tunnels, and platforms. The arrangement was changed every 3 days to maintain the novelty of the environment. To stimulate social interactions, six to eight mice were housed in each EE cage. Both groups were maintained under the same 12 h (8:00 to 20:00) light-dark cycle in controlled environmental conditions of humidity (60%) and temperature (22 ± 1ºC), with free access to food and water. In both experiments, only females were used given that

transgenic male mice showed hierarchical behavior, as similarly seen in Ts65Dn mice (Martinez-Cué et al. 2005).

Computational model

A family of models with similar assumptions to ours have been used to explore spontaneous activity generation in primary neuronal cultures (Orlandi et al., 2013), horizontal connectivity in the mammalian cortex (Voges et al., 2010) and basic features of cortical networks (Feldt, Bonifazi, & Cossart, 2011). Here I implemented and refined a computational generative model developed by (Orlandi et al., 2013) (originally devised for neuronal cultures) in order to simulate the local horizontal connectivity of cortical layers II/III in which I then introduce detailed dendritic tree neuromorphological properties (dendritic tree size, its variability, dendritic complexity and spine density). **Figure 4** schematically shows the circuit building process.

All the software development and computational analysis was performed in an HP-Z620 Workstation (equipped with an Intel Xeon E5-2620, 64GB RAM, Nvidia Quadro K4000 and 1TB SSD drive) running Ubuntu 16.04. In order to introduce the dependence on neuromorphological metrics and to have an efficient instantiation, I implemented the model in C++. Random number generators and optimization of the compiled code required the libraries GSL (Gough, 2009) and BOOST (Siek, Lee, & Lumsdaine, 2001). The source code can be found at https://bitbucket.org/linusmg/2d_model_bitbucket.

Our implementation homogeneously locates somata (defined as circles with diameter d_s) in a synthetic 2D space. Subsequently, from each soma emerges a quasi-straight path (axon) given by a biased random walk (10 μm segments are subsequently located forming an angle with previous segments given by a uniform distribution). The average length of the axons is and each single axon length is obtained from a Rayleigh distribution with mean and scale parameter σ_a. Dendritic trees for each soma are generated as circles with radii given by a gaussian distribution with mean $\overline{r_d}$ and sigma σ_d (See *Parametrization of the 2D minimal model* and **Table** 2 for an overview of the parameters from the literature used).

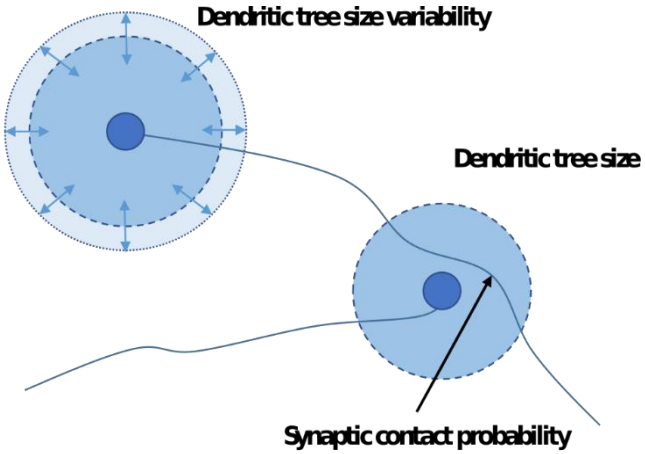

Figure 4: Schematic representation of the circuit building process. Circles with diameter d_s representing somas are located randomly in a synthetic 2D space. From the somas emerge quasi-straight paths representing axons. Each single axon length is obtained from a Rayleigh distribution with mean $\overline{l_a}$ and scale parameter σ_a. Dendritic trees are circles with radius $\overline{r_d}$ and sigma σ_d. In every point of the synthetic 2D space having an overlap between an axon and a dendritic tree, a new connection between the two neurons is added with probability α.

A connection between the two neurons is obtained in every point of the 2D space where a dendritic tree and an axon overlap, with a probability α that has been assumed to be constant in existing models (see **Figure 4**). However, this does not take into account fine neuromorphological aspects such as dendritic complexity and spine density that are relevant since they determine the spatial distribution of synaptic contacts in neuronal trees. In order to introduce those in the model, I assumed that the probability of finding a spine at a specific radius of the tree overlapping with an axon is equivalent to the probability of a synaptic contact. I defined the probability for a synaptic contact α(r) at a given radius r from the soma as the probability of finding a dendrite at *r*, and a spine in a dendritic fragment of length Δl. This probability is given by the spine $sd(r)$ and dendritic $bp(r)$ densities at r:

$$\alpha(r) = \frac{bp(r) \cdot w}{2\pi r} \cdot sd(r) \cdot \Delta l \qquad \textbf{Equation 1}$$

Where w is the diameter of a dendrite (set as 1μm in our model), and $\Delta l = 1\mu m$ is determined by the spatial discretization of the model.

Thus, the synaptic contact probability in our modified 2D model depends on the radial distributions of both dendritic branches and spine densities. Interestingly, using the wild-type experimental data for spine and dendritic densities, the mean synaptic contact

probability $\overline{\alpha(r)}$ is approximately 0.3. This proved to be anatomically correct by being close to estimated connection probability values in the mammalian cortex (Markram, 2006; Orlandi et al., 2013). Once all the neurons have been positioned, scanning all the points in the 2D space, and calculating the synaptic contact probability in each axon overlapping a dendritic tree, allows to obtain pairwise connections between all the neurons in the network. Taking into account that redundant synapses can occur between a pair of neurons leads to the generation of a weighted adjacency matrix.

Parameterization of the 2D minimal model

To study the implications of single-neuron morphology on network connectivity, it has been necessary to perform a systematic revision and selection of existing data. I parameterized generic neuronal properties with data from previously published articles (Ballesteros-Yáñez, Benavides-Piccione, Elston, Yuste, & DeFelipe, 2006; Komulainen et al., 2014; Orlandi et al., 2013) accounting for cortical layer II/III morphological properties including soma diameter, axonal length and tortuosity, and synaptic contact probability in wild-type mice. The values and sources used are summarized in **Table 2**.

Among the generic properties introduced in the model it is worth mentioning the neuronal density and axon parameterization chosen. Using a realistic neuronal density is not possible due to computational limitations (Orlandi et al., 2013; Voges et al., 2010). Thus, I subsampled to a reduced neuron density by, instead of assuming a projection of the complete layer II/III, simulating a thin sublayer of the width of a single soma diameter. This subsampling leads to a neuron 2D density of 1350 neurons/mm^2, obtained by multiplying the neuronal density in the 3D layer by the width of the thin layer modeled. Based on this assumption, I located randomly 3037 neurons in the area of the synthetic circuit, set to 2.25mm^2 (1.5mm sided square with periodic boundary conditions). The axonal mean length used is 500µm in order to simulate only local horizontal connections (given by the local axonal tree in layer II/III) following experimental data in the mouse M2 cortical layer II/III (Voges et al., 2010), and disregarding horizontal patchy connections, connections between cortical layers and interhemispheric projections.

Table 2: Neuromorphological parameter set for the instantiation of the 2D model. Values and units for each parameter are specified along with the literature reference they were obtained from.

Variable	Description	Value	Units	Reference
d_s	Soma diameter	15	µm	(Komulainen et al., 2014)
$\overline{r_d}$	Dendritic mean radius	150	µm	(Ballesteros-Yáñez et al., 2006)
σ_d	Sigma of the dendritic radius Gaussian distribution	40	µm	(Orlandi et al., 2013)
α	Synaptic contact probability	0.3	-	(Markram, 2006; Orlandi et al., 2013)
$\overline{l_a}$	Axon mean length	500	µm	(Voges et al., 2010)
σ_a	Scale parameter of the axonal length Rayleigh distribution	100	µm	(Orlandi et al., 2013)
dl	Axonal biased random walk segment length	10	µm	(Orlandi et al., 2013)
σ_θ	Sigma of the axonal biased random walk angle Gaussian distribution	6	º	(Orlandi et al., 2013)

To introduce dendritic morphological information of **Table 4** in the model, I need to include the synaptic contact probability, which is defined by **Equation 1**. I obtained the $bp(r)$ and $sd(r)$ distributions for cortical layer II/III basal trees of wild-type C57BL/6J mice based on data from the literature (Ballesteros-Yáñez et al., 2006) (see **Figure 5**). To obtain mathematical expressions, I performed polynomial regressions on the dendritic and spine density distributions. Fitting was done using the lm function in R, and 5th and 6th degree polynomial expressions were obtained. The obtained polynomials were introduced in **Equation 1** to calculate the synaptic contact probability at any radius of the modeled dendritic trees.

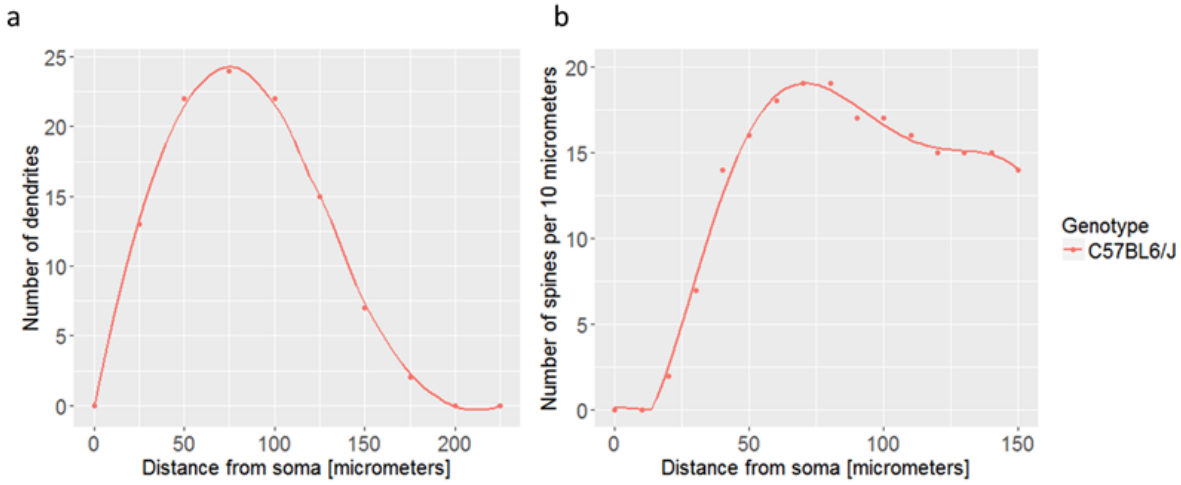

Figure 5: Dendritic and spine numbers dependency on the dendritic tree radius in wild-type C57BL/6J mice. Distributions of dendrite (a) and spine (b) numbers in function of the distance from the soma. Mean values obtained from the literature characterizing basal dendritic trees of M2 in the layer II/III of the cortex (Ballesteros-Yáñez et al., 2006).

1.2.3. Network topology characterization using graph theory

I analyzed the adjacency matrices (square matrices that represent all the vertices of a graph and the connections among them) of the instantiated networks using graph theory. Due to the properties of the model, I expect the generated networks to be close to random, but to deviate slightly from purely random (Erdös-Rényi) networks by the fact that neurons close to each other have higher probability of connection. Previous studies have shown that expected consequences of the distance-dependent connection probability on topological properties of the network are: an *excess of reciprocal connections* (if neuron i is an afferent of j, the probability of j being an afferent of i increases), an increased *clustering coefficient* (probability to find a connection between adjacent neurons to a given neuron i) (Vegue et al., 2017), the existence of neurons with high values in the *degree distribution* (with the degree of a node being the amount of connections received and sent by that neuron) (Girvan & Newman, 2002) and increased *small-worldness* (ratio between the clustering coefficient and the path length of a network)(Bassett & Bullmore, 2006). Those metrics were obtained using the iGraph package in R.

To study properties of the network as proxies of behavior, I focused on three topological metrics that can be related to computational capacities of networks processing information: routing efficiency, storage capacity and cost, that have been previously defined for whole-

brain tractography-based networks (Griffa et al., 2014) or single cells (Poirazi & Mel, 2001) and defined what I call the efficiency space.

Routing efficiency

Routing efficiency is the shortest path length φ_{ij} between any pair of nodes (neurons) i and j. φ_{ij} is inversely proportional to the amount of intermediate nodes separating i and j. Thus, when two neurons in the network are closely connected or have more synapses, the efficiency gets higher. The shortest path length matrices were obtained using the "distances" function in iGraph (http://igraph.org/r/doc/distances.html), which computes pairwise distances taking into account weighted connections using the Dijkstra algorithm (Ahuja, Mehlhorn, Orlin, & Tarjan, 1990). Then, the formal definition for the routing efficiency is as follows:

$$E_{rout} = \sum_{i,j} \frac{1/\varphi_{ij}}{N(N-1)}, i \neq j \qquad \textbf{Equation 2}$$

Where φ_{ij} is the graph path length between the nodes *i* and *j*, and *N* is the total number of nodes in the graph.

Storage capacity

I estimated the storage capacity of the instantiated network as the total number of non-redundant possible states for a given neuron receiving s synapses provided by d presynaptic neurons as previously defined by Poirazi and Mel (Poirazi & Mel, 2001). Briefly, assuming that the dendritic location of inputs (synapses) does not affect the integration of the signal in a given neuron (linear model), the combinatorial "n chose k" quantification of possible states for a post-synaptic neuron expressed in bits (basic unit of information) is given by:

$$B_L = 2log_2\binom{s+d-1}{s} \qquad \textbf{Equation 3}$$

Where *s* is the number of received synaptic connections and *d* is the number of unique afferents providing them.

Cost

The cost of the network is given by the product of the number of synapses and the physical distance between any pair of neurons. Thus, the cost is proportional to the connection weight (amount of synapses to be maintained) and physical distance between any pair of neurons. This measure quantifies the cost of making and maintaining anatomical connections between neurons (Griffa et al., 2014). The cost of a connection between neurons i and j can be expressed as the product between the amount of synapses connecting them (synaptic weight w_{ij}) and the physical distance separating them (l_{ij}). Then, the total wiring cost of the whole network is:

$$cost = \sum_{i<j}^{N} w_{ij} l_{ij} \qquad \textbf{Equation 4}$$

Where w_{ij} is the number of synaptic connections between neurons *i* and *j*, and l_{ij} the physical distance between them.

Pareto optimality

Cajal's law for conservation of cytoplasm and conduction time suggests that there is a tradeoff between material cost and signal integration efficiency in single neurons. I here propose that a similar tradeoff exists between the cost of wiring a network and its routing efficiency or storage capacity, so that that neuronal networks are optimally wired to maximize routing efficiency and storage capacity while preserving material cost. This concept is closely related to the single-neuron wiring optimality mentioned in **Section 1.2.1**. The concept of maximizing more than one property simultaneously (multi-objective optimality) is not novel and was first tackled by Vilfredo Pareto (Griffa et al., 2014) in the scope of economical sciences. Following his definition, a Pareto-optimal system implies that no change can be made to improve any aspect (i.e.increasing routing efficiency or storage capacity, or reducing the material cost) without deteriorating another one. Thus, a Pareto-suboptimal system can undergo a Pareto improvement by improving an aspect without deteriorating any other (e.g. by a rearrangement of connections, a neuronal network could have higher routing efficiency without increasing its cost).

In order to include this concept in our analyses, once computational capacities were obtained for each point in the dendritic morphospace, I identified the Pareto front of the explored region in the efficiency space with the MATLAB function *prtp* (https://es.mathworks.com/matlabcentral/fileexchange/22507-calculation-of-pareto-points) and compared relative distances between instantiated networks and the Pareto front to assess their multi-objective optimality.

1.3. Results

1.3.1. Single-neuron wiring optimality in models of intellectual disability

In order to assess putative implications of dendritic alterations for signal integration I obtained and analyzed basal dendritic tree reconstructions of LY stained neurons of Ts65Dn and Dyrk1A +/- and compared them with their respective wild-type littermates (6 neurons from 2 animals per group, **Figure 6**). The studies previously performed in our laboratory showed morphological alterations in the basal dendritic trees of layer II/III motor cortex pyramidal neurons in intellectual disability mouse models. Specifically, dendritic tree size and complexity, and synaptic density were reduced in the Ts65Dn (M Dierssen et al., 2003), and Dyrk1A+/-(Benavides-Piccione et al., 2005) models.

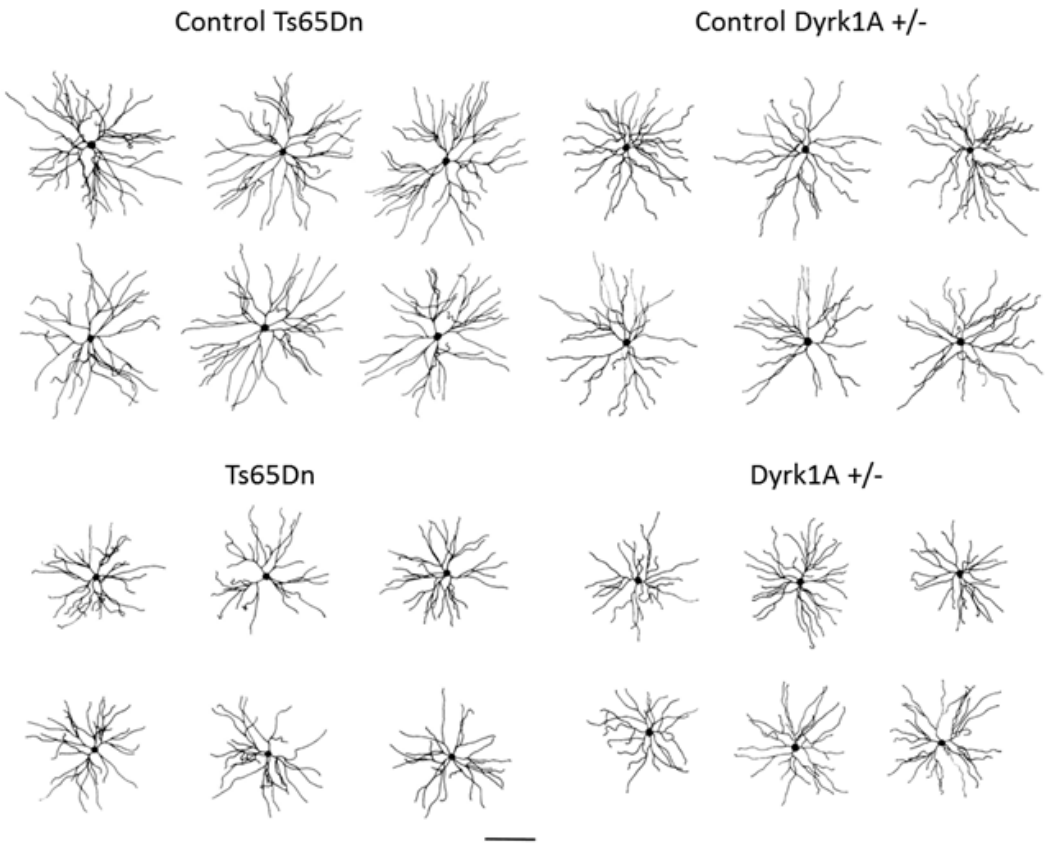

Figure 6: Camera lucida drawings of the basal dendritic trees of layer II/III motor cortex pyramidal neurons of Ts65Dn, Dyrk1A +/- and their respective controls. The drawings represent a 2D projection of the basal tree seen in the tangential plane to the cortical layers. Qualitatively, Ts65Dn and Dyrk1A+/- appear to be smaller and less complex than their wild-type counterparts. Scale bar = 100μm.

Here I used camera lucida drawings (**Figure 6**) to evaluate dendritic tree morphological features and performed a statistical analysis using Trees Toolbox. An overview of metrics summarizing the analysis can be seen in **Figure 8**. A Trees Toolbox workspace with all the reconstructions can be found at https://bitbucket.org/linusmg/2d_model_bitbucket.

Dendrograms of representative trees provide an overview of the morphological differences between the two mouse models and their controls. Regarding the impact of genetic background, the comparison of wild-type mice of two strains (B6EiC3Sn and C57BL/6J-129Ola) showed similarly long dendrites reaching a maximum length close to 200 μm. However, dendritic complexity for those single trees was higher in the Ts65Dn control, with 44 branches, and slightly lower in the Dyrk1A+/- control, with 36 branches. Both Ts65Dn and Dyrk1A+/- neurons show reduced branch length, reaching maximum dendritic lengths close to 125 μm for Ts65Dn neurons and slightly below 120 μm in Dyrk1A+/- and reduced dendritic complexity (31 branches in Ts65Dn neurons and 25 branches in Dyrk1A+/- neurons, respectively).

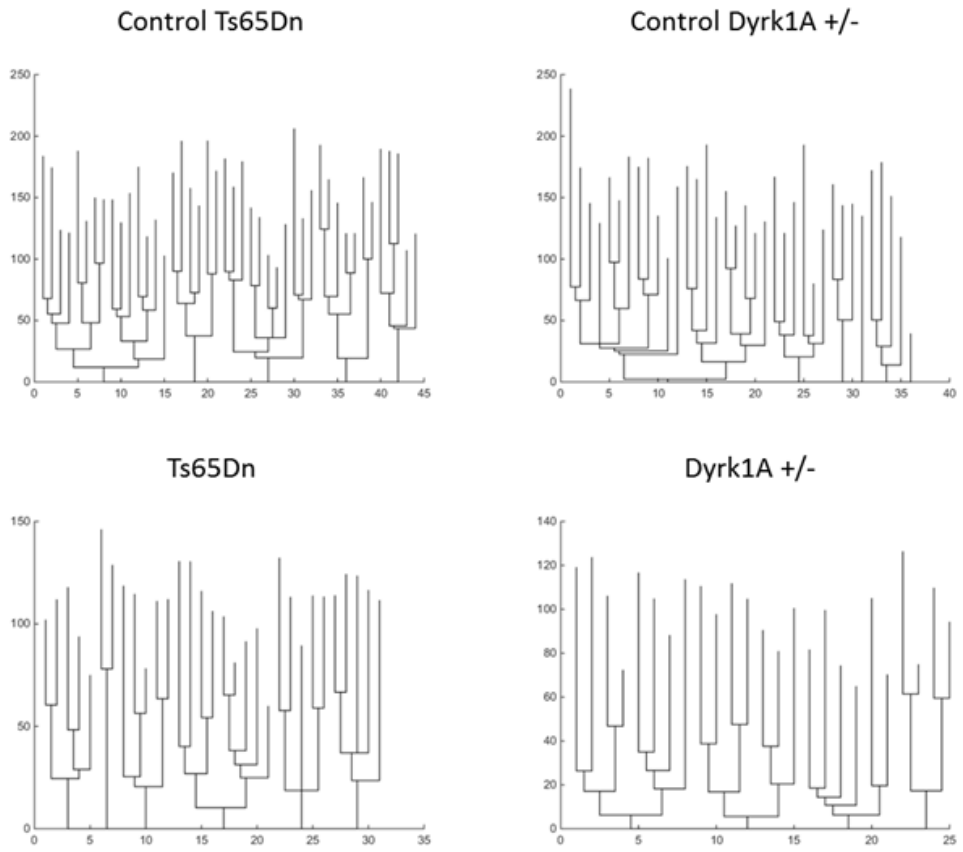

Figure 7: **Dendrograms for four representative neurons.** The plot represents the amount of branches versus their length. Ts65Dn and Dyrk1A+/- neurons show reduced dendritic complexity and shorter dendritic segments than controls.

To assess the morphological differences in detail, I used the series of metrics described in **Table 3**. Those provide a complete description of the dendritic tree size, complexity and morphological properties of the dendrites (length, straightness and branching angle). First, I performed a one-way ANOVA test to identify significant differences among the four conditions and two-way unpaired t-tests with post-hoc Bonferroni corrections to identify pairwise significant differences.

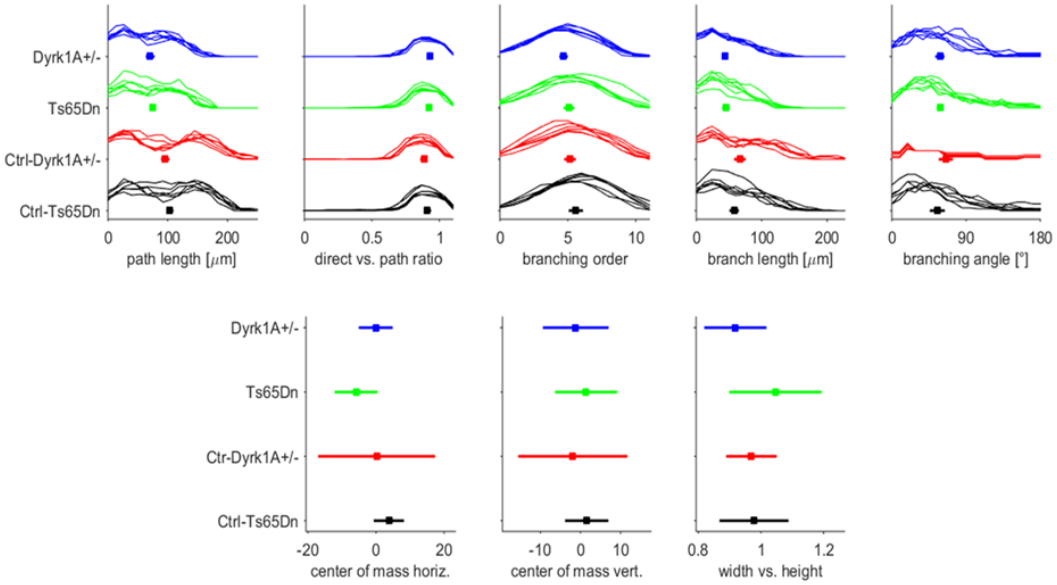

Figure 8: Overview of the neuromorphological metrics obtained in the statistical analysis with the Trees Toolbox. Each panel shows series of distributions of morphological metrics for Ts65Dn control (black), Dyrk1A+/- control, Ts65Dn and Dyrk1A+/- mice. Each line is a density plot of a single metric for all the branches of a single neuron. The square colored dots and lines indicate the mean and standard deviation of the distributions.

The total dendritic length (sum of the lengths of dendritic segments) is severely reduced in both mutant models ($F_{(3,20)} = 46.357$, $p = 3.44 \times 10^{-9}$; **Figure 9** upper left panel) as compared to their controls. Ts65Dn neurons show a statistically significant reduction respect to their controls (2251 ± 99 μm versus 3954 ± 403 μm, respectively, Bonferroni *post-hoc* correction; $p = 7.10 \times 10^{-8}$). In a similar trend, Dyrk1A+/- neurons have reduced dendritic length than their wild-type controls (2143 ± 334 μm and 3415 ± 352 μm respectively; Bonferroni-corrected $p = 6.34 \times 10^{-6}$). Finally, the comparison between the two control groups (B6EiC3Sn and C57BL/6J-129Ola) show a tendency to have trees with less dendritic material (sum of the lengths of dendritic segments: 3954 ± 403 μm and 3415 ± 352 μm respectively; Bonferroni-corrected $p = 0.051$) in the C57BL/6J-129Ola strain. Spanning area (**Figure 9** bottom left panel), maximum path length (**Figure 9** upper middle panel) and mean density (**Figure 9** middle right panel) follow similar trends, with a marked reduction in both mutant mouse models and subtle differences between control strains, if any (see **Table 3**). Interestingly, the number of branch points (**Figure 9** middle left panel), which provides an estimation of tree complexity, shows also significant overall differences ($F_{(3,20)} = 7.39$, $p = 1.60 \times 10^{-3}$). Specifically, it is reduced in Ts65Dn neurons compared to their controls (27.8 ± 2.6 and 37.3 ± 5.9 respectively; Bonferroni-corrected $p = 7.35 \times 10^{-3}$), but also in C57BL/6J-

129Ola versus B6EiC3Sn neurons (28.5 ± 4.3 and 37.33 ± 5.9 respectively; Bonferroni-corrected p = 0.014). This trend is also observed for the mean branch order (see **Table 3**), indicating that less complex dendritic trees tend to have reduced branching hierarchies.
Our analysis shows that both Ts65Dn and Dyrk1A+/- neurons have reduced mean branch length (**Figure 9** upper right panel) compared to controls ($F_{(3,20)}$ = 29.85, p = 1.39 x 10^{-7}). There are significant differences between Ts65Dn and their controls (45.2 ± 3.9 μm and 57.8 ± 5.2 μm respectively; Bonferroni-corrected p = 1.53 x 10^{-3}), and between Dyrk1A+/- and their controls (43.2 ± 2.7 μm and 66.5 ± 6.9 μm respectively; Bonferroni-corrected p = 4.79 x 10^{-7}). The neurons from mixed background C57BL/6J-129Ola mice have longer segments than B6EiC3Sn neurons (66.5 ± 6.9 μm versus 57.8 ± 5.2 μm respectively; Bonferroni-corrected p = 0.039). The mean density is also lower in both Ts65Dn and Dyrk1A+/- versus their controls, and increased in C57BL/6J-129Ola versus B6EiC3Sn (see **Table 3**).

Finally, straightness (**Figure 9** bottom middle panel) and the mean branching angle (**Figure 9** bottom right panel) show similar values in Ts65Dn, Dyrk1A+/- and the C57BL/6J-129Ola control groups. However, ANOVA revealed significant overall differences $F_{(3,20)}$ = 10.35, p = 2.53 x 10^{-4} for straightness and $F_{(3,20)}$ = 3.52, p = 0.034 for mean branching angle) mainly driven by the different phenotype of the B6EiC3Sn control neurons. Specifically, compared to the B6EiC3Sn strain, C57BL/6J-129Ola wild-type neurons show reduced straightness (0.884 ± 0.017 and 0.911 ± 0.017 respectively; Bonferroni-corrected p = 0.023), and increased mean branching angle (0.96 ± 0.13 rad and 1.14 ± 0.12 respectively; Bonferroni-corrected p = 0.031).

One-way ANOVA tests among the four groups did not show significant differences for the center of mass of the trees, the maximum branch order, the width vs. height ratio and the mean asymmetry (data not shown).

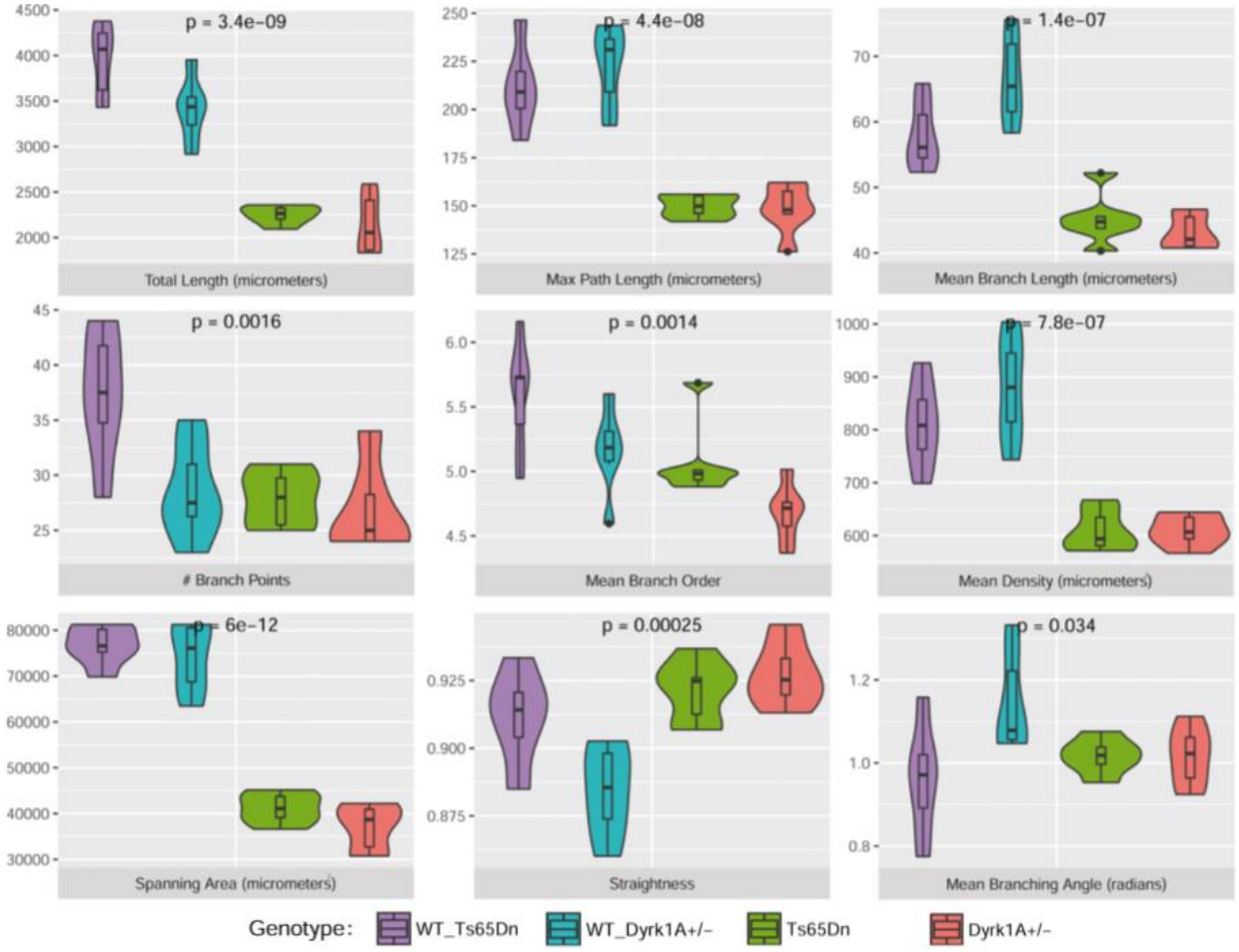

Figure 9: Boxplots of single-neuron morphological metrics. Each panel shows violin and boxplots for metrics having significant differences in one-way ANOVA tests between the Ts65Dn, Dyrk1A+/- and their respective controls, the p-value of the test is shown on top of each panel. Each metric units are specified in the panel label. Each colored box/violin plot represents the distribution of the metric for each group. Spanning area, mean and maximum path length, mean branch length and dendritic area are reduced in both Ts65Dn and Dyrk1A+/- mice. Dyrk1A+/- control littermates show decreased total length and branch points, increased mean branch length (accompanied by reduced straightness), increased mean branching angle and increased mean density.

Table 3: Statistical comparisons between single-neuron morphological metrics. The table summarizes both the mean and standard deviation values for controls and mutant mouse models, the t-values, degrees of freedom and Bonferroni-corrected p-values for pairwise t-tests between each mutant mouse model and its respective control. The three last columns show Bonferroni corrected p-values for comparisons between wild-type strains, the variation between sample means F and the one-way ANOVA test p-value.

		Control		ID model							
Metric	Study	Mean	SD	Mean	SD	t-value	degrees of freedom	ID model comparison Bonferroni-corrected p-value	WT comparison Bonferroni-corrected p-value	ANOVA F	ANOVA p-value
Total length	Ts65Dn	3953.67	403.03	2250.97	98.87	10.05	5.60	**7.10E-08**	0.05	**46.36**	**3.44E-09**
	Dyrk1A+/-	3415.15	352.24	2142.93	334.03	6.42	9.97	**6.34E-06**			
Max path length	Ts65Dn	211.63	21.34	149.88	5.98	6.82	5.78	**1.64E-05**	1	**34.32**	**4.43E-08**
	Dyrk1A+/-	222.98	21.02	148.32	12.91	7.41	8.30	**1.03E-06**			
# Branch points	Ts65Dn	37.33	5.92	27.83	2.56	3.61	6.81	**7.35E-03**	**1.36E-02**	**7.39**	**1.60E-03**
	Dyrk1A+/-	28.50	4.32	26.83	4.02	0.69	9.95	1			
Straightness	Ts65Dn	0.91	0.02	0.92	0.01	-1.16	8.81	1	**2.26E-02**	**10.35**	**2.53E-04**
	Dyrk1A+/-	0.88	0.02	0.93	0.01	-5.13	8.98	**3.02E-04**			
Max branch order	Ts65Dn	9.33	0.52	8.83	1.17	0.96	6.88	1	1	2.81	0.07
	Dyrk1A+/-	9.17	0.75	8.00	0.89	2.44	9.72	0.18			
Branching angle	Ts65Dn	0.96	0.13	1.02	0.04	-0.95	6.01	1	**3.18E-02**	**3.52**	**3.38E-02**
	Dyrk1A+/-	1.14	0.12	1.02	0.07	2.16	8.01	0.24			
Branch length	Ts65Dn	57.85	5.20	45.21	3.92	4.75	9.30	**1.53E-03**	**3.87E-02**	**29.85**	**1.39E-07**
	Dyrk1A+/-	66.51	6.91	43.15	2.70	7.71	6.50	**4.79E-07**			
Path length	Ts65Dn	103.66	3.68	75.40	3.07	14.46	9.69	**2.38E-09**	**2.80E-02**	**80.58**	**2.42E-11**
	Dyrk1A+/-	95.70	5.00	70.52	5.23	8.53	9.98	**1.73E-08**			
Branch order	Ts65Dn	5.59	0.43	5.08	0.30	2.40	8.99	0.08	0.21	**7.61**	**1.39E-03**
	Dyrk1A+/-	5.16	0.33	4.69	0.22	2.90	8.66	0.13			
Width vs. Height	Ts65Dn	0.98	0.11	1.05	0.14	-0.94	9.21	1	1	1.42	0.27
	Dyrk1A+/-	0.97	0.08	0.92	0.10	1.02	9.57	1			
Center of mass horiz.	Ts65Dn	3.80	4.07	-5.90	5.92	3.31	8.87	0.54	1	1.08	0.38
	Dyrk1A+/-	0.18	16.83	-0.09	4.63	0.04	5.75	1			
Center of mass vert.	Ts65Dn	1.54	5.07	1.39	7.40	0.04	8.84	1	1	0.24	0.87
	Dyrk1A+/-	-1.95	13.31	-1.18	7.87	-0.12	8.12	1			
Spanning area	Ts65Dn	76751	4288	41192	3310	16.08	9.40	**1.59E-09**	1	**93.69**	**6.00E-12**
	Dyrk1A+/-	74224	7634	37133	5101	9.90	8.72	**7.55E-10**			
Asymmetry	Ts65Dn	0.38	0.02	0.38	0.03	0.11	7.67	1	1	0.77	0.52
	Dyrk1A+/-	0.37	0.01	0.39	0.02	-1.71	7.54	0.92			
Dendritic area	Ts65Dn	810.42	81.29	608.55	39.52	5.47	7.24	**6.17E-04**	1	**19.75**	**3.40E-06**
	Dyrk1A+/-	877.94	100.42	609.71	30.12	6.27	5.89	**1.42E-04**			

Principal component analysis

To identify metrics that explain the differences found in those intellectual disability models or account for the strain-dependent neuromorphological variability, I performed a Principal Component Analysis (PCA) of the mutant and wild type mice. The two first principal components explain 59.7% of the variance in the data (**Figure 10**). Principal Component 1 (PC1, 45.7% explained variance) is mainly contributed by measures that account for the size of the tree: the dendritic spanning area, the total length of the tree and the maximum and mean path length. Following those metrics, straightness, branch order and density show considerable contributions to PC1. Principal Component 2 (PC2, 14.0% explained variance) is mainly contributed by the mean branching angle, followed by the number of branch points, the horizontal center of mass and the mean branching asymmetry.

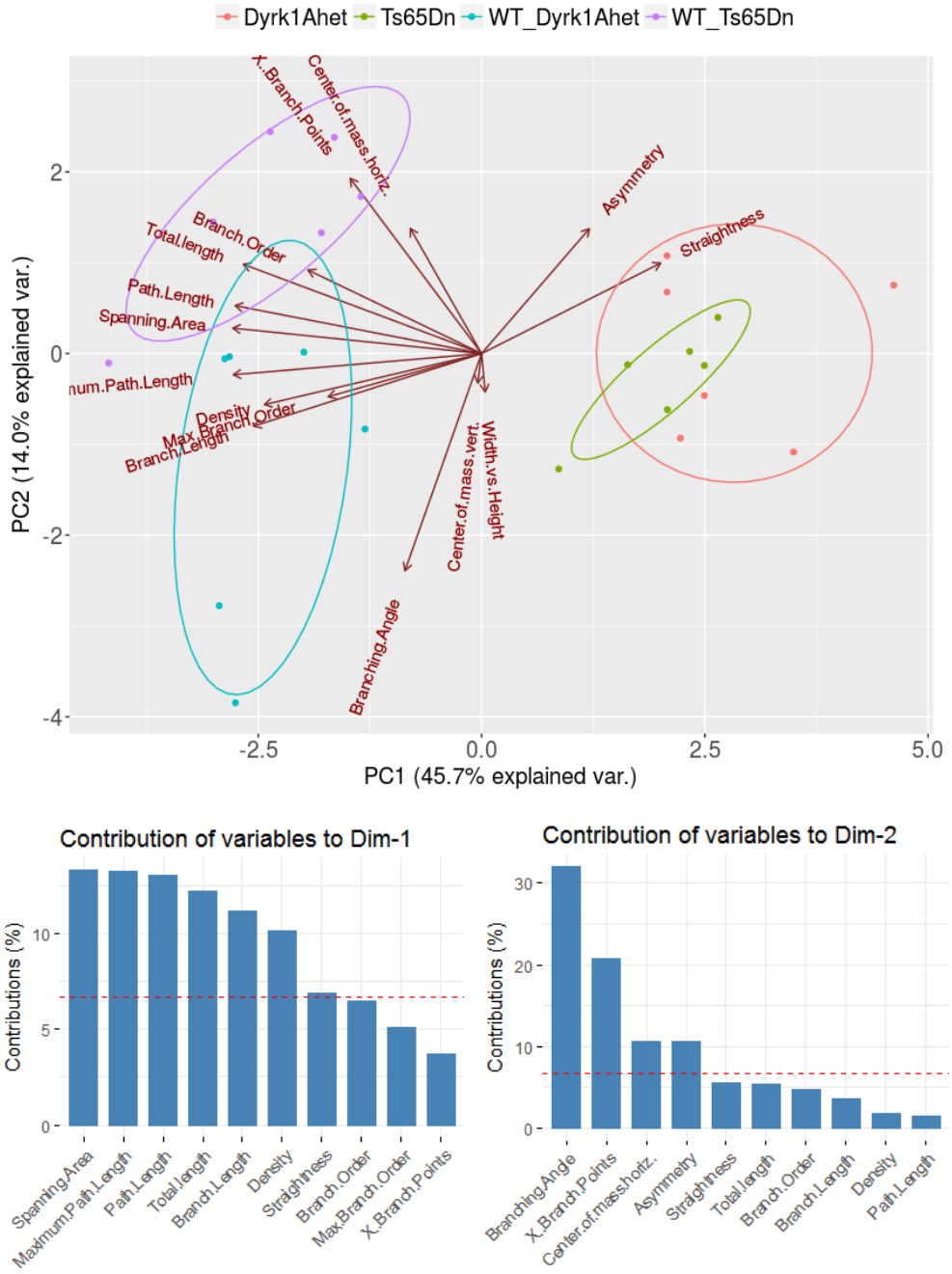

Figure 10: Principal component analysis. PCA of the variables, where arrows represent the direction of each variable in the PCA space. Longer arrows belong to variables that are well represented by the two principal components. Each of the points represents one neuron, colored by the group they belong to. 68% confidence normal data ellipses for each group are drawn with solid lines. Bottom Bar plots showing the percentage of explained variance for each principal component. Bars represent the contribution (%) of each variable and the red dashed lines indicate the expected average contribution. The first principal component is a composite variable accounting for the dendritic tree size and the total dendrite length. The second principal component is a composite variable accounting for other morphological measurements, mainly the branching angle, the number of branch points and the horizontal center of mass and mean asymmetry.

A 2D projection overview of those principal components shows that the neurons clustered by genotype, being the wild-type and mutants mainly separated in PC1, while the different genetic background by PC2. Thus genetic background dependent neuromorphological differences are mainly related to mean branching angle and number of branch points. Instead, the variables contributing more to the difference between wild-types and mutants are mostly related to the tree span, its complexity and the straightness of the branches, being the most relevant metrics for dendritic wiring optimality. These results suggest that intellectual disability mouse models could have an excess of branches in small trees.

Wiring optimality

Cuntz, Mathy, and Häusser 2012 demonstrated using a large set of morphological reconstructions from the NeuroMorpho.org database, that dendrites of the various neuronal classes balance wiring costs differently, but the relationships between key features in their morphology followed scaling laws that could be predicted by models based on wiring minimization principles. If a set of *n* points is distributed in 2D with a density $d = n/S$, the average surface occupied by a single point is $s' = d^{-1}$, and the average minimal distance between points is proportional to the square root of s': $r = c \cdot d^{-1/2}$ with proportionality constant *c*. If the average distance between connected points is minimal, the total length of dendrite connecting the *n* points is proportional to *S* and given by $L = c \cdot S \cdot d \cdot d^{-1/2} = c \cdot S \cdot d^{1/2}$. Assuming a constant ratio between the number of contact points and the number of branch points (Cuntz et al., 2012), the total dendritic length scales with the number of branch points following a ½ power law in any optimally wired 2D tree. I thus asked whether the differences in dendritic arborization that I detected in behaviorally affected mouse models (Ts65Dn and Dyrk1A+/-) and between two different strains could affect wiring optimality.

In our reconstructions, I assumed branch points as the target points of the dendrites, since those can unambiguously be counted. Thus, to test the optimality, I fitted a power law to the total dendritic length vs. number of branch points, both normalized by the dendritic tree spanning area. I found that the B6EiC3Sn Ctrl-Ts65Dn trees follow a close-to-optimal space fitting a power law of 0.45 s.e.= 0.13, while both the Ts65Dn and Dyrk1A +/- neurons deviate from the 0.5 optimal value, with power laws of 0.74 s.e.=0.15 and 0.75 s.e.=0.16, respectively. Interestingly, the Ctrl-Dyrk1A+/- group (C57BL/6J-129Ola), present an

intermediate phenotype, with a power fit of 0.65 s.e.=0.11 indicating slightly suboptimal tree wiring.

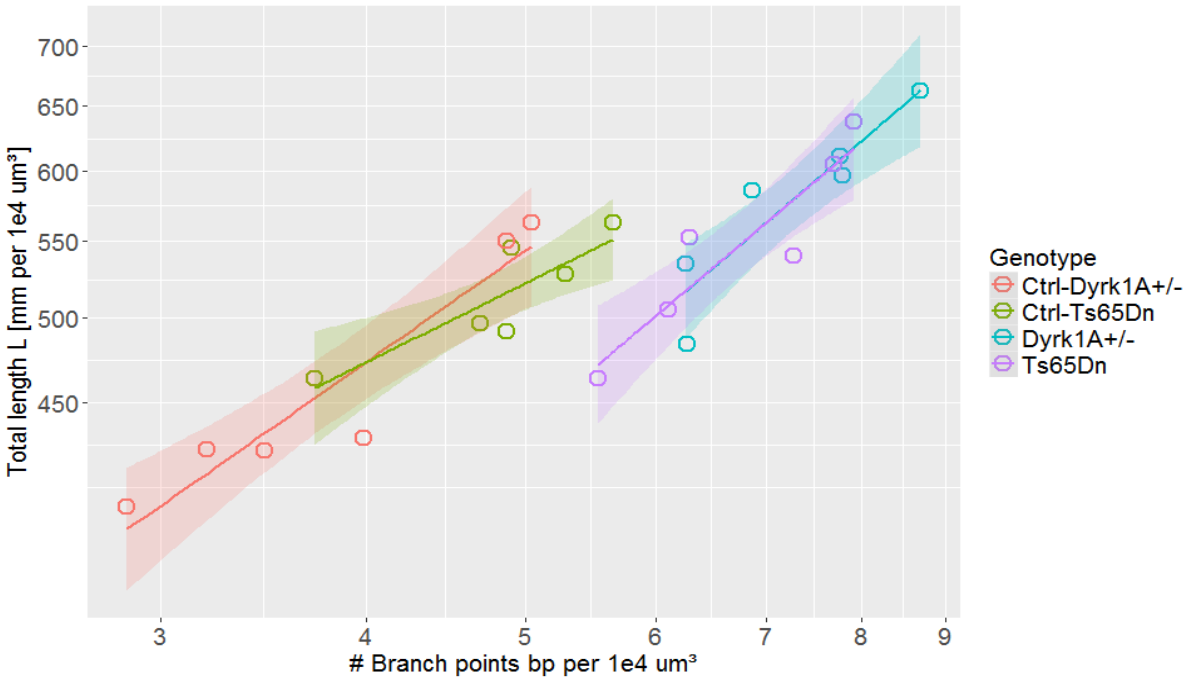

Figure 11: Power law relations between total dendritic length and branch number for layer II/III basal tree reconstructions of Ts65Dn and Dyrk1A+/- neurons, and their respective controls. The ½ optimal power for 2D trees is only followed by the B6EiC3Sn Ts65Dn control trees (power = 0.45±0.13), while both Ts65Dn (0.74±0.15) and Dyrk1A+/- (0.75±0.16) show a strong deviation, and C57BL/6J-129Ola Dyrk1A+/- controls (0.65±0.11) slightly deviate. The number of branch points and total length were normalized by the dendritic surface (S=10.000 μm²). Shaded regions indicate 95% confidence level interval of the power law fit.

1.3.2. Network computational capacities

In order to investigate whether the micropatterning properties of dendritic trees can have a significant impact on network topology, I used a minimal model (see **Section 1.2.3**) and as a first step, I did an in silico exploration of the impact of specific variables on the efficiency of a cortical layer II/III morphospace.

Exploration of the wild-type cortical layer II/III local network morphospace

The 2D minimal model parameterized as described in **Section 1.2.2** is a template of a wild-type cortical layer II/III local network. By modifying its parameterization, new networks can be instantiated and this allows the exploration of the effects of neuromorphological variations of dendritic trees on the network connectivity and, ultimately, on the network topological properties as defined in **Section 1.2.3**.

To explore the dendritic morphospace I scaled the parameters mean $\overline{r_d}$ (mean dendritic diameter), σ_d (standard deviation of the dendritic diameter), and α_c (synaptic contact probability, contributed by dendritic complexity and spine density). I scaled the parameters above and below the values estimated for the wild-type template (from 0.5 times to 1.5 times the control mean value with a step of 0.1 in the case of $\overline{r_d}$, and from 0.4 to 2.4 times the control mean value with a step of 0.2 in the case of σ_d). Those parameterizations imply variations in dendritic size and its variability, dendritic complexity and spine density.

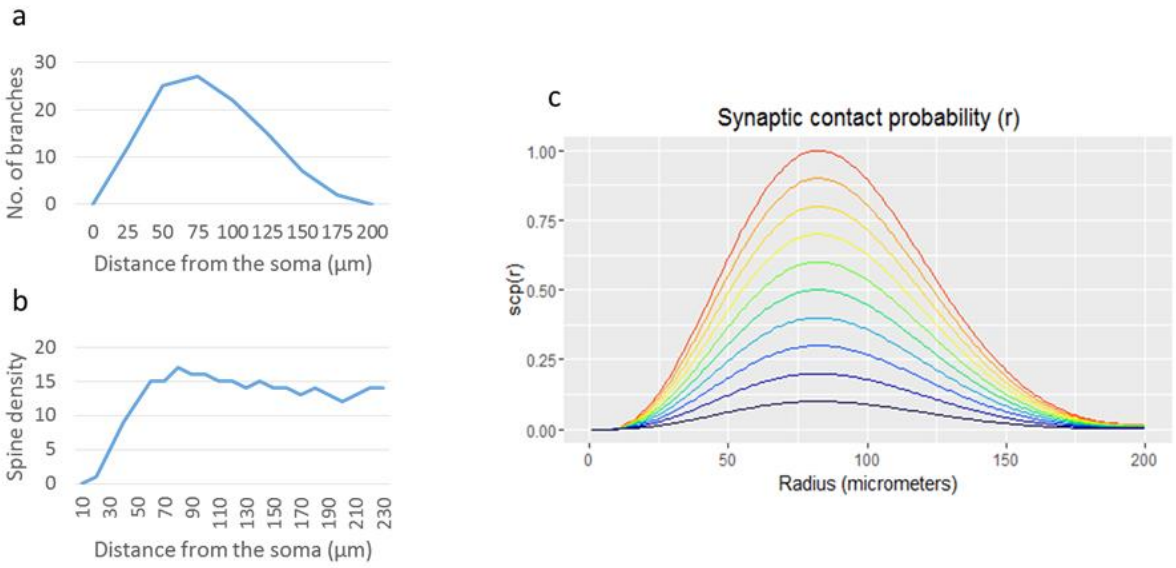

Figure 12: **Synaptic contact probability extraction from experimental data.** Schematic example for (a) dendritic and (b) spine density distributions of a pyramidal layer II/III basal tree, and for the synaptic contact probability as calculated **Equation 1**. The colored lines represent arbitrarily scaling of the synaptic contact probability along the y axis, which simulates scaling at the same time the numbers of dendrites and/or spines found along the dendritic tree radius.

Dendritic and spine density distributions are not homogeneous in real neurons, and they imply a variable distribution of synaptic contacts along the space covered by the dendritic

tree. A common point of view is that dendritic tree morphology determines the balance of received inputs and is constrained by (1) the computations to be done in specific neuronal layers (ultimately determined by neurodevelopment) (Wen, Stepanyants, Elston, Grosberg, & Chklovskii, 2009), and (2) the wiring optimality discussed by (Cuntz et al., 2012) and described further in **Section 1.3.1**.

I asked how relevant the basal tree synaptic contact distribution observed in cortical layer II/III is for the local network connectivity. To answer this question, I explored variations in the synaptic contact probability by performing two sets of simulations. In the first set of simulations I used a constant synaptic contact probability α_c. This contact probability has been estimated to be between 0.1-0.2 in overlapping axons and dendritic trees in the rat cortex (Markram, Lübke, Frotscher, Roth, & Sakmann, 1997). This probability is ultimately dependent on the morphology of the neurons, thus neurons with highly complex and big amounts of synaptic contacts will have high synaptic contact probability, and a low one for low complexity trees making few synapses. To explore how variations among these cases would affect the network topology and given the reduced dimensionality of our network (Orlandi et al., 2013), I scaled its values between 0.1 and 1 with a step of 0.1 in order to explore values around a biologically meaningful range (Markram et al., 1997). In the second set of simulations, the analytic expressions for the control dendritic and spine density distributions were scaled between 0.5 times to 1.5 times the control mean value with a step of 0.1 to explore a range of synaptic density values that could be modulated by environmental conditions or pharmacological treatments.
For each combination of parameters I generated 10 networks, following Orlandi et al. and analyzed their topological properties and computational capacities(Orlandi et al., 2013). Those are defined in **Section 1.2.3** and the model source code and analysis R scripts can be found at https://bitbucket.org/linusmg/2d_model_bitbucket.

Synaptic contact probability and dendritic tree size modulate routing efficiency and storage capacity

First, inspired by already existing similar models of local 2D networks, I explored the morphospace by assuming that the synaptic contact probability is constant along the

dendritic trees (**Figure 13**; blue symbols). After, I introduce a synaptic contact probability extracted from experimental data. In the constant synaptic contact probability condition, the cost of wiring the network grows linearly when increasing synaptic contact probability. The superlinear growth network cost detected when increasing dendritic tree size, suggests that the amount of contacts in the network depends less of the radius and more of the spanning area of the neuron. As compared to those parameters, increasing dendritic tree size variability only produces a slight linear increase of the cost (see **Figure 13**, lower panel).

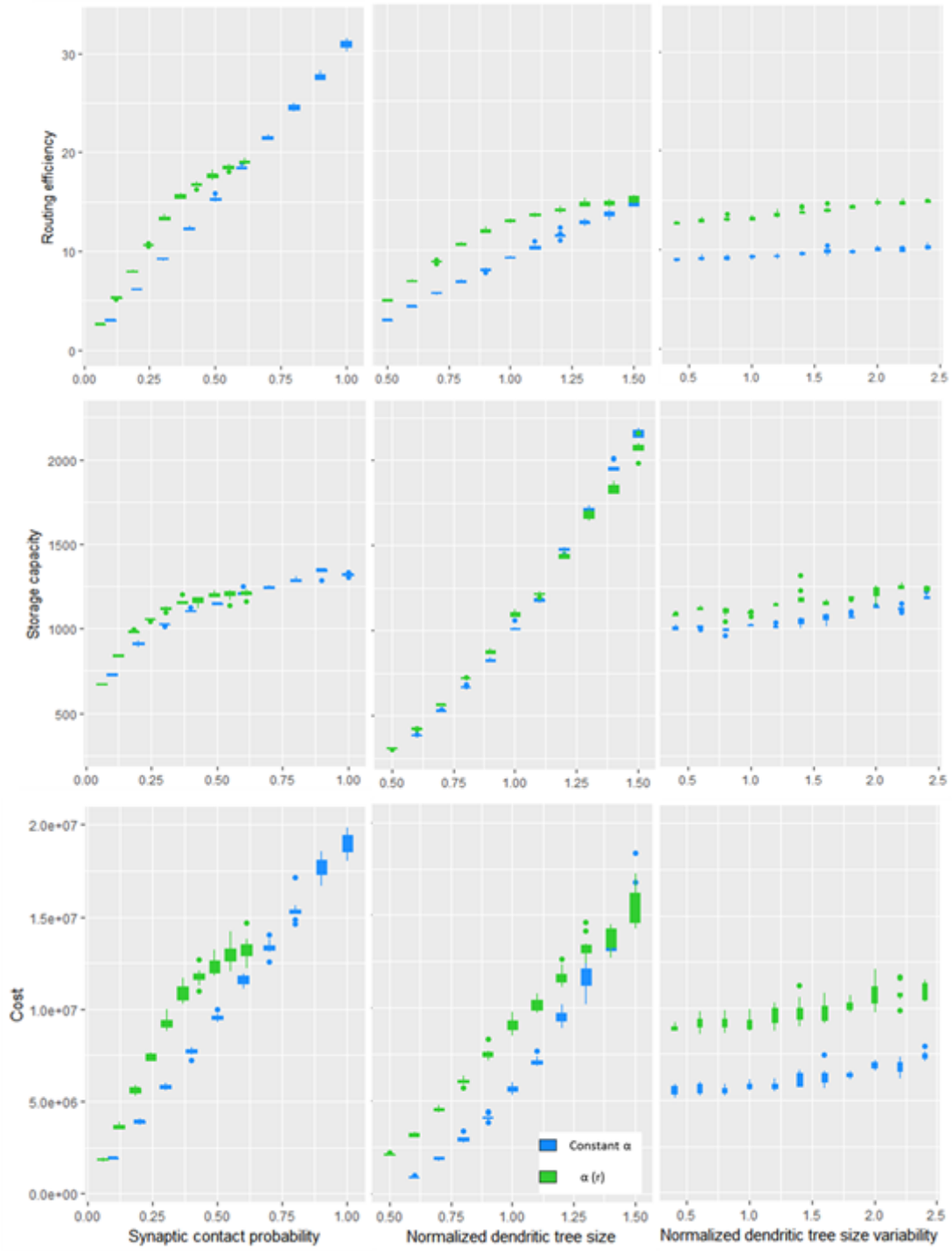

Figure 13: Implications of the morphospace exploration on the computational capacities of the cortical layer II/III local network model. Box plots for routing efficiency (1st row), storage capacity (2nd row) and cost (3rd row) in the 2D model upon the variation of the synaptic contact probability (1st column), normalized dendritic tree size (2nd column) and dendritic tree size variability (3rd column). In blue, instantiations of the network with a constant synaptic probability α, in green instantiations with synaptic contact probability dependent on the radius $\alpha(r)$ (**Equation 1**). Each box plot represents 10 simulations with the same parameterization.

Both increases in dendritic tree size and synaptic contact probability (contributed by dendritic complexity and synaptic density), increase linearly the network routing efficiency (**Figure 13**, upper panel). However, the impact of increasing synaptic or dendritic densities is stronger than that of increasing dendritic tree size. A similar effect was encountered when increasing dendritic tree size variability, which only slightly increases the network routing efficiency.

Regarding storage capacity of the network, I found that it is increased linearly by increasing dendritic tree size and asymptotically with synaptic contact probability (**Figure 13**, middle panel). Again, increasing dendritic tree size variability only slightly increases storage capacity. Interestingly, I observed that storage capacity gets to a plateau for synaptic contact probability values of the magnitude reported in the mammalian cortex (0.1-0.4) (Markram, 2006). This might be counterintuitive, since it would suggest that if assuming that storage capacity is constant along the dendrite, then it would be saturated in basal conditions. Thus, in a second round of simulations, I explored the same morphospace while introducing the radial dependence on the synaptic contact probability (**Section 1.2.3**1.2.3. Network topology characterization using graph theory see **Figure 13**; green symbols).

In fact, even considering its radial dependence, the mean synaptic contact probability gets to the same plateau as above (disregarding radial dependency), for synaptic contact probability values (0.1-0.4), I found that in this case the amount of connections is higher than in the case of constant synaptic probability ($\propto_c$), as shown by the shape of the curve of the network cost, which is directly proportional to the number of connections (**Figure 13**, lower panel). The increased number of connections implies slightly increased storage capacity and routing efficiency (**Figure 13**, upper and middle panels). It should be noted that storage capacity starts to saturate for $\alpha(r)$ values for which the amount of synaptic contacts (cost) is still growing. This implies that the saturation is not produced because the trees are not making new contacts, but because those are coming from the same afferents. Also, the routing efficiency grows asymptotically for increasing dendritic tree size. Together with the increased storage capacity, this defines a "sweet spot" around the wild-type values, where storage capacity and routing efficiency are maximally increased in comparison to the constant synaptic contact probability instantiations.

Finally, when the dendritic tree size is increased, the higher amounts of contacts (cost) introduced by the radial dependency does not grow superlinearly, meaning that the contacts do not increase proportionally to the dendritic tree area, but to its radius, and the increasing dendritic tree size variability again produced a slight linear increase in both cost, storage capacity and routing efficiency.

To test if the explored morphospace could also be constraining topological properties such as deviations from randomness, promoting higher clustering in the network and a small-world organization. I obtained mean degree distributions, small-worldness ratios and reciprocities. The analysis shows that log degree distributions do not deviate from exponential, implying that the networks have a random network topology (data not shown). Increased synaptic contact probability does not increase clustering, decreases small-worldness asymptotically and increases reciprocity asymptotically. A similar behavior is observed with increased dendritic tree size: clustering and reciprocity increase but the *small-worldness* ratio decreases. Dendritic tree size variability increases clustering linearly, and decreases small-worldness ratio and reciprocity linearly.

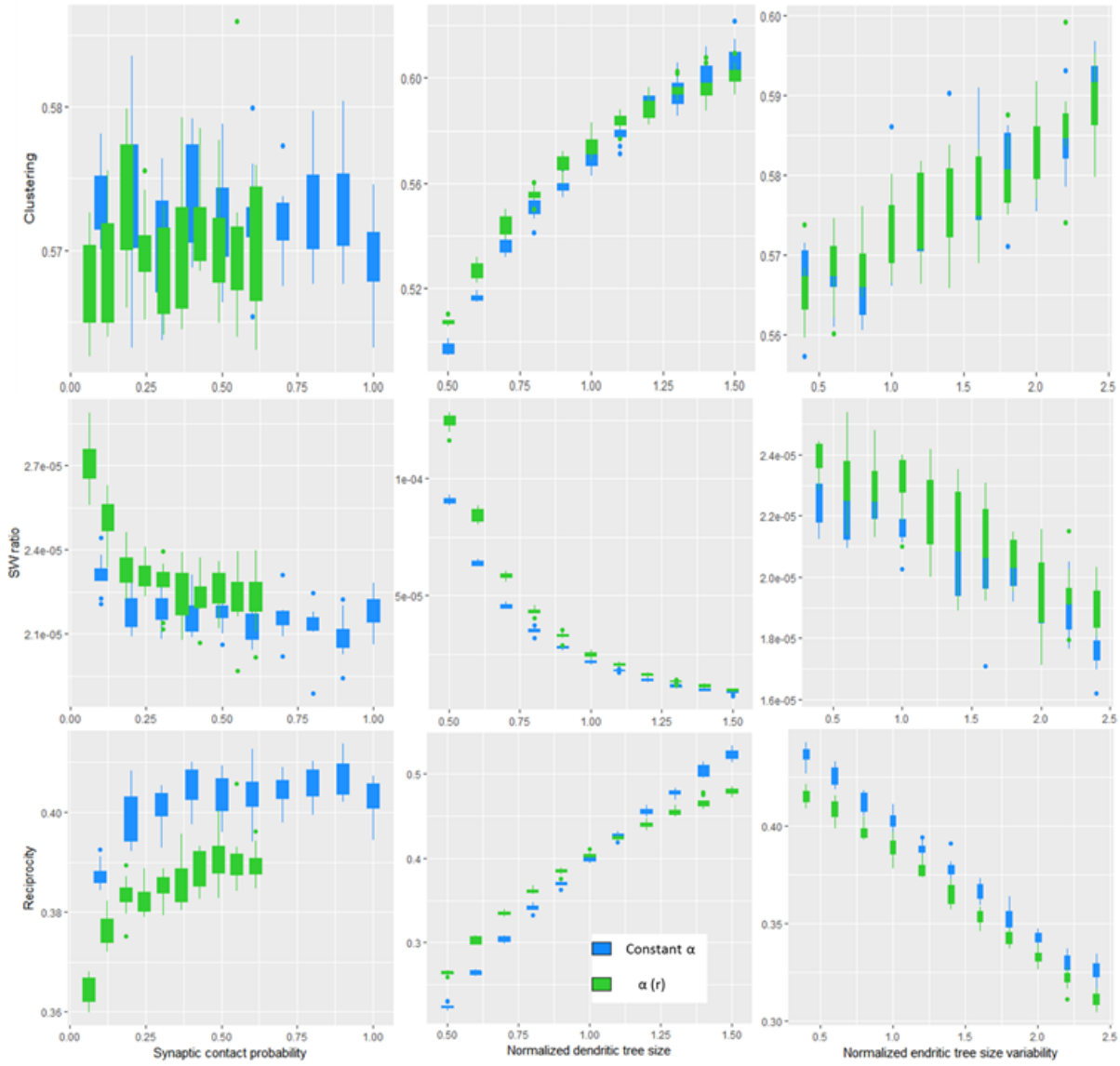

Figure 14: Implications of the morphospace exploration on topological properties of the cortical layer II/III local network model. Box plots for clustering (1st row), small-worldness ratio (2nd row) and reciprocity (3rd row) in the 2D model upon the variation of the synaptic contact probability (1st column), normalized dendritic tree size (2nd column) and dendritic tree size variability (3rd column). In blue, instantiations of the network with a constant synaptic probability α, in green instantiations with synaptic contact probability dependent on the radius $\alpha(r)$ (**Equation 1**). Each box plot represents 10 simulations with the same parameterization.

Dendritic abnormalities of mutant mouse models lead to reduced computational capacities

Our computational model allows to directly incorporate the neuromorphological metrics obtained previously in our laboratory, allowing us to also incorporate in the analysis a mouse model overexpressing *DYRK1A*, the TgDyrk1A published neuromorphological data (de

Lagran et al., 2012) along with the Ts65Dn and Dyrk1A+/-. This provided the opportunity to explore subtle gene dosage effects and the influence of slightly different genetic background on dendritic arborization. To do so, I used the published Sholl and spine density quantifications of our models but since I had no access to the cell density, axonal length and axon tortuosity, I used published control values. For this reason, in our instantiation of mutant networks I focus on dendritic architecture and do not assess the putative contributions of these other morphological properties on the network connectivity.

The published Sholl analysis data for all the models and their wild-type counterparts are listed in **Table 4** and **Table 5**. Those parameters provide a description of the dendritic complexity and synaptic densities in all the biological conditions that I aim to assess in our simulations.

Table 4: **Sholl analysis average values for Ts65Dn, Dyrk1A+/- cortical layer II/III basal trees and their wild-type counterparts.** Mean numbers of dendritic branches intersecting radii at increasing 25µm steps of distance to the soma for the Ts65Dn and Dyrk1A+/- DS mouse models and their respective controls.The last row indicates the references from which those values were obtained.

	Ctrl-Ts65Dn	Ts65Dn	Ctrl-Ts65Dn-EE	Ts65Dn-EE	Ctrl-TgDyrk1A	TgDyrk1A	Ctrl-Dyrk1A+/-	Dyrk1A+/-
Distance from soma (µm)	Number of dendrites (Sholl analysis)							
25	12	16	13	16	26	19	17	17
50	22	23	25	23	39	25	26	22
75	24	16	27	13	33	22	27	18
100	21	7	22	5	22	14	22	10
125	15	2	13	2	9	5	13	4
150	7	0	5	0	2	1	5	1
175	3	0	1	0	0	0	2	0
200	0	0	0	0	0	0	1	0
Reference	Dierssen et al. 2003				Martinez de Lagran et al. 2012		Benavides-Piccione et al. 2005	

Table 5: Average synaptic densities along the radius of Ts65Dn, Dyrk1A+/- cortical layer II/III basal trees and their wild-type counterparts. Mean numbers of spines in 10µm segments (see **Section 1.2.1**) in function of the distance to the soma for the Ts65Dn and Dyrk1A+/- DS mouse models and their respective controls.The last row indicates the references from which those values were obtained.

	Ctrl-Ts65Dn	Ts65Dn	Ctrl-Ts65Dn-EE	Ts65Dn-EE	Ctrl-TgDyrk1A	TgDyrk1A	Ctrl-Dyrk1A+/-	Dyrk1A+/-
Distance from soma (um)	Number of spines							
10	0	0	0	0	0	1	3	1
20	1	7	6	6	5	5	9	6
30	5	15	14	14	12	10	13	11
40	9	17	20	17	16	14	15	12
50	12	19	25	20	17	15	15	12
60	15	19	25	20	18	15	17	11.5
70	15	18	24	20	19	16	16	11
80	17	19	24	19	19	15	15	12
90	16	17	22	19	15	13	15	11.5
100	16	15	23	17	-	-	14.5	11
110	15	15	21	17	-	-	14	11
120	15	13	21	16	-	-	13.5	10.5
130	14	18	21	17	-	-	13	9
140	15	-	19	12	-	-	13	11

150	14	-	18	12	-	-	11	12
160	14	-	17	-	-	-	9	10
170	13	-	20	-	-	-	14	-
180	14	-	19	-	-	-	13	-
190	13	-	10	-	-	-	13	-
200	12	-	9	-	-	-	15	-
210	13	-	-	-	-	-	-	-
220	14	-	-	-	-	-	-	-
230	14	-	-	-	-	-	-	-
Reference	Dierssen et al. 2003				Martinez de Lagran et al. 2012		Benavides-Piccione et al. 2005	

Even though the experimental conditions and procedures were very similar in the three published experiments, the cross comparison among experimental controls showed variations in the amount and radial distributions of dendrites and spines (

Figure 15 a), but to ensure a meaningful comparison between experimental conditions, and even though these differences may be biologically relevant and possibly represent genetic background-dependent differences, I curated the data as follows: all the dendritic and spine density distributions were normalized to their respective control values for each single experiment and, in order to compare experimental conditions, I scaled the normalized distributions to a common control curve obtained from the literature data of layer II/III basal trees in M2 for B6EiC3Sn wild-type mice (

Figure 15 b and **Tables 4 and 5**).

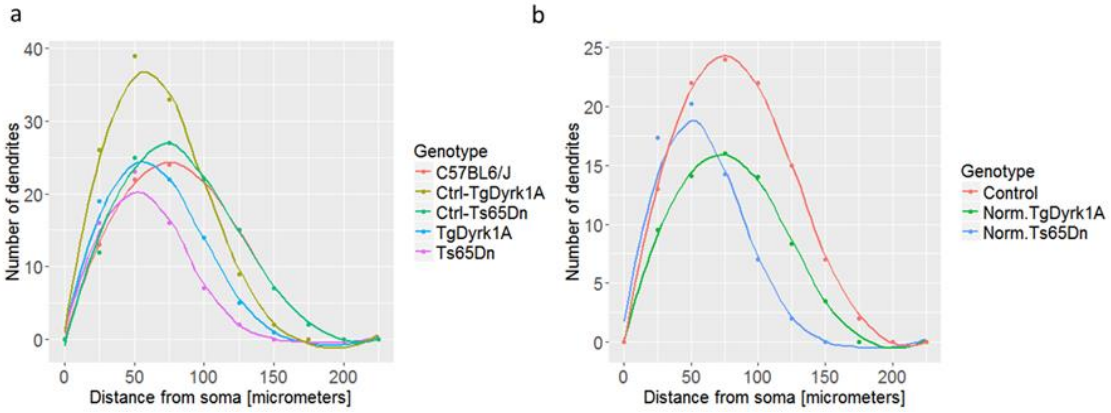

Figure 15: Normalization of dendritic radial distributions to the C57BL6/J strain wild-type data. (a) Distributions of dendrite numbers in function of the distance from the soma obtained from experimental data of different experiments. Each colored set of points shows the mean values obtained in the experiments, each line is a polynomial fit to those data points: in red, the common control used in our 2D computational model (C57BL6/J strain); in brown, the TgDyrk1A control; in green, the Ts65Dn control; in blue, the TgDyrk1A DS mouse model; and in purple, the Ts65Dn mouse model. Mean values obtained from the literature specified in the main text, characterizing basal dendritic trees of M2 in the layer II/III of the cortex. (b) Distributions of dendrite numbers along the radius of the tree for the Ts65Dn and TgDyrk1A DS mouse models normalized to a common control (C57BL6/J strain).

I obtained analytic expressions for dendritic and spine density distributions by performing polynomial regressions on the normalized distributions. Fitting was done using the lm function in R as described in **Section 1.2.2**. Normalized experimental data and polynomial regressions are shown in **Figure 16**. The obtained polynomials were directly introduced in the model in order to compute the synaptic contact probability in function of the distance from the soma as explained in **Section 1.2.2**.

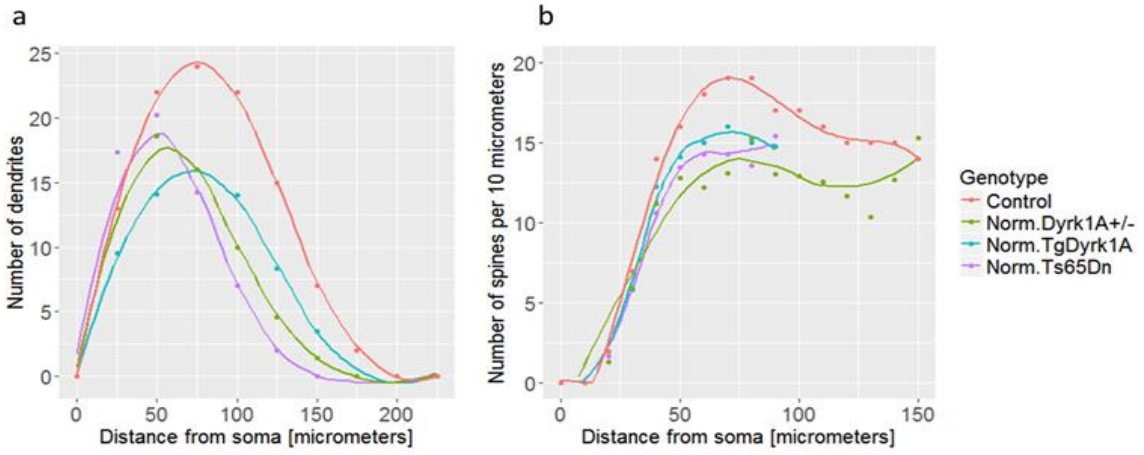

Figure 16: Dendritic and spine radial distributions normalized to wild-type C57BL6/J mice. Distributions of dendrite (a) and spine (b) numbers along the radius of the tree for the Dyrk1A+/- (green), TgDyrk1A (blue) and Ts65Dn (purple) DS mouse models normalized to a common control (C57BL6/J strain: in red).

I then introduced experimental dendritic and synaptic spine distributions from the Down syndrome mouse models (Ts65Dn, TgDyrk1A and Dyrk1A+/-) and generated 10 networks using the normalized distributions. These normalized distributions were used to assess the impact of the specific alterations found in the different DS mouse models on the topology and computational capacities of the modeled network.

I performed a one-way ANOVA test to identify significant differences among all the groups, and two-way unpaired t-tests with post-hoc Bonferroni corrections to identify pairwise significant differences. The three studied mouse models show reduced routing efficiency ($F_{(5,54)} = 7681$, $p = 1.07 \times 10^{-75}$) and storage capacity ($F_{(5,54)} = 8202$, $p = 1.83 \times 10^{-76}$). Storage capacity is strongly reduced, in Ts65Dn (587.2 ± 5.1 bits; Bonferroni-corrected $p = 6.34 \times 10^{-71}$) and Dyrk1A+/- (560.7 ± 4.9 bits; Bonferroni-corrected $p = 3.02 \times 10^{-72}$) networks, and to a lower extent in TgDyrk1A (857.9 ± 3.9 bits; Bonferroni-corrected $p = 6.55 \times 10^{-50}$) as compared to the C57BL/6J control (1042.6 ± 9.0 bits). Routing efficiency is also reduced in Ts65Dn (7.23 ± 0.07 A.U.; Bonferroni-corrected $p = 3.71 \times 10^{-66}$), TgDyrk1A (7.45 ± 0.07 A.U.; Bonferroni-corrected $p = 3.22 \times 10^{-65}$) and Dyrk1A+/- (6.21 ± 0.09 A.U.; Bonferroni-corrected $p = 4.33 \times 10^{-70}$) networks in comparison to the wild-type (12.80 ± 0.05 A.U.). From the position of the different models in the efficiency space, I can infer that while the three models deviate from the computational capacities of the wild-type, the one with worse implications in our simulations is the Dyrk1A+/- that shows 49% routing efficiency and 54% storage capacity of the control group. The comparison between the Ts65Dn and the TgDyrk1A is worth mentioning: while they show similar levels of routing efficiency (56% and 58% respectively), the Ts65Dn shows much less storage capacity (56%) than the TgDyrk1A (82%). This difference is caused mainly by the reduced tree size of the trisomic mice. At the same time, the fact that Ts65Dn and Dyrk1A+/- mice have very similar tree size, implies that the reduction almost exclusive in routing efficiency for Dyrk1A+/- networks versus Ts65Dn (-14%) is produced by the lower spine density observed in the heterozygous model.

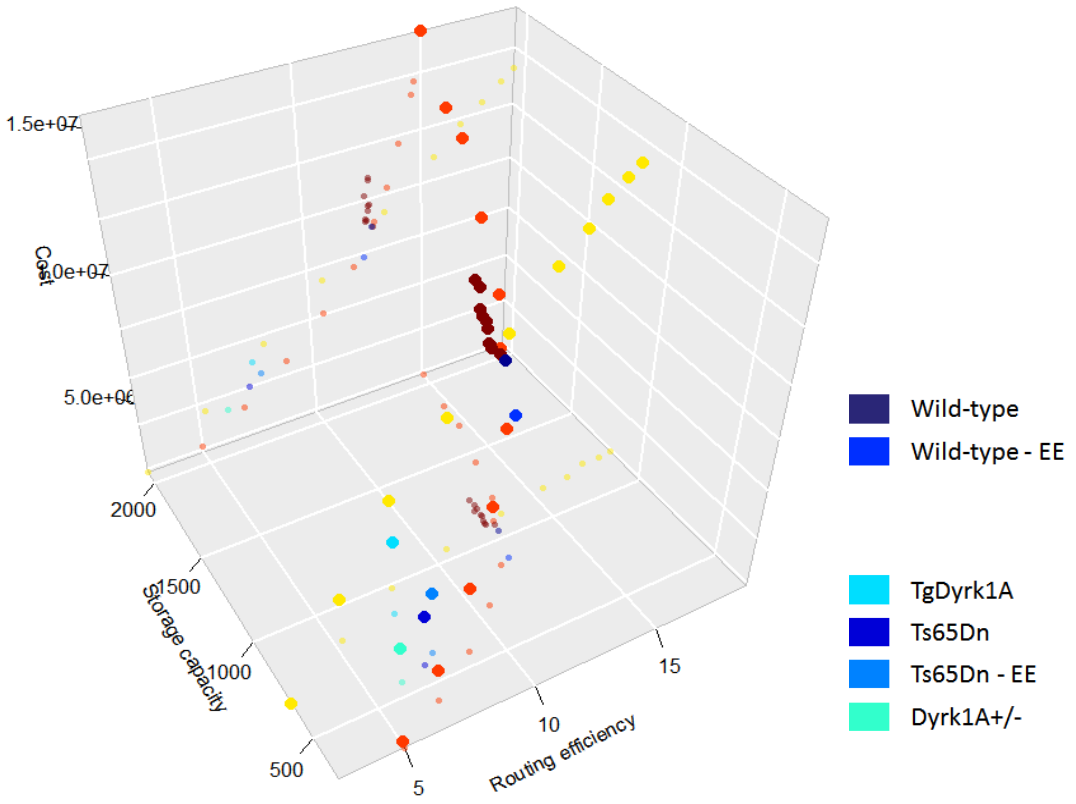

Figure 17: Overview of the morphospace exploration in the cortical layer II/III local network model. 3D representation of the data points for routing efficiency, storage capacity and cost, for (1) the morphospace exploration of our computational 2D model shown in **Figure 13** and **Figure 14**, and (2) the different mouse models instantiated. The red points were obtained by scaling the dendritic tree size; in yellow, the synaptic contact probability; in brown, the dendritic tree size variability; in tones of blue the DS mouse model instantiations (see legend). A 3D animation can be seen in: https://www.youtube.com/watch?v=tAwNar6VTo0, stop at seconds 0, 1 and 3 for 2D projections of each combination of dimensions.

1.3.3. Dendritic rewiring effects on network computational capacities

I investigated how neuromorphological variations detected upon treatment with environmental enrichment, which has shown beneficial effects in Ts65Dn and wild-type mice (M Dierssen et al. 2003; Martínez-Cué et al. 2002), affect the routing efficiency and storage capacity of our model cortical layer II/III networks.

As expected by the mild effect produced by environmental enrichment at the morphological level, the Ts65Dn mice only show a modest (yet significant) increase in storage capacity (7%) versus the non-enriched situation (625.3 ± 5.8 bits and 587.2 ± 5.1 bits; Bonferroni-corrected

$p = 3.35 \times 10^{-16}$). A similar change is seen in routing efficiency (7% increase; 7.74 ± 0.10 A.U. and 7.23 ± 0.07 A.U.; Bonferroni-corrected $p = 3.85 \times 10^{-14}$).

In the case of wild-type mice reared in environmental enrichment conditions, strikingly, the storage capacity drops by a 15% with respect to non-enriched conditions (893.0 ± 9.3 bits and 1042.6 ± 9.0 bits; Bonferroni-corrected $p = 4.68 \times 10^{-45}$) while routing efficiency is mildly reduced by a 3%. From this exploration, I can hypothesize how putative treatments could imply a rescue of the computational capacities in the network. While an increase in synaptic density reaches storage capacity saturation at a high cost, an increase in dendritic tree size (even subtle) would efficiently rescue the studied capacities and provide a stronger therapeutical effect.

1.3.4. Pareto optimality for computational capacities

By focusing on the two dimensions of the efficiency space given by the cost and the routing efficiency, I can link conceptually our single-neuron wiring optimality study with the exploration made at the network level, as described in the Methods section. Taking a similar routing efficiency for Ts65Dn, Tg Dyrk1A and 0.6 times downscaled wild-type networks (7.22 ± 0.07, 7.45 ± 0.07 and 6.90 ± 0.13 A.U. respectively), I observe that the parametrized mutant networks show higher cost than the wild-type networks that underwent dendritic tree size 0.6 times downscaling ($4.00 \pm 0.12 \times 10^6$, $5.00 \pm 0.13 \times 10^6$ and $3.18 \pm 0.07 \times 10^6$ A.U. respectively). This implies that mutant networks are not Pareto optimal for routing and material efficiency, a situation that could be explained by the fact that for the same spanning area, mutant dendritic trees have increased number of branches compared to their wild-type counterparts (
Table 4). At the same time, the increased dendritic complexity for the spanning area of the trees in both Ts65Dn, environmentally enriched Ts65Dn and TgDyrk1A in comparison to 0.6 times downscaled wild-type trees implies an increase in storage capacity (587.2 ± 5.1, 857.9 ± 3.9 and 422.1 ± 2.4 bits respectively), pointing at a possible self-regulation to increase the amount of synaptic contacts received by single neurons.

1.4. Discussion and conclusions

Single-neuron wiring optimality

Our morphological analysis of Ts65Dn, Dyrk1A+/- mice and their respective controls has confirmed previous observations. The original studies (Benavides-Piccione et al., 2005; M Dierssen et al., 2003) already pointed in the direction of a similar phenotype for both models. Here I confirmed that both Ts65Dn and Dyrk1A+/- neurons show reduced dendritic length and complexity, and higher amount of branches per normalized dendritic length. A substantial number of studies have associated morphological differences in ID mouse models with cognitive impairment measured by performance indices in cognitive tasks (Escorihuela, Fernández-Teruel, et al., 1995; Sago et al., 1998). Lesion and activation/inactivation studies in the M2 cortex have been shown to affect motor function (Manita et al., 2015). Ts65Dn mice show hyperactivity in various behavioral tests: open field lighting or open arms of the raised cross-shaped maze; being also hyperactive when surrounded with plenty of new stimuli, as with environmental enrichment (Coussons-Read & Crnic, 1996) . Conversely, Dyrk1A +/- mice show marked hypoactivity (de Lagran et al., 2007). In fact Dyrk1A+/- neurons have more marked alterations than Ts65Dn in the case of the mean branch order and spanning area that were significantly smaller in heterozygous mice.

However, our analysis suggests that those could be driven by the strain differences between B6EiC3Sn and C57BL/6J-129Ola wild-type mice. Among those differences, the reduced number of branch points and straightness and higher dendritic area and mean branching angle versus the B6EiC3Sn wild-type. In fact, those are relevant features for signal integration that could be involved in the mild behavioral impairment observed in this strain.

Until now these structural differences have been assumed to determine functional changes in these mutant strains. Here I decided to analyze if those differences of dendritic branching patterns still fit to an optimal dendritic wiring law. The optimal wiring comparison shows that cortical layer II/III basal trees are sub-optimally wired in the Ts65Dn and Dyrk1A+/- mouse models and in C57BL/6J-129Ola wild-type mice. Interestingly, Ts65Dn and Dyrk1A+/- neurons apart from showing a clear deviation from optimality in the proportion of branches per total dendritic length, they also show a reduced proportion of area occupied

by dendrites. This quantity has been used as a proxy for wiring optimality as proposed by Chklovskii et al (Chklovskii et al., 2002). The interesting point is that C57BL/6J-129Ola wild-type mice show the same dendritic occupation ratio than B6EiC3Sn mice, implying that the deviation seen in the power law for those neurons is given by the amount of branches per length of dendrite (too high for small dendritic trees) and not by the dendritic occupation ratio. If the subtle morphological differences of C57BL/6J-129Ola wild-type could be causally linked to their behavioral phenotype, this would suggest that Cuntz' approximation to dendritic wiring optimality is more complete than the dendritic occupation ratio.

Based on our single-neuron morphology and wiring optimality studies, I could speculate that the Ts65Dn and TgDyrk1A mouse models could have altered signal integration efficiency at the single cell level, leading to over-represented connections from the same afferent neurons (optimal wiring, **Figure 11**, and increase in the occupied area fraction, **Figure 9**). This hypothesis could be tested functionally by checking whether neurons deviating from optimality have increased synaptic response to groups of neurons innervating the region (e.g. thalamic or cortical projections from other sensory areas) (Grillner, 2015). This scenario could ultimately lead to an overactivation of M2 contributing to the hyperactive phenotype of those mouse models. In fact, unpublished data from our laboratory showed increased excitability in the motor cortex of Down syndrome patients (Principe et al, unpublished) using functional studies analyzing motor evoked potentials upon transcranial magnetic stimulation.

In contrast, the reduced straightness found in the C57BL/6J-129Ola strain, suggests that afferent synaptic signals could have delayed integration, possibly altering their response and introducing alterations in the activity dynamics of the region upon activation. Nevertheless, this explanation does not stand for all the behavioral phenotypes. While the dendritic architecture of the Dyrk1A+/- neurons is very similar to the Ts65Dn phenotype, behaviorally Dyrk1A+/- show marked hypoactivity (in contrast with the hyperactivity of Ts65Dn mice). Of course I need to bear in mind other aspects accompanying *Dyrk1A* underexpression. Previous work in our lab (de Lagran et al., 2007), showed decreased striatal dopamine levels and a reduced number of dopaminergic neurons in the substantia nigra pars compacta, that certainly contribute to the final motor behavior phenotype in this strain. Thus, understanding the hyper/hypo-activity phenotype also requires disentangling the

morphological and functional contributions at the higher-order network level. Even so, instantiating local networks in a systematic way can provide interesting information about the emergent functional phenotypes.

As the main limitation of this analysis, it should be noted that the numbers of neurons used in this study are very small, and thus in my opinion should not be generalized to the whole population. Even so, the important morphological differences among wild-type and mutant neurons, imply statistically significant differences. However, increasing the number of biological replicates, reproducing the study and complementing this knowledge with other models of intellectual disability in cortical layer II/III remains a necessary task. Additionally, the design of studies combining behavioral information of single animals and their morphological characterization, even though not allowing a full prediction as discussed above, would provide interesting correlations between the architectural traits and behavioral differences.

In conclusion, single-cell reconstructions have been extensively used to understand the relationship between dendritic morphology and the computations performed by neurons. However, the impact of neuronal geometry on the network properties is much less understood even though a wealth of knowledge about the physiology and morphology of some of these neurons is established. I here took a computational approach that can serve as a "hypothesis tester". For example, I can ask if the morphologies of the optimized neurons resemble the mutant neurons, or it can also be used in an exploratory manner, in which case the model neurons are used to identify the morphological parameters of theoretical interest. In this way, my approach can serve as a "hypothesis pump".

Network exploration

Our first goal was to disentangle the differential contributions of various neuromorphological features to the network computational capacities. Our *in-silico* exploration suggests that the density of synaptic contacts has less impact than dendritic tree size on the connectivity of the network and its computational capacities. Increasing dendritic tree size and synaptic contact densities implies a linear growth in the routing efficiency and cost of the network. Storage capacity grows asymptotically with synaptic contact probability and linearly with dendritic tree size. Of note are the facts that taking into account the radial

dependency in synaptic contact probability increases the number of contacts made by the neurons, and increases the small-worldness ratio of the network. Thus, contributing to the deviation from purely random topologies in neuronal networks (Vegue et al., 2017) and showing that taking the radial dependency into account in simple neuronal models can be contributing significantly to the network properties (concept not underlined in existing approximations to our knowledge).

The cortical layer II/III network instantiation parameterized with experimental data from our Down syndrome mutant models shows slightly differential affectations at the network level, given by small differences in their dendritic and spine radial distributions (see **Figure 16**). I first discuss the implications of those differences for wiring optimality, and second their connection with behavioral studies.

The analysis of the network routing efficiency seems to accompany the optimal wiring proposed by Cuntz et al. (derived from Cajal's laws for cytoplasm and conduction time), showing that morphologically altered neurons lead to suboptimal network connectivity. The mutant networks have excessive material in regards of the routing efficiency reached, while wild-type optimal morphologies lead to network topologies that are Pareto-optimal for routing and material efficiency. Even though the two optimality concepts seem to be related, it remains to be tested whether all network configurations non Pareto-optimal for routing efficiency also imply suboptimal dendritic tree wiring/occupation.

While our results appear to be consistent regarding the single-neuron and network optimality, associating them with the behavioral perspective does not clarify the doubts raised by the wiring optimality study. However, they suggest testing whether the network stimuli processing efficiency (and its dynamics) could be impaired differentially in Ts65Dn and Dyrk1A+/- mice, possibly linking the single-neuron description with the network dynamics through altered intercolumnar communication.

By taking into account that the M2 local connectivity participates into a larger network involved in the learning of motor repertoire (Barthas & Kwan, 2017), the impairment in storage capacity for the DS mouse models can be discussed in relation to executive function tasks. In this case, the literature available only consists in a single study assessing the Puzzle Box task performance in TgDyrk1A mouse model. Their impairment suggests that the

reduction in storage capacity seen in our model can be associated with the behavior. To test whether the relationship between architectural features and storage capacity follows the relationship I assumed, behavioral experiments comparing the executive function and/or motor repertoire acquisition capabilities of the different DS mouse models are needed.

The parameterization of data obtained from mice undergoing pro-cognitive treatment tackling dendritic rewiring can also contribute to the comparative analysis between neuromorphological conditions and cognitive capacities. In the case of environmental enrichment, an increase in spine densities in both wild-type and Ts65Dn mice has been shown (M Dierssen et al., 2003). In the case of wild-type mice the treatment also improved cognitive performance in the Puzzle Box task (O'Connor, Burton, Leamey, & Sawatari, 2014). The subtle 7% increase in routing efficiency and storage capacity for Ts65Dn in our computational model should undergo behavioral testing. However, the marked reduction in storage capacity (15%) and almost unchanged routing efficiency (3%) obtained with the environmentally-enriched wild-type parametrization imply that the model contradicts the improved Puzzle Box performance of wild-type mice. The storage capacity reduction originates in the subtly smaller dendritic trees of environmentally-enriched wild-type mice and is magnified by the high sensitivity of storage capacity towards dendritic tree size. While experimental data in the hippocampus shows a clear increase in dendritic tree size (Beauquis, Roig, De Nicola, & Saravia, 2010), additional experiments in cortical layer II/III to corroborate the subtle shrinkage observed in the dataset I used is lacking. Nevertheless, the strong effect of dendritic tree size in storage capacity suggests a cautious interpretation of their relationship. To assess whether the definition of storage capacity used is meaningful, a better estimate could be obtained by training neuronal networks with the instantiated topologies to store combinations of connectivity patterns and assessing their reliability in function of the morphospace exploration I have done (Poirazi & Mel, 2001).

Additionally, an important limitation of our model is the assumption of homogeneity, which forces a strong constraint hindering the modular and hierarchical organization of neuronal circuits(Bassett & Bullmore, 2006). Similarly, I have not explored other questions of interest, such as the subpopulation of abnormal neurons needed to impair significantly the network computational capacities, how neuronal densities could be affecting the obtained results, how detailed branching patterns could be modulating the network connectivity or how dynamical activity patterns emerging from different network topologies would differ. However, I consider it as a manageable test scenario for a conceptual framework that I aim to apply to

whole circuits involved in specific cognitive functions (e.g. entorhinal cortex - hippocampal circuit and its involvement in spatial/single item recognition learning). I think that this study can be a useful founding piece for comparative micro-connectomics in the frame of intellectual disabilities.

2. CHAPTER II. IMPACT OF SINGLE-NEURON STRUCTURAL DIVERSITY IN HIPPOCAMPAL CA1 POPULATIONS

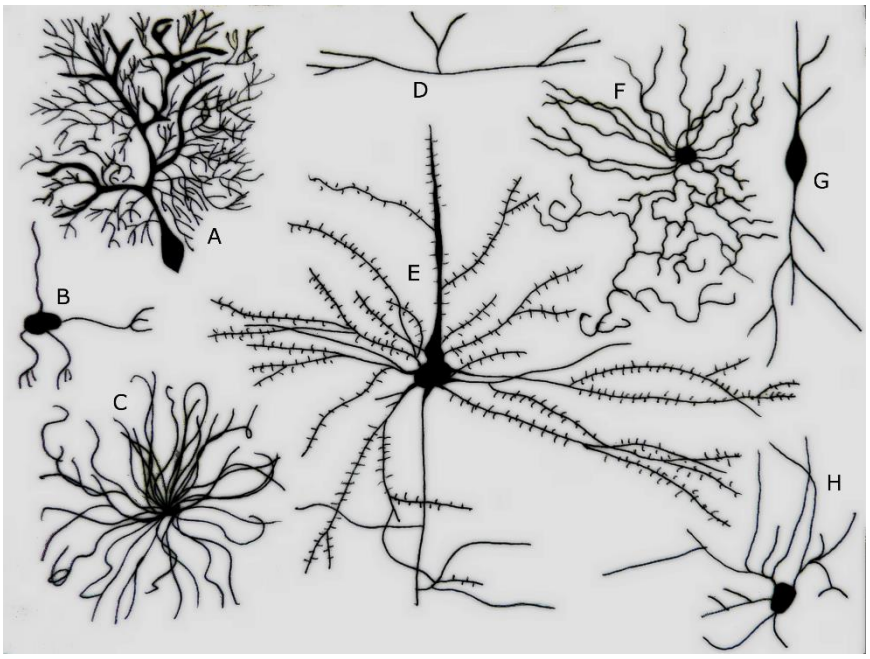

Different Types of Neurons. A. Purkinje cell B. Granule cell C. Motor neuron D. Tripolar neuron E. Pyramidal Cell F. Chandelier cell G. Spindle neuron H. Stellate cell (Credit: Ferris Jabr; based on reconstructions and drawings by Cajal)

"Unfortunately, nature seems unaware of our intellectual need for convenience and unity, and very often takes delight in complication and diversity."

Santiago Ramón y Cajal, in his 1906 Nobel lecture The structure and connexions of neurons

2.1. Introduction

The results presented in Chapter I showed that morphological properties of single cells are relevant for the network connectivity. Their wiring depends on 1) the 3D morphology of dendritic trees, which determines the balanced integration of afferent synapses carrying diverse information, and 2) the arrangement of those trees throughout the layers they are embedded into, which ultimately determines the specific computations done in each neuronal layer. However, to explore the relationship between the morphospace and network topology in networks responsible for specific cognitive functions, it is necessary to account for population level descriptions of neuronal circuits.

Cytoarchitectonic variation in cortical regions

A number of studies in the literature have revealed that the cerebral cortex is characterized by regional variations in its structure across different spatial planes. Conel (J LeRoy Conel 1941, 1947, 1955, 1959, 1963, 1967) thoroughly examined these regional differences by quantifying cell structure variation in several cortical areas in the cortex of a developing human brain. Thus, the question that immediately arises is: do the intrinsic properties of a specific brain structure vary across its extension, along with the within-class neuronal structure variability, or is the neuronal circuitry structure fixed and performing a conserved computation along a structurally non-homogeneous structure?

In fact the most frequently regarded paradigm to address this question has been a reductionist approach based on cell types, according to which discrete cell types are assumed to be homogeneous in terms of structure and function. Following this approach, identifying how different types of cells interact and contribute to a system allows for studying the emergent processing of the system as a whole.
Neurons in the brain are commonly grouped into discrete cell types based upon morphology, marker-gene expression, electrophysiology, and location within their respective circuit motifs. Each of those cell classes has been assumed to retain constant properties, and thus they have been used in computational models as "clonal" stereotypic elements. For example pyramidal neurons, the most abundant type of neuron in the neocortex, display notably similar dendritic arborization patterns among different areas of the brain and between

different cortical layers, in spite of their broad functional range. Dense arborizations of basal dendrites with multiple proximal branches wreathe the cell bodies of pyramidal neurons, with a single apical dendrite projecting towards the pial surface, which eventually branches as it enters layer I (Larkman & Mason, 1990). This conserved shape justifies the application of systematic morphological analyses without considering morphologic peculiarities of individual neurons. Although the effects of such peculiarities on the function of pyramidal neurons are not known, apical and basal dendrites likely correspond to different circuit inputs producing specific contributions to pyramidal cell excitability and long term synaptic plasticity (Cauller, Clancy, & Connors, 1998; Dudman, Tsay, & Siegelbaum, 2007).

However, a number of studies have demonstrated that differences in organizational principles may also be present, wherein within-class variability may be an important aspect of neuronal systems (Solstez, 2006). This question has been systemically investigated using microanatomical and gene-expression studies of pyramidal cells. Several lines of anatomical and physiological evidence have identified differences in CA1 in each of the dorsal-ventral (Amaral and Witter 1989; Dougherty et al., 2012, Dougherty et al., 2013, Malik et al., 2015), proximal-distal (Graves et al., 2012; Igarashi, Ito, Moser, & Moser, 2014; Jarsky, Mady, Kennedy, & Spruston, 2008), and superficial-deep (S.-H. Lee et al., 2014; Mizuseki, Diba, Pastalkova, & Buzsáki, 2011; Slomianka, Amrein, Knuesel, Sørensen, & Wolfer, 2011) axes of the hippocampus.

Similar variations have been reported also for other brain regions, such as the cerebral cortex (Defelipe, González-Albo, Del R'\io, & Elston, 1999) or the striatum (Cossette, Lecomte, & Parent, 2005) that may account for the well-established extensively reported notorious functional variability, both among different neurons, but even within the same neuron neural responses: the same stimulus can evoke a different response on each presentation (Henry, Bishop, Tupper, & Dreher, 1973; Tomko & Crapper, 1974). However, even though there have been great advances in characterizing the detailed patterns and statistical structure of cortical variability (Ecker et al., 2014; Feng, Zhao, & Kim, 2015; Goris, Movshon, & Simoncelli, 2014; Kohn & Smith, 2005), it has mainly been considered as pure noise or nuisance (Carandini, 2004; Moreno-Bote et al., 2014; Shadlen & Newsome, 1998; Tolhurst, Movshon, & Dean, 1983), and only recently some authors have suggested that it underlies functional aspects such as the representation of perceptual uncertainty (Sancristóbal,

Rebollo, Boada, Sanchez-Vives, & Garcia-Ojalvo, 2016; von Helmholtz, 1962). In fact, during neocortex development, the molecular specification cues exhibit smooth, graded profiles that span multiple cortical areas, suggesting graded cell properties (Sansom & Livesey, 2009). Also, in primates (Bernard et al., 2012) and humans (M. J. Hawrylycz et al., 2012) spatial proximity correlates with gene-expression similarity for neocortical regions and continuously variable immunohistochemical (Kondo, Hashikawa, Tanaka, & Jones, 1994; Xu, Tanigawa, & Fujita, 2003), morphological (Guy N Elston, 2002), and anatomical(Freese & Amaral, 2005) neocortical properties have been found, suggesting that continual variation may be a general feature of repeated, spatially extended circuit motifs in the brain.

Population-based analyses

Until now, however, I only have incomplete descriptions of the within-class variation in neuronal networks, and most studies neglect the underlying spatial structural variation that shapes connectional topology. To address this, efforts are being done to atlasing individual neurons, from their molecular phenotype to generating complete morphological reconstructions of individual neurons from datasets of whole mouse brains imaged at sub-micron resolution (https://www.janelia.org/project-team/mouselight) or obtaining complete subanatomical descriptions (i.e. Electron Microscopy) of tissue volumes containing big populations of neurons, but this is still an important challenge given the low throughput of the technique (Zheng et al., 2017) and the fact that it is difficult to identify what subcellular structures correspond to bona-fide neurons.

Single-neuron reconstructions provide enough anatomical detail to explore such within-class variability. However, until now, the reductionistic cell-type specific perspective taken in most neuroanatomical studies has left an empty gap regarding its study. For example, the most complete single-neuron morphology database (https://neuromorpho.org, Ascoli, Donohue, and Halavi 2007) contains at this moment more than 70000 single neuron reconstructions, but those cells lack information about their position. Similarly, the more recent Allen Institute neuron cell type database (http://celltypes.brain-map.org/) combines morphological, electrophysiological and transcriptomic layers of information, but still misses the link with topological or functional segregation. This is starting to be resolved through the latests efforts in mapping whole single neurons (including axonal projections), accounting

for their position (Mouselight, https://www.janelia.org/project-team/mouselight), but until now only few have been completely traced.

Thus, a systematic characterization of neuromorphological properties while considering the topographical positioning of the neurons is required. In order to generalize the detailed knowledge obtained with single-neuron data, it could be combined with population-based information (such as immunostainings or transgenic population labeling). In this regard, population-based measurements could be taken as descriptors of neuromorphological properties that can be relevant for within-class variability.

Even so there is a need for more comprehensive studies characterizing those inhomogeneities. To this end three aspects are necessary: first, the systematic study of neuronal morphology across single neuronal layers. Second, the developments of population-based measurements are able to account for within-class neuromorphological diversity. And third, a computational modeling framework that enables the exploration of their impact in the connectivity of neuronal circuits. The aim of this part of the Thesis is to assess those three aspects.

The hippocampus as a model system

The hippocampus is a privileged model system to clarify the extent to which higher-level (e.g., functional and behavioral) and lower-level (e.g., cellular and circuit) properties covary across space. A wealth of evidence has illustrated that there is profound functional segregation across the long hippocampal axis (Moser & Moser, 1998; Strange, Witter, Lein, & Moser, 2014), with both input to (Dolorfo & Amaral, 1998) and output from (Gibble, Kishi, & Peake, 2006; Groenewegen, te der Zee, Te Kortschot, & Witter, 1987; Risold & Swanson, 1996) the hippocampus exhibiting graded topographical mapping across the long axis.

Most of the cerebral cortex is neocortex. However, there are phylogenetically older areas of cortex termed the allocortex. These more primitive areas are located in the medial temporal lobes and are involved with olfaction and survival functions such as visceral and emotional reactions. In turn, the allocortex has two components: the paleocortex and archicortex. The

paleocortex includes the piriform lobe, specialized for olfaction, and the entorhinal cortex. The archicortex consists of the hippocampus, which is a three-layered cortex.

The hippocampal formation has long been recognized as necessary for the integrity of memory in mammals and other vertebrates, and relatively limited disturbances of the hippocampal circuitry have been reported to produce serious memory impairment. The anatomical basis of this system is the so called trisynaptic circuit formed by the perforant path arising in the entorhinal cortex, which terminates onto the dendrites of the granule cells of the dentate gyrus. The axons of the dentate gyrus granule cells form the mossy fibers that make synaptic contact with the pyramidal cells of the CA3. The axons of CA3 pyramidal cells form the Schaffer's collaterals that make synaptic contact with the pyramids of CA1.

Despite involving only three layers of processing, has been shown to be fundamental for encoding declarative memory and spatial information (Marr, Willshaw, & McNaughton, 1991). Sensory information is received in the dentate gyrus, that has been proposed to perform pattern separation (Hasselmo & Wyble, 1997; Marr et al., 1991; McNaughton & Morris, 1987; O'reilly & McClelland, 1994; Treves & Rolls, 1994). Axonal projections from the dentate gyrus innervate CA3 (Perforant Path), which has extensive recurrent connectivity and has been proposed to form associations between encoded memory patterns (Hasselmo, Schnell, & Barkai, 1995; Hasselmo & Wyble, 1997; Norman & O'reilly, 2003; Treves & Rolls, 1992, 1994). Finally, CA1 receives input from both CA3 (Schaffer collaterals, innervating the *stratum pyramidale* sublayer) and the entorhinal cortex (Perforant Path, innervating the *stratum lacunosum* sublayer), and has been suggested to behave as a comparator between the stored memories in CA3 and the sensory input from the entorhinal cortex (Gray, 1982; Hasselmo & Schnell, 1994; Hasselmo & Wyble, 1997).

In this chapter, I focused on the dorsal CA1 given the existing information regarding its anatomical and functional proximal-distal inhomogeneities (Cembrowski et al., 2016; Graves et al., 2012; Igarashi et al., 2014; Jarsky et al., 2008). In the rodent, area CA1 of the hippocampus has a C shape that extends millimeters in the anterior-posterior, medial-lateral, and dorsal-ventral axes (**Figure 18**).

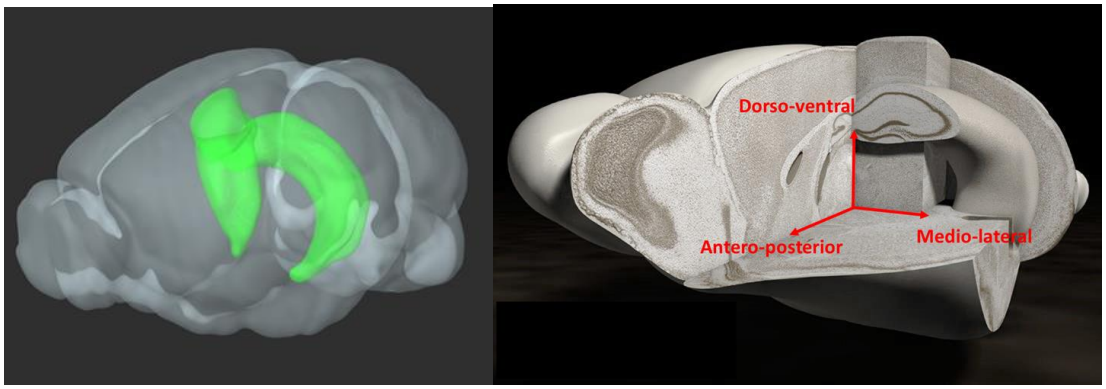

Figure 18: 3D rendering of the mouse hippocampus. (Left) 3D view of a whole mouse brain (gray) and its hippocampus (green) obtained from Allen Brain Explorer (Jones, Overly, & Sunkin, 2009). (Right) 3D rendering of a brain showing its anatomical axes.

As viewed in coronal sections, near its most rostral point, CA1 occupies approximately the top half of the continuous CA field. More caudally, the full dorsal-ventral extent of the CA1 region can be visualized; here, the most lateral band of cells comprises CA1. Conventionally, this 3D structure is described by three axes: the most prominent axis (dorsal-ventral) is typically referred to as the long axis and spans the length of CA1. Two-dimensional cross-sections perpendicular to the long axis reveal the proximal-distal axis (spanning from the CA2/CA1 "proximal" border to the CA1/subiculum "distal" border) and the superficial-deep axis (spanning from "superficial" cell bodies located closest to stratum radiatum to "deep" cell bodies located closest to stratum oriens).

Those subregions define functionally relevant differences. The dorsal hippocampus has been related to spatial and contextual memories, while the ventral region has been suggested to be involved in fear conditioning and anxiety (Fanselow & Dong, 2010). Additionally, recent studies have shown functional segregation along the proximo-distal axis of the dorsal hippocampus, being the proximal part more related to spatial memories and the distal one to contextual memories (stronger/weaker place cell firing) (Igarashi et al., 2014).

Down syndrome presents hippocampal structural and functional abnormalities

Hippocampal pathology is likely to contribute to cognitive disability in Down syndrome, yet the neural network basis of this pathology and its contributions to different facets of cognitive impairment remain unclear.

The adult Down syndrome brain has a characteristic morphology that includes reductions in overall brain weight and volume, with disproportionate volume reductions in the frontal and temporal lobes (**Table 6**). In addition, the brain is brachycephalic, with disproportionately small cerebellar volumes, a simplified gyral appearance, and a narrow superior temporal gyrus. Conversely, the parahippocampal gyrus is larger than normal in Down syndrome, although greater gray matter reductions have been described in the frontal lobe, the hippocampus and at the level of cerebellum (Menghini, Costanzo, & Vicari, 2011; Pinter, Eliez, Schmitt, Capone, & Reiss, 2001; Rigoldi et al., 2009). No abnormalities in pattern of brain asymmetry have been noted(Pinter et al., 2001).

Structural neuroimaging studies have confirmed the findings of post-mortem studies showing reduced volume of the hippocampus system and disproportionately smaller frontal lobe in adults with Down syndrome(Beacher et al., 2010; Jernigan, Bellugi, Sowell, Doherty, & Hesselink, 1993; White, Alkire, & Haier, 2003). Neuroimaging investigations have also shown that such individuals have decreased volume of grey matter tissue in the cerebellum, frontal lobe, right middle–superior temporal gyrus, and the left CA2–CA3 region of the hippocampus, and have highlighted that these brain areas have major roles in the specific mnesic alterations that are exhibited in this disorder(Krasuski, Alexander, Horwitz, Rapoport, & Schapiro, 2002; Raz et al., 1995; Teipel et al., 2004).

In contrast to cortical regions, subcortical regions show relatively preserved volumes in Down syndrome(Jernigan et al., 1993; Pinter et al., 2001). In the context of significantly smaller overall cerebral volumes, the relatively large size of these latter structures, suggests that there is a dissociation of the development of cortical versus subcortical regions, which will affect neurological development with some functions being compensated for while others are not. Along with these structural alterations, atypical patterns of brain activation have been demonstrated in Down syndrome(Jacola et al., 2011), allowing predictions on structural–functional maps in this disorder (Colom, Karama, Jung, & Haier, 2010). For

example, the poor performances of individuals with Down syndrome in linguistic tasks could be partially explained in terms of impairment of the connectivity of frontocerebellar structures that are involved in articulation and verbal working memory (Fabbro, Libera, & Tavano, 2002), whereas the reduced long-term memory capacities may be related to the frontotemporal lobes and, specifically, to hippocampal dysfunction (Pennington, Moon, Edgin, Stedron, & Nadel, 2003).

In DS mouse models, and specifically the Ts65Dn model, significant learning deficits in various behavioral tasks that are putatively hippocampal-dependent (Demas, Nelson, Krueger, & Yarowsky, 1998; Hunter, Bimonte, & Granholm, 2003; Stasko & Costa, 2004). Also, significantly lower numbers of neurons in the dentate gyrus of Ts65Dn mice compared to control animals have been reported (Insausti et al., 1998). The presence of these 'hippocampal phenotypes' in Ts65Dn mice has acquired renewed importance with the finding that, in persons with DS, hippocampal function may be disproportionally affected in the general context of their cognitive disabilities(Pennington et al., 2003). In fact a significant reduction in the number of neurons has been reported in the granule cell layer of the dentate gyrus in Ts65Dn. This may well lead to a concomitant decrease in the number of synaptic sites available in the dentate gyrus for receiving information through the perforant path; it may well provide the morphologic basis of spatial memory impairment since fewer granule cells would decrease the total number of mossy fibers that could make synapses onto CA3 neurons. Furthermore, stereological studies have revealed a significant increase in the number of CA3 neurons in Ts65Dn mice. This result may be explained as an attempt to compensate for the loss of mossy fiber synaptic terminals by making available a larger postsynaptic territory.

Table 6: Brain alterations in Down syndrome. Alterations found in Down syndrome subjects shown by brain area and age (newborns, adults between 20 and 50 years old, and individuals aged over 50).

Brain alterations in Down syndrome			
Brain region	**Newborns**	**Adults (20-50)**	**Aged individuals (> 50)**
Whole brain	Almost normal weight	Reduction in weight; brachicephalic	Smaller overall cerebral volumes
Prefrontal cortex	Reduction in volume	Reduction in volume	Reduction in volume
Parietal cortex	Normal or reduction in volume	Reduction in volume	Unknown
Temporal cortex	Narrow superior temporal gyrus	Reduction in volume of right middle or superior temporal gyrus	Decreased gray matter volume in posterior cingulate and entorhinal cortex
Hippocampus	Unknown	Reduction in volume	Early degeneration
Parahippocampal region	Unknown	Increase in size of the parahippocampal gyrus	Reduction in volume
Cerebellum	Reduction in volume	Reduction in volume	Reduction in volume
Brain stem	Reduction in volume	Increase in gray matter volume	Degeneration of locus coeruleus
Subcortical areas	Almost normal size	Normal	Degeneration of basal prosencephalon cholinergic nuclei (nucleus of Meynert); reduction in amygdala volume

2.2. Methods

In this part of the Thesis, I combined histological experiments and classical technique for neuronal reconstruction and cellularity estimations, with the development of a computational framework for population analysis and a generative model.

The first step was to characterize within-class variability of single-cell morphology in the hippocampus of healthy and perturbed scenarios such as those provided by Down syndrome models. Those might either show generalized abnormalities or, more interestingly, show partial alterations implicating specific segregated functions, providing additional information about the relevance of within-class variability.

I focused on the dendritic tree architecture of pyramidal CA1 cells (*stratum radiatum)* across the proximal-distal axis. To identify relevant structural features, I used again transgenic mice overexpressing *Dyrk1A* (TgDyrk1A; see Chapter I, **Section 1.2.1** and (Altafaj et al., 2001) and their wild-type controls, that would define the "healthy" structural features.

I first used classical single-cell reconstruction methods to identify within-class neuromorphological variability along the proximo-distal axis in pyramidal neurons of both wild-type and TgDyrk1A mice. In a second series of experiments, I used a genetic approach, crossing TgDyrk1A to a strain expressing yellow fluorescent protein (YFP) in a subset of pyramidal cells, to obtain population-based measurements accounting for cellular and dendritic density.

Finally, I obtained cellular density measurements along the antero-posterior axis to feed a custom-developed computational framework that enables the study of neuronal network connectivity from a multi-scale data-driven perspective.

2.2.1. Single-cell analysis: morphological within-class variability of CA1 pyramidal neurons along the anterio-posterior hippocampal axis in wild-type and TgDyrk1A

For single-cell analysis I used transgenic mice overexpressing *Dyrk1A* (TgDyrk1A) obtained as previously described (see Chapter I, **Section 1.2.1** and Altafaj et al. 2001). All animal procedures were approved by the local ethical committee (CEEA-PRBB, MDS-08-1060P1 and JMC-07-1001P2-MDS), and met the guidelines of the local (Real Decreto 53/2013) and European regulations (EU directive 2010/63/EU and 2007/526/EC) and the Standards for

Use of Laboratory Animals n° A5388-01 (NIH). The CRG is authorized to work with genetically modified organisms (A/ES/05/I-13 and A/ES/05/14).

Lucifer Yellow injections in TgDyrk1A mice in single CA1 pyramids

To compare dendritic tree architecture in the *stratum radiatum* of pyramidal CA1 cells across the proximal-distal axis I used Lucifer Yellow injections in manually selected single cells, of hippocampal CA1 pyramidal neurons and reconstructed 3D dendritic trees (see below). Four wild-type and TgDyrk1A two-month-old mice (N=4) were used. Animals were perfused with 4% PFA, and 150 μm coronal sections were obtained with a vibratome. Intracellular injections by continuous current of fluorescent Lucifer Yellow (LY) (described in detail in (Benavides-Piccione et al., 2005; M Dierssen et al., 2003) were performed in CA1 pyramidal neurons. The injections were performed in the dorsal hippocampus according to the stereotaxic coordinates Bregma, -1.34 to -2.34 mm, obtained from a mouse brain atlas (Paxinos & Franklin, 2004) 4 to 12 neurons were injected in each section along the mediolateral axis of CA1. The sections were counterstained with antibodies against LY. Sections were washed with PBS and 0.3 % PBS-T to make the cells permeable. To minimise the background staining, the slices were treated with 50 mM glycine (minimum 99 % TLC, Sigma-Aldrich,) in 0.3 % PBS-T for 20 min. After washing with 0.3 % PBS-T, the samples were treated for 2 h at room temperature with 3 % bovine serum albumin (BSA, Sigma-Aldrich) in 0.3 % PBS-T as a blocking agent and were incubated overnight at 4 ºC in polyclonal rabbit IgG fraction anti-Lucifer yellow (1:500, Life Technologies, Thermo Fisher Scientific, Cat # A-5750) in 0.3 % PBS-T and 1 % BSA. After washing with 0.3 % PBS-T, they were incubated 2 h at room temperature in goat anti-rabbit IgG 488 (1:200, Invitrogen, Thermo Fisher Scientific, Cat # A11034) in 1 % BSA in 0.3 % PBS-T. Finally, sections were washed with 0.3 % PBS-T and PBS and were coverslipped using mowiol mounting medium.

Neuronal reconstruction and neuromorphological analysis

The preparations obtained as described in the previous section were used for accurate neuronal reconstruction. To position the reconstructed neurons in CA1, I mapped their coordinates in a common reference space. I defined an anteroposterior position given by the Bregma coordinates between -1.34 and -2.34 mm (obtained from a mouse brain atlas, Paxinos and others 2013). The mediolateral and dorsoventral coordinates were measured in low magnification (11.5x) images of the brain sections taking the dorsal tip of the 3rd ventricle as the origin. The low magnification images were obtained using a stereomicroscope MZ16F (Leica Microsystems, Wetzlar, Germany).

Single apical tree stacks were acquired with a confocal microscope (SP5 Upright; Leica Microsystems) with a 20x air objective and 0.347µm z steps (final voxel size of 0.296x0.296 µm). Three stacks per sample were collected, aligned, and averaged to reduce noise. I used Leica Smart Gain in the Leica Application Suite software to adjust brightness, in order to equalize the fluorescence signal intensity in depth in the samples.

The signal to noise ratio was measured for each of the obtained stacks at 100 µm depth to account for a representative dendritic segment and an equivalent area of the same depth containing only background. Images with SNR<1.2 were discarded for subsequent analysis. The stacks underwent 2 pixel wide 2D gaussian blurring, background subtraction (50 pixel sliding paraboloid without smoothing) and contrast enhancement (with 0.3% saturated pixels and using the stack histogram) in Fiji.

Dendritic trees of 20 neurons per genotype obtained from 4 wild-type and 4 TgDyrk1A animals were reconstructed with NeuTube1.0 (Feng et al., 2015) (see Chapter I) given that the semi-automatic tracing of this software outperforms other open-source applications in processing time and usability, allowing neuronal reconstruction with minimal interaction.

Statistical and principal component analysis

To analyze the reconstructed trees, I followed the procedure described in **Section 1.2.2** (Chapter I). Briefly, morphological metric statistics were obtained with the Trees Toolbox (Cuntz, Forstner, Borst, & Häusser, 2011) function *stats_tree*, a scaled PCA was performed in R, and wiring optimality was assessed by fitting a power law to the relation between total tree

length and amount of branch points (see **Section 1.2.2** and Cuntz, Mathy, and Häusser 2012). In this case, the numbers of Sholl intersections were obtained using the *sholl_tree* function in the Trees Toolbox. In order to get a precise distribution of dendritic densities, I used a Sholl radius step of 1μm.

In order to use as many neurons as possible, in this study I used an unbalanced block design, that allows an unequal number of observations per groups (in our case, numbers of neurons reconstructed per genotype and areas). The neuromorphological metric distributions were compared among positions by fitting a mixed-effect linear model with the residual maximum likelihood (REML) method and blocking for biological replicates, the analysis was performed using R (version 3.4.1) and its package *lme4* (version 1.1-13). P-values were obtained from the adjusted denominator degrees of freedom for linear estimates and *t* distributions calculated using the Kenward-Roger approximation (*pbkrtest* R package, version 0.4-7). Results were considered significant when $p<0.05$.

2.2.2. Population-based analysis

For population-based analysis, I required a systematic view of the cells along the whole structure that cannot be obtained through labour intense single neuron injections, but are also not conveniently obtained through immunohistochemical techniques that would stain the whole population of cells making estimations more complicated.
I thus generated double transgenic mice (Thy1-YFP/TgDyrk1A) by crossing TgDyrk1A male mice with *Thy1-Yellow Fluorescent Protein (YFP)* female mice (strain B6.Cg-Tg(Thy1-YFPH)2Jrs/J nº003782; The Jackson Laboratories), that expresses yellow fluorescent protein in a proportion of pyramidal cells driven by the Thy1 promoter and their non-transgenic littermates as controls. The Thy1-YFP line H has been reported to express the fluorescent protein in a large number of pyramidal neurons in several fields of the hippocampal formation. This model offers the advantage of having sparse YFP-stained pyramidal neurons that will also serve the purpose of population based analysis.

I first used classical stereology methods for unbiased "bona-fide" estimations of hippocampal CA1 volumes and neuronal density that thereafter served for validating a computational framework for population-based analysis that I developed to:

1) estimate the spatial embedding by determining the volume of the specific hippocampal subregion (CA1); 2) estimate the number neurons; and 3) estimate dendritic densities.

Unbiased cellularity estimations along the antero-posterior axis of CA1 in TgDyrk1A

The relative importance of the intrinsic and extrinsic factors determining the variety of geometric shapes exhibited by dendritic trees remains unclear but important extrinsic determinants of dendritic shape are the spatial embedding and the cellularity, that constrain geometrical properties of dendritic trees. To this aim I investigated variations in cellularity and the volume occupied by CA1 along the anteroposterior axis.

For the study of cellular and dendritic densities across CA1, two-month-old Thy1-YFP mice (N=4) were sacrificed and perfused intracardially with phosphate buffered saline (PBS), followed by chilled 4% paraformaldehyde (PFA; Sigma). The brains were removed from the skull, postfixed in the same fixative at 4ºC overnight, and cryoprotected in 30% sucrose. One-hundred fifty μm coronal brain sections were obtained using a vibratome (VT1000S, Leica Microsystems), washed extensively with 0.1M PBS, and mounted and coverslipped with mowiol reagent.

Total neuronal densities were also analyzed using a NeuN staining in a similar setup with samples from TgDyrk1A and their wild-type littermates (N=3). To ensure the antibody penetration throughout the sample, forty μm coronal sections were obtained using a cryostat (CM3050 S, Leica Microsystems). Then, sections were permeabilized with 0.5 % Triton X-100 (Merck) in PBS (PBS-T 0.5 %) (3x15'), and blocked with 10% of Normal Goat Serum (NGS) for two hours at room temperature. Sections were incubated overnight at 4ºC in mouse IgG anti-NeuN (1:500, Millipore, Cat # MAB377), PBS-T 0.5% and NGS 5 %. Slices were washed with PBS-T 0.5 % (3x15') and incubated for two hours at room temperature in 488 goat anti-mouse IgG (1:500, Invitrogen, Cat # A11001) antibodies in incubation buffer (PBS-T 0.5 % + NGS 5 %) and protected from light. Finally, sections were washed with 0.3 % PBS-T and PBS and were coverslipped using mowiol mounting medium.

Stereological estimations

I used design-based stereology methods for neuronal counting (Optical Disector, Harding, Halliday, and Cullen 1994; Rosen and Harry 1990) and and volume estimation (Rosen & Harry, 1990). This method eliminates the need of information about the geometry of the objects to be counted, resulting in more robust and unbiased estimates of total neuron number, because potential sources of systematic errors in the calculations are eliminated. I used 150 µm Thy1-labeled and NeuN-stained coronal sections that are thick enough to allow many focal planes through the disector and to allow for guard zones. There must be multiple focal planes through the disector so that: one particle can be told apart from another; there will be a small leading edge that is detected; and there is room to focus up and down and make a good decision about whether the leading edge of the particle is contained in the disector or not.

I used a Leica DMI 6000B inverted microscope (Leica Microsystems, Wetzlar, Germany) equipped with a 20x air objective, a motorized scanning stage and a microcator and a digital camera connected to a PC to obtain microscopic captures. Images were analyzed with the newCAST™ software (Version: 5.3.0.1562, Visiopharm, Denmark) from Visiopharm Integrator System.

Volume estimation of the selected ROIs was calculated according to the Cavalieri principle. A specific point configuration was configured to ensure that more than 200 points in total were counted for every ROI across all the selected slices. 100% coverage of the area of each ROI was chosen for sampling. Volume estimation for the whole ROI and for every slice was calculated according to:

$$V_{ref} = T \cdot a(p) \cdot \sum P \qquad \textbf{Equation 5}$$

Where *T* is the spacing between sections, a(p) the area per point (dependent on each specific configuration), and $\sum$ P the sum of points inside the ROI.

To obtain Thy1+ cell densities, seven Thy1-labeled 150 µm thick consecutive slices (Bregma, -1.34 to -2.34 mm, mouse brain atlas, Franklin & Paxinos, 2012) were quantified. NeuN quantifications, due to the thinner sectioning, were performed in every 4th slice, discarding 3 consecutive slices between quantifications. I used an Optical Disector and sampled 21-24

counting frames in each analyzed region of interest (ROI). I obtained an estimate of the real thickness of the planar sections (60μm) by measuring the z-axis distribution of the cell number and identifying the z extent having a uniform distribution of counts. Each counting frame covered 1% of field of view given by the 20x objective having the following dimensions: 58.1 x 58.1 x 60 μm. the optical plane was moved throughout the whole thickness of the preparation section to ensure correct cell identification. Cell densities (N_v) were calculated according to the following equation (Dorph-Petersen & Lewis, 2011):

$$N_v = \frac{\overline{t_{Q^-}}}{BA} \cdot \frac{\Sigma Q^-}{h \cdot (a/p) \cdot \Sigma P} \qquad \textbf{Equation 6}$$

Where t_{Q^-} is the number-weighted mean section thickness, BA is the Block Advance (the cut thickness of the section on a calibrated cutting device), h the disector height, (a/p): a is the area of the CF and p the number of points associated to the frame (1 - using the upper right corner of the CF), and ∑ P: is the sum of corner points hitting reference tissue.

The total number of cells (N) was estimated by the product of the cell density (N_v) and the volume (V_{ref}) obtained from Cavalieri estimations.

$$N = V_{ref} \cdot N_V \qquad \textbf{Equation 7}$$

All the estimations were performed in one hemisphere, chosen at random as no differences are reported to exist between both hippocampal formations. Stereological estimations were performed in the CA1 pyramidal cell layer of the hippocampus. ROIs were manually delineated according to (Paxinos & Others, 2013) mouse brain atlas.

2.2.3. Development of a customized pipeline for population-based analysis in histological sections

As described above, neuron morphologies capture some features of selected cell types, but they are hard to generalize to the whole cell population, given the inhomogeneities that have been reported. One bottleneck is that describing the shape of neurons requires quantitatively specifying many morphological features, examples of which are the length and branching patterns of neurites, and their spatial distribution. Another is that obtaining accurate 3D digital representations of neurons has traditionally been a slow, expensive, manual process. Here I developed a computational analysis pipeline to obtain population-based measurements semi-automatically and define dendritic and cellular density maps. Experimental data were obtained from Thy1-labeled mice in dorsal CA1 thus allowing the comparison with single-cell reconstructions and stereological.

Imaging and segmentation

Images of the dorsal hippocampus according to the stereotaxic coordinates Bregma, -1.34 to -2.34 mm, obtained from a mouse brain atlas (Paxinos & Others, 2013) have been taken using a widefield microscope (Zeiss Cell Observer HS) with a 10x magnification objective with a field view of 895.26 x 670.80 μm and resolution of 0.643 μm/pixel. Using the Panorama acquisition module (ZEN blue edition, Zeiss) adjacent images with 5% overlapping edges were taken covering the whole brain section for each of the 6-8 brain sections analyzed per animal.

Images covering the whole section were reconstructed using the ImageJ Grid/Collection Stitching plugin with 5% tile overlap, the Linear Blending fusion method and its default thresholds, a regression threshold of 0.30, an average displacement threshold of 2.50 and an absolute displacement threshold of 3.50. Stacks containing the whole section images of each animal were downsampled 20 times in the X-Y dimensions and aligned using the RegisterVirtualStacks plugin with the Rigid feature extraction and registration model and applying shrinkage constraint. The obtained transformations were multiplied by the downsampling factor and applied to the original large stacks.

Masks for the whole section and the left hemisphere regions CA1 and its somatic layer stratum pyramidale (CA1-sp) were manually segmented according to the Allen P56 mouse brain Reference Atlas (Dong, 2008) using Fiji's Segmentation Editor (

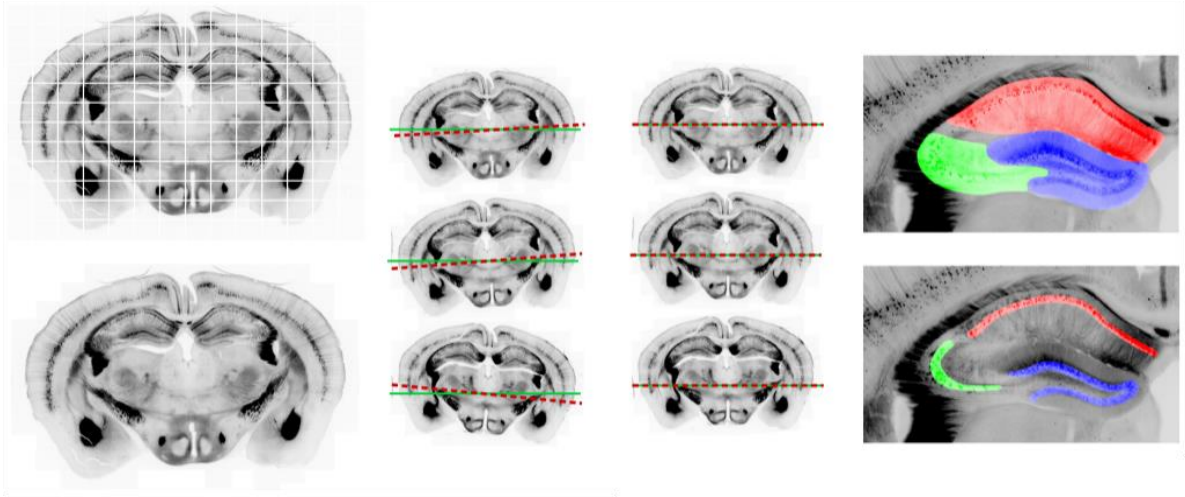

Figure 19).

Figure 19 : Overview of the imaging, stitching, alignment and segmentation procedure. (Top left) Serial images covering the whole section were obtained with a 5% tile overlap. (Left) Stitching was performed using the ImageJ Grid/Collection Stitching plugin. (Middle) Consecutive sections were aligned using the RegisterVirtualStacks plugin. (Right) 2D segmentations for CA1 dendritic (top) and pyramidal (bottom) layers were manually delineated using the Fiji's Segmentation Editor and based on the Allen P56 mouse brain Reference Atlas.

In order to increase the extensibility of our approach I chose Fiji plugins as basic tools for our quantifications. I selected Fiji because it is an open source image processing package based on ImageJ with many bundled plugins. Fiji features an integrated updating system and provides a high number of users with a coherent menu structure, extensive documentation in the form of detailed algorithm descriptions and tutorials, and the ability to avoid the need to install multiple components from different sources.

For both cell and dendritic density mapping, the processing done in Fiji is aided by Matlab and Python scripts developed in-house that can be easily used in processing pipeline management tools. I first describe the examples of population metrics for which I have developed analysis algorithms and subsequently an interactive pipeline structure that allows a user-friendly application of our methods and their extension.

Cell density

A first requirement to obtain whole-CA1 cell density maps is to locate nuclei in the imaging datasets. An extensive literature on computational methods has tackled this challenge (Irshad, Veillard, Roux, & Racoceanu, 2014). Developing an optimal method to identify cells in microscopy imaging datasets is beyond the scope of this Thesis, but I aim to show that, by analyzing 2D datasets, I can obtain 3D cell density maps that are representative of the macroscopic scale properties of the tissue and give unprecedented detail and allow innovative analysis methods.

I wrote a Fiji macro that locates nuclei in segmented somatic layers of 2D microscopy images (CA1 stratum pyramidale in this case) and creates 2D cell density maps along them. The macro can either use Fiji's simplest method for identifying cells (2D maxima detection plugin) or can generate the density maps based on lists of cell coordinates provided by the user. It is important to note that the datasets used have been background subtracted with a rolling ball (radius = 15 μm) in order to highlight signal coming from somas and reduce signal intensity in thin neurites. The script needs as inputs the binary segmentation of the analyzed layer and either the original image or a list of 2D coordinates obtained with an alternative method. It first obtains the midline of the layer and subsequently quantifies the amount of identified cells in adjacent circular areas following the midline (**Figure 20**). The circles are located along the midline so that they are big enough to cover tenths of cells (radius = 160 μm in our datasets) and have some amount of overlap among them (distance = 130 μm in our datasets). In each circular area, a cell density (cells/1e7μm^3) is calculated based on the measured cell quantity, the somatic layer area covered by the circle and the depth of the imaged sections. The 1e7μm^3 scaling factor is introduced in order to obtain gray intensity values in the range of an 8-bit image. In the areas covered by overlapping circles, the cell density is set as the average of repeated measurements. Finally, the macro applies a gaussian blur (radius = 30 μm) and creates a 16-bit image expressing the cell density as the image intensity at each point. The resulting maps represent inhomogeneous cell body distributions along the analyzed layers (**Figure 20**).

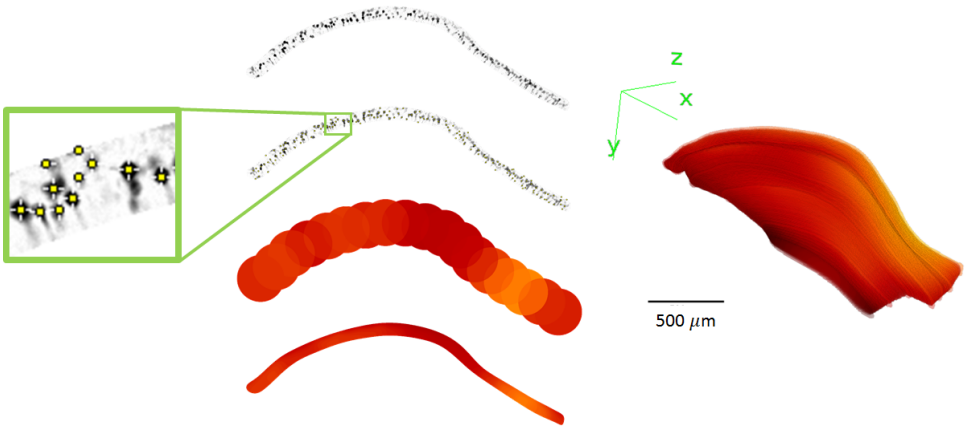

Figure 20: Overview of the cell density mapping procedure. A segmented somatic layer is preprocessed with a background subtraction of rolling ball radius = 15μm in order to highlight somas. The amount of cells in equispaced (130 μm) circles (radius = 160 μm) is measured and shown as image intensity. A gaussian blur (radius=30 μm) is applied and the intensity map masked again. (Right) 3D rendering of an interpolated (see **Section 2.2.2**) cell density map for the CA1 pyramidal layer (Bregma from -1.34 to -2.34).

Dendritic density

While population-based labeling (Thy1-like) has been used to quantify cells and axonal projections, information related to dendritic complexity has been disregarded. I developed a novel method to quantify dendritic density that can be understood as an extension of the Sholl analysis for single neurons. In the classical single-cell version of the analysis, the amount of dendritic branches crossing concentric circles of increasing radius is quantified. The information obtained can be seen as a signature of dendritic tree architecture and has been studied in depth in neuronal cells from several organisms, brain regions and neuronal subtypes. In order to analyze similarly population-labeled 2D section microscopy images, I have developed a method to quantify the density of dendritic branches along the axis normal to any studied layer. I implemented it in a Fiji macro that computes the midline of a layer and uses it to scan the space surrounding it. A fluorescence intensity profile is obtained along the scanning line and local maxima accounting for dendritic segments are quantified. The quantification is subdivided in curved rectangles with height = 2 μm and length = 40 μm, allowing the detection of spatial inhomogeneities. In each curved rectangle, a 16-bit pixel intensity codes for the measured dendritic density (# dendrites/10^6μm³). The 1e6μm³ scaling factor is introduced in order to obtain gray intensity values in the range of a 16-bit image. Finally, a gaussian blur (radius = 30 μm) is applied and a smoothed image/stack containing

the dendritic density map is created. The resulting maps represent dendritic density accounting for both sublayer inhomogeneities (e.g. Stratum Oriens, Radiatum and Lacunosum in CA1) and variations along the somatic layer (e.g. Medio-Lateral axis in a coronal section). **Figure 21** shows an overview of this procedure.

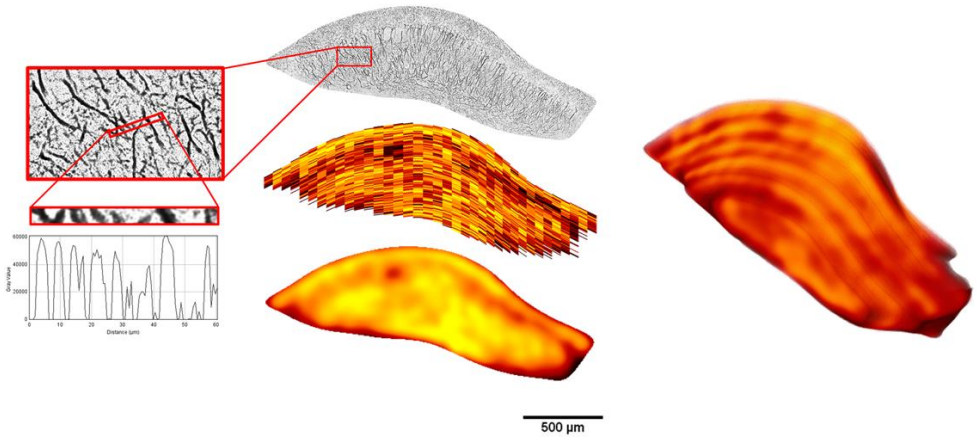

Figure 21: Overview of the dendritic density mapping procedure. A segmented somatic layer is preprocessed with a background subtraction of rolling ball radius = 2µm in order to highlight neurites. The amount of intersections in neighboring curved rectangles (height = 2µm and length = 40µm) along lines parallel to the somatic layer is measured and shown as image intensity. A gaussian blur (radius=30 µm) is applied and the intensity map masked again. (Right) 3D rendering of an interpolated (see **Section 2.2.2**) dendriticl density map for the CA1 pyramidal layer (Bregma from -1.34 to -2.34).

Interpolation

The advantages of generating 3D maps are apparent when those are put in the context of a global analysis pipeline. However, usually researchers work with sparse histological sections. Thus the numerical values of the intermediate positions are not available, and for generating 3D maps I have to use interpolation methods to attain bona fide numerical values.

Intensity-based interpolation and triangulation methods could not generate satisfactory 3D masks, given that these methods lead to artifacts in the reconstructed morphology of thin structures. I explored the usage of contour information for constructing the interpolated masks. Even though methods based on distance transforms have been proposed to improve segmentation quality (Grevera & Udupa, 1996), they were not sufficient for the interpolation of thin somatic layers. Thus, I decided to use the information of the contour in order to

guide the interpolation. To do so, I wrote an ImageJ macro that (1) obtains n equispaced points ordered along the contour of each of two consecutive slices, (2) linearly interpolates the X-Y positions of the obtained points for as many slices needed to fill the Z dimension and (3) creates the mask defined by the interpolated points in each of the interpolated slices. The only additional requirement that the algorithm has is the definition of a starting point for each originally segmented slice that should lay on the same anatomical landmark of the reconstructed region (e.g. CA1 distal tip). Despite its simplicity, this algorithm has yielded optimal results in our analysis, recapitulating bona fide the results obtained by single-cell reconstruction.

Another caveat in the use of single-dimension intensity interpolation is the introduction of artifacts derived from inhomogeneous density maps, that may produce a mismatch when trying to interpolate values between section embedding structural displacements.. In order to avoid those artifacts, I generalized the contour-informed interpolation method to generate 3D density maps. I developed a Fiji macro that obtains the contour of two consequent intensity map 2D slices. The basic algorithm evaluates the intensity signal at n points of each of the contours and generates an intermediate slice with interpolated coordinates and intensity. This is iteratively done for concentric contours until the whole area has been interpolated. The resulting 3D volumes show a qualitative improvement with respect to intensity- and triangulation-based interpolation methods. **Figure 22** shows a schematic representation of the interpolation procedure.
The developed source-code, a user-friendly ImageJ plugin and supplementary information can be found in https://bitbucket.org/linusmg/population_analysis.

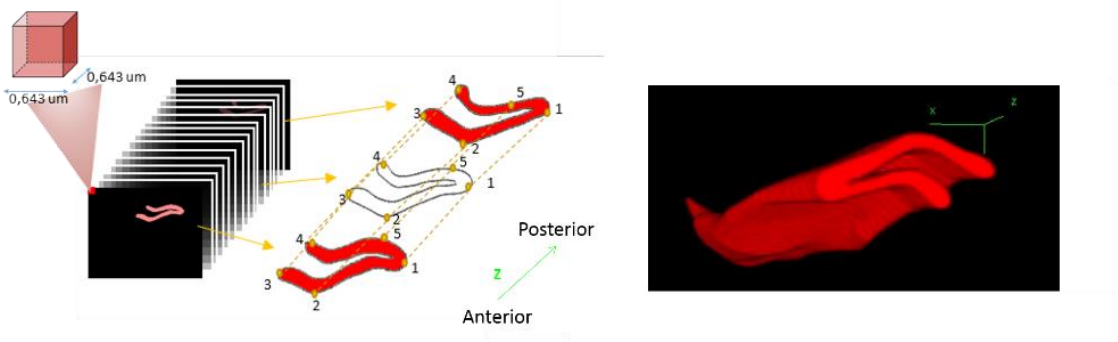

Figure 22 : Schematic representation of interpolation method developed. I show the third-dimension reconstruction of a dentate gyrus somatic layer as an example. (Left) Segmentations for each hippocampal

region were defined manually on each of the consecutive slices, according to YFP labeling and mouse brain atlas. (Middle) Blank slices were interleaved in between each 2 slices in order to fill the spatial gaps, according to voxel size (the figure represents in detail the space between 2 specific slices). Coordinates of the sorted contour points of each pair of consecutive original segmentations were used to interpolate the coordinates for the contour of each in-between slice. In the image only 5 of the 1000 analogous points used to do the interpolation are shown. (Right) Resulting reconstructed volume for the region in-between two slices.

Voxel-based analysis of interpolated cellular and dendritic density maps

The analysis of Thy1-labeled mouse brain sections using the tools described above, assess cellular or dendritic densities at specific Bregma coordinates from a 2D perspective, interpolating missing values, and allowing to provide semi-generative 3D maps. I here a developed a standardized 3D common coordinate framework and provided a simplified the statistical analysis to the application of already existing methods and software.

I took advantage of existing methods for MRI analyses and devised a pipeline that is based on three major steps: (1) the segmentation of the analysed ROIs and generation of sample group templates, (2) the generation of neuromoporphological metric 3D maps and (3) the registration of maps to their templates and their voxel-based statistical analysis.

The segmentation of the ROIs is implemented as previously described. In order to generate group-specific templates, I used state-of-the-art methods based on minimum deformation averaging (Janke & Ullmann, 2015). MDA is the iterative registration of all the group samples to their average and the inverse registration of this average towards the original sample morphologies. The iterative procedure tends to zero deformation of the average, after some iterations (10-20) a template of the group is obtained. In the field of pediatric neuroimaging it has been proposed as a high accuracy method for obtaining templates of small groups of samples. I implemented it on our wild-type dorsal hippocampus segmentations by using the Nipype port of Volgenmodel. **Figure 23** shows a schematic representation of the template generation procedure.

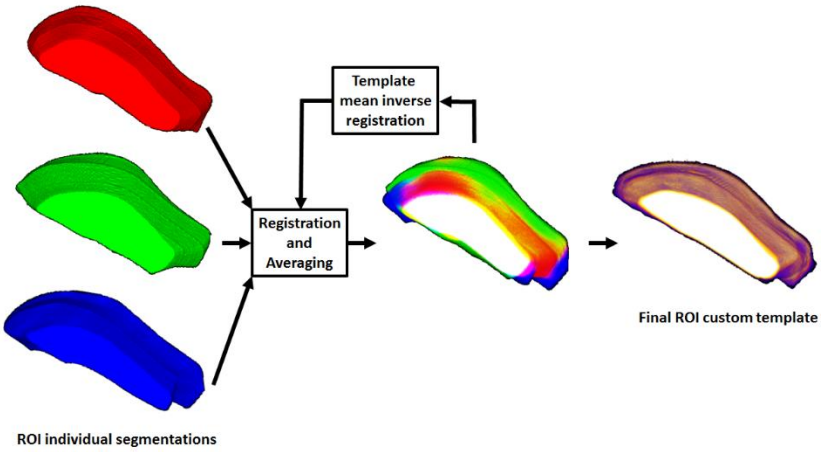

Figure 23: Schematic representation for the MDA procedure to the generation of anatomical templates. (Left) Three segmentations of CA1 dendritic field obtained from individual mouse brains. (Middle) First, an average of the three structures is obtained. All the samples are registered to the average and the transformations are used to perform an inverse registration from the average towards the original sample morphologies. The iterative procedure tends to zero deformation of the average, after some iterations (10-20) a template of the group is obtained.

Whole layer (CA1 dendritic field in this case) binary segmentations were registered to the wild-type template by automatic multiple step (rigid followed by non-linear) mutual information-based ANTs (Avants, Tustison, & Song, 2009) sample to template registration. In order to assess volumetric variability around the generated template, I saved displacement and volumetric change (Jacobian determinant) voxel-based maps of the non-linear registration. The transformations obtained with the binary masks were also applied to the 3D cellular and dendritic density maps. Finally, the registered 3D maps were compared statistically by using RMINC (https://github.com/Mouse-Imaging-Centre/RMINC), a versatile R package that facilitates fast fit of statistical models and false discovery rate (FDR) analysis in a voxel-based manner and user-friendly visual representation of the results.

Analysis of genotype dependent and environmentally driven dendritic modifications

Using the methods described above I aimed at characterizing the genoptype dependent abnormalities of CA1 cellular and dendritic maps and their possible modification with environmental conditions. To test dendritic rewiring effects I used environmental enrichment (See Chapter I).

Data lineage

In order to integrate the developed toolbox with a focus on data lineage, parameter exploration and interactive simultaneous visualization and analysis of multiple datasets, I implemented part of the described workflow in VisTrails by contributing modules calling the used and developed tools. The open-source code of our workflow and all the software tools can be found at https://bitbucket.org/linusmg/population_analysis.

2.2.4. Development of computational tools for generative modeling of 3D neuronal circuits

To interrogate the organizational principles underlying the architecture of brain networks, I developed a customizable simulation environment (Figure X) that allows to directly investigate how morphostructural features of brain circuits sculpt the emergent functional activity, and quantify the effects of targeted *in silico* perturbations. In that way, the model offers the unique opportunity to define the functional relevance of the network morphospace underlying the brain circuit of interest.

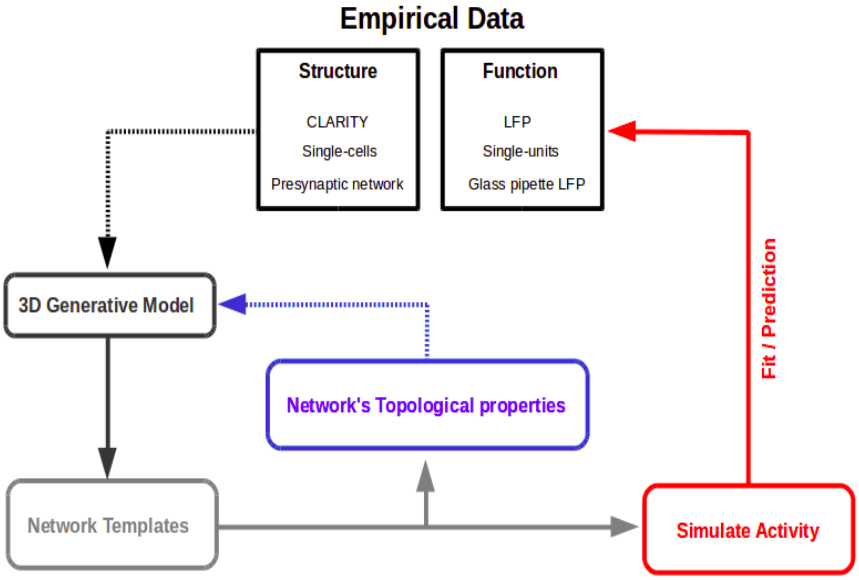

Figure 24: Our aim is to use population-based structural properties to parametrize a generative model leading to realistic network templates. These will be used to quantify topological properties of the network at an unprecedented level of detail, and enable posterior dynamical activity simulation. These properties depend on the morphostructural parameters used to generate the templates, that can be manipulated to obtain new templates showing desired topological characteristics, allowing to simulate network activity after targeted perturbation of the underlying topology.

My approach builds upon existing tools, supplying an easy-to-use and customizable unified toolkit to obtain, manipulate and visualize realistic 3D templates of network connectivity from population and single-cell structural data.

The model integrates self-developed MATLAB scripts and functionalities of the Trees Toolbox (Cuntz et al., 2011), and consists on a generative model of circuit connectivity in defined synthetic 3D Regions Of Interest (in our case, the layers of the hippocampal trisynaptic circuit). This model can incorporate realistic neuromorphological features both at the single-cell and at the population level.

First, ROI segmentations are used to define a 3D synthetic space in Matlab. This space is formed by multi-resolution HDF5 3D matrices representing the simulated region. Regions of the space that can be occupied by somata, dendritic trees or axonal projections are labeled with integer indices. Using the HDF5 memory-mapped format allows to generate volumes as large as needed with on-the-fly compression, scalable and parallelizable access and processing of subvolumes.

I instantiated empty pyramidal layers using synthetic 3D ROIs of the layers of the hippocampal trisynaptic circuit, in Matlab (see methods). In this model I incorporated realistic neuromorphological features both at the single-cell and at the population level. Specifically, I used a parallel algorithm to locate spherical somata in the pyramidal layers (DG, CA3 and CA1 in our case) at a specified cell density obtained from our stereological countings. However, the cell density can be introduced either with a single homogeneous value, or by constraining it locally using cell density maps. Given that the soma location is done in local subvolumes, the local density can easily be adjusted in function of experimental 3D cellularity maps. Once each soma was located, its coordinates and the tangential angle to the dendritic layer boundary were saved for the posterior orientation and embedding of dendritic trees. At the same time, a supplementary HDF5 volume stored, in each voxel of the synthetic space, a neuronal identification number. Scanning for spatially close pairs of voxels belonging to different neurons allowed the generation of the connectivity matrix at the end of the instantiation.

Based on groups of single neuron *.swc experimental reconstructions obtained from wild type animals aligned along their principal axis, a 3D branch density cloud for a stereotypical morphology (e.g. CA1 dendritic or axonal tree) was generated with the *gdens_tree* function using the Trees Toolbox.

To obtain arbitrarily large neuronal populations, the dendritic density cloud was then used to generate clones. This was done by obtaining a subset of points in a 3D space. The probability of selecting a specific coordinate was given by the 3D branch density cloud. Thus, coordinates in regions with high dendritic density have more probability to be chosen. Each new clone was generated using the obtained set of points and the *xMST_tree* function, which generates a minimum spanning tree connecting the selected points.

This procedure allowed not only to generate as many clones as needed to fill any neuronal layer, but also to modify the morphological properties of the trees by modulating the branch density clouds, the amount of points used to generate the trees and the options of the *xMST_tree* function. By scaling the branch density cloud with a population-based experimental dendritic density map obtained from either histological sections (see **Section 2.2.2**) or 3D imaging data (Chapter III), the tree embedding is constrained across neuronal layers, e.g. a thinner neuronal layer would imply smaller trees and a less intense dendritic density map, less complex trees.

Each neuron grows first an axon by translating (to the soma coordinates) and rotating (along the direction tangential to the layer) an axonal tree clone obtained as specified above. The translated and rotated tree is embedded by indexing free voxels in the HDF5 volume and taking into account the radius of the tree segments. An equivalent procedure is used to grow dendritic trees. When a tree segment intersects another, the minimum circumventing path is found by obtaining an obstacle distance map and performing a 3D fast marching between the two points of the tree that remain unconnected with the *perform_fmstar_3d* Matlab function.

Once axonal and dendritic trees were embedded, the HDF5 volume was visualized with Vaa3D. Finally, the populated synthetic space generated a connectivity matrix based on axon-dendrite, axon-soma, dendrite-dendrite and axon-axon pairs proximity (Stepanyants &

Chklovskii, 2005) for all the synthetic cells. I introduced information about dendritic tree properties (such as cell type, branch order, distance from the soma, spine densities etc.) that could modulate synaptic contact probability.

Programming environment

The development of the computational modeling framework required Matlab (version 2014b) including the Trees and the Statistics Toolboxes. A repository with the source code and all the Matlab functions required for compilation can be found at (https://bitbucket.org/linusmg/nem4o-generative_model)

2.3. Results

2.3.1. Morphological properties of TgDyrk1A CA1 pyramidal neurons

In order to assess within-class variability in the dorsal hippocampus, I analyzed the morphology of apical trees from pyramidal CA1 neurons by comparing LY stained neurons from wild-type mice and also compared them with TgDyrk1A littermates (20 neurons from 4 animals across different positions for each genetic condition).

After obtaining 20 neuronal reconstructions, I generated mean density plots of the neuromorphological metrics distributions for the two genotypes. The analysis revealed that the tip-to-soma path length distribution is skewed to larger values for the wild-type (**Figure 25**), showing significant differences in the number of short (*plen*<120 µm) and intermediate-length (260µm<*plen*<310µm) branches. This indicates that the dendritic branches of wild-type animals reach further distance than those of TgDyrk1A littermates. Similarly, the wild-type vs TgDyrk1A branch length distributions shown significantly higher probability density for intermediate length branches and lower probability for short branch fragments in the wild-type (data not shown). Conversely, the branch order distribution did not show differences among the two groups, indicating that tree span, rather than dendritic complexity, are altered in the model.

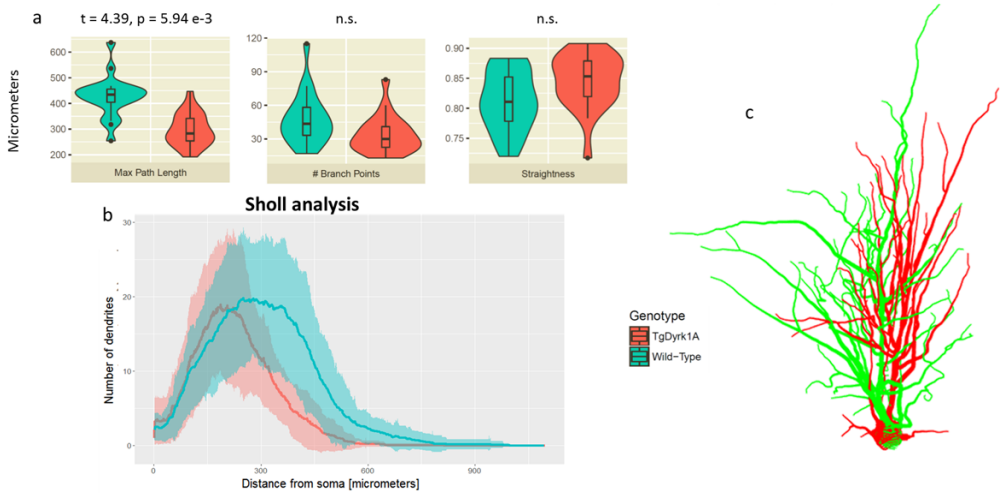

Figure 25: Genotype-dependent dendritic tree architectural modifications. (a) Box and violin plots showing the distributions of maximum path length, number of branch points and straightness of CA1 apical dendritic reconstructions from wild-type (blue) and TgDyrk1A (red) mice. (b) The thick line represents the mean number of branches for each genotype in function of the radius, the shaded region indicates the standard deviation around the mean values. (c) Representative reconstructions of wild-type and TgDyrk1A neurons.

The comparison of the maximum path length distributions shows a significant difference (t=4.39, p=5.94e-3, mixed effects linear model blocking for biological replicates) when comparing TgDyrk1A (427 ± 80 μm) vs. wild-type (298 ± 63 μm) neurons.

When I analyzed the center of mass of the trees (see "Neuromorphological analysis in Chapter 1), I observed that in the transgenic model it was displaced towards the pyramidal layer in the dorso-ventral (D-V) axis (-100 ± 28 μm vs. -139 ± 21 μm; t=-4.99 p=6.03e-3), indicating shorter trees in this direction. Finally, the spanning volume shows a tendency ($2.17x10^6 \pm 1.11x10^6$ μm^3 vs. $5.31x10^6 \pm 4.36x10^6$ μm^3; t=2.11 p=8.23e-2) to be higher in the wild-type, also showing higher variance. These results are shown in **Supplementary Figure 1**.

Given that the branching order distribution is similar in the two genotypes (**Supplementary Figure 1**), I performed the Sholl analysis to check whether the distribution of branches along the dendritic trees is the same in both genotypes. The analysis shows that even though in both cases the trees reach maximum branching of about 20 branches per Sholl radius, in the case of the TgDyrk1A the distribution is skewed to smaller radii, reaching its maximum at ~200 μm vs ~300 μm in the case of the wild-type (**Figure 25** b).

Principal component analysis

To identify metrics that explain the differences found in TgDyrk1A and account for the genotype-dependent neuromorphological variability, I performed a PCA with all of them (**Figure 26** top). The two first principal components explain 54.15% of the variance in the data. Principal Component 1 (PC1, 31.45% explained variance) is mainly contributed by measures that account for the size of the tree: the total length of the tree, the amount of branch points and the dendritic spanning volume. Principal Component 2 (PC2, 22.70% explained variance) is mainly contributed by measures that account for the symmetry of the trees (**Figure 26** bottom).: the center of mass in the dorso-ventral axis, followed by the mean path length, the mean branching asymmetry and the center of mass on the medio-lateral and antero-posterior axes. An overview provided by a 2D projection on those principal components shows that the neurons cluster by genotype, and that the variables contributing more to the difference among groups are the maximum and mean path length, and the center of mass in the dorso-ventral axis, followed by the spanning volume.

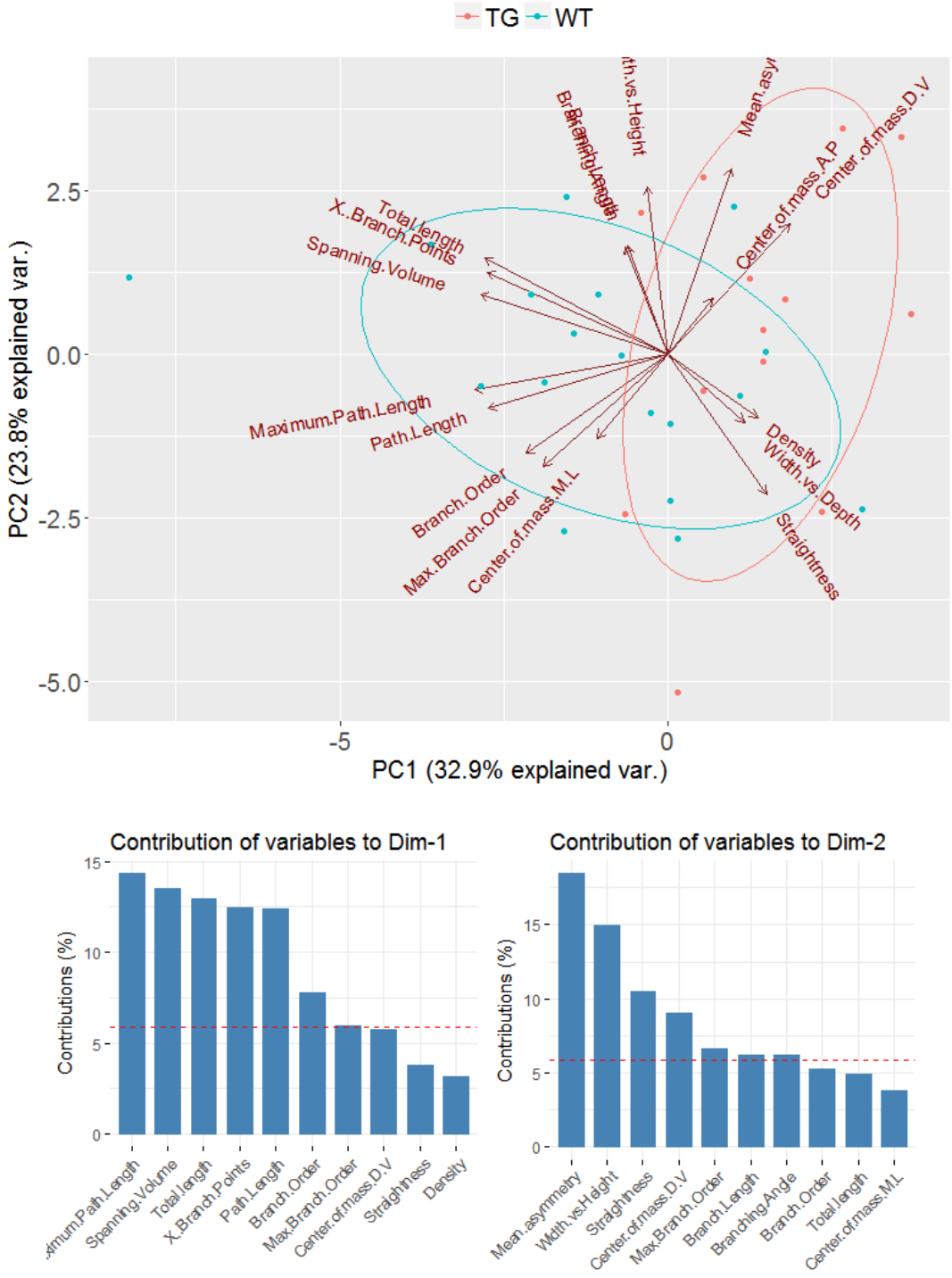

Figure 26: Principal component analysis (PCA) of the neuromorphological and geometric variables of the dendritic tree. PCA of the variables, where arrows represent the direction of each variable in the PCA space. Longer arrows belong to variables that are well represented by the two principal components. Each of the points represents one neuron, colored by the group they belong to. 68% confidence normal data ellipses for each group are drawn with solid lines. (Bottom) Bar plots showing the percentage of explained variance for each principal component. Bars represent the contribution (%) of each variable and the red dashed lines indicate the expected average contribution. The first principal component is a composite variable accounting for the dendritic tree size and the total dendrite length. The second principal component is a composite variable

accounting for other morphological measurements, mainly the branching angle, the number of branch points and the horizontal center of mass and mean asymmetry.

Wiring optimality

Understanding the implication of these architectural abnormalities on the hippocampal circuit and its functional capacities is beyond the scope of this study. However, as for cortical neurons, I explored how optimal are the wild-type and TgDyrk1A dendritic trees. When comparing wild-type vs TgDyrk1A reconstructions and their scaling laws between total length and amount of branch points, I found that both wild-type and TgDyrk1A follow closely the ⅔ optimal power found to be conserved among organisms and brain regions (exponent $b = 0.72 \pm 0.06$ and 0.66 ± 0.06respectively; **Figure 27**). This result indicates that hippocampal transgenic neurons are as optimal as their wild-type counterparts for signal integration.

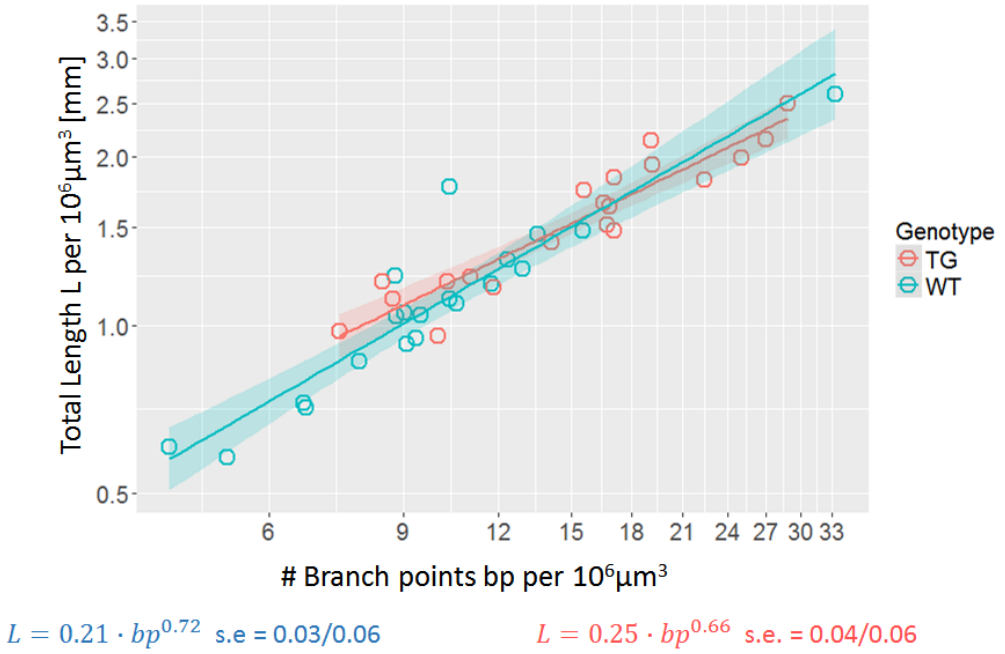

Figure 27: Power law relations between total dendritic length and branch number for layer II/III basal tree reconstructions of wild-type and TgDyrk1A neurons. The ⅔ optimal power for 3D trees is followed by the control trees (power = 0.72±0.06) and TgDyrk1A (0.66±0.06). The number of branch points and total length was normalized by the dendritic surface (S=10.000 µm²). Shaded regions indicate 95% confidence level interval of the power law fit.

Within-class CA1 pyramidal dendritic morphology variability along the proximal-distal axis

To address the question of within-class variability I selected CA1 pyramidal neurons positioned along the proximal-distal axis and analyzed whether their microstructural variability could be explained by their position along CA1. I here grouped the reconstructed neurons in two subgroups depending on their position: distal and central. **Figure 29** shows box plots of the mean path length and maximum branch order in neurons at distal and central positions along the proximal-distal axis of CA1. The analysis shows that in wild-type mice, there are subtle changes in the mean path length and branching, suggesting that CA1 pyramidal cells increase their dendritic length while decreasing their complexity from distal to central positions (path length: distal 185 ± 25 μm vs. central 203 ± 25 μm; maximum branching order: distal 17.7 ± 3.3 vs. central 14.7 ± 3.8).

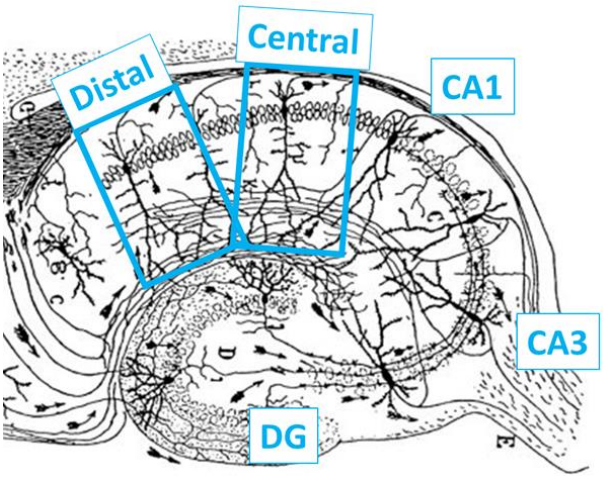

Figure 28: **CA1 along the proximal-distal axis.** Schematic representation of the hippocampus using a modified drawing by Ramon y Cajal showing orientative positions for the reconstructed and analyzed neurons in this section.

TgDyrk1A also show a similar positional dependency of their microstructure. However, even though the path length shows the same tendency to increase observed in wild-type (path length: distal 131 ± 24 μm vs. central 150 ± 22 μm), complexity shows the opposite tendency, being increased in central positions (maximum branching order: distal 12.5 ± 4.0 vs. central 16.7 ± 4.9).

Regarding genotype-dependent differences, the mean path length shows a tendency to be lower in TgDyrk1A neurons vs wild-type for both distal (131 ± 24 μm vs. 185 ± 25 μm) and central (150 ± 22 μm vs. 203 ± 25 μm) positions ($t=3.35$, $p=0.057$; and $t=4.18$, $p=0.27$ respectively). However, the maximum branching order shows a tendency to be lower in distal

TgDyrk1A neurons (12.5 ± 4.0 vs. 17.7 ± 3.3; t=1.68, p=0.20) while in central positions this tendency is lost (16.7 ± 4.9 vs. 14.7 ± 3.8; t=-0.85, p=0.65), leading to similar branch order distributions in the pooled analysis.

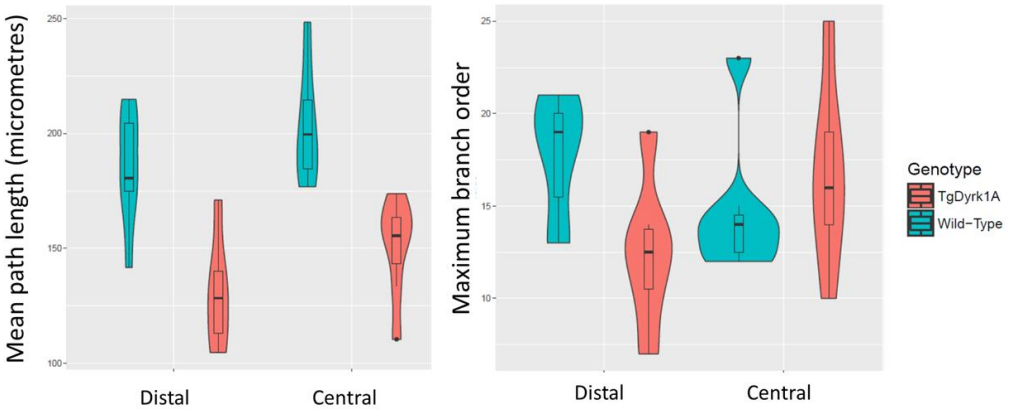

Figure 29: Genotype-dependent differences in neurite path length and branch order in TgDyrk1A. Box and violin plots representing mean path length (left) and maximum branch order (right) distributions for wild-type (blue) and TgDyrk1A (red) CA1 apical dendritic trees. The two labels in the x axis indicate the proximal-distal position along the pyramidal layer (see **Figure 28**).

2.3.2. Cellularity and volume variations along the antero-posterior axis of dorsal CA1 in TgDyrk1A

Stereological estimations

The representativeness of variations in neuromorphological properties that I have detected have to be considered in the scope of the volume and neuronal density of the layer. Specifically, Thy1 transgenic mice express fluorescent proteins in neuronal subpopulations but, even though its expression is seemingly consistent, quantitative studies estimating the percentage of fluorescent cells are lacking. To this aim, I obtained stereological volume and Thy1-labeled cell quantifications along the dorsal CA1 of wild-type and TgDyrk1A mice (N=3).

I first performed the same analysis using NeuN (a general marker of neurons) stained slices and found that neuronal densities show significant variation along the antero-posterior position, with an increase between Bregma -1.34 and -1.94 mm and a decrease between Bregma -1.94 and -2.34 mm ($3.78 \pm 0.68 \times 10^5$ cells/mm^3, $5.64 \pm 0.63 \times 10^5$ mm^3, $3.40 \pm 0.72 \times 10^5$ mm^3 respectively; **Figure 30** right), while the volume of the layer increases linearly (**Figure 30** left). Conversely, TgDyrk1A mice show a slight tendency to decreased densities towards posterior Bregma, while the volume follows a similar increase in TgDyrk1A than in wild-type mice.

I compared the NeuN densities with the Thy1-labeled cell population in the wild-type (**Figure 30** middle). Cell density increases from $0.89 \pm 0.27 \times 10^4$ cells/mm^3 at Bregma -1.34 to a maximum at Bregma -1.94 ($1.66 \pm 0.94 \times 10^4$ cells/mm^3), decreasing again towards Bregma -2.34 ($1.15 \pm 0.17 \times 10^4$ cells/mm^3). Conversely, TgDyrk1A mice show a consistent increase in the amount of labeled cells ($1.45 \pm 0.68 \times 10^4$ cells/mm^3, $1.97 \pm 0.91 \times 10^4$ cells/mm^3, $2.39 \pm 0.77 \times 10^4$ cells/mm^3; at Bregma -1.34, -1.94 and -2.34 respectively).

By comparing the Thy1 labeling with respect to NeuN positive cells, I found that the proportion of neurons labeled with Thy1 is in the range of 2-3%. Instead, TgDyrk1A mice show a constant Thy1+ neuronal density in all slices analyzed ($2.38 \pm 0.29 \times 10^5$ mm^3, $2.56 \pm 0.34 \times 10^5$ mm^3, $2.45 \pm 0.43 \times 10^5$ mm^3; at Bregma -1.34, -1.94 and -2.34 respectively).

These results indicate that Thy1-labeled cells do not provide reliable estimates for neuronal density in the wild-type case, and suggest that Thy1-driven expression may be altered in TgDyrk1A.

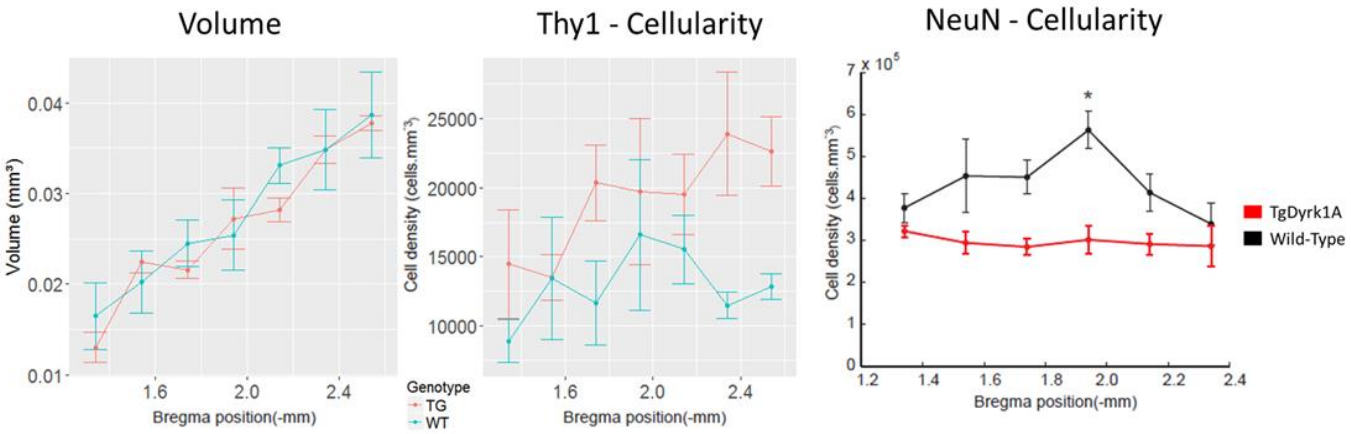

Figure 30: **Stereological estimations for volume (left) and cellular density of Thy1-labeled (middle) and NeuN immunostained (right) neurons in CA1 pyramidal layer.** Data are shown for wild-type (blue and black) and TgDyrk1A mice (red) estimated at increasing Bregma (in mm), as defined in Paxinos. Left panel: Volume estimations using Cavalieri. Note that increases linearly for both genotypes, with no genotype-dependent differences. Central panel: Thy1 labeled cellularity estimations obtained using the optical dissector in newCAST. Thy1 estimations show a peak in cellularity at Bregma -1.94 in wild-type mice and a consistent increase in TgDyrk1A mice. Right panel: NeuN labeled cellularity estimations obtained using the optical dissector in newCAST. Note that a maximum for NeuN stained neurons is detected in wild-type while no changes or even a slight decrease is detected in TgDyrk1A mice. Points indicate mean values and error bars standard deviations. * ($P \leq 0.05$) (ANOVA one-way test).

Population-based structural metrics through computational cellular and dendritic density mapping

In order to link the detailed information obtained by microscopy imaging of sliced histological samples with a population perspective, I have developed an analysis pipeline allowing 3D neuromorphological mapping in 2D sectioned brain.

I developed algorithms for obtaining 3D maps of the 2D population-based metrics (see **Section 2.2.2**): (1) the volume of neuronal layers, (2) the location and densities of cell bodies, and (3) the density of dendritic branches. Using the software I developed, I could obtain semi-automatic measures of the layer volume and cellular densities. Those semi-automatic quantifications broadly recapitulate the stereological measurements (**Figure 31**). Quantifications in the wild-type samples show again a convex curve along Bregma coordinates (1.31 ± 0.52 x10^4 cells/mm^3, 1.77 ± 0.49 x10^4 cells/mm^3, 0.87 ± 0.09 x10^4

cells/mm^3; at Bregma -1.34, -2.14 and -2.54 respectively), and TgDyrk1A show the consistent increase mentioned in the previous section (1.22 ± 0.89 x10^4 cells/mm^3, 2.61 ± 1.00 x10^4 cells/mm^3, 2.75 ± 0.60 x10^4 cells/mm^3; at Bregma -1.34, -2.14 and -2.54 respectively).

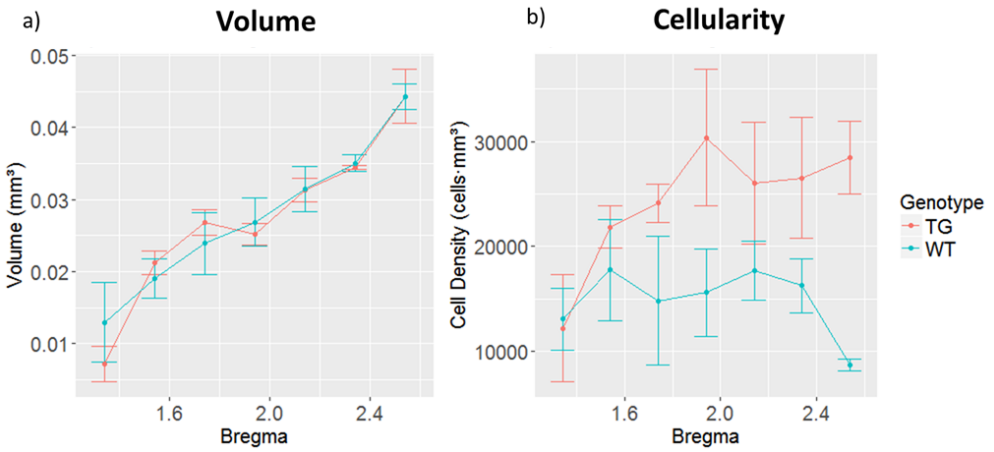

Figure 31: Volume and cellular density quantifications of CA1 pyramidal layer with the computational methods for population analysis. Volume shows a linear increase towards posterior Bregma for both wild-type (blue) and TgDyrk1A (red) mice. Cellular density in wild-type mice shows a plateau from Bregma -1.54 to -2.34, while in TgDyrk1A increases towards posterior positions. Points indicate mean values and error bars standard deviations.

In order to validate our computational method (**Section 2.2.2**), I obtained Bland-Altman plots for analyzing the agreement between our methods and the stereological quantifications of wild-type dorsal CA1 volume and cellularity. The mean and the difference between the two alternative measurements are obtained and plotted against each other. Also, lines showing the magnitude of 1.96 standard deviations with a 95% confidence interval are drawn in the plot (Altman & Bland, 1983).

The Bland-Altman plots of the pyramidal layer volume show (**Figure 32**) that differences between stereological and computational quantifications were distributed around 0, indicating that volumetric estimations were similar with both methods. Instead, the differences between stereological and computational cellularity estimations are distributed around ~3000 cells/mm^3 difference, indicating that cellularity is systematically overestimated by our computational method.

It is important to note that for both volume and cellularity the variance is in the order of the smallest measurements and does not seem to depend on the magnitude of the volume and

cellularity values. Such high variance is found in both methods, as seen by the error bars (s.d. ~ 0.5-1 x 10^4 cells/mm^3; **Figure 30 and Figure 31**). This suggests that most probably the variance can be explained by the small size of our sample (N=3) rather than low precision in the measurements.

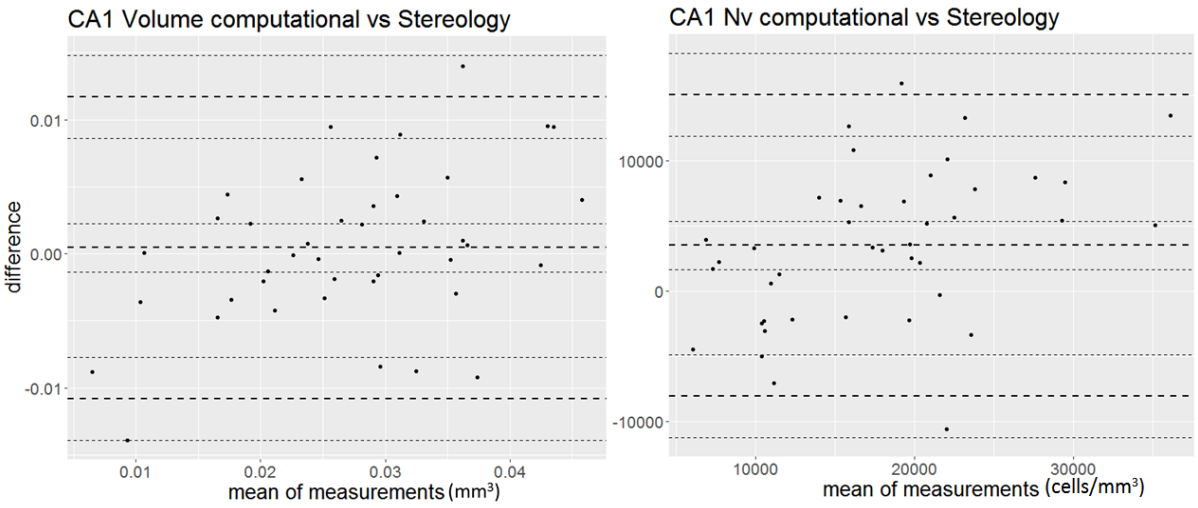

Figure 32: Bland-Altman plots of differences between the computational method and stereology vs. the mean of the two measurements. Plots for CA1 pyramidal layer volume (left) and cellular density (right) quantifications. Bold dashed lines in the centre of the plot represent the mean of the difference between to the estimations while bold dashed lines in top and bottom of the plot represents 2 times the standard deviation of the mean value. Light dashed lines indicate the 95% confidence intervals around those quantities.

To assess whether our method is able to detect gross morphological properties with biological meaning, I compared the cellular and dendritic densities between hippocampal layers CA1 and CA3. The marked reduction in CA3 cell density (**Figure 33** left), along with the quantifications validated with stereology in CA1, show that our method captures relevant changes in cellular density. Similarly, to assess whether our method for dendritic density quantification is meaningful, I compared the dendritic occupancy ratio between CA1 and CA3 after normalizing the amount of measured dendrites by the amount of labeled cells. The ratio between CA3 and CA1 is 1.46, indicating higher dendritic occupancy as seen in previous estimations found in the literature.

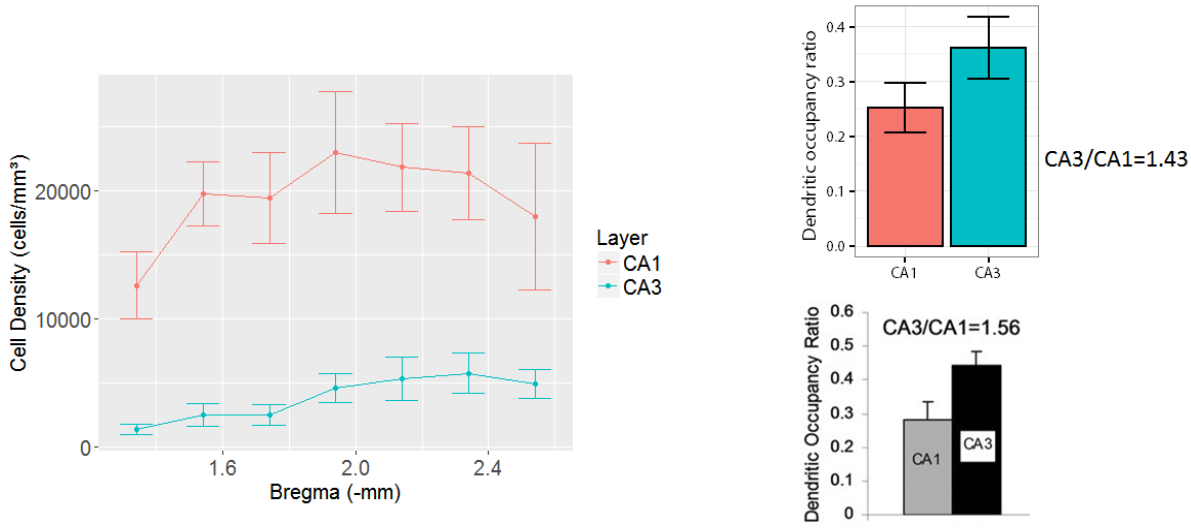

Figure 33: Cell density and dendritic occupancy in CA1 and CA3. (Left) Cellular density quantifications of CA1 (red) and CA3 (blue) pyramidal layers with the computational methods I developed. Points indicate mean values and error bars standard deviations. (Right) Dendritic occupancy ratio in CA1 and CA3 as calculated by our dendritic density measurements (up) and as estimated by Ropireddy, Bachus, and Ascoli 2012. Bars indicate mean values and error bars standard deviations.

Voxel-based morphometry in dendritic density maps recapitulates single-neuron dendritic alterations

The neuronal reconstruction and stereological measurements obtained, highlight the fact that the percentage of cells labeled with Thy1 is very low and that there is a high within-cell variability. Thus, sampling small numbers of neurons is not representative for neurons throughout neuronal layers. To overcome this problem I here assumed that Thy1 labeling defines a Single-cell class.

To study their morphological properties from a population perspective, I use the computational methods I developed for quantifying cell and dendritic density (see **Section 2.2.2**) and generating 3D maps. As part of my method, I create a standardized spatial registration to a common coordinate framework for the analyzed samples, controlling for spatial variability and physical deformations that commonly arise during sample processing. The 3D mapping of those features is inspired in the field of neuroimaging, where statistical differences between groups of datasets are identified in a voxel-based manner. Thus, the generated maps allow neuroimaging-like 3D statistical comparisons among sample groups by the application of methods based on Voxel-Based-Morphometry (VBM)(White et al., 2003).

As a proof of concept, I used the analysis pipeline exposed in **Section 2.2.2** in two groups (wild-type vs TgDyrk1A; N=4) of Thy1-labeled samples to map cellular and dendritic densities across the dorsal CA1 (Bregma -1.34 to -2.34). Even though the statistical power of our analysis is too low to identify significant differences after the False Discovery Rate analysis, **Figure 34** shows the t-statistic of a voxel-wise linear model testing whether the genotype of the samples predicts (wild-type respect to TgDyrk1A; voxels with t>0.83, have a 20% probability of being false discoveries, **Table 7**) the measured dendritic density values of each voxel along the antero-posterior axis in dorsal CA1. A close-up at Bregma -1.94 shows a tendency to increased dendritic density in distal CA1 of wild-type mice and slightly decreased in proximal CA1. The results in distal CA1 are consistent with the lower dendritic complexity observed in our single-neuron reconstructions (**Figure 29**).

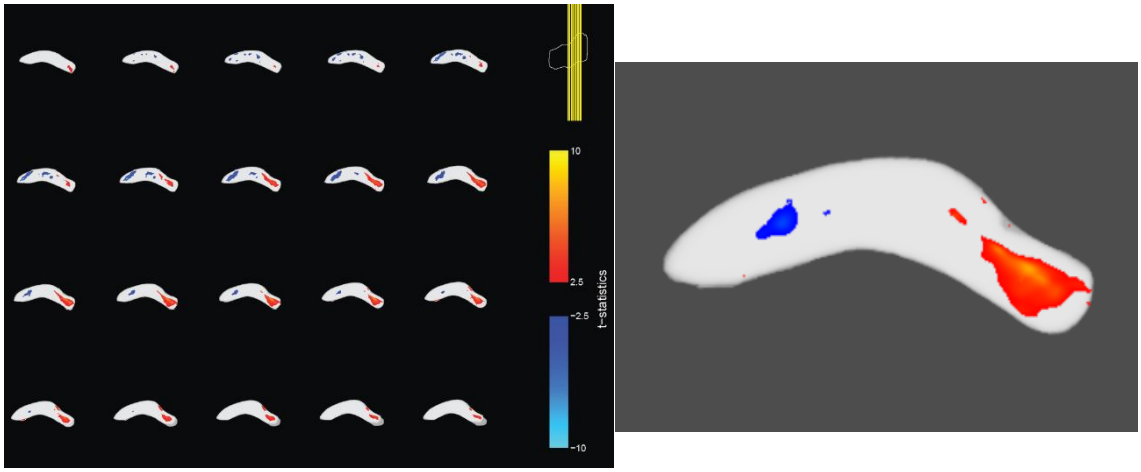

Figure 34: VBM analysis of dendritic density in CA1 from wild-type vs. TgDyrk1A mice. (Left) Series of coronal slices from Bregma -1.54 to -2.34. The colored scales show positive (fire) and negative (blue) values for the t-statistic of the linear model applied to each voxel. (Right) Close-up visualization to a coronal CA1 slice at Bregma -1.94. Values t<4.83 have been masked in the images.

Table 7: FDR analysis of the VBM dendritic density in CA1 comparison between wild-type vs. TgDyrk1A mice. The table summarizes the F-statistic, the t intercept and its value for various false disovery rates.

FDR	F-statistic	tvalue-(Intercept)	tvalue-ConditionWT
0.01	NA	3.401163	NA
0.05	NA	2.321877	NA
0.1	86.34038	1.867018	9.291953
0.15	65.49135	1.598359	8.092672
0.2	23.33567	1.401925	4.830701

Linking single neuron reconstructions to whole-layer dendritic density maps

In order to assess to what extent the population-based dendritic density maps are representative of single neuron dendritic tree morphology, I have compared measurements with the Sholl analysis and our modified-Sholl method in synthetic 2D trees arranged in an homogeneous layer. The analysis of synthetic 2D trees shows that both Sholl's and our method give comparable signatures (k=1.62, int=-2.04, R^2=0.951 for the Sholl analysis and k=1.70, int=-1.64, R^2=0.947 for our method). When a population of cloned trees is analyzed with our method, the dendritic density signature is also clear (k=1.77, int=-1.48, R^2=0.958), even showing qualitatively dendritic tree subregions in the Sholl Linear fit (i.e. Stratum Radiatum and Lacunosum).

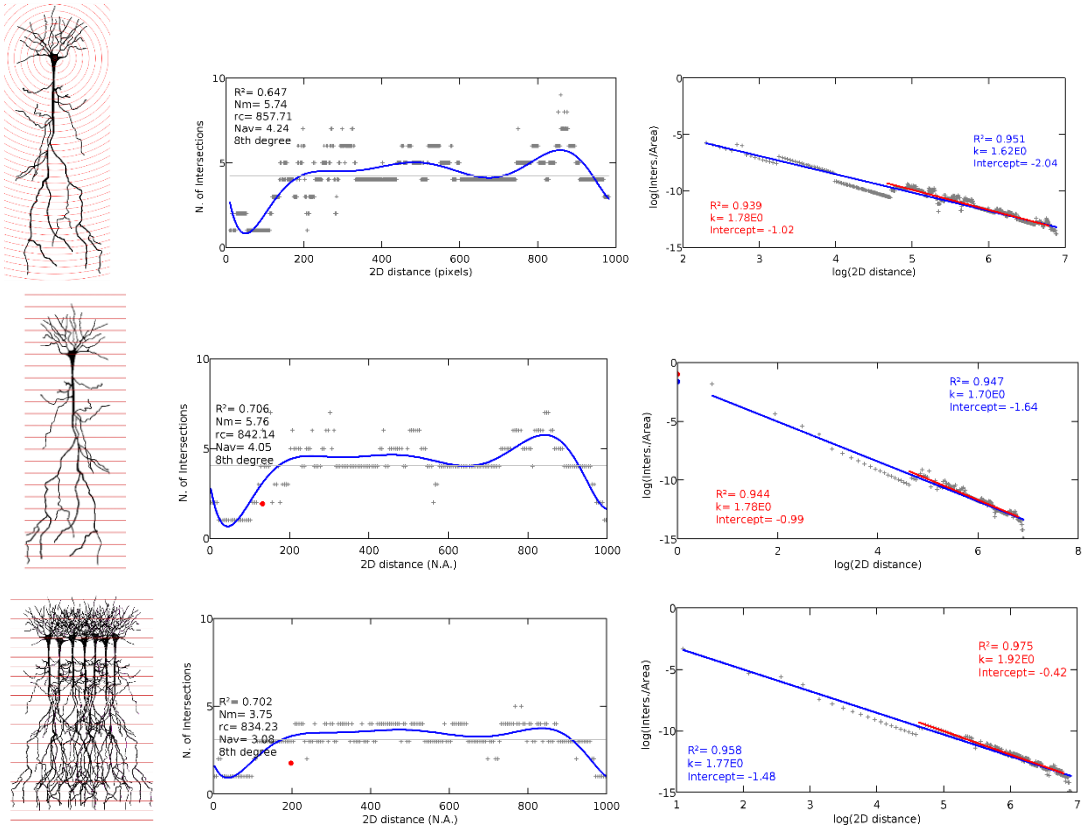

Figure 35: Comparison between single-cell and population-based Sholl analyses. (Left) Schematic representations of the analyses. (Middle) Linear Sholl plot of the number of intersections in function of the distance to the soma, a polynomial fit (blue and black parameters). (Right) Loglog Sholl analysis plot of the logarithm of the number of intersections per area versus the logarithm of the distance to the soma. In blue and red linear fit and parameters for a 95% of the data points and all points respectively. (Top) Single-cell default sholl analysis. Analysis done only for the apical tree.

Rewiring effects of environmental enrichment in CA1 apical dendritic trees: proof of concept

Thus, our population-based analysis can be used to identify dendritic complexity variations throughout neuronal layers. I used it to assess whether environmental enrichment could be rewiring CA1 neuromorphology. By focusing on the distal region seen to have lower dendritic density in TgDyrk1A, I obtained "layer-Sholl" plots along the layer perpendicular axis (from stratum lacunosum, through stratum radiatum until stratum oriens). Plotting the dendritic density obtained in the maps I generated, I can observe a dendritic signature characteristic from CA1 pyramidal neurons. Even though the tendencies are not significant (N=3), the plots show a tendency towards smaller and less complex stratum radiatum in TgDyrk1A mice compared to wild-types. Both TgDyrk1A and wild-type mice show an increase in dendritic complexity in the stratum radiatum upon environmental enrichment. In the case of the environmentally enriched wild-types, the analysis shows a reduction of the span in stratum lacunosum and an increase in dendritic density in stratum oriens (**Figure 36**).

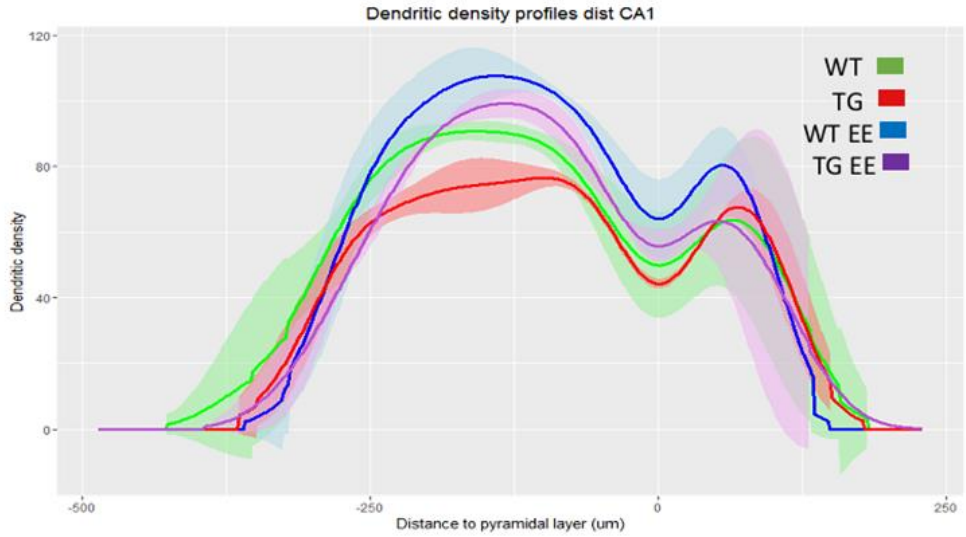

Figure 36: Dendritic density plot for distal CA1. Projection of the voxel values obtained from the CA1 dendritic density maps of wild-type (green), TgDyrk1A (red), and both groups upon environmental enrichment (blue and purple respectively). Mean (line) ± S.E.M. (shade) is represented.

Generation of realistic trisynaptic circuit templates

Even though I could not present here an exploration in the generative model I have developed, the developed software allows the synthetic instantiation of circuits I are interested in **Figure 37** shows a snapshot of a 3D rendering of the trisynaptic circuit in dorsal CA1. The model allows to generate circuits based on minimal input: Dendritic, somatic and axonal layer segmentations, cellular density values, and a group of tree reconstructions.

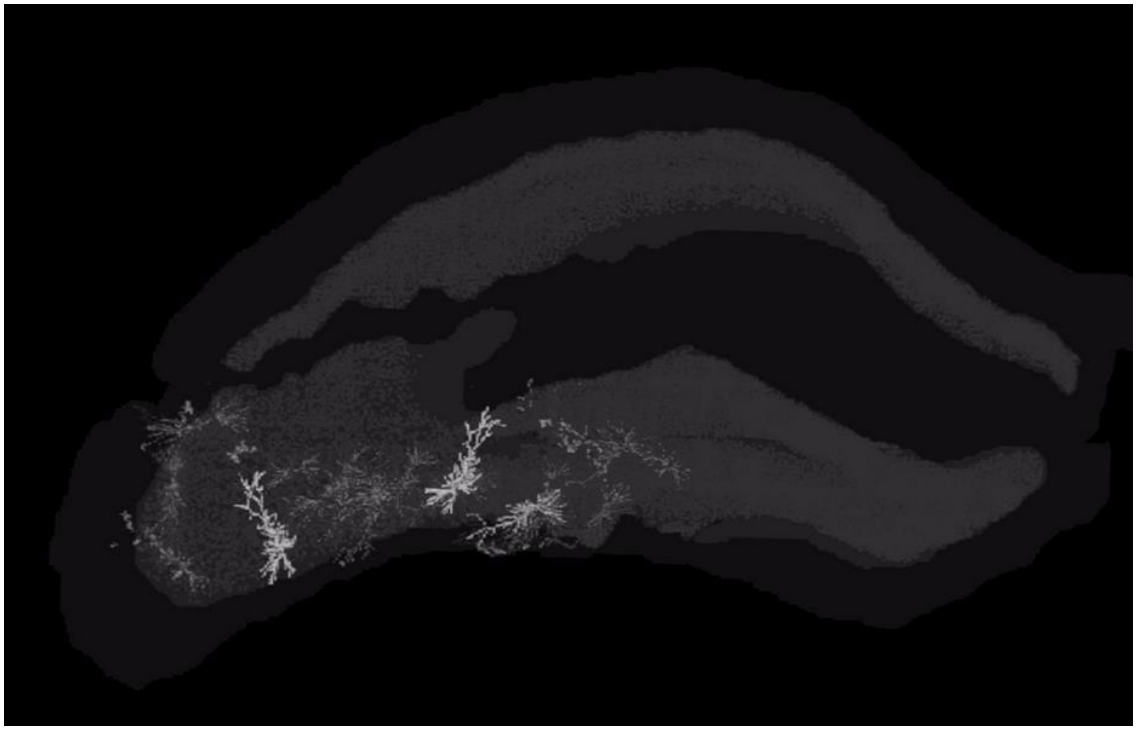

Figure 37: 3D model for the instantiation of biologically realistic neuronal circuitry. An overview of an instantiation of the hippocampus. The levels of grey indicate the layer segmentations and instantiated nuclei and, with increased brightness 10 embedded neurons.

2.4. Discussion and conclusions

Overall, the work done in this Chapter contributes to two main aspects: first, the characterization of neuromorphological properties by taking into account within-class variability in wild-type and TgDyrk1A mice. Second, the development of computational methods to visualize, quantify and incorporate population-based neuromorphological quantification methods in a neuronal circuitry simulation framework.

Dendritic architecture of TgDyrk1A CA1 apical trees

Altogether, the dendritic tree alterations found suggest that the transgenic mouse model could have an imbalance in the integration of afferent signals to the *stratum radiatum* and *stratum lacunosum* (including long-range incoming axons from CA3 and the Entorhinal Cortex, and short-range CA1 intrinsic modulation).

Morphological within-class variability of hippocampal neurons

Even though anatomical inhomogeneities across neuronal layers have been well known for decades(Ahmad & Henikoff, 2002; Jinno & Kosaka, 2009; Rihn & Claiborne, 1990) but largely overlooked in the study of neuronal circuits, assuming they are irrelevant for function. Recent evidence suggests that functional segregations is linked with such variations(Igarashi et al., 2014). Our systematic study of dendritic trees in a small region of the dorsal hippocampus suggests that within-class variability depends on the neuron location along the proximal-distal axis. However, the power of our analysis is very low due to the small numbers of neurons per location. Thus, a completion (ongoing work) of the dataset is necessary to detect significant differences among positions, and dissect the variability of within-class neuromorphological properties along the proximal-distal and antero-posterior axes of dorsal CA1.

Nevertheless, interestingly, I found that dendritic tree span is reduced in the neurons of TgDyrk1A mice both in distal and central positions along the proximal-distal axis, while dendritic complexity is selectively reduced in the distal region of the dorsal CA1. Those differences are concomitant with a marked behavioral impairment in single object recognition tests(Pons-Espinal, de Lagran, & Dierssen, 2013) , and a mild impairment in

spatial learning(Torre et al., 2014). Given the recent evidence for functional segregation between distal (contextual) and proximal (spatial) regions of CA1(Igarashi et al., 2014), this suggests that the reduced dendritic branching reaching the *stratum lacunosum* observed in TgDyrk1A neurons could be impairing the integration of sensory information provided by entorhinal cortex afferents.

Cellularity along the antero-posterior axis of CA1 in TgDyrk1A

Moreover, the stereological analysis of NeuN-immunostained neurons in dorsal CA1, indicates that gross morphological features, i.e. cellularity and volume, of the pyramidal layer tend to vary with antero-posterior coordinates at a local spatial scale (~500μm). While cellularity variations along the septo-temporal axis of the hippocampus had been described at the scale of few millimetres(Gaarskjaer, 1978; Jinno & Kosaka, 2009), I show that those variations can be relevant at a shorter spatial range. Thus, the position-dependent variability is a confounding factor to take into account when analyzing the properties of neuronal populations even locally.

Computational methods for population-based analysis of cellular and dendritic density

To overcome the small number sampling issue, population based labelings (such as Thy1 induced fluorescent protein expression) can provide a holistic perspective to properties of neuronal layers, while tailoring the studies by constraining the analysis to specific cell classes. However, our stereological quantifications using NeuN and Thy1-labeled cells show that selecting a specific neuronal class as a representative set must be done carefully. In our study, cell density quantifications differ between the two labelings, and the Thy1 expression pattern in dorsal CA1 seems to be affected by the transgenic expression of Dyrk1A in the studied DS mouse model. Thus, a systematic validation and cautious interpretation of conclusions drawn from Thy1-dependent population-based labeling is needed.

In order to tackle the population-based measurements that can overcome the issue of small number samplings, and taking into account that stereological measurements have too low throughput for systematic detailed studies, I explored the development of population-based computational analysis tools. I developed algorithms for mapping cellular and dendritic

density on Thy1-labeled neuronal populations. The obtained quantifications are consistent with the stereological measurements and our single-neuron morphology analysis. Thus, being sensitive enough to identify local variations. This unprecedented sensitivity suggests that the developed tools, beyond the issues related to the Thy1 labeling, allow comparative morphological analysis with unprecedented detail that could help understanding functional segregation, explaining specific behavioral traits in the TgDyrk1A DS mouse model.

Previous studies have shown an increase in dendritic tree size and complexity in CA1 pyramidal neurons upon environmental enrichment in wild-type mice (Beauquis et al., 2010) I observed increased dendritic density in the *stratum radiatum* and *stratum lacunosum* fields. However, our data suggests that the span of the dendritic trees is smaller. Our results show a similar tendency in the case of TgDyrk1A mice. This recovery, mainly relevant for the *stratum lacunosum* region of the tree, could explain cognitive improvement in spatial memory tasks by environmental enrichment. Ongoing experiments to obtain single neuron reconstructions in environmental enrichment conditions will confirm the tendencies seen in the population-based analysis.

Generation of realistic trisynaptic circuits

Despite the extensive and ever-growing literature about the functional implications of topological properties of large-scale anatomical brain networks, the methodological limitations of the microscopic description of neuronal morphology have bounded the ability to analyze and characterize the topological organization of brain microcircuits from a systems perspective. Computational attempts to reproducing *in silico* the dynamical properties exhibited by different brain regions (Blue Brain Project, Markram 2006; Human Brain Project, Shepherd et al. 1998) do not provide the versatility needed to assess the impact of subtle neuromorphological alterations, neither the possibility of parameterizing the models with CLARITY experimental data. Thus, the neuroscientific community lacks a simple open-source extensible tool able to bridge this gap.

Even though our modeling framework has not been tested yet, our analysis in Chapter I suggests that interesting outcomes will be obtained once the model is instantiated, the morphospace explored, and the wild-type and TgDyrk1A cases parameterized based on experimental. I think that, together with the population-based computational analysis tools I developed, the studies enabled by the first steps presented here will be relevant for

understanding functional segregation and, ultimately, the impact of subtle neuromorphological properties on the computations performed by specific neuronal layers.

3. CHAPTER III. RECONSTRUCTING AND MODELING THE TRANSPARENT WHOLE BRAIN

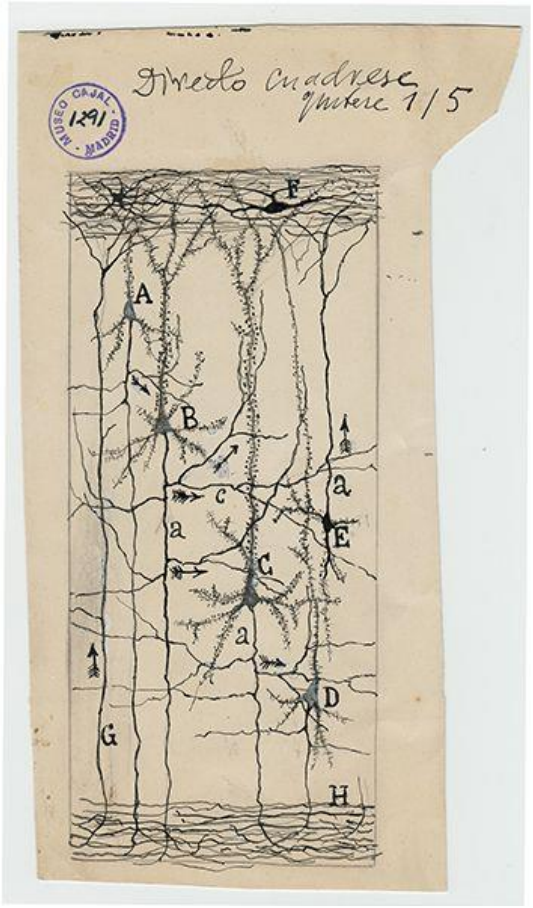

The "arrows" of Cajal. The drawing represents with arrows direction of information flow in cortical neurons. Courtesy of Instituto Cajal

"To understand mental activity it is necessary to understand molecular modifications and changes in neuronal relationships. Of course one must know the complete and exact histology of cerebral centres, and their tracts, but that is not enough"

Santiago Ramón y Cajal

3.1. Introduction

Charting cellular localizations, projections, and network activity throughout the whole brain is a mandatory step to understand network properties, but the tools for combining these levels of description are not available yet. Many efforts in the Neuroscience field are devoted to build cellular-resolution, brain-wide neuroanatomical atlases of the mouse brain, but technical limitation to obtain whole brain structural information with microscopic resolution has hampered our capability of understanding micro-connectomics at a system level. I are usually faced with having either poor spatial scale (examining only a small part of a larger brain network) or poor spatial resolution (examining a large network but at the cost of understanding microstructure). Most experiments still involve slicing the brain into relatively thin sections (20-50 μm) before histological staining, imaging, and quantification. These techniques have yielded very good results for atlasing (e.g. Allen Brain Atlas) and are still being used in high-throughput mapping projects. For example, the MouseLight Project (https://www.janelia.org/project-team/mouselight) of Janelia that is mapping the complete axonal projections of individual neurons across the entire mouse brain (

Figure 38). However, sectioning the brain has its own drawbacks. For instance, light continues to be scattered even within relatively thin brain sections (limiting axial resolution), sectioning may damage and/or distort the tissue, and much of the rich structural information may be lost in sectioned tissue, even if attempts are made to accurately reconstruct 3D images.

Figure 38: 3D structural analysis of whole mouse brains. A reconstruction of three neurons that span the mouse brain. MOUSELIGHT PROJECT TEAM, Janelia Reseach Campus. Scale bar = 2000μm.

A recent technique called CLARITY, allows rendering intact biological tissues transparent by lipid-exchange, by embedding the tissue in an anatomically rigid, imaging/immunostaining compatible, tissue hydrogel (Chung et al., 2013). The technique overcomes existing limitations to produce transparent tissue without quenching endogenous fluorescence, and this tissue can also be labeled via immunohistochemistry. This provides a unique opportunity to bridge anatomical scales from subcellular to whole brain. In the last years, a number of research groups have implemented new tissue clearing techniques (CLARITY, CUBIC, Lumos, STP, 3DISCO, Sca/e, or SeeDB)[x] allowing comprehensive microscopic imaging of rodent whole brains. The power of these techniques relies on bridging *de facto* the macroscopic and microscopic scale descriptions of the system, allowing high-throughput imaging of whole brains with cellular resolution.

The CLARITY protocol was originally published by the Deisseroth lab (Chung et al. 2013; see **Figure 39**) and methods to optimize the imaging component subsequently added (Tomer, Ye, Hsueh, & Deisseroth, 2014). A modified CLARITY protocol, using only passive clearing techniques to avoid the possible tissue damage produced by electrophoretic current, was also recently described (Tomer et al., 2014; Yang et al., 2014; Zhang et al., 2014). However, to effectively take advantage of CLARITY, it is crucial to obtain brains that are highly transparent (for deep imaging) and rigid (to facilitate registration to a reference atlas). While passive clearing may produce transparent tissue, electrophoresis is necessary to achieve the full potential of CLARITY. The original protocol for CLARITY proposes FocusClear as a refractive index matching (RIM) medium for clear imaging, as well as a glycerol solution

as an alternative (Chung et al., 2013). However, previous results in the lab show that the resolution decreases when trying to track axons on more than 3 mm in depth in the sample. Different media have been reported in order to improve the transparency and, so, the resolution in depth, such as a solution based on diatrizoic acid (M. J. Hawrylycz et al., 2012)(Kim et al., 2015).

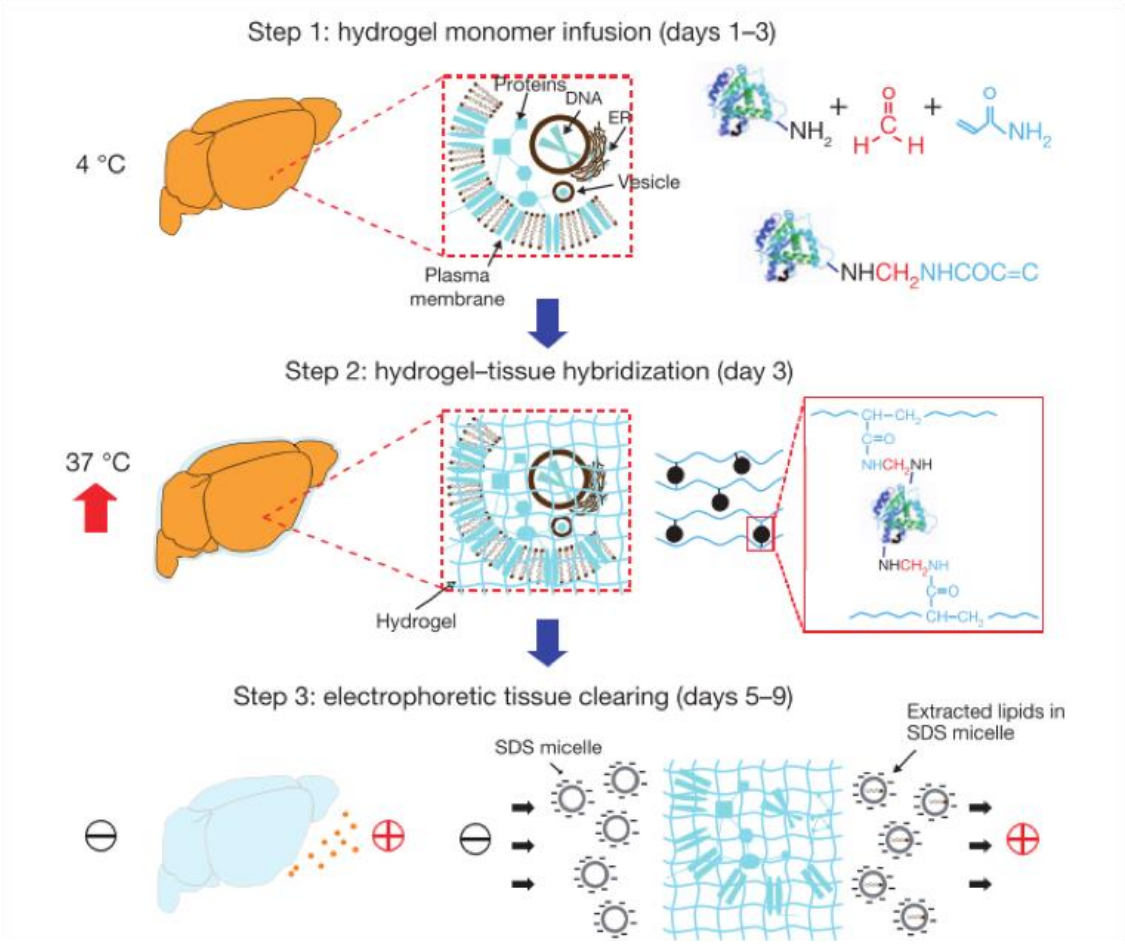

Figure 39: Schematic representation of CLARITY protocol basis. Tissue is crosslinked with formaldehyde (red) in the presence of hydrogel monomers (blue), covalently linking tissue elements to monomers that are then polymerized into a hydrogel mesh. Electric fields could be applied across the sample to actively transport ionic detergent micelles into the tissue, carrying the lipids out of the sample and leaving fine-structure and crosslinked biomolecules in place. Step 3 can also be done passively implying higher clearing time. Figure from (Chung et al., 2013).

Another limitation is that, up to date a relatively low effort has focused on developing standardized, extensible, and scalable analysis tools. Although whole brain imaging would enable multiscale and population-based analysis, at the moment many data arise from classical neuromorphological studies by histological sectioning. In order to avoid reductionist

or homogeneity-assuming perspectives, this work aims to develop a computational toolset for multiscale and population-based characterization of brain regions by brain slices data reconstruction.

The aim of this part of my Thesis was to implement a new cost-efficient CLARITY protocol, and to start filling the analysis gap by developing a suite of unified softwares to construct multiscale structure-function maps from brain-clearing experiments, with specific subworkflows for understanding topological dependencies on a brain-wide scale. The set of tools I propose are a first step towards a systems perspective description of neuronal circuits' microscopic structural and population-based properties. Such framework can help to link the extensive kinds of information available from cellular and molecular neuroscience with whole brain perspective studies. Besides, the proposed suite of tools can be used to bridge structural data with functional descriptions.

3.2. Methods

The aim of this chapter was to integrate the approaches and tools developed in chapters I and II in the scope of studying whole neuronal circuits in the mouse brain. To this end, a set of tools for imaging, analyzing and modelling whole brain data needed to be implemented. I first implemented and modified the CLARITY technique in our lab. To reach high quality whole mouse brain imaging I assessed existing alternatives for steps of the experimental protocol important for imaging quality and optimized them. Second, I searched, modified and gathered together a set of tools for the visualization and analysis of CLARITY datasets, setting up an analysis pipeline for whole brain imaging. Finally, I developed a 3D generative modelling platform for the instantiation of multi-scale neuronal networks, able to account for fine details in neuronal architecture, to be parameterized accounting CLARITY experimental data, and to simulate neuronal connectivity in arbitrarily large volumes.

3.2.1. Brain clearing technique (CLARITY)

To implement and optimize the CLARITY technique, I used the same Thy1-Yellow Fluorescent Protein (YFP) transgenic mice (strain B6.Cg-Tg(Thy1-YFPH)2Jrs/J nº003782; The Jackson Laboratories) used in Chapter II. Housing conditions, breeding and genotyping are described in the Methods Section of Chapter II. All animal procedures and housing conditions followed the guidelines of local and European regulations.

Brain sample obtention and clearing

For the clearing experiments I used eighteen 3-month-old adult wild-type mice. The mice were sacrificed and transcardially perfused with cold phosphate buffered saline (PBS), followed by cold CLARITY hydrogel solution, prepared as previously described (Chung, K.; Wallace et al., 2013). The brains were removed from the skull, immersed in 20 mL of hydrogel solution and stored at 4ºC shielded from light. After 2-3 days at 4ºC, hydrogel polymerization was induced by 3h incubation at 37ºC. Contact with oxygen was prevented

with a vegetal oil layer. Thereafter, the already polymerized surrounding hydrogel was removed. Entire brains were immersed in 50 mL of clearing solution (Chung, K.; Wallace et al., 2013) and stored in a water bath at 45ºC. Slices were arranged in a 48 well plate with 800 µL of clearing solution and stored in an incubator at 45ºC. After 2 months of incubation in clearing solution for passive clearing, optical transparent brains were washed with 50 mL PBST (0.1% TritonX in 1X PBS) twice for 24 hours each, at 45ºC. After that the samples were immersed in a Refractive Index Matching (RIM) medium for 2 days before imaging.

Refractive index matching (RIM) solution preparation and transparency evaluation

The first step was to optimize transparency in our samples. To this aim, I tested four RIM solutions: FocusClear, glycerol solution (Glycerol 87% + 2.5 mg/mL DABCO), diatrizoic acid solution (75 g diatrizoic acid, 70 g d-sorbitol and 23 g n-methyl-d-glucamine in 100 mL of water) and TDE solution (2,2-thiodiethanol 83% + 4 mg/mL n-methyl-d-glucamine). All reagents are from Sigma.

Transparency was evaluated on whole brain cleared samples under exposure to RIM media candidates. Four brain samples (N=4) were incubated with 50 mL of each RIM medium candidate during 4 days at 45ºC. Transparency of the samples was assessed at days 2 and 4 after incubation by measuring the light transmittance. The samples were immersed in the corresponding medium in a Petri dish, which was situated on a white light source covered by a white paper with a printed grid. Images were taken by means of a stereomicroscope (LEICA MZ16F), using different sets of filters for increasing wavelengths: CFP (Cyan-Fluorescent Protein_excitation wavelengths (exc.) 426-446 nm, emission wavelengths (em.) 460-500 nm), GFP3 (Green-Fluorescent Protein 3_exc. 450-490 nm, em. 500-550 nm), DSR (DsRed_exc. 510-560 nm, em.590-650 nm), Cy5 (exc. 590-650 nm, em.663-738 nm). Also the total white light transmittance was evaluated by using no filter. Using ImageJ, the mean grey value was measured in the area occupied by the sample. This value was normalized by the mean grey value in the same area for the image taken, with the same filter and exposure conditions, when only the corresponding medium without the sample was in the Petri dish. Sharpness measurements were obtained by using the Matlab *sharpness* function (https://es.mathworks.com/matlabcentral/fileexchange/32397-sharpness-estimation-from-image-gradients). Sharpness is estimated by measuring the magnitude of intensity

gradients in an image. The function was run on the images used for measuring the transmittance.

The deformation of the samples (Swelling Ratio) upon RIM incubation was assessed by measuring the linear expansion of the sample under exposure to each RIM media candidate. Measurements of pixel areas covered by the samples 2d and 4d after immersed in the RIM media candidates are normalized for pixel areas of images taken to the same samples at day 0 (0d) in PBS-T. The pixel area was measured by making polygonal selections around the brain contour were done using ImageJ tool.

Fluorescence signal to Noise Ratio

One of the possible problems in using specific RIM media is the loss of the sample fluorescence, and I had some problems with fluorescence loss after passive CLARITY. This is especially important for endogenous YFP, since I use transgenic mouse lines that express this fluorescent protein to visualize specific cell populations. Thus I aimed at finding optimum clearing protocol for genetically labeled neurons. In my experiments, I used cleared half brain coronal sections (1 mm) to assess the fluorescence signal under exposure to RIM media candidates. Four sections (N=4) of the same region were incubated in a 48 well plate with 800 µL of RIM media candidates at 45ºC during 10 days. I assessed the fluorescence signal of the cleared sample at days 2 and 10. Stacks of 100 µm of depth with a step size of 2.98 µm were taken for each of the samples in the cortical area using a confocal microscope (Leica TCS SP5 CFS) with a 20x objective and the appropriate set of filter for YFP. All the imaging parameters were maintained constant for all the images. Z-projections at maximum intensity of the stacks were thresholded using Otsu's method (Otsu, 1979). Mean intensity and standard deviation were measured both in the thresholded zone and also in the background. These parameters were used to evaluate Contrast-to-Noise Ratio (CNR) as previously described (Magliaro et al., 2016).

3.2.2. CLARITY Whole-brain imaging and data preprocessing

I have developed a framework for visualization and analysis of 3D images of cleared brains. I combined existing open-source computational tools and self-developed scripts and developed simplified user interfaces for integrated processing, visualization, and analysis.

Imaging

Tissues cleared using the above methods were then imaged in 3D. Briefly, cleared whole brains were immersed in 50 mL of Diatrizoic Acid solution (DA; 75 g diatrizoic acid, 70 g d-sorbitol and 23 g n-methyl-d-glucamine in 100 mL of water) at 45ºC for 48hr. After incubation in DA the samples were imaged in a custom-built Single Plane Illumination Microscopy (SPIM) set-up. SPIM is a fluorescence microscopy technique that uses a focused light-sheet to illuminate the specimen from the side. SPIM achieves excellent resolution at high penetration depths while being minimally invasive at the same time. SPIM offers a number of advantages over established techniques such as strongly reduced photo-bleaching, high dynamic range, and high acquisition speed. The idea behind SPIM and other light-sheet-based microscopy techniques is to illuminate the sample from the side in a well-defined volume around the focal plane of the detection optics. The microscope, built in James Sharpe's lab and used in collaboration with Jim Swoger, is designed to image 3D samples with sizes of about 1 cm. I used a detection lens with magnification 5x and a laser wavelength of 488 for fluorescence excitation. The sample is mounted to a micro-manipulation stage that allows translation in 3 dimensions and rotation about the vertical axis, to allow orientation for optimal imaging, inside a cuvette filled with 50 mL of RIM. The SPIM software has been written in Labview to control the instrument and automates scanning of samples that require up to 10s of thousands of individual images. Acquiring complete data sets covering a whole mouse brain hemisphere takes ~36h for a single-channel and generates ~0.5Tb, uncompressed data.

Tera-voxel sized dataset stitching

The most common format in which fluorescence microscopy data is obtained in neurobiology labs is adjacent image stacks covering the regions of interest. In case of being interested on features at the mesoscale or macroscale of the samples, the first necessary step is to stitch the tiled data obtaining a unique dataset for the whole system of interest (in our case, the whole brain). The recently developed Terastitcher software allows this kind of preprocessing using small RAM amounts and by a user-friendly straightforward procedure that is compatible across platforms. Furthermore, it allows the export of the data in both the multi-resolution pyramid format used by Vaa3D Teramanager or single stacks in a variety of

image formats that can then be used in any other image analysis software. This has been already assessed in Bria and Iannello, 2012.

Visualization

Once the dataset has been stitched a first visualization of the raw data is important in order to both check its quality and to allow the investigators to identify cues that can be informative of the analyzed samples and can orient subsequent analysis steps. As mentioned above there are currently two solutions for the visualization of teravoxel-sized imaging datasets, Vaa3D's TeraFly (Bria, Iannello, Onofri, & Peng, 2016) and Fiji's BigDataViewer (Pietzsch, Saalfeld, Preibisch, & Tomancak, 2015) plugins.

Segmentation

In the rodent brain case, the regions to be segmented are given by anatomical regions of the brain and are already well defined in atlases such as (Allen Nissl). However, the kind of processing performed here can also be compatible with self-generated compartmentalizations of any sample of interest.

Registration and template generation

As assessed in chapter II, the voxel-based statistical comparison of volumetric data requires both a reference space, and the spatial registration of the analyzed the datasets to the common reference. While the tools used in chapter II ANTs and Volgenmodel are the robust tools for spatial normalization and template generation, they are not devised to process teravoxel sized datasets. To overcome this problem I also used Fiji's BigWarp plugin (https://imagej.net/BigWarp), which allows landmark-based spatial registration of arbitrarily large datasets.

Mouse brain common coordinate framework

In order to instantiate our 3D generative model in a reference volume, I used the Allen Institute Common Coordinate Framework (CCF v3) of the adult (P56) mouse brain(M. Hawrylycz et al., 2011). The 10um precision volume with its segmentation labels was used. I generated binary hippocampal reference volumes by isolating single labeled regions for DG (Molecular, granule cell and polymorph layers), CA3 (Stratum oriens, pyramidale and

radiatum) and CA1 (Stratum oriens, pyramidale, radiatum and lacunosum) in Fiji. This was done by thresholding the original volume above and below the value of the label of interest. Multi-resolution copies of the obtained volumes were saved in the HDF5 format using Fiji (default parameters in the BigDataViewer plugin) as ready-to-use input files for the generative model.

Computational environment

A programming environment in a workstation running Ubuntu 16.04 was set in order to fulfill all necessary software and library dependencies, including: Python 2.7, Fiji(Schindelin et al., 2012), Vaa3D (Peng, Bria, Zhou, Iannello, & Long, 2014), Terastitcher (Bria & Iannello, 2012), MINC-TOOLS (Vincent et al., 2004), ANTS(Avants et al., 2009), nipype (Gorgolewski et al., 2011), Volgenmodel (Janke & Ullmann, 2015), R and RMINC. Additional Python wrappers and source-code can be found at (https://bitbucket.org/linusmg/nem4o-analysis). Big datasets were stored locally in a series of RAID system hard-drives (3x16GB WD MyBook Duo).

3.2.3. Statistical analysis

Data for transmittance, CNR and deformation were expressed as mean ± S.E.M. Two-way analysis of variance (ANOVA) were performed using R commander package for Windows, version 3.1.1. In the case of transmittance, one ANOVA for each filter was performed, considering the factors medium and time. For both fluorescence and deformation, one ANOVA was done, considering the medium and the time as the factors. Effects for each factor were considered statistically significant when $p<0.05$. Bonferroni was used for post-hoc analysis when a significant, or a trend to, medium x time interaction was found ($p<0.09$).

Voxel-based comparisons of neuromorphological metric 3D maps were performed implementing the mixed-effect linear model in RMINC (version 1.4.2.1). Significance for observed relationships were assessed with a False Discovery Rate (FDR) analysis.

3.3. Results and discussion

3.3.1. Cost-effective optimization of tissue clearing techniques

I have implemented cost-effective optimizations in the CLARITY protocol achieving in-depth imaging quality improvement. Clearing of ~2 cm^3 samples has been implemented in our lab on intact mouse brains achieving > 5 mm depth imaging with a custom-built Single Plane Illumination Microscope (SPIM).

Transparency

I tested brains cleared with the four candidate RIM media and compared their transparency as measured by light transmittance after two and four days of incubation, as compared to transmittance before incubation.

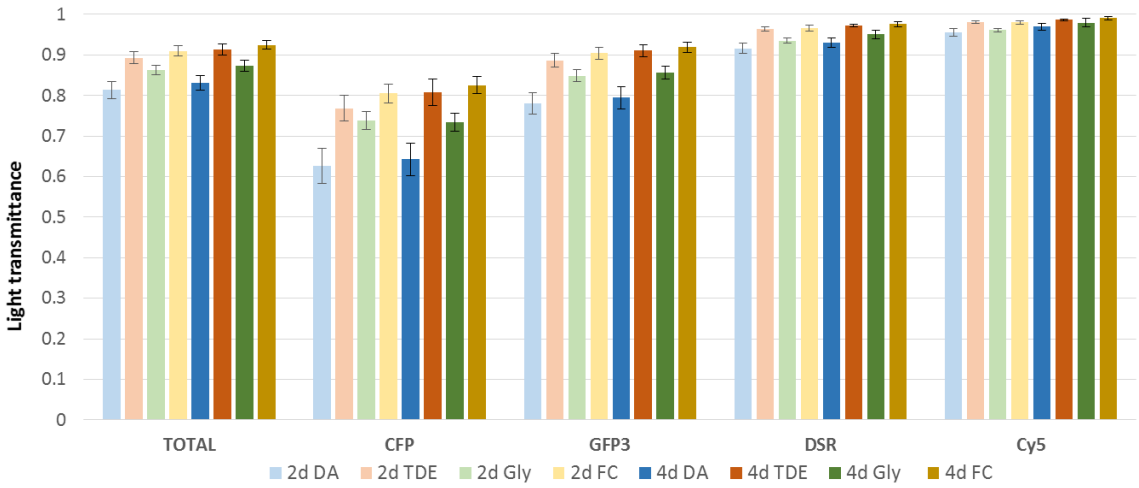

Figure 40: Comparison of transparency of RIM candidates. Light transmittance evaluated on different increasing wavelengths for the cleared samples under exposure to each of the four RIM media candidates (DA: diatrizoic acid based solution; FC: Focus Clear; Gly: glycerol-based solution; TDE: 2,2-thiodiethanol based solution). For each group the mean and the standard error are represented (n=4).

The results of the evaluation at different wavelengths reveals that samples exhibit better light transmittance at higher wavelengths and relative differences among media are maintained at different wavelengths. YFP has an excitation wavelength of 488-512 nm and an emission wavelength of 532-554 nm. In this way, when imaging the endogenous fluorescence of the sample, values of transmittance will be considerably close to 1. Overall, it can be seen that 2'-Thiodiethanol (TDE) transparency is comparable to that of the original proposed

FocusClear (FC), being one of the best RIM medium regarding transmittance. The diatrizoic acid-based (DA) solution presents the lowest values of transmittance, and glycerol shows intermediate values. **Figure 40** shows a representative sample for each group before exposure to the RIM medium candidate Quantitative measures are consistent with qualitative evaluation of the samples (**Figure 42**).

However, our observations when imaging whole brains in a SPIM setup were not consistent with these results, given that imaging in DA produced clear and sharp images through 6mm in depth in the samples (see **Figure 42** for a representative example). Thus, I revised the method for assessing transparency. Instead of using the transmittance, I measured the sharpness in the images. By normalizing this measure after RIM exposure to its value in PBS-T, I obtained a sharpness ratio with respect to the original conditions. The measurements obtained (**Figure 41**), shown that after 48hr incubations, 87%-Glycerol has the lowest sharpness ratio (1.09 ± 0.10), followed by DA (1.16 ± 0.03), while showing impressive results with 83%-TDE (1.41 ± 0.11). Unfortunately, due to its cost, I could not include FC in this experiment.

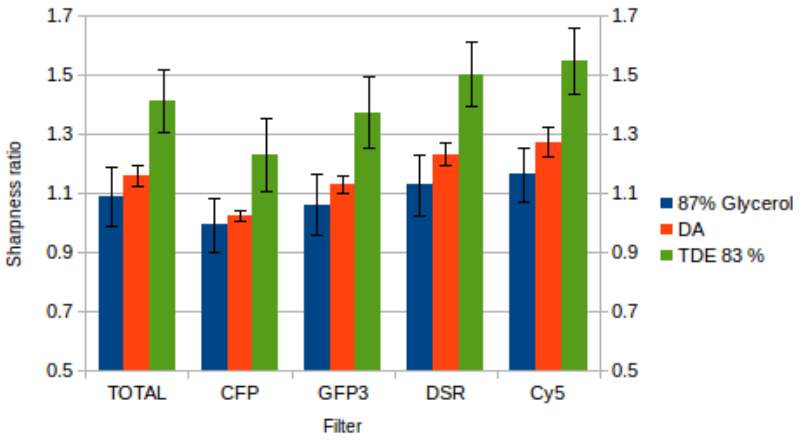

Figure 41: Comparison Sharpness ratio for RIM media candidates. Normalized sharpness evaluated on different increasing wavelengths for the cleared samples under exposure to three RIM media candidates (DA: diatrizoic acid based solution; Gly: glycerol-based solution; TDE: 2,2-thiodiethanol based solution). For each group the mean and the standard error are represented (n=4).

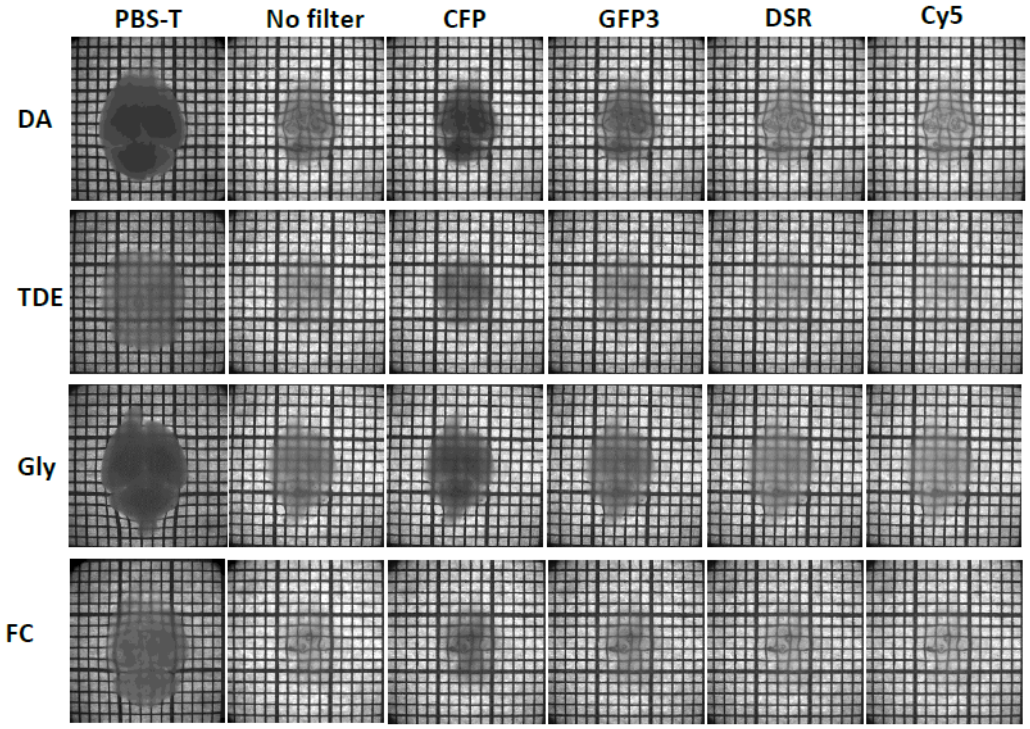

Figure 42: Stereomicroscope images for the assessment of sample transmittance under the different RIM media candidates. DA: diatrizoic acid based solution; FC: Focus Clear; Gly: glycerol-based solution; TDE: 2,2-thiodiethanol based solution. Samples are shown immersed in PBS-T at day 0 and after 2 days of incubation with the respective medium on day 2. Above the images the filters that were used to take the images on day 2 are indicated.

Fluorescence

Slices of the Thy-YFP mouse brain were used to measure the signal quality after 2 and 10 days of immersion to RIM media candidates. Confocal microscope imaging shows that TDE causes a significant decrease in YFP signal after 2 days, being more evident after 10 days. TDE slices conserve the labelling in some regions of the cortex, although the intensity of the signal is decreased with respect to other media (**Figure 43**). Quantification of the signal quality by Contrast to Noise Ratio (CNR) (**Figure 44**) demonstrate that TDE caused complete quenching of the signal compared to the other media. In the case of TDE slices, images were taken in specific regions were labelling was found, so the CNR characterization is not a reliable measure for the signal quality in the whole brain. Measures for TDE after 10 days cannot be done because of lack of signal.

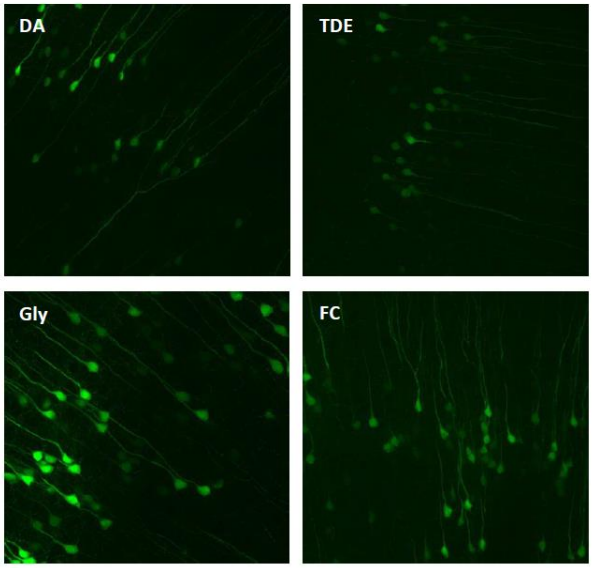

Figure 43: Comparison of fluorescence intensity in Thy1-YFP brain samples. Z-projection of the maximum intensity in a 100 um stack of cortical region in Thy-YFP brain slices, after incubation of 2 days in RIM media candidates (DA, TDE83%, Glycerol87% and FocusClear).

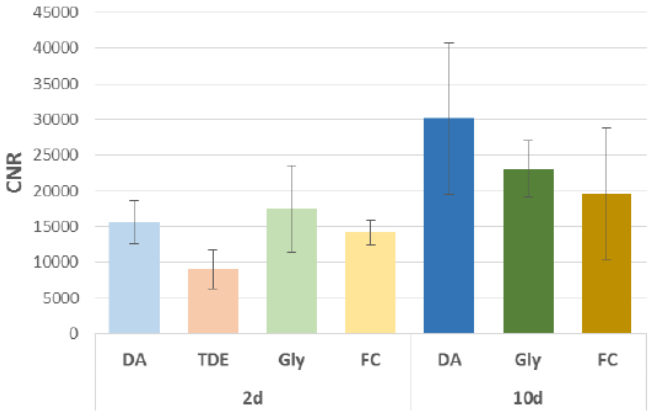

Figure 44: Contrast to Noise Ratio of the fluorescence microscope images obtained from slices under exposure to each of the four RIM media candidates. DA, TDE83%, Glycerol87% and FocusClear incubation during 2 days (2d) and 10 days (10d). Measure for 10 days for TDE is not available as no fluorescence was observed on the slices. For each group the mean and the standard error are represented (n=4).

Deformation

Deformation of the samples was assessed by measuring the variation of linear size of the brains immersed in the RIM candidate medium with respect to their initial expanded size in PBS-T. Taking into account that samples suffer an expansion when immersed in PBS-T, **Figure 45** represents the degree of recuperation of the original physiological size due to the incubation in RIM medium during 2 and 4 days. It can be seen that FocusClear is the best

one at reversing the expansion in a permanent way. Diatrizoic acid solution also presents a permanent effect, although it is no so hard. In any case, the qualitative evaluation of the samples evidence that no shrinkage with respect to the original size is caused. TDE 83% presents values similar to FocusClear, although the variability is higher and the effect not so durable, being at 4 days similar to diatrizoic acid solution values. Finally, glycerol presents a low recuperation of sample size, joined with high variability and low permanence of the results.

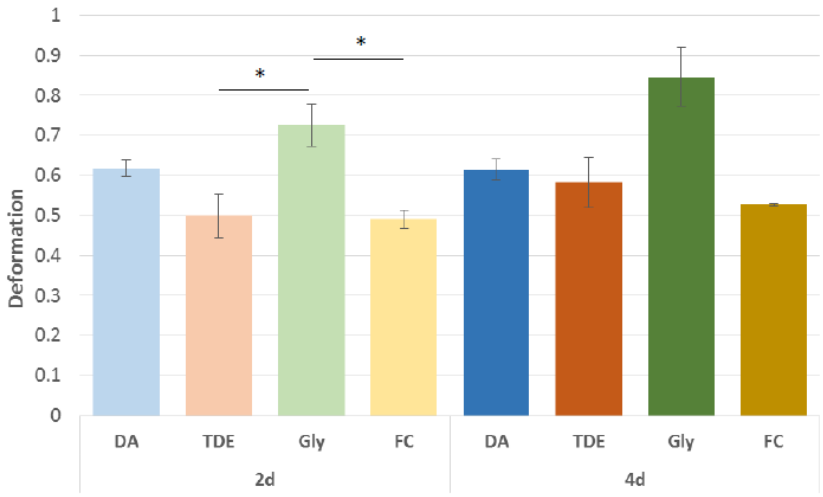

Figure 45: Deformation of the samples under 2 days (2d) and 4 days (4d) of incubation in RIM media candidates: Chung (diatrizoic acid solution), TDE83 (TDE 83% solution), Gly (glycerol 87% solution) and FC (FocusClear). The value is obtained by normalizing the area inside the brain contour in each medium by the same parameter of the brain immersed in PBS-T at day 0. For each group the mean and the standard error are represented (n=4).

3.3.2. Computational pipeline for CLARITY based whole-brain structural interrogation

To establish and prove that our pipeline is suitable for the data analysis I aim to do implied a significant amount of time. Despite the fact that I cannot show a quantitative analysis comparing TgDyrk1A and wild-type mice, I have done a proof of concept of all the necessary steps.

Six brains have already been scanned. Three have undergone stitching and both multi-resolution datasets and subsets of the imaged volumes have been used for the proof of concept.

The stitching has been done using Terastitcher (**Section 3.2.2**). While the processing time is slow (~2d per sample), the procedure is reliable and the latest updates of the software allow doing the processing in a computing cluster. **Figure 46** shows an overview of a high-resolution maximum projection of a representative stitched imaging volume of a whole mouse hemisphere.

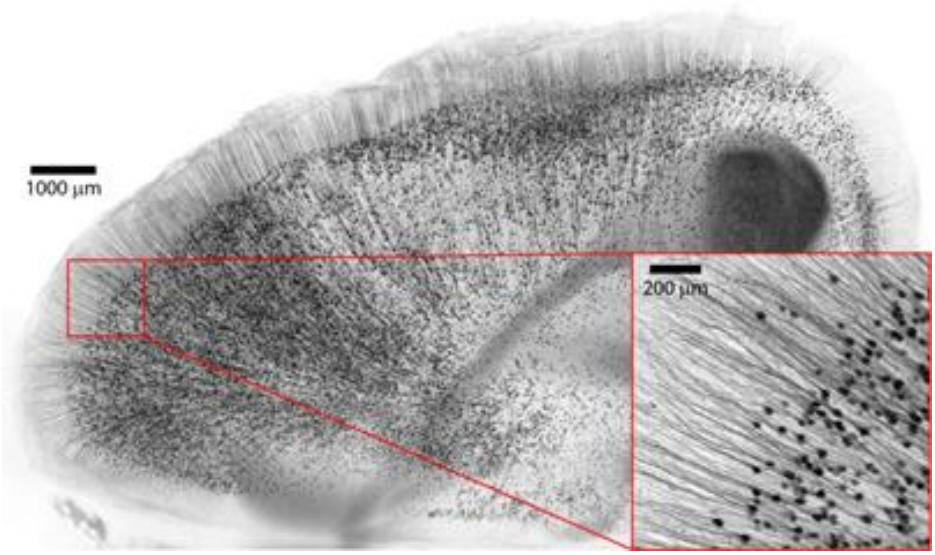

Figure 46: Maximum-value projections (inverted contrast) through one hemisphere of a B6.Cg-Tg(Thy1-YFP)HJrs/J mouse brain scanned at 5x magnification (scale bar = 1000µm). Close-up magnification of an unspecific region in the frontal cortex. Thy1-labeled cortical layer V nuclei and their apical dendrites can be appreciated (scalebar = 200µm).

Following our protocol optimizations, samples will undergo passive clearing for 45 days to obtain high transparency and imaging quality, with adequate refractive index matching.

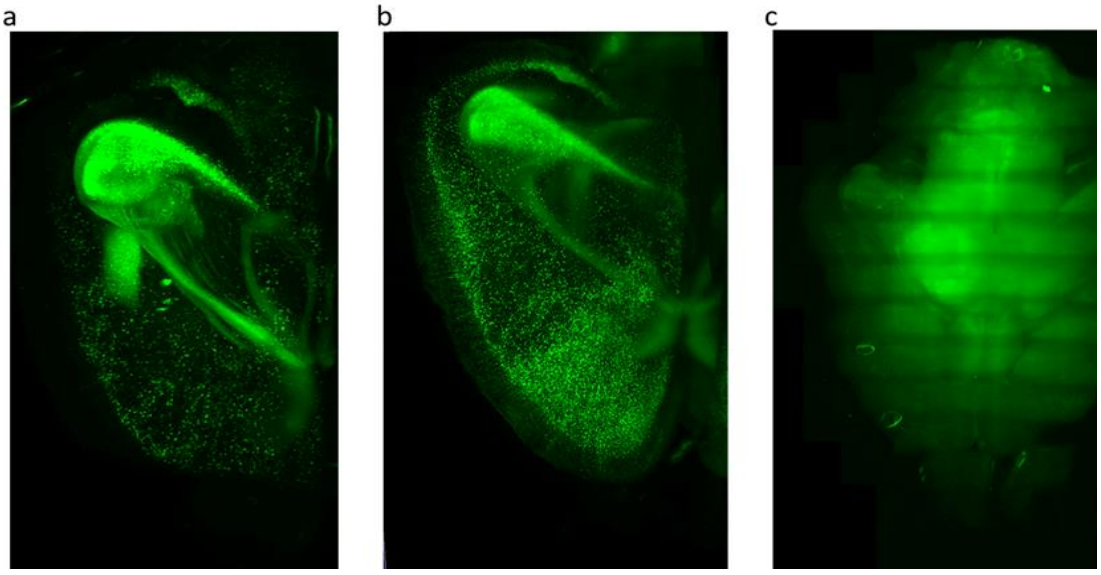

Figure 47 shows the qualitatively the improvement reached with the the information of the experiments shown in **Section 3.3.1**.

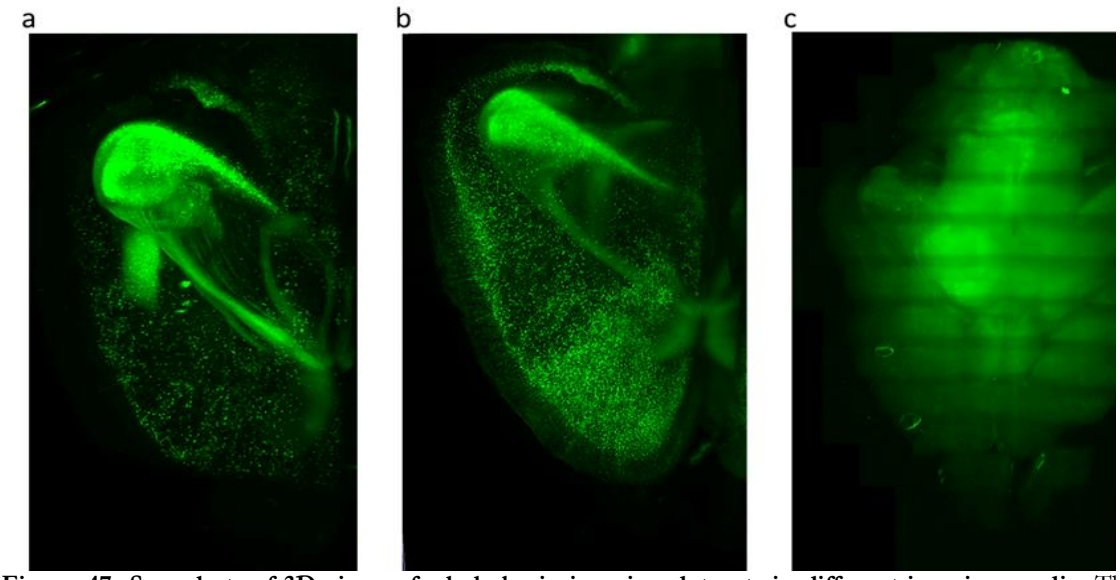

Figure 47: Snapshots of 3D views of whole brain imaging datasets in different imaging media. The three samples undergone 45 days-long passive clearing and were incubated in the imaging medium for 48hr previous to imaging. Note the difference in background fluorescence. The higher the signal to noise ratio, the less background can be appreciated in the 3D volume. Each sample was imaged in the following RIM: (a) diatrizoic acid solution, (b) 87% glycerol and (c) 87% TDE.

The stitched volumes were visualized in Vaa3D Terafly (see **Section 3.2.1**). The visualization was also tested in modest computers showing to be efficient and compatible across platforms. **Figure 48** (a,b,c) shows snapshots of the 3D visualization at different magnifications in the dataset. The improved imaging quality reached provides a high amount of detail, **Figure 48** (c) shows a high magnification maximum-value projection of the volume below cortical layer V. Axonal projections from layer V pyramidal neurons can be easily seen and tracked.

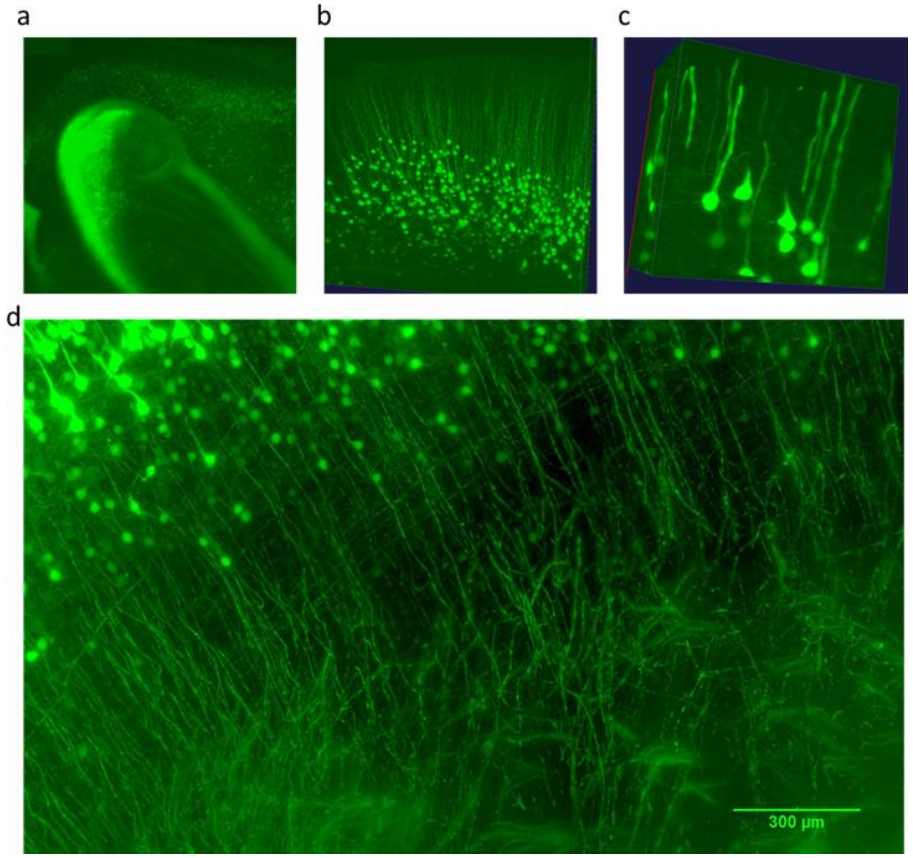

Figure 48: Multi-resolution imaging in a cleared whole mouse brain. (a,b,c) Snapshots of 3D views at different magnifications in a single dataset. (b) Maximum-value projection of an imaged volume showing partially layer V pyramidal neurons and their axonal projections.

Any quantitative analysis on volumetric data requires the previous step of the spatial registration to a common coordinate framework for all the analyzed samples. The basic step required for this procedure, is 3D spatial registration. I already developed a pipeline for mutual information-based spatial registration in **Section 2.2.3**. I here have adapted the procedure to teravoxel-sized datasets. To overcome the requirement of using the whole datasets, I have downsampled the whole brain volumes to an isotropic resolution of 10µm per voxel. The downscaled volumes can undergo all the procedures required for generating a common template and to spatially register each sample to this template. Once the transformations among the samples are known, it is applied to the coordinates of a set of markers (grid of points in the 3D space). The marker sets can then be scaled back to the original full resolution and can be used to warp the high resolution volume to a high resolution common coordinate space. **Figure 49** shows a sagittal view of an optical slice of

a whole hemisphere 3D dataset before (a) and after (b) mutual information-based registration to another sample.

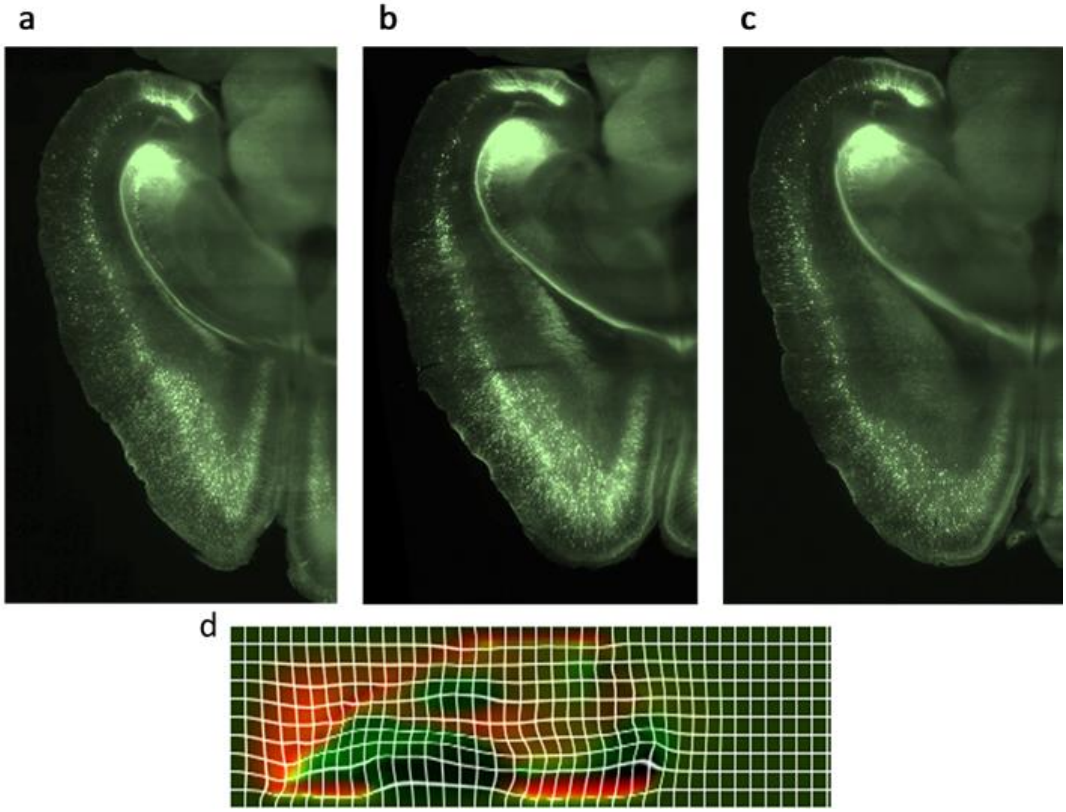

Figure 49: Deformation-based morphometry. (a,b,c) Sagittal view of a 2D slice of a whole hemisphere 3D dataset before (a) and after (b) mutual information-based registration to another sample. (d) 2D horizontal slice of deformation and compression maps obtained from a manually segmented CA1 volume nonlinear registration to a previously obtained MDA template of the region. In green, the Jacobian determinants of volumetric compression and in red displacements for each voxel in the image.

Proper definition and management of regions of interest (ROI) is needed at all levels of processing, visualization, and analysis. The 3D spatial registration is a basic step for further analysis because it allows automatic segmentation for posterior analysis. **Figure 50** shows a sagittal view of an optical slice of a whole hemisphere volume that has been manually registered (via landmark selection) to the segmentation of the Allen Institute Common Coordinate Framework (CCF v3) of the adult (P56) mouse brain. Thus, the high resolution annotated volume allows to choose ROI-specific processing. Manual segmentation is also possible the combination of our self-developed Fiji scripts, allowing high quality interpolation of thin structure segmentations.

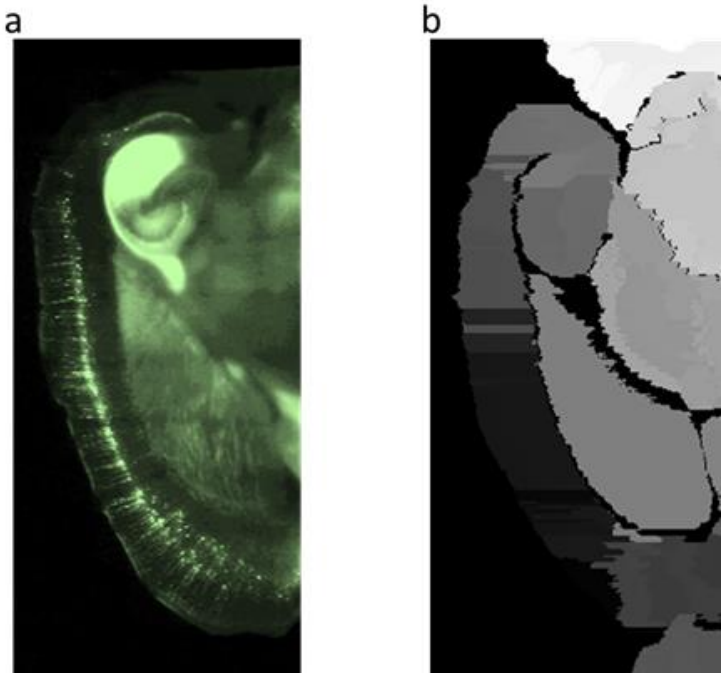

Figure 50: Registration to a common template for automatic segmentation. (a) Sagittal view of a 2D slice of a whole hemisphere 3D dataset after a landmark-based registration to the segmentation of the Allen Institute Common Coordinate Framework (CCF v3) of the adult (P56) mouse brain (b). Different shades of gray indicate standard delineated brain regions.

The steps until now, allow to obtain comparable whole brain volumes. To analyze them, I take advantage of the methods developed in Chapter II (**Section 2.2.2**). The multi-resolution structure of the data, allows to access small chunks and analyze them in parallel, generating small subvolumes containing cellular and dendritic density maps. I aim to generate python wrappers that will allow to apply any Fiji plugin throughout multi-resolution CLARITY datasets.

One of the great opportunities provided by whole brain imaging techniques, is the possibility of obtaining information about axonal projections with higher resolution than Diffusion Tensor Imaging (DTI). I propose to use the fluorescence structure tensor for large sample fluorescence microscopy datasets to study axonal pathways from densely labeled axonal projections of studied circuits (HC-mPFC in our case). I have developed Python code for obtaining and transforming multi-shell HARDI-like structure tensor datasets from CLARITY imaging datasets. This allows to generate Fibre Orientation Distribution (FOD) maps, robust FOD-based tractography and perform the structural connectomics and fixel-based analysis that MRtrix3 offers (**Figure 51**).

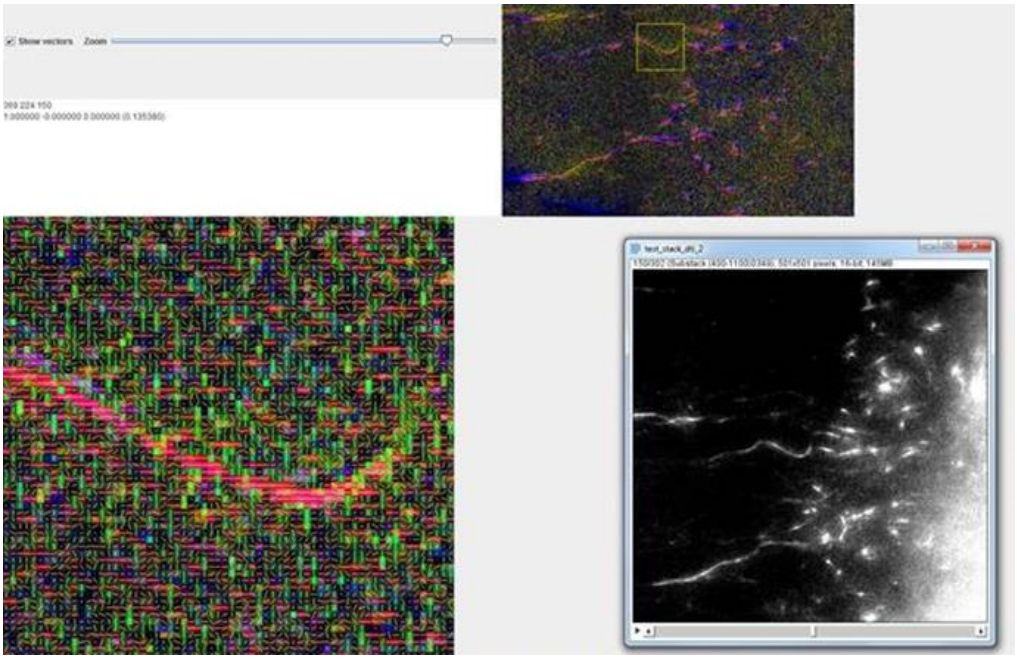

Figure 51: Structural tensor for axonal tracking. Snapshot showing an optical slice with representations of structural tensors in every voxel of the image (magnified in the lower left panel). The color indicates the orientation and white lines in each voxel represent the direction of maximum anisotropy of each tensor. The same optical slice in the original whole brain imaging dataset (lower right).

Altogether those tools allow the structural interrogation of whole brain datasets with a focus on a holistic perspective for the analysis of cellular, dendritic and axonal densities. But also provide a robust framework to elaborate on quantitative mapping that could be of interest for any particular application (e.g. analyzing patterns of genetic expression, or presence of specific proteins). Also, the direct link with the in-silico parametrization of neuronal networks in the generative model presented in Chapter II opens many possibilities for the interaction between experimental interrogation of whole brains and the simulation of neuronal circuits.

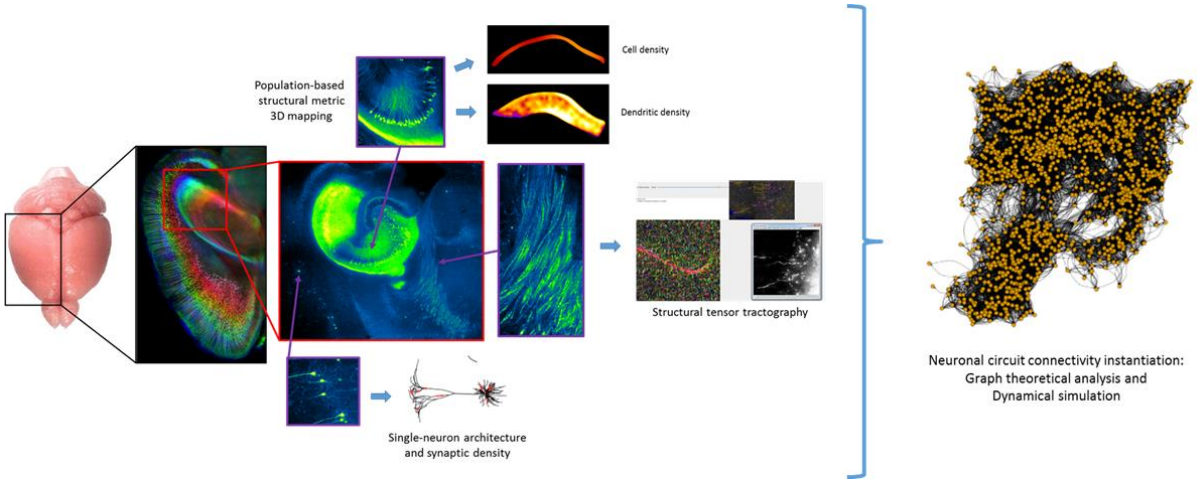

Figure 52: **Overview of the whole-brain analysis and modelling workflow.** I obtain structural experimental data from cleared brains which constrain computational modelling and analysis tools to explore neuronal circuit topology. Thus, providing a tool to investigate the organizational principles of mammalian neuronal networks.

3.4. Discussion and conclusions

The development, refinement, and use of techniques that allow high-throughput imaging of whole brains with cellular resolution will help us understand the complex functions of the brain. Such techniques are crucial for the analysis of complete neuronal morphology—anatomical and functional—connectivity, and repeated molecular phenotyping. Recently developed tissue clearing protocols like Scale(Hama et al., 2011), CLARITY(Chung et al., 2013) or iDisco (Renier et al., 2014), together with the possibility of imaging whole brains at microscopic resolution in confocal or light-sheet fluorescence microscopes, allow virtually any neurobiology lab to obtain datasets that until now were only considered in the framework of big collaborative projects. However, many laboratories that try to use the techniques realize that the implementation of the clearing and labeling protocols is not straightforward and that many times the resulting imaging quality is not sufficient for the detailed microscopic analysis pursued. Thus, in the field of whole brain imaging, optimization of the protocols is a recurrent topic (Epp et al., 2015; H. Lee, Park, Seo, Park, & Kim, 2014). Our experiments modifying specific steps of the CLARITY technique have shown that the refractive index matching medium is crucial for imaging quality.

I have corroborated that FC is an optimal imaging medium regarding transparency, native fluorescence conservation, and deformation of the samples. Our results also point at DA as a good candidate, showing relatively high sharpness ratio and very stable fluorescence conservation (higher than in FC) while preserving sample size. This has been corroborated by our experience when imaging whole brains in SPIM. Nevertheless, the striking capacity of TDE to render cleared samples highly transparent, highlights its potentiality for whole brain imaging. The quenching effect I have observed, has also been observed in previous studies (Aoyagi, Kawakami, Osanai, Hibi, & Nemoto, 2015; Staudt, Lang, Medda, Engelhardt, & Hell, 2007), and it seems to be highly dependent on TDE concentration (Hasegawa et al., 2016). Our trials shown that adjusting to basic pH does not avoid quenching, and that in some cases, even at 83% concentration quenching does not occur (data not shown). This, together with the fact that the red fluorescent protein mutant (RFP) is not quenched by TDE(Staudt et al., 2007) suggests that the observed quenching must depend on very specific properties of GFP-like mutants (GFP, eGFP and eYFP). To investigate this I have explored molecular dynamics simulations of the protein at different solvation concentrations of TDE (see ANNEX II).

It is worth mentioning, that our quantifications also highlighted the importance of a robust methodological framework and standardized measurements to compare the effectiveness of clearing protocols. I highlight the importance of normalization among measurements done in different samples and propose the sharpness ratio and CNR as consistent measures for transparency and fluorescence signal level.

Computational pipeline for whole-brain structural interrogation

The characterization done, allowed us to obtain high quality imaging datasets, that contain big amounts of structural information that characterizing neuronal circuitry in our mice. Whole rodent brain light-sheet imaging not only allow the generation of brain structural maps with unprecedented resolution, but also offer multiplexed molecular interrogation of the studied samples. Some efforts following the appearance of the first whole-brain microscopy imaging studies have generated basic tools needed to take advantage of the wealth of information they contain (atlas registration, fluorescence signal raw statistics (Renier et al., 2014), cell counting (Frasconi et al., 2014) and axonal projection density (Ye et al., 2016)). However, except for axonal projection densities, those analyses still miss a link between the information at the microscopic level and a meaningful analysis for its implications on brain function. Specifically, in the samples I image, I choose the study of transgenically labelled neuronal subpopulations as sufficient to show how detailed microscopic properties and a whole-brain perspective can be linked.

The challenges that remain to be solved for any possible quantification in those datasets are two: (1) to determine which measures can be informative of populations of labeled cells or molecules and (2) to analyze those data taking into account the topographical information throughout the whole sample. The solution to those challenges has already been thoroughly explored in the neuroimaging field and has already been discussed in Chapter II. I have proposed novel methods for analyzing volumetric datasets and obtaining population-based cellular and dendritic density maps, and developed a computational generative model that will allow to assess the implications of multi-scale morphological properties on network topology.

Our proof of concept in this part of the Thesis, takes advantage of the framework developed for population-based analysis and modelling, and puts it in the context of whole brain imaging. By solving the spatial registration and generating wrappers that allow to perform common image analyses in whole brains by chunks, I open many possibilities for the analysis and development of neuromorphological metric mapping. Thus, in the framework presented here, I gathered together many existing tools that by being combined provide a powerful and extensible platform to study neuronal circuits from a systems perspective.

GENERAL DISCUSSION

GENERAL DISCUSSION

More than 100 years ago, Santiago Ramón y Cajal found that neurons are polarized cells with dendrites and axons, the input and output ends of neurons respectively. His discoveries were based on optical microscopy of histological preparations and single neuron reconstructions. I now know that a neuron's structure is intimately related to its function. Neuronal geometry shapes how synaptic inputs are integrated and predicts a neuron's position within a circuit. The arborization zones of neuronal axons determine which downstream neurons and brain areas receive information from the neuron, thus forming the basis of circuit organization.

Recent anatomical tracing studies have yielded substantial amounts of data on the areal connectivity underlying distributed processing in cortex, yet the fundamental principles that govern the large-scale organization of cortex remain unknown. I here took a different approach: a mixed experimental and computational modeling approach for analyzing the repercussion of single-cell neuromorphological properties on the neuronal network. Computational models allow the exploration of theoretical relationships between morphology and connectivity, however, the physiological relevance of the findings is not always clear. In this regard, mouse models showing different alterations of the dendritic morphospace along with cognitive impairment provide a convenient scenario for testing those findings.

First I extracted functional properties (dendritic wiring optimality) from specific neuromorphological metrics that I obtained from neuronal reconstructions of two mouse models (Ts65Dn and a Dyrk1A heterozygous) showing Down syndrome-like neuronal structure abnormalities and cognitive deficits. In order to explore the impact of dendritic architectural properties on the horizontal connectivity of cortical layer II/III, I implemented a computational model to explore and instantiate 2D homogeneous neuronal networks based on an existing model (Orlandi et al., 2013). I used this model to explore how the modification of dendritic tree size, its complexity and the density of synaptic contacts modulates the network topology and computational capacities.

The *in-silico* exploration done in healthy neurons, was performed in a highly simplified scenario (2D homogeneous population of simplified neurons), in the supplementary motor

cortices layer II/III pyramidal neurons. This could be viewed as a disadvantage, but, in contrast to the large and sparsely connected architecture of many networks of the brain, cortical areal networks are relatively small and densely connected: the mouse neocortex consists of roughly 40 areas per hemisphere with ~50% of the possible connections present (Oh et al., 2014; Zingg et al., 2014). In such networks, the properties that define conventional complex networks, such as the degree distribution (number of areas connected to an area), average path length (smallest number of connected steps between a pair of areas), and clustering (density of connections among areas connected to the same area), are by themselves informative, thus providing a fruitful scenario for exploring the morphospace-network topology/computational capacities relationship.

Existing complex network models provide an incomplete description of the cortical areal network because they neglect the underlying spatial structure that shapes connectional topology (Chklovskii et al., 2002; Ercsey-Ravasz et al., 2013; Klimm, Bassett, Carlson, & Mucha, 2014; Raj & Chen, 2011). In this Thesis, the theoretical exploration of the morphospace has shown that dendritic architectural features have differential effects on the network connectivity and dendritic tree size is especially relevant both for its routing efficiency and its storage capacity. The introduction of a synaptic contact probability dependent on the position in the radius of the dendritic tree has shown to imply a series of interesting effects on the network topology. Being the most important one, the increase in the quantity of synaptic contacts made while conserving the mean synaptic contact probability along the tree radius. The fact that both storage capacity and routing efficiency saturate for increased values of dendritic tree size or synaptic contact probability indicates that the wild-type parameterization is optimal for reaching computational capacity with minimal cost.

Moreover, our analysis highlighted genetic background differences between the B6EiC3Sn and C57BL/6J-129Ola, underlining increased tortuosity in C57BL/6J-129Ola wild-type mice as the responsible for a slight deviation from optimal wiring. This also could imply that the wiring optimality concept related to optimal space filling by number of branches per dendritic length is more sensitive than previous approximations using proportion of occupied volume/area as a proxy. While the conclusions of this part of the work should not be

generalized to the whole population of M2 layer II/III basal trees due to the small numbers of neurons used, they provide an interesting starting point for addressing the fundamental aim of this Thesis: linking single neuron architecture with neuronal network wiring.

Intellectual disability optimality and its impact on network topology

Abnormalities in dendritic structure are a characteristic feature of many brain disorders. One clear example are individuals with intellectual disability that presents reduced dendritic branching patterns, shortened dendritic lengths, loss of spines and changes in spine shape and size (Kulkarni & Firestein, 2012). These alterations may most probably have strong implications on single-neuron wiring and its optimality. However, while in healthy phenotypes the studies assessing optimality questions are still limited (Schröter et al., 2017), the analysis of intellectual disability models has not even been used. Thus, our study constitutes a first step towards the identification of fundamental properties for optimal wiring through the comparative analysis of intellectual disability.

I found in fact that basal tree architecture in M2 cortical layer II/III has shown that the Ts65Dn and Dyrk1A+/- DS mouse models have suboptimal dendritic wiring. This indicates dendritic integration disturbances that could alter the dynamics of cortical networks and lead to imbalanced patterns of activity and, ultimately, to the motor activity abnormal behavior observed in the mouse models. In fact, combining functional, anatomical, and computational approaches, previous work in our lab identified decreased neuronal firing rate and deficits in gamma frequency in the prefrontal cortices of transgenic mice overexpressing Dyrk1A (Ruiz-Mejias et al., 2016). In that work, I also identified a reduction of vesicular GABA transporter punctae specifically on parvalbumin positive interneurons, that was assumed to be causal in the alterations of oscillatory activity. Our present data suggest that dendritic tree dismorphology should be accounted for in these assumptions. The instantiation of different DS mouse models in our computational model, led to differential affectations regarding computational capacities, which were severely reduced in all the cases, thus reinforcing this argument. This provides an interesting line of investigation, where comparative studies between the different mouse models could corroborate or discard the hypotheses drawn from our computational exploration. In the model, the relationship between the network cost and the routing efficiency seems to be related to the single neuron optimal wiring, and this is differentially disrupted in the different mouse models used.

Impact of single-neuron structural diversity in hippocampal CA1 populations

Altogether, this statistical and computational exploration of the cortical morphospace served as a founding stone for building a conceptual framework that can now be extended and used to develop a computational hypothesis generation - experimental testing feedback loop. However, it was important to proof its validity in other complex neuronal circuits such as the hippocampus. To do so, in Chapters II and III I tackled the analysis and simulation of neuromorphological properties in a neuronal circuit fundamental for learning and memory, the hippocampal trisynaptic circuit.

The hippocampal formation has long been recognized as necessary for the integrity of memory in mammals and other vertebrates, and relatively limited disturbances of the hippocampal circuitry, such as those found in Down syndrome, have been reported to produce serious memory impairment. The anatomical basis of this system is the so called trisynaptic circuit formed by the perforant path arising in the entorhinal cortex, which terminates onto the dendrites of the granule cells of the dentate gyrus. The axons of the dentate gyrus granule cells form the mossy fibers that make synaptic contact with the pyramidal cells of the CA3. The axons of CA3 pyramidal cells form the Schaffer's collaterals that make synaptic contact with the pyramids of CA1.

The CA1 pyramidal neurons have been assumed to retain constant properties, and thus they have been used in computational models as "clonal" stereotypic elements, regardless of the variability in the details of individual neuronal morphology. Although the functional implications of the peculiar morphology of pyramidal neurons are not known, it is likely that apical and basal dendrites correspond to different circuit inputs producing specific contributions to pyramidal cell excitability and long term synaptic plasticity (Cauller et al., 1998; Dudman et al., 2007).

I here explored the degree of similarity in the dendritic arborization pattern, along different areas of the hippocampus. I have shown that the neuronal class defined by Thy1+ cells presents spatial inhomogeneities in cellularity. This supports several lines of anatomical and physiological evidence have identified differences in CA1 in each of the dorsal-ventral (Amaral & Witter, 1989), proximal-distal (Graves et al., 2012; Igarashi et al., 2014; Jarsky et

al., 2008), and superficial-deep (H. Lee et al., 2014; Mizuseki et al., 2011; Slomianka et al., 2011) axes of the hippocampus.

I also showed that neuromorphological properties at a local scale of pathological neurons of TgDyrk1A, present neuromorphological inhomogeneities that tend to correlate with the positioning in CA1. Interestingly, TgDyrk1A inhomogeneities are different to those shown in a healthy hippocampus, and are concomitant with behavioral alterations in the Tg Dyrk1A mouse model.

For this work I used mice expressing *Thy1-Yellow Fluorescent Protein (YFP)* (strain B6.Cg-Tg(Thy1-YFPH)2Jrs/J nº003782; The Jackson Laboratories), that expresses yellow fluorescent protein in a proportion of pyramidal cells driven by the Thy1 promoter. Specifically, the Thy1-YFP line H has been reported to express the fluorescent protein in a large number of pyramidal neurons in several fields of the hippocampal formation (Porrero, Rubio-Garrido, Avendaño, & Clascá, 2010).

Of course this offers the advantage of having sparse YFP-stained pyramidal neurons that allows to perform population-based analysis, and estimate the spatial embedding by determining the volume of the specific hippocampal subregion (CA1) However, there are no published data on the proportion of Thy1 labeled cells with respect to the total number of neurons (Neu-N staining). This is important in the context of the present work, since it would constrain how representative are our findings of the total pyramidal cell population. In fact, I found that the Thy1-YFP population only represents 2-3% of the total NeuN population. Even taking into account that inhibitory cells are 20% of the neuronal population, the numbers are still very low. This is obviously a limitation in our analysis.

Moreover, it should be noted that the spatial changes in the density of Thy-labeled cells do not coincide with the NeuN general neuronal marker, suggesting that the expression of Thy may not follow the same spatial-dependent changes than neuronal dendritic architecture.

Also, the proportion of YFP positive cells along the hippocampal anterio-posterior axes, are different in wild type and transgenic mice, thus suggesting that Thy1 expression may be

affected by Dyrk1A overexpression. Overall, thus conclusions drawn from the analysis of Thy1-dependent labelings have to be interpreted with caution.

Thus, the question that still arises is: do the intrinsic properties of a specific brain structure vary across its extension, along with the within-class neuronal structure variability, or is the neuronal circuitry structure fixed and performing a conserved computation along a structurally non-homogeneous structure?

Reconstructing the whole brain with cellular resolution

Although single-neuron reconstructions have revealed much about neural computation, mapping and analysing larger neuronal populations and topologies can lead to fundamentally different insights. To promote a holistic perspective on neuromorphological characterization of neuronal networks I have developed and validated population-based computational analysis methods for cellular and dendritic density. The classical techniques only allow to structurally map a fraction of the number of neurons in the brain, typically tiny. This is limitation arises from constraints on the number of neurons that can be imaged at the same time and the total brain size of the animal under study. Thus, interactions between neurons in different brain areas are easily missed, and functionally related ensembles of neurons are undetectable. Not only would the ability to simultaneously map all neurons in a brain make it possible to address questions that cannot be answered with conventional techniques, it also would vastly speed up the throughput of experiments that can be performed with existing approaches.

CLARITY (Chung et al., 2013) overcomes these limitations to produce transparent tissue without quenching endogenous fluorescence, and this tissue can also be labeled via immunohistochemistry. This provides a unique opportunity to bridge anatomical scales from subcellular to whole brain.

In the last years, a number of research groups have implemented new tissue clearing techniques (CLARITY, CUBIC, Lumos, STP, 3DISCO, Scale, or SeeDB) allowing comprehensive microscopic imaging of rodent whole brains (Hama et al., 2011). The power of these techniques relies on bridging *de facto* the macroscopic and microscopic scale

descriptions of the system, allowing high-throughput imaging of whole brains with cellular resolution.

However, previous results in the lab show that the resolution decreases when trying to track axons on more than 3 mm in depth in the sample. Different media have been reported in order to improve the transparency and, so, the resolution in depth, such as a solution based on diatrizoic acid (Kim et al., 2015). Thus, I implemented and optimized the CLARITY technique, and generated and proof of concept of an analysis pipeline, allowing now to generate high quality whole mouse brain datasets that are providing a wealth of data to investigate morphological differences between wild-type and DS mouse models.

Another limitation is that, up to date a relatively low effort has focused on developing standardized, extensible, and scalable analysis tools. Thus, I also aimed at implementing a new suite of unified softwares to construct multiscale structure-function maps from brain-clearing experiments, with specific subworkflows for understanding topological dependencies on a brain-wide scale. Moreover, I developed computational generative model for instantiating biologically realistic neuronal circuits with a focus on the integration of information at multiple scales, from single neuron wiring architecture, to macroscopic morphology.

While the mean weakness throughout the work is the small numbers of samples and relatively low statistical power, its strength is the focus on the development of a conceptual and methodological framework that I think will be useful to investigate fundamental properties of neuronal wiring by means of the comparative analysis of cognitive impairment.

CONCLUSIONS

CONCLUSIONS

The work of this Thesis has revealed that the size and shape of dendritic trees are strong determinants of neuronal information processing because of their influence on network topology, and that pathological perturbations of dendritic trees impair this topological properties. I have also provide new computational tools to interrogate biological networks about the best strategy to rewire neuronal connectivity.

1. Within the neuromorphological parameters analyzed, dendritic tree size and synaptic contact probability of single pyramidal neurons are those that exert an influence the topology of modeled cortical layer II/III local networks. Network routing efficiency is mainly given by synaptic contact probability, while storage capacity, clustering and small-worldness ratio is mostly determined by dendritic tree size.
2. The dendritic architecture abnormalities in cortical layer II/III basal trees of intellectual disability models (Ts65Dn, Dyrk1A+/- and C57BL/6J-129Ola) determines suboptimal target space filling. This possibly contributes to an impaired integration of afferent synapses at the single-neuron level.
3. Introducing a distribution of synaptic contacts along dendritic trees extracted from experimental data modifies the topology of modeled networks, increasing the amount of contacts made by the neurons, the routing efficiency of the network and, to a lower extent, its storage capacity and small-worldness ratio.
4. Ts65Dn and Dyrk1A+/- Down syndrome mouse models mouse show a 40-50% reduction in storage capacity and routing efficiency with respect to the wild type.
5. Environmental enrichment increase in 7% routing efficiency and storage capacity in Ts65Dn mice, suggesting that therapeutical approaches modifying dendritic tree size rather than synaptic contact probability could have stronger impact on the functionality of Down syndrome neuronal networks.
6. Mice overexpressing DYRK1A show dendritic abnormalities in dorsal CA1 *stratum radiatum* with reduced storage capacity (18%). However, differential architectural phenotypes are detected along the proximal-distal axis, being aberrations more marked in distal CA1.
7. The population-based neuromorphological analysis methods developed in this work presented a strategy towards the assessment of neuronal circuitry composition and

architecture, providing a first step towards a holistic perspective in the study of neuronal networks at the cellular scale.

8. The multi-scale generative model for the instantiation of biologically realistic neuronal circuits allows the exploration of the morphospace impact on neuronal network topology based on multi-scale experimental data.
9. The analysis pipeline for population-based structural interrogation of whole brains allows population-based structural interrogation methods from a systems perspective.
10. Altogether, the analyses and tools developed in this Thesis constitute a methodological and conceptual framework that can now be used to explore a computational hypothesis generation - experimental testing feedback loop in the scope of comparative microconnectomics.

BIBLIOGRAPHY

BIBLIOGRAPHY

Ahmad, K., & Henikoff, S. (2002). Epigenetic consequences of nucleosome dynamics. *Cell*, *111*(3), 281–284.

Ahuja, R. K., Mehlhorn, K., Orlin, J., & Tarjan, R. E. (1990). Faster algorithms for the shortest path problem. *Journal of the ACM (JACM)*, *37*(2), 213–223.

Altafaj, X., Dierssen, M., Baamonde, C., Martí, E., Visa, J., Guimerà, J., … Others. (2001). Neurodevelopmental delay, motor abnormalities and cognitive deficits in transgenic mice overexpressing Dyrk1A (minibrain), a murine model of Down's syndrome. *Human Molecular Genetics*, *10*(18), 1915–1923.

Altman, D. G., & Bland, J. M. (1983). Measurement in medicine: the analysis of method comparison studies. *The Statistician*, 307–317.

Amaral, D. G., & Witter, M. P. (1989). The three-dimensional organization of the hippocampal formation: a review of anatomical data. *Neuroscience*, *31*(3), 571–591.

Aoyagi, Y., Kawakami, R., Osanai, H., Hibi, T., & Nemoto, T. (2015). A rapid optical clearing protocol using 2, 2'-thiodiethanol for microscopic observation of fixed mouse brain. *Plos One*, *10*(1), e0116280.

Artola, A., Von Frijtag, J. C., Fermont, P. C. J., Gispen, W. H., Schrama, L. H., Kamal, A., & Spruijt, B. M. (2006). Long-lasting modulation of the induction of LTD and LTP in rat hippocampal CA1 by behavioural stress and environmental enrichment. *European Journal of Neuroscience*, *23*(1), 261–272.

Artzy-Randrup, Y., Fleishman, S. J., Ben-Tal, N., & Stone, L. (2004). Comment on" Network motifs: simple building blocks of complex networks" and" Superfamilies of evolved and designed networks." *Science*, *305*(5687), 1107.

Ascoli, G. A., Donohue, D. E., & Halavi, M. (2007). NeuroMorpho.Org: A Central Resource for Neuronal Morphologies. *Journal of Neuroscience*, *27*(35), 9247–9251. https://doi.org/10.1523/JNEUROSCI.2055-07.2007

Avants, B. B., Tustison, N., & Song, G. (2009). Advanced normalization tools (ANTS). *Insight J*, *2*, 1–35.

Ballesteros-Yáñez, I., Benavides-Piccione, R., Elston, G. N., Yuste, R., & DeFelipe, J. (2006). Density and morphology of dendritic spines in mouse neocortex. *Neuroscience*, *138*(2), 403–409.

Barrett, K. E., & Others. (2010). Ganong's review of medical physiology. McGraw-Hill

Medical New York, NY.

Barthas, F., & Kwan, A. C. (2017). Secondary motor cortex: where sensory meets motorin the rodent frontal cortex. *Trends in Neurosciences*, *40*(3), 181–193.

Bartoletti, A., Medini, P., Berardi, N., & Maffei, L. (2004). Environmental enrichment prevents effects of dark-rearing in the rat visual cortex. *Nature Neuroscience*, *7*(3), 215–216.

Bassett, D. S., & Bullmore, E. D. (2006). Small-world brain networks. *The Neuroscientist*, *12*(6), 512–523.

Beacher, F., Daly, E., Simmons, A., Prasher, V., Morris, R., Robinson, C., … Murphy, D. G. M. (2010). Brain anatomy and ageing in non-demented adults with Down's syndrome: an in vivo MRI study. *Psychological Medicine*, *40*(4), 611–619.

Beauquis, J., Roig, P., De Nicola, A. F., & Saravia, F. (2010). Short-term environmental enrichment enhances adult neurogenesis, vascular network and dendritic complexity in the hippocampus of type 1 diabetic mice. *PloS One*, *5*(11), e13993.

Belichenko, P. V, Kleschevnikov, A. M., Masliah, E., Wu, C., Takimoto-Kimura, R., Salehi, A., & Mobley, W. C. (2009). Excitatory-inhibitory relationship in the fascia dentata in the Ts65Dn mouse model of Down syndrome. *Journal of Comparative Neurology*, *512*(4), 453–466.

Benavides-Piccione, R., Dierssen, M., Ballesteros-Yanez, I., de Lagrán, M. M., Arbones, M. L., Fotaki, V., … Elston, G. N. (2005). Alterations in the phenotype of neocortical pyramidal cells in the Dyrk1A+/- mouse. *Neurobiology of Disease*, *20*(1), 115–122.

Bernard, A., Lubbers, L. S., Tanis, K. Q., Luo, R., Podtelezhnikov, A. A., Finney, E. M., … Others. (2012). Transcriptional architecture of the primate neocortex. *Neuron*, *73*(6), 1083–1099.

Bria, A., & Iannello, G. (2012). TeraStitcher-a tool for fast automatic 3D-stitching of teravoxel-sized microscopy images. *BMC Bioinformatics*, *13*(1), 316.

Bria, A., Iannello, G., Onofri, L., & Peng, H. (2016). TeraFly: real-time three-dimensional visualization and annotation of terabytes of multidimensional volumetric images. *Nature Methods*, *13*(3), 192–194.

Bullmore, E., & Sporns, O. (2009). Complex brain networks: graph theoretical analysis of structural and functional systems. *Nature Reviews Neuroscience*, *10*(3), 186–198.

Bullock, T., & Horridge, G. A. (1965). Structure and function in the nervous systems of invertebrates.

Cairns, N. J. (2001). Molecular neuropathology of transgenic mouse models of Down syndrome. In *Protein Expression in Down Syndrome Brain* (pp. 289–301). Springer.

Carandini, M. (2004). Amplification of trial-to-trial response variability by neurons in visual cortex. *PLoS Biology*, *2*(9), e264.

Cauller, L. J., Clancy, B., & Connors, B. W. (1998). Backward cortical projections to primary somatosensory cortex in rats extend long horizontal axons in layer I. *Journal of Comparative Neurology*, *390*(2), 297–310.

Cembrowski, M. S., Bachman, J. L., Wang, L., Sugino, K., Shields, B. C., & Spruston, N. (2016). Spatial gene-expression gradients underlie prominent heterogeneity of CA1 pyramidal neurons. *Neuron*, *89*(2), 351–368.

Chen, B. L., Hall, D. H., & Chklovskii, D. B. (2006). Wiring optimization can relate neuronal structure and function. *Proceedings of the National Academy of Sciences of the United States of America*, *103*(12), 4723–4728.

Chklovskii, D. B. (2004). Exact solution for the optimal neuronal layout problem. *Neural Computation*, *16*(10), 2067–2078.

Chklovskii, D. B., Schikorski, T., & Stevens, C. F. (2002). Wiring optimization in cortical circuits. *Neuron*, *34*(3), 341–347.

Chung, K., Wallace, J., Kim, S.-Y., Kalyanasundaram, S., Andalman, A. S., Davidson, T. J., … Others. (2013). Structural and molecular interrogation of intact biological systems. *Nature*, *497*(7449), 332–337.

Colom, R., Karama, S., Jung, R. E., & Haier, R. J. (2010). Human intelligence and brain networks. *Dialogues in Clinical Neuroscience*, *12*(4), 489.

Conel, J. L. (1941). *The postnatal development of the human cerebral cortex: The cortex of the one-month infant*.

Conel, J. L. (1947). *The postnatal development of the human cerebral cortex: the cortex of the three-month infant*.

Conel, J. L. (1955). *The Postnatal Development of the Human Cerebral Cortex: The Cortex of the Fifteen-month Infant*.

Conel, J. L. (1959). *The Postnatal Development of the Human Cerebral Cortex: The Cortex of the Twenty-four-month Infant*.

Conel, J. L. (1963). *The Postnatal Development of the Human Cerebral Cortex, V. 7: The Cortex of the Four-year Child*. Harvard University Press.

Conel, J. L. (1967). The Postnatal Development of the Human Cerebral Cortex: Vol. VIII.

The cortex of six-year child. *Harvard Univeristy Press*.

Cossette, M., Lecomte, F., & Parent, A. (2005). Morphology and distribution of dopaminergic neurons intrinsic to the human striatum. *Journal of Chemical Neuroanatomy*, *29*(1), 1–11.

Coussons-Read, M. E., & Crnic, L. S. (1996). Behavioral assessment of the Ts65Dn mouse, a model for Down syndrome: altered behavior in the elevated plus maze and open field. *Behavior Genetics*, *26*(1), 7–13.

Cuntz, H., Forstner, F., Borst, A., & Häusser, M. (2010). One rule to grow them all: a general theory of neuronal branching and its practical application. *PLoS Computational Biology*, *6*(8), e1000877.

Cuntz, H., Forstner, F., Borst, A., & Häusser, M. (2011). The TREES toolbox probing the basis of axonal and dendritic branching. *Neuroinformatics*, *9*(1), 91–96.

Cuntz, H., Mathy, A., & Häusser, M. (2012). A scaling law derived from optimal dendritic wiring. *Proceedings of the National Academy of Sciences*, *109*(27), 11014–11018.

Davisson, M. T., Schmidt, C., & Akeson, E. C. (1990). Segmental trisomy of murine chromosome 16: a new model system for studying Down syndrome. *Progress in Clinical and Biological Research*, *360*, 263.

de Lagran, M., Benavides-Piccione, R., Ballesteros-Yañez, I., Calvo, M., Morales, M., Fillat, C., … Dierssen, M. (2012). Dyrk1A influences neuronal morphogenesis through regulation of cytoskeletal dynamics in mammalian cortical neurons. *Cerebral Cortex*, *22*(12), 2867–2877.

de Lagran, M., Bortolozzi, A., Millan, O., Gispert, J. D., Gonzalez, J. R., Arbones, M. L., … Dierssen, M. (2007). Dopaminergic deficiency in mice with reduced levels of the dual-specificity tyrosine-phosphorylated and regulated kinase 1A, Dyrk1A+/-. *Genes, Brain and Behavior*, *6*(6), 569–578.

Defelipe, J., González-Albo, M. C., Del R'\io, M. R., & Elston, G. N. (1999). Distribution and patterns of connectivity of interneurons containing calbindin, calretinin, and parvalbumin in visual areas of the occipital and temporal lobes of the macaque monkey. *Journal of Comparative Neurology*, *412*(3), 515–526.

Demas, G. E., Nelson, R. J., Krueger, B. K., & Yarowsky, P. J. (1998). Impaired spatial working and reference memory in segmental trisomy (Ts65Dn) mice. *Behavioural Brain Research*, *90*(2), 199–201.

Diamond, M. C., Krech, D., & Rosenzweig, M. R. (1964). The effects of an enriched

environment on the histology of the rat cerebral cortex. *Journal of Comparative Neurology*, *123*(1), 111–119.

Dierssen, M., Benavides-Piccione, R., Martinez-Cue, C., Estivill, X., Florez, J., Elston, G. N., & DeFelipe, J. (2003). Alterations of neocortical pyramidal cell phenotype in the Ts65Dn mouse model of Down syndrome: effects of environmental enrichment. *Cerebral Cortex*, *13*(7), 758–764.

Dierssen, M., Herault, Y., & Estivill, X. (2009). Aneuploidy: from a physiological mechanism of variance to Down syndrome. *Physiological Reviews*, *89*(3), 887–920.

Dolorfo, C. L., & Amaral, D. G. (1998). Entorhinal cortex of the rat: topographic organization of the cells of origin of the perforant path projection to the dentate gyrus. *Journal of Comparative Neurology*, *398*(1), 25–48.

Dong, H. W. (2008). *The Allen reference atlas: A digital color brain atlas of the C57Bl/6J male mouse*. John Wiley & Sons Inc.

Dudman, J. T., Tsay, D., & Siegelbaum, S. A. (2007). A role for synaptic inputs at distal dendrites: instructive signals for hippocampal long-term plasticity. *Neuron*, *56*(5), 866–879.

Duffy, S. N., Craddock, K. J., Abel, T., & Nguyen, P. V. (2001). Environmental enrichment modifies the PKA-dependence of hippocampal LTP and improves hippocampus-dependent memory. *Learning & Memory*, *8*(1), 26–34.

Ecker, A. S., Berens, P., Cotton, R. J., Subramaniyan, M., Denfield, G. H., Cadwell, C. R., … Tolias, A. S. (2014). State dependence of noise correlations in macaque primary visual cortex. *Neuron*, *82*(1), 235–248.

Elston, G. N. (2002). Cortical heterogeneity: implications for visual processing and polysensory integration. *Journal of Neurocytology*, *31*(3–5), 317–335.

Elston, G. N., Benavides-Piccione, R., & DeFelipe, J. (2001). The pyramidal cell in cognition: a comparative study in human and monkey. *Journal of Neuroscience*, *21*(17).

Elston, G. N., & Rosa, M. G. (1997). The occipitoparietal pathway of the macaque monkey: comparison of pyramidal cell morphology in layer III of functionally related cortical visual areas. *Cerebral Cortex (New York, NY: 1991)*, *7*(5), 432–452.

Epp, J. R., Niibori, Y., Hsiang, H.-L. L., Mercaldo, V., Deisseroth, K., Josselyn, S. A., & Frankland, P. W. (2015). Optimization of CLARITY for clearing whole-brain and other intact organs. *eNeuro*, *2*(3), ENEURO----0022.

Ercsey-Ravasz, M., Markov, N. T., Lamy, C., Van Essen, D. C., Knoblauch, K., Toroczkai,

Z., & Kennedy, H. (2013). A predictive network model of cerebral cortical connectivity based on a distance rule. *Neuron*, *80*(1), 184–197.

Escorihuela, R. M., Fernández-Teruel, A., Vallina, I. F., Baamonde, C., Lumbreras, M. A., Dierssen, M., … Flórez, J. (1995). A behavioral assessment of Ts65Dn mice: a putative Down syndrome model. *Neuroscience Letters*, *199*(2), 143–146.

Escorihuela, R. M., Fernandezteruel, A., Tobena, A., Vivas, N. M., Marmol, F., Badia, A., & Dierssen, M. (1995). Early environmental stimulation produces long-lasting changes on β-adrenoceptor transduction system. *Neurobiology of Learning and Memory*, *64*(1), 49–57.

Eyal, G., Mansvelder, H. D., de Kock, C. P. J., & Segev, I. (2014). Dendrites impact the encoding capabilities of the axon. *Journal of Neuroscience*, *34*(24), 8063–8071.

Fabbro, F., Libera, L., & Tavano, A. (2002). A callosal transfer deficit in children with developmental language disorder. *Neuropsychologia*, *40*(9), 1541–1546.

Fanselow, M. S., & Dong, H.-W. (2010). Are the dorsal and ventral hippocampus functionally distinct structures? *Neuron*, *65*(1), 7–19.

Feldt, S., Bonifazi, P., & Cossart, R. (2011). Dissecting functional connectivity of neuronal microcircuits: experimental and theoretical insights. *Trends in Neurosciences*, *34*(5), 225–236.

Feng, L., Zhao, T., & Kim, J. (2015). neuTube 1.0: A New Design for Efficient Neuron Reconstruction Software Based on the SWC Format. *eNeuro*, *2*(1). https://doi.org/10.1523/ENEURO.0049-14.2014

Foster, T. C., & Dumas, T. C. (2001). Mechanism for increased hippocampal synaptic strength following differential experience. *Journal of Neurophysiology*, *85*(4), 1377–1383.

Frasconi, P., Silvestri, L., Soda, P., Cortini, R., Pavone, F. S., & Iannello, G. (2014). Large-scale automated identification of mouse brain cells in confocal light sheet microscopy images. *Bioinformatics*, *30*(17), i587----i593.

Freese, J. L., & Amaral, D. G. (2005). The organization of projections from the amygdala to visual cortical areas TE and V1 in the macaque monkey. *Journal of Comparative Neurology*, *486*(4), 295–317.

Gaarskjaer, F. B. (1978). Organization of the mossy fiber system of the rat studied in extended hippocampi. I. Terminal area related to number of granule and pyramidal cells. *Journal of Comparative Neurology*, *178*(1), 49–71.

Galdzicki, Z., & J Siarey, R. (2003). Understanding mental retardation in Down's syndrome

using trisomy 16 mouse models. *Genes, Brain and Behavior*, *2*(3), 167–178.

Gibble, K. L., Kishi, G. T., & Peake, J. W. (2006). Method, system, and program for moving data among storage units. Google Patents.

Girvan, M., & Newman, M. E. J. (2002). Community structure in social and biological networks. *Proceedings of the National Academy of Sciences*, *99*(12), 7821–7826.

Gorgolewski, K., Burns, C. D., Madison, C., Clark, D., Halchenko, Y. O., Waskom, M. L., & Ghosh, S. S. (2011). Nipype: a flexible, lightweight and extensible neuroimaging data processing framework in python. *Frontiers in Neuroinformatics*, *5*.

Goris, R. L. T., Movshon, J. A., & Simoncelli, E. P. (2014). Partitioning neuronal variability. *Nature Neuroscience*, *17*(6), 858–865.

Gough, B. (2009). *GNU scientific library reference manual*. Network Theory Ltd.

Graves, A. R., Moore, S. J., Bloss, E. B., Mensh, B. D., Kath, W. L., & Spruston, N. (2012). Hippocampal pyramidal neurons comprise two distinct cell types that are countermodulated by metabotropic receptors. *Neuron*, *76*(4), 776–789.

Gray, J. A. (1982). On mapping anxiety. *Behavioral and Brain Sciences*, *5*(3), 506–534.

Grevera, G. J., & Udupa, J. K. (1996). Shape-based interpolation of multidimensional grey-level images. *IEEE Transactions on Medical Imaging*, *15*(6), 881–892.

Griffa, A., Hagmann, P., Thiran, J.-P., Sporns, O., Avena-Koenigsberger, A., Goñi, J., … van den Heuvel, M. P. (2014). Using Pareto optimality to explore the topology and dynamics.

Grillner, S. (2015). Action: The Role of Motor Cortex Challenged. *Current Biology*, *25*(12), R508-- R511. https://doi.org/https://doi.org/10.1016/j.cub.2015.04.023

Groenewegen, H. J., te der Zee, E., Te Kortschot, A., & Witter, M. P. (1987). Organization of the projections from the subiculum to the ventral striatum in the rat. A study using anterograde transport of Phaseolus vulgaris leucoagglutinin. *Neuroscience*, *23*(1), 103–120.

Hama, H., Kurokawa, H., Kawano, H., Ando, R., Shimogori, T., Noda, H., … Miyawaki, A. (2011). Scale: a chemical approach for fluorescence imaging and reconstruction of transparent mouse brain. *Nature Neuroscience*, *14*(11), 1481–1488.

Harding, A. J., Halliday, G. M., & Cullen, K. (1994). Practical considerations for the use of the optical disector in estimating neuronal number. *Journal of Neuroscience Methods*, *51*(1), 83–89.

Hasegawa, J., Sakamoto, Y., Nakagami, S., Aida, M., Sawa, S., & Matsunaga, S. (2016).

Three-dimensional imaging of plant organs using a simple and rapid transparency technique. *Plant and Cell Physiology*, *57*(3), 462–472.

Hasselmo, M. E., & Schnell, E. (1994). Laminar selectivity of the cholinergic suppression of synaptic transmission in rat hippocampal region CA1: computational modeling and brain slice physiology. *Journal of Neuroscience*, *14*(6), 3898–3914.

Hasselmo, M. E., Schnell, E., & Barkai, E. (1995). Dynamics of learning and recall at excitatory recurrent synapses and cholinergic modulation in rat hippocampal region CA3. *Journal of Neuroscience*, *15*(7), 5249–5262.

Hasselmo, M. E., & Wyble, B. P. (1997). Free recall and recognition in a network model of the hippocampus: simulating effects of scopolamine on human memory function. *Behavioural Brain Research*, *89*(1), 1–34.

Hawrylycz, M., Baldock, R. A., Burger, A., Hashikawa, T., Johnson, G. A., Martone, M., … Others. (2011). Digital atlasing and standardization in the mouse brain. *PLoS Computational Biology*, *7*(2), e1001065.

Hawrylycz, M. J., Lein, E. S., Guillozet-Bongaarts, A. L., Shen, E. H., Ng, L., Miller, J. A., … Others. (2012). An anatomically comprehensive atlas of the adult human brain transcriptome. *Nature*, *489*(7416), 391–399.

Henry, G. H., Bishop, P. O., Tupper, R. M., & Dreher, B. (1973). Orientation specificity and response variability of cells in the striate cortex. *Vision Research*, *13*(9), 1771–1779. https://doi.org/https://doi.org/10.1016/0042-6989(73)90094-1

Hill, S. L., Wang, Y., Riachi, I., Schürmann, F., & Markram, H. (2012). Statistical connectivity provides a sufficient foundation for specific functional connectivity in neocortical neural microcircuits. *Proceedings of the National Academy of Sciences*, *109*(42), E2885----E2894.

Hunter, C. L., Bimonte, H. A., & Granholm, A.-C. E. (2003). Behavioral comparison of 4 and 6 month-old Ts65Dn mice:: Age-related impairments in working and reference memory. *Behavioural Brain Research*, *138*(2), 121–131.

Huttenlocher, P. R. (1970). Dendritic development and mental defect. *Neurology*, *20*(4), 381.

Huttenlocher, P. R. (1974). Dendritic development in neocortex of children with mental defect and infantile spasms. *Neurology*, *24*(3), 203.

Igarashi, K. M., Ito, H. T., Moser, E. I., & Moser, M.-B. (2014). Functional diversity along the transverse axis of hippocampal area CA1. *FEBS Letters*, *588*(15), 2470–2476.

Ilin, V., Malyshev, A., Wolf, F., & Volgushev, M. (2013). Fast computations in cortical

ensembles require rapid initiation of action potentials. *Journal of Neuroscience*, *33*(6), 2281–2292.

Insausti, A. M., Megías, M., Crespo, D., Cruz-Orive, L. M., Dierssen, M., Vallina, T. F., … Florez, J. (1998). Hippocampal volume and neuronal number in Ts65Dn mice: a murine model of Down syndrome. *Neuroscience Letters*, *253*(3), 175–178.

Irshad, H., Veillard, A., Roux, L., & Racoceanu, D. (2014). Methods for nuclei detection, segmentation, and classification in digital histopathology: a review current status and future potential. *IEEE Reviews in Biomedical Engineering*, *7*, 97–114.

Irvine, G. I., & Abraham, W. C. (2005). Enriched environment exposure alters the input-output dynamics of synaptic transmission in area CA1 of freely moving rats. *Neuroscience Letters*, *391*(1), 32–37.

Iyer, E. P. R., Iyer, S. C., Sullivan, L., Wang, D., Meduri, R., Graybeal, L. L., & Cox, D. N. (2013). Functional genomic analyses of two morphologically distinct classes of Drosophila sensory neurons: post-mitotic roles of transcription factors in dendritic patterning. *PLoS One*, *8*(8), e72434.

Jacola, L. M., Byars, A. W., Chalfonte-Evans, M., Schmithorst, V. J., Hickey, F., Patterson, B., … Others. (2011). Functional magnetic resonance imaging of cognitive processing in young adults with Down syndrome. *American Journal on Intellectual and Developmental Disabilities*, *116*(5), 344–359.

Janke, A. L., & Ullmann, J. F. P. (2015). Robust methods to create ex vivo minimum deformation atlases for brain mapping. *Methods*, *73*, 18–26.

Jarsky, T., Mady, R., Kennedy, B., & Spruston, N. (2008). Distribution of bursting neurons in the CA1 region and the subiculum of the rat hippocampus. *Journal of Comparative Neurology*, *506*(4), 535–547.

Jernigan, T. L., Bellugi, U., Sowell, E., Doherty, S., & Hesselink, J. R. (1993). Cerebral morphologic distinctions between Williams and Down syndromes. *Archives of Neurology*, *50*(2), 186–191.

Jinno, S., & Kosaka, T. (2009). Neuronal circuit-dependent alterations in expression of two isoforms of glutamic acid decarboxylase in the hippocampus following electroconvulsive shock: A stereology-based study. *Hippocampus*, *19*(11), 1130–1141.

Jones, A. R., Overly, C. C., & Sunkin, S. M. (2009). The Allen brain atlas: 5 years and beyond. *Nature Reviews Neuroscience*, *10*(11), 821–828.

Kim, S.-Y., Cho, J. H., Murray, E., Bakh, N., Choi, H., Ohn, K., … others. (2015).

Stochastic electrotransport selectively enhances the transport of highly electromobile molecules. *Proceedings of the National Academy of Sciences*, *112*(46), E6274--E6283.

Klimm, F., Bassett, D. S., Carlson, J. M., & Mucha, P. J. (2014). Resolving structural variability in network models and the brain. *PLoS Computational Biology*, *10*(3), e1003491.

Kohn, A., & Smith, M. A. (2005). Stimulus dependence of neuronal correlation in primary visual cortex of the macaque. *Journal of Neuroscience*, *25*(14), 3661–3673.

Kolb, B., & Gibb, R. (1991). Environmental enrichment and cortical injury: behavioral and anatomical consequences of frontal cortex lesions. *Cerebral Cortex*, *1*(2), 189–198.

Komulainen, E., Zdrojewska, J., Freemantle, E., Mohammad, H., Kulesskaya, N., Deshpande, P., … Others. (2014). JNK1 controls dendritic field size in L2/3 and L5 of the motor cortex, constrains soma size, and influences fine motor coordination. *Frontiers in Cellular Neuroscience*, *8*.

Kondo, H., Hashikawa, T., Tanaka, K., & Jones, E. G. (1994). Neurochemical gradient along the monkey occipito-temporal cortical pathway. *Neuroreport*, *5*(5), 613–616.

Krasuski, J. S., Alexander, G. E., Horwitz, B., Rapoport, S. I., & Schapiro, M. B. (2002). Relation of medial temporal lobe volumes to age and memory function in nondemented adults with Down's syndrome: implications for the prodromal phase of Alzheimer's disease. *American Journal of Psychiatry*, *159*(1), 74–81.

Kulkarni, V. A., & Firestein, B. L. (2012). The dendritic tree and brain disorders. *Molecular and Cellular Neuroscience*, *50*(1), 10–20.

Kurt, M. A., Davies, D. C., Kidd, M., Dierssen, M., & Flórez, J. (2000). Synaptic deficit in the temporal cortex of partial trisomy 16 (Ts65Dn) mice. *Brain Research*, *858*(1), 191–197.

Kurt, M. A., Kafa, M. I., Dierssen, M., & Davies, D. C. (2004). Deficits of neuronal density in CA1 and synaptic density in the dentate gyrus, CA3 and CA1, in a mouse model of Down syndrome. *Brain Research*, *1022*(1), 101–109.

Larkman, A., & Mason, A. (1990). Correlations between morphology and electrophysiology of pyramidal neurons in slices of rat visual cortex. I. Establishment of cell classes. *Journal of Neuroscience*, *10*(5), 1407–1414.

Lee, H., Park, J.-H., Seo, I., Park, S.-H., & Kim, S. (2014). Improved application of the electrophoretic tissue clearing technology, CLARITY, to intact solid organs including brain, pancreas, liver, kidney, lung, and intestine. *BMC Developmental Biology*, *14*(1), 48.

Lee, S.-H., Marchionni, I., Bezaire, M., Varga, C., Danielson, N., Lovett-Barron, M., … Soltesz, I. (2014). Parvalbumin-positive basket cells differentiate among hippocampal pyramidal cells. *Neuron*, *82*(5), 1129–1144.

Lefebvre, J. L., Sanes, J. R., & Kay, J. N. (2015). Development of dendritic form and function. *Annual Review of Cell and Developmental Biology*, *31*, 741–777.

Leggio, M. G., Mandolesi, L., Federico, F., Spirito, F., Ricci, B., Gelfo, F., & Petrosini, L. (2005). Environmental enrichment promotes improved spatial abilities and enhanced dendritic growth in the rat. *Behavioural Brain Research*, *163*(1), 78–90.

Leguey, I., Bielza, C., Larrañaga, P., Kastanauskaite, A., Rojo, C., Benavides-Piccione, R., & DeFelipe, J. (2016). Dendritic branching angles of pyramidal cells across layers of the juvenile rat somatosensory cortex. *Journal of Comparative Neurology*, *524*(13), 2567–2576.

Longair, M. H., Baker, D. A., & Armstrong, J. D. (2011). Simple Neurite Tracer: open source software for reconstruction, visualization and analysis of neuronal processes. *Bioinformatics*, *27*(17), 2453–2454.

Lübke, J., Markram, H., Frotscher, M., & Sakmann, B. (1996). Frequency and dendritic distribution of autapses established by layer 5 pyramidal neurons in the developing rat neocortex: comparison with synaptic innervation of adjacent neurons of the same class. *Journal of Neuroscience*, *16*(10), 3209–3218.

Mainen, Z. F., Sejnowski, T. J., & Others. (1996). Influence of dendritic structure on firing pattern in model neocortical neurons. *Nature*, *382*(6589), 363–366.

Manita, S., Suzuki, T., Homma, C., Matsumoto, T., Odagawa, M., Yamada, K., … Others. (2015). A top-down cortical circuit for accurate sensory perception. *Neuron*, *86*(5), 1304–1316.

Markram, H. (2006). The blue brain project. *Nature Reviews Neuroscience*, *7*(2), 153–160.

Markram, H., Lübke, J., Frotscher, M., Roth, A., & Sakmann, B. (1997). Physiology and anatomy of synaptic connections between thick tufted pyramidal neurones in the developing rat neocortex. *The Journal of Physiology*, *500*(2), 409–440.

Markram, H., Toledo-Rodriguez, M., Wang, Y., Gupta, A., Silberberg, G., & Wu, C. (2004). Interneurons of the neocortical inhibitory system. *Nature Reviews Neuroscience*, *5*(10), 793–807.

Marr, D., Willshaw, D., & McNaughton, B. (1991). Simple memory: a theory for archicortex. In *From the Retina to the Neocortex* (pp. 59–128). Springer.

Martínez-Cué, C., Baamonde, C., Lumbreras, M., Paz, J., Davisson, M. T., Schmidt, C., …

Flórez, J. (2002). Differential effects of environmental enrichment on behavior and learning of male and female Ts65Dn mice, a model for Down syndrome. *Behavioural Brain Research*, *134*(1), 185–200.

Martínez-Cué, C., Rueda, N., García, E., Davisson, M. T., Schmidt, C., & Flórez, J. (2005). Behavioral, cognitive and biochemical responses to different environmental conditions in male Ts65Dn mice, a model of Down syndrome. *Behavioural Brain Research*, *163*(2), 174–185.

McNaughton, B. L., & Morris, R. G. M. (1987). Hippocampal synaptic enhancement and information storage within a distributed memory system. *Trends in Neurosciences*, *10*(10), 408–415.

Menghini, D., Costanzo, F., & Vicari, S. (2011). Relationship between brain and cognitive processes in Down syndrome. *Behavior Genetics*, *41*(3), 381–393.

Mizuseki, K., Diba, K., Pastalkova, E., & Buzsáki, G. (2011). Hippocampal CA1 pyramidal cells form functionally distinct sublayers. *Nature Neuroscience*, *14*(9), 1174–1181.

Moreno-Bote, R., Beck, J., Kanitscheider, I., Pitkow, X., Latham, P., & Pouget, A. (2014). Information-limiting correlations. *Nature Neuroscience*, *17*(10), 1410–1417.

Moser, M.-B., & Moser, E. I. (1998). Functional differentiation in the hippocampus. *Hippocampus*, *8*(6), 608–619.

Nambu, J. R., Lewis, J. O., Wharton, K. A., & Crews, S. T. (1991). The Drosophila single-minded gene encodes a helix-loop-helix protein that acts as a master regulator of CNS midline development. *Cell*, *67*(6), 1157–1167.

Nieuwenhuys, R., & Nicholson, C. (1998). Lampreys, petromyzontoidea. In *The central nervous system of vertebrates* (pp. 397–495). Springer.

Norman, K. A., & O'reilly, R. C. (2003). Modeling hippocampal and neocortical contributions to recognition memory: a complementary-learning-systems approach. *Psychological Review*, *110*(4), 611.

O'Connor, A. M., Burton, T. J., Leamey, C. A., & Sawatari, A. (2014). The Use of the Puzzle Box as a Means of Assessing the Efficacy of Environmental Enrichment. *Journal of Visualized Experiments: JoVE*, (94).

O'reilly, R. C., & McClelland, J. L. (1994). Hippocampal conjunctive encoding, storage, and recall: avoiding a trade-off. *Hippocampus*, *4*(6), 661–682.

Oh, S. W., Harris, J. A., Ng, L., Winslow, B., Cain, N., Mihalas, S., … others. (2014). A mesoscale connectome of the mouse brain. *Nature*, *508*(7495), 207–214.

Orlandi, J. G., Soriano, J., Alvarez-Lacalle, E., Teller, S., & Casademunt, J. (2013). Noise focusing and the emergence of coherent activity in neuronal cultures. *Nature Physics*, *9*(9), 582–590.

Paxinos, G., & Franklin, K. B. J. (2004). *The mouse brain in stereotaxic coordinates*. Gulf Professional Publishing.

Paxinos, G., & Others. (2013). *Paxinos and Franklin's the mouse brain in stereotaxic coordinates*. Academic Press.

Paxinos, G., Watson, C., Pennisi, M., & Topple, A. (1985). Bregma, lambda and the interaural midpoint in stereotaxic surgery with rats of different sex, strain and weight. *Journal of Neuroscience Methods*, *13*(2), 139–143.

Peng, H., Bria, A., Zhou, Z., Iannello, G., & Long, F. (2014). Extensible visualization and analysis for multidimensional images using Vaa3D. *Nature Protocols*, *9*(1), 193–208.

Pennington, B. F., Moon, J., Edgin, J., Stedron, J., & Nadel, L. (2003). The neuropsychology of Down syndrome: evidence for hippocampal dysfunction. *Child Development*, *74*(1), 75–93.

Pietzsch, T., Saalfeld, S., Preibisch, S., & Tomancak, P. (2015). BigDataViewer: visualization and processing for large image data sets. *Nature Methods*, *12*(6), 481–483.

Pinter, J. D., Eliez, S., Schmitt, J. E., Capone, G. T., & Reiss, A. L. (2001). Neuroanatomy of Down's syndrome: a high-resolution MRI study. *American Journal of Psychiatry*, *158*(10), 1659–1665.

Poirazi, P., & Mel, B. W. (2001). Impact of active dendrites and structural plasticity on the memory capacity of neural tissue. *Neuron*, *29*(3), 779–796.

Polavaram, S., Gillette, T. A., Parekh, R., & Ascoli, G. A. (2014). Statistical analysis and data mining of digital reconstructions of dendritic morphologies. *Frontiers in Neuroanatomy*, *8*.

Pons-Espinal, M., de Lagran, M. M., & Dierssen, M. (2013). Environmental enrichment rescues DYRK1A activity and hippocampal adult neurogenesis in TgDyrk1A. *Neurobiology of Disease*, *60*, 18–31.

Porrero, C., Rubio-Garrido, P., Avendaño, C., & Clascá, F. (2010). Mapping of fluorescent protein-expressing neurons and axon pathways in adult and developing Thy1-eYFP-H transgenic mice. *Brain Research*, *1345*, 59–72.

Purpura, D. P. (1974). Dendritic spine" dysgenesis" and mental retardation. *Science*, *186*(4169), 1126–1128.

Raj, A., & Chen, Y. (2011). The wiring economy principle: connectivity determines anatomy in the human brain. *PloS One*, *6*(9), e14832.

Ramón, F., Moore, J. W., Joyner, R. W., & Westerfield, M. (1976). Squid giant axons. A model for the neuron soma? *Biophysical Journal*, *16*(8), 953–963.

Raz, N., Torres, I. J., Briggs, S. D., Spencer, W. D., Thornton, A. E., Loken, W. J., … Acker, J. D. (1995). Selective neuroanatornic abnormalities in Down's syndrome and their cognitive correlates Evidence from MRI morphometry. *Neurology*, *45*(2), 356–366.

Reimann, M. W., Nolte, M., Scolamiero, M., Turner, K., Perin, R., Chindemi, G., … Markram, H. (2017). Cliques of Neurons Bound into Cavities Provide a Missing Link between Structure and Function. *Frontiers in Computational Neuroscience*, *11*, 48.

Renier, N., Wu, Z., Simon, D. J., Yang, J., Ariel, P., & Tessier-Lavigne, M. (2014). iDISCO: a simple, rapid method to immunolabel large tissue samples for volume imaging. *Cell*, *159*(4), 896–910.

Rigoldi, C., Galli, M., Tenore, N., Onorati, P., Carducci, F., Crivellini, M., & Albertini, G. (2009). Relation between quantitative motion analysis and cerebral volumes analysis in Down syndrome subjects. *Gait & Posture*, *29*, e31.

Rihn, L. L., & Claiborne, B. J. (1990). Dendritic growth and regression in rat dentate granule cells during late postnatal development. *Developmental Brain Research*, *54*(1), 115–124.

Risold, P. Y., & Swanson, L. W. (1996). Structural evidence for functional domains in the rat hippocampus. *Science*, *272*(5267), 1484.

Ropireddy, D., Bachus, S. E., & Ascoli, G. A. (2012). Non-homogeneous stereological properties of the rat hippocampus from high-resolution 3D serial reconstruction of thin histological sections. *Neuroscience*, *205*, 91–111.

Rosen, G. D., & Harry, J. D. (1990). Brain volume estimation from serial section measurements: a comparison of methodologies. *Journal of Neuroscience Methods*, *35*(2), 115–124.

Ruiz-Mejias, M., de Lagran, M. M., Mattia, M., Castano-Prat, P., Perez-Mendez, L., Ciria-Suarez, L., … others. (2016). Overexpression of Dyrk1A, a down syndrome candidate, decreases excitability and impairs gamma oscillations in the prefrontal cortex. *Journal of Neuroscience*, *36*(13), 3648–3659.

Sago, H., Carlson, E. J., Smith, D. J., Kilbridge, J., Rubin, E. M., Mobley, W. C., … Huang,

T.-T. (1998). Ts1Cje, a partial trisomy 16 mouse model for Down syndrome, exhibits learning and behavioral abnormalities. *Proceedings of the National Academy of Sciences*, *95*(11), 6256–6261.

Sancristóbal, B., Rebollo, B., Boada, P., Sanchez-Vives, M. V, & Garcia-Ojalvo, J. (2016). Collective stochastic coherence in recurrent neuronal networks. *Nature Physics*, *12*(9), 881–887.

Sansom, S. N., & Livesey, F. J. (2009). Gradients in the brain: the control of the development of form and function in the cerebral cortex. *Cold Spring Harbor Perspectives in Biology*, *1*(2), a002519.

Sasaki, T., Matsuki, N., & Ikegaya, Y. (2011). Action-potential modulation during axonal conduction. *Science*, *331*(6017), 599–601.

Sasaki, T., Matsuki, N., & Ikegaya, Y. (2012). Effects of axonal topology on the somatic modulation of synaptic outputs. *Journal of Neuroscience*, *32*(8), 2868–2876.

Schindelin, J., Arganda-Carreras, I., Frise, E., Kaynig, V., Longair, M., Pietzsch, T., … Others. (2012). Fiji: an open-source platform for biological-image analysis. *Nature Methods*, *9*(7), 676–682.

Schröter, M., Paulsen, O., & Bullmore, E. T. (2017). Micro-connectomics: probing the organization of neuronal networks at the cellular scale. *Nature Reviews Neuroscience*, *18*(3), 131–146.

Segev, I., & Rall, W. (1998). Excitable dendrites and spines: earlier theoretical insights elucidate recent direct observations. *Trends in Neurosciences*, *21*(11), 453–460.

Seib, L. M., & Wellman, C. L. (2003). Daily injections alter spine density in rat medial prefrontal cortex. *Neuroscience Letters*, *337*(1), 29–32.

Shadlen, M. N., & Newsome, W. T. (1998). The variable discharge of cortical neurons: implications for connectivity, computation, and information coding. *Journal of Neuroscience*, *18*(10), 3870–3896.

Shepherd, G. M., Mirsky, J. S., Healy, M. D., Singer, M. S., Skoufos, E., Hines, M. S., … Miller, P. L. (1998). The Human Brain Project: neuroinformatics tools for integrating, searching and modeling multidisciplinary neuroscience data. *Trends in Neurosciences*, *21*(11), 460–468.

Siarey, R. J., Carlson, E. J., Epstein, C. J., Balbo, A., Rapoport, S. I., & Galdzicki, Z. (1999). Increased synaptic depression in the Ts65Dn mouse, a model for mental retardation in Down syndrome. *Neuropharmacology*, *38*(12), 1917–1920.

Siarey, R. J., Stoll, J., Rapoport, S. I., & Galdzicki, Z. (1997). Altered long-term potentiation in the young and old Ts65Dn mouse, a model for Down Syndrome. *Neuropharmacology*, *36*(11), 1549–1554.

Siek, J. G., Lee, L.-Q., & Lumsdaine, A. (2001). *The Boost Graph Library: User Guide and Reference Manual, Portable Documents*. Pearson Education.

Slomianka, L., Amrein, I., Knuesel, I., Sørensen, J. C., & Wolfer, D. P. (2011). Hippocampal pyramidal cells: the reemergence of cortical lamination. *Brain Structure and Function*, *216*(4), 301.

Smith, D. O. (1977). Ultrastructural basis of impulse propagation failure in a nonbranching axon. *Journal of Comparative Neurology*, *176*(4), 659–669.

Solstez, I. (2006). *Diversity in the Neuronal Machine: Order and Variability in Interneuronal Microcircuits*.

Sporns, O., Chialvo, D. R., Kaiser, M., & Hilgetag, C. C. (2004). Organization, development and function of complex brain networks. *Trends in Cognitive Sciences*, *8*(9), 418–425.

Stasko, M. R., & Costa, A. C. S. (2004). Experimental parameters affecting the Morris water maze performance of a mouse model of Down syndrome. *Behavioural Brain Research*, *154*(1), 1–17.

Staudt, T., Lang, M. C., Medda, R., Engelhardt, J., & Hell, S. W. (2007). 2, 2'-thiodiethanol: a new water soluble mounting medium for high resolution optical microscopy. *Microscopy Research and Technique*, *70*(1), 1–9.

Stepanyants, A., & Chklovskii, D. B. (2005). Neurogeometry and potential synaptic connectivity. *Trends in Neurosciences*, *28*(7), 387–394.

Stockbridge, N., & Stockbridge, L. L. (1988). Differential conduction at axonal bifurcations. I. Effect of electrotonic length. *Journal of Neurophysiology*, *59*(4), 1277–1285.

Strange, B. A., Witter, M. P., Lein, E. S., & Moser, E. I. (2014). Functional organization of the hippocampal longitudinal axis. *Nature Reviews Neuroscience*, *15*(10), 655–669.

Strausfeld, N. J. (2012). *Atlas of an insect brain*. Springer Science & Business Media.

Szigeti, B., Gleeson, P., Vella, M., Khayrulin, S., Palyanov, A., Hokanson, J., … Larson, S. (2014). OpenWorm: an open-science approach to modeling Caenorhabditis elegans. *Frontiers in Computational Neuroscience*, *8*.

Teipel, S. J., Alexander, G. E., Schapiro, M. B., Möller, H.-J., Rapoport, S. I., & Hampel, H.

(2004). Age-related cortical grey matter reductions in non-demented Down's syndrome adults determined by MRI with voxel-based morphometry. *Brain*, *127*(4), 811–824.

Tolhurst, D. J., Movshon, J. A., & Dean, A. F. (1983). The statistical reliability of signals in single neurons in cat and monkey visual cortex. *Vision Research*, *23*(8), 775–785.

Tomer, R., Ye, L., Hsueh, B., & Deisseroth, K. (2014). Advanced CLARITY for rapid and high-resolution imaging of intact tissues. *Nature Protocols*, *9*(7), 1682–1697.

Tomizuka, K., Yoshida, H., Uejima, H., Kugoh, H., Sato, K., Ohguma, A., … Ishida, I. (1997). Functional expression and germline atransmission of a human chromosome fragment in chimaeric mice. *Nature Genetics*, *16*(2), 133–143.

Tomko, G. J., & Crapper, D. R. (1974). Neuronal variability: non-stationary responses to identical visual stimuli. *Brain Research*, *79*(3), 405–418.

Torre, R., Sola, S., Pons, M., Duchon, A., Lagran, M. M., Farré, M., … Others. (2014). Epigallocatechin-3-gallate, a DYRK1A inhibitor, rescues cognitive deficits in Down syndrome mouse models and in humans. *Molecular Nutrition & Food Research*, *58*(2), 278–288.

Treves, A., & Rolls, E. T. (1992). Computational constraints suggest the need for two distinct input systems to the hippocampal CA3 network. *Hippocampus*, *2*(2), 189–199.

Treves, A., & Rolls, E. T. (1994). Computational analysis of the role of the hippocampus in memory. *Hippocampus*, *4*(3), 374–391.

van Elburg, R. A. J., & van Ooyen, A. (2010). Impact of dendritic size and dendritic topology on burst firing in pyramidal cells. *PLoS Computational Biology*, *6*(5), e1000781.

Vegue, M., Perin, R., & Roxin, A. (2017). On the structure of cortical micro-circuits inferred from small sample sizes. *bioRxiv*, 118471.

Vincent, R. D., Janke, A., Sled, J. G., Baghdadi, L., Neelin, P., & Evans, A. C. (2004). MINC 2.0: a modality independent format for multidimensional medical images. In *10th Annual Meeting of the Organization for Human Brain Mapping* (Vol. 2003, p. 2003).

Voges, N., Schüz, A., Aertsen, A., & Rotter, S. (2010). A modeler's view on the spatial structure of intrinsic horizontal connectivity in the neocortex. *Progress in Neurobiology*, *92*(3), 277–292.

Volkmar, F. R., & Greenough, W. T. (1972). Rearing complexity affects branching of dendrites in the visual cortex of the rat. *Science*, *176*(4042), 1445–1447.

von Helmholtz, H. (1962). Treatise on physiological optics. *Helmholtz. NY: Dover*, *593*, 42.

Wen, Q., Stepanyants, A., Elston, G. N., Grosberg, A. Y., & Chklovskii, D. B. (2009). Maximization of the connectivity repertoire as a statistical principle governing the shapes of dendritic arbors. *Proceedings of the National Academy of Sciences*, *106*(30), 12536–12541.

White, N. S., Alkire, M. T., & Haier, R. J. (2003). A voxel-based morphometric study of nondemented adults with Down Syndrome. *Neuroimage*, *20*(1), 393–403.

Wold, S., Esbensen, K., & Geladi, P. (1987). Principal component analysis. *Chemometrics and Intelligent Laboratory Systems*, *2*(1–3), 37–52.

Xu, L., Tanigawa, H., & Fujita, I. (2003). Distribution of $\alpha{\$}-amino-3-hydroxy-5-methyl-4-isoxazolepropionate-type glutamate receptor subunits (GluR2/3) along the ventral visual pathway in the monkey. *Journal of Comparative Neurology*, *456*(4), 396–407.

y Cajal, S. R. (1995). *Histology of the nervous system of man and vertebrates* (Vol. 1). Oxford University Press, USA.

Yang, B., Treweek, J. B., Kulkarni, R. P., Deverman, B. E., Chen, C.-K., Lubeck, E., … Gradinaru, V. (2014). Single-cell phenotyping within transparent intact tissue through whole-body clearing. *Cell*, *158*(4), 945–958.

Ye, L., Allen, W. E., Thompson, K. R., Tian, Q., Hsueh, B., Ramakrishnan, C., … Others. (2016). Wiring and molecular features of prefrontal ensembles representing distinct experiences. *Cell*, *165*(7), 1776–1788.

Yuste, R., & Tank, D. W. (1996). Dendritic integration in mammalian neurons, a century after Cajal. *Neuron*, *16*(4), 701–716.

Zhang, M.-D., Tortoriello, G., Hsueh, B., Tomer, R., Ye, L., Mitsios, N., … Others. (2014). Neuronal calcium-binding proteins 1/2 localize to dorsal root ganglia and excitatory spinal neurons and are regulated by nerve injury. *Proceedings of the National Academy of Sciences*, *111*(12), E1149----E1158.

Zheng, Z., Lauritzen, J. S., Perlman, E., Robinson, C. G., Nichols, M., Milkie, D., … Bock, D. D. (2017). A Complete Electron Microscopy Volume Of The Brain Of Adult Drosophila melanogaster. *bioRxiv*. https://doi.org/10.1101/140905

Zingg, B., Hintiryan, H., Gou, L., Song, M. Y., Bay, M., Bienkowski, M. S., … others. (2014). Neural networks of the mouse neocortex. *Cell*, *156*(5), 1096–1111.

ANNEX

ANNEX I: Supplementary Figure

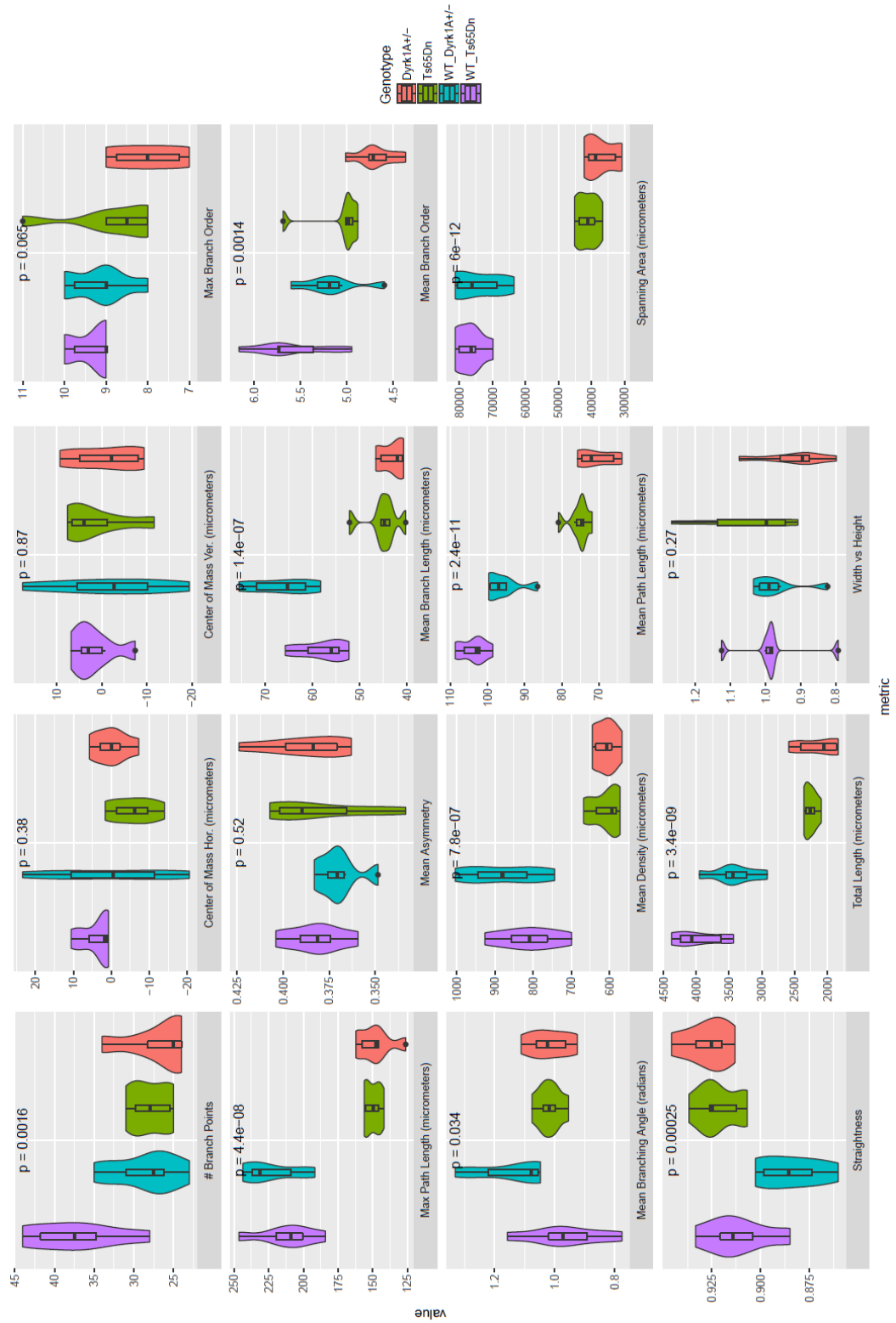

Supplementary Figure 1. Boxplots of single-neuron morphological metrics. Each panel shows violin and boxplots for metrics having significant differences in one-way ANOVA tests between the Ts65Dn, Dyrk1A+/- and their respective controls, the p-value of the test is shown on top of each panel. Each metric units are specified in the panel label. Each colored box/violin plot represents the distribution of the metric for each group.

ANNEX II: Computational and experimental approaches for optimizing cleared whole-brain fluorescence microscopy imaging

In recent decades, development of fluorescent proteins and laser scanning microscopy techniques that can achieve deep tissue imaging of the fluorescently labeled tissues opened new venues for the application of tissue clearing. However, the use of most of the methods degrades the fluorescent signal quickly, and hence limited its application to small tissues with strong fluorescence expression. Fluorescence microscopy of genetically encoded fluorescent proteins (FPs) is helpful for tracking neuronal morphology in fixed, cleared tissue. In well-cleared tissue, FPs can be imaged if the signal is strong, but FPs expressed at endogenous levels may not be bright enough to be seen over background, and fluorescence can be quenched if imaging is not done carefully or if a solvent-based clearing procedure, needed for lipid removal, is used. Most FPs require an aqueous environment to fluoresce. The selection of media is usually done by essay-error, which is labour-intensive, and not cost-effective. Here I capitalized on molecular dynamic techniques to develop a method for predict the clearing agents that would better avoid FP quenching and lessen scatter.

Channel identification

Crystallographic structures for fluorescent protein mutants with a ~2A resolution were obtained from the Protein Data Bank (PDB): eYFP-3V3D, YFP-1F0B, eGFP-2Y0G, GFP-1EMB, RFP-2VAD, mCherry-2H5Q, BFP-1BFP, eCFP-2WSN. The MolAxis standalone version 1.0 was used in order to identify the barrel holes that allow proton exchange and chromophore resonance. The obtained channels were visualized with VMD.

Molecular dynamics simulations

Pymol was used in order to obtain net charge, hydrophobicity and Van der Waals surfaces in the analyzed proteins based on the mention PDB files. All the molecular dynamics system building and simulations were performed using HTMD. The original PDB files were automatically prepared with *proteinprepare*, including the titration of the protonation states using *PROPKA 3.1*, addition of missing atoms and overall optimization of the H-network using *PDB2PQR 2.1*. Topology and parameter files for small molecules of interest (TDE, Glycerol, Diatrizoic acid, N-Methyl-D-Glucamine, DEG, TEA and D-Sorbitol) in the CHARMM format were obtained with the *parameterize* tool. This HTMD

optimizes the parametrization including minimization and Quantum Mechanics calculations. Default full QM calculations were used with the PSI4 open-source engine. The system was built with the parametrized solvents at specific concentrations in water using periodic cell boundaries and equilibrated for 40ns at 310K. 20ns (310K) simulations were run in high throughput using HTMD's adaptive sampling (attach source code).

Docking simulations

A molecule library was generated from the ZINC15 database with ready-to-dock 3D mol2 format structures for compounds being hydrophilic (logP<=0), having mid-reference pHs, all the available sizes (from 200 to >500 Daltons) and charge between -2 and +2. To define a docking volume surrounding previously identified holes in the fluorescent protein barrel, the biggest compound of the library was used in the rDock cavity generation functionality. A high-throughput exhaustive docking with 50 runs per molecule was performed in a computing cluster.

Computational resources

The workstation used to run all the HTMD simulations has been described previously (HP-Z620 equipped with an Nvidia Quadro K4000 graphics card). Additionally, the ligand parametrization and docking was run on a high performance computing cluster (3,020 Linux cores, 200 computing nodes and a total storage capacity of 5 PB). I used 32 nodes by setting batch jobs.

Protein denaturation assay

Purified fluorescent protein mutants were obtained from BioVision inc. Tryptophan intrinsic fluorescence was measured in candidate buffers using an Infinite M200 plate reader (Tecan Life Sciences). Temperature was raised to 42ºC at a rate of 1ºC/minute.

Development of a computational pipeline for the assessment of XFP fluorescence conservation

I investigated whether molecular dynamics simulations could explain the highly specific fluorescent protein quenching upon immersion in TDE at high concentration. E-YFP and

RFP crystallographic structures were solvated (pure H2O, 87% glycerol, 63% TDE, 83% TDE and DA solution) and their molecular dynamics simulated at 310K for 20 ns.

Absence of protein denaturation or direct interaction between solvent molecules and the chromophore

The simulations shown that the Root-Mean-Square Deviation of the chromophore coordinates was low (~1 ± 0.3 Å) and almost the same for the tested solvating media, indicating that TDE quenching is not caused by direct interaction with the chromophore. Similarly, the whole protein RMSD was similar in the studied solutions and in water (~2.5 ± 0.5 Å), pointing that at the simulated timescales the protein is not undergoing denaturation.

Water density around the fluorophore is solvent concentration-dependent

In order to check whether the water tunnel between the e-YFP chromophore and the bulk necessary for protonation and fluorescence is formed, I measured the water density in a shell containing the chromophore and the channel for all the combinations of proteins and solvents. Our simulations show that the amount of water molecules is significantly reduced in 83% TDE versus 63% TDE or H2O solvation, as expected by the reduction of water molecules in the solution.

Small molecules can increase water density in the fluorophore

Give the results obtained in the molecular dynamics simulations, I focused on the water channels connecting the chromophore with the bulk. A quick analysis of channel sizes and paths using MolAxis in both mutants (e-YFP and RFP) shows that RFP has more and thicker channels (n_{RFP}=4, n_{eYFP}=3, $r_{max,RFP}$=1.2, $r_{max,eYFP}$=0.7 Å). Additionally, when plotting hydrophobicity and net charge on the protein surface around the channels necessary for the water tunnel formation, it can be qualitatively observed that those properties have different spatial distributions. Those observations, together with the fact that TDE is significantly more hydrophobic than the other solvents, point at the possibility of avoiding e-YFP quenching by the addition of highly hydrophilic small molecules with high affinity for the protein surface region around the channel. In order to find those anti-quenching candidates, I have screened all the hydrophilic, commercially available, small molecules in the ZINC15 database. In order to assess their affinity for the surface around the channels, I obtained 3D representations of those molecules and used rDock to run high throughput docking simulations. A PCA combining the available information of the molecules and the docking scores obtained, shows that the physico-chemical properties of the molecules do not

correlate with docking scores, meaning that those are not reliable proxies for pinpointing candidates with high affinity for the protein surface around the channel. Thus, I selected some candidates based on their docking score and hydrophilicity. The selected molecules, constrained by commercial availability, were Guanosine 5'-DiPhosphate and D-Fructose. I then simulated molecular dynamics of e-YFP in 83% TDE concentration with small quantities of the putative anti-quenching molecules.

Computational pipeline for the assessment of XFP fluorescence conservation

I first aimed at identifying channels in the fluorescent proteins and differences among mutants. I specifically explored the presence of water-filled channels connecting the chromophore to the β-barrel exterior

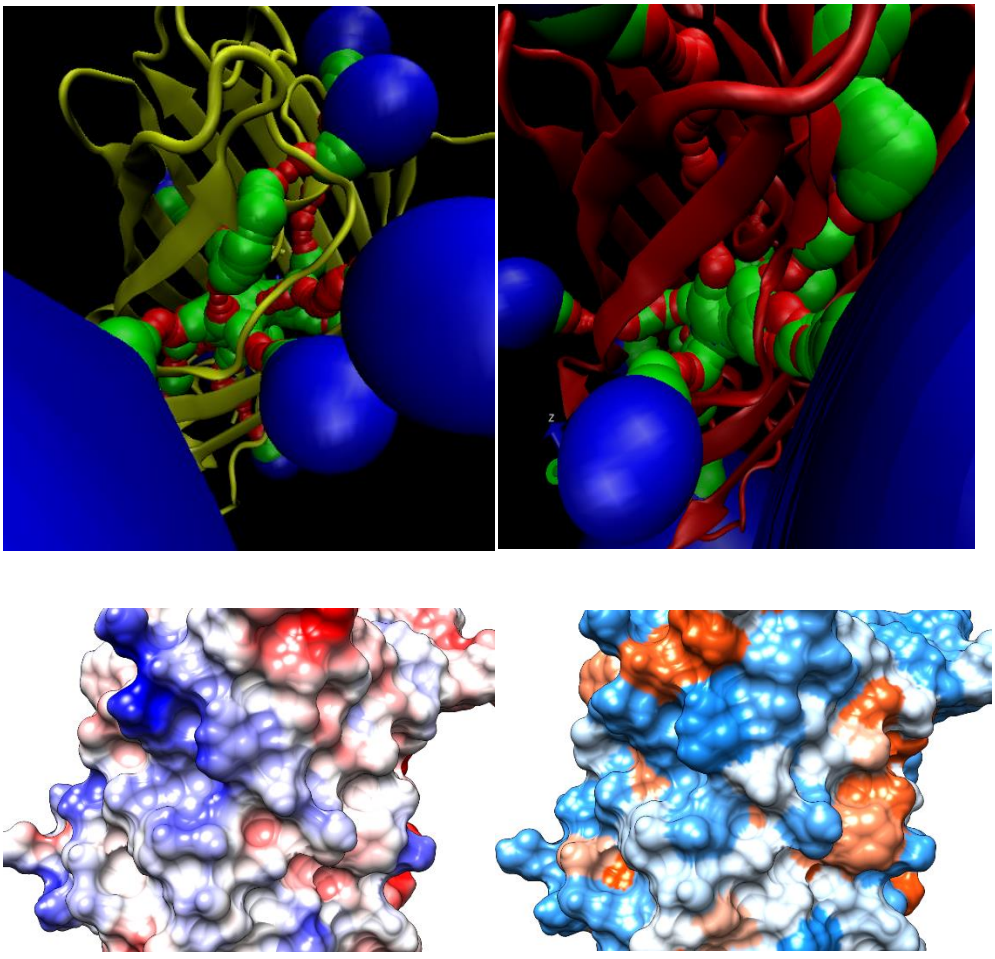

Hydrophobicity Charge

I then explored how concentration and hydrophobicity of imaging media has an impact on XFP fluorescence. In particular, hydrophobicity has a strong influence on interactions with the substrate, thus highlighting the importance of the water tunnel and the need of molecular dynamic simulations. Here I already showed that different concentrations of Tidioethanol (TDE, see Figure below), affect water tunnels.

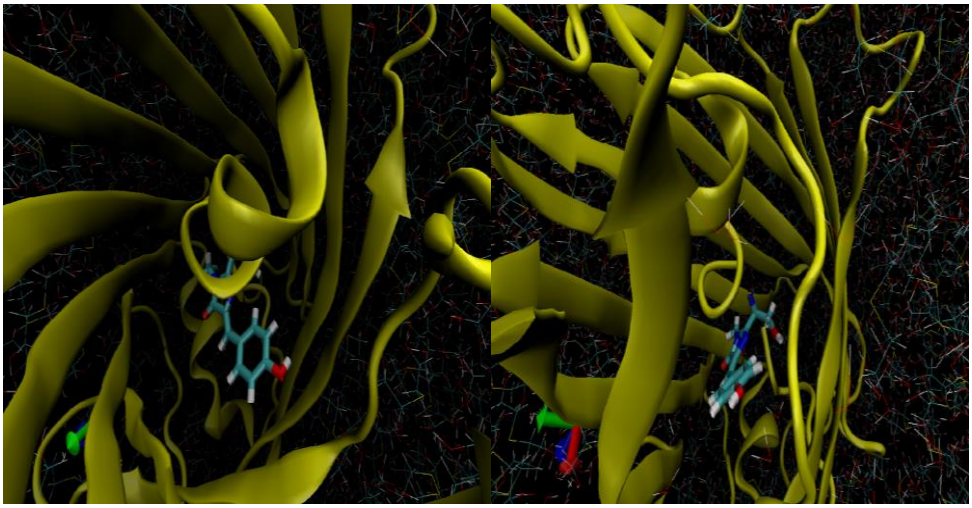

TDE 83% **TDE 63%**

I performed docking simulations for screening of compounds that could be useful for imaging. The results are provided below, representing the Root Mean Square Deviation (RMSD) value for the protein and chromophore, and the water density in a shell containing the water.

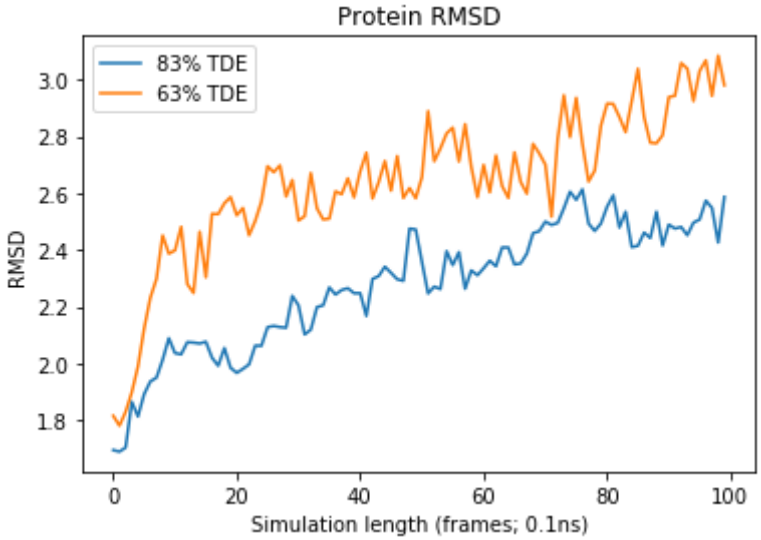
Protein RMSD
83% TDE
63% TDE
RMSD
3.0
2.8
2.6
2.4
2.2
2.0
1.8
0
20
40
60
80
100
Simulation length (frames; 0.1ns)

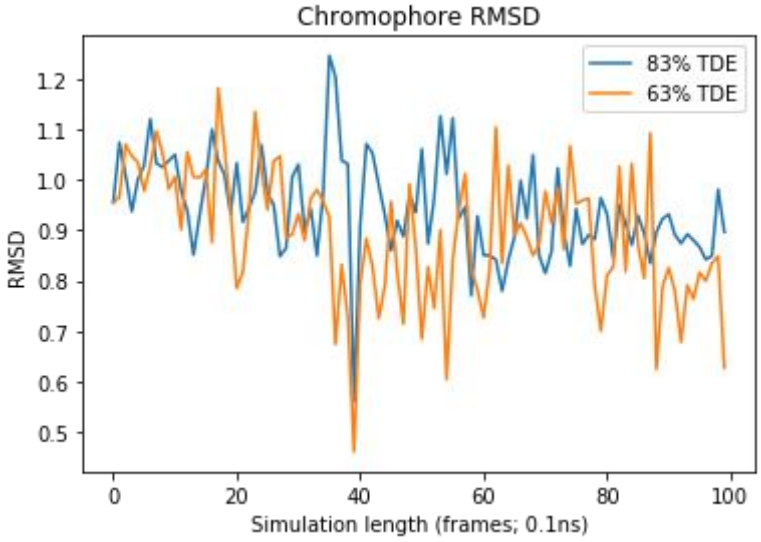
Chromophore RMSD
83% TDE
63% TDE
RMSD
1.2
1.1
1.0
0.9
0.8
0.7
0.6
0.5
0
20
40
60
80
100
Simulation length (frames; 0.1ns)

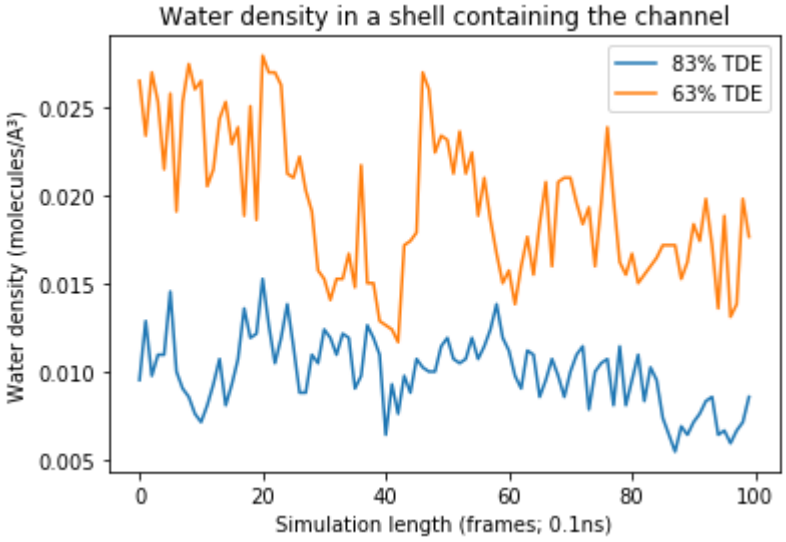
Water density in a shell containing the channel
83% TDE
63% TDE
Water density (molecules/A³)
0.025
0.020
0.015
0.010
0.005
0
20
40
60
80
100
Simulation length (frames; 0.1ns)

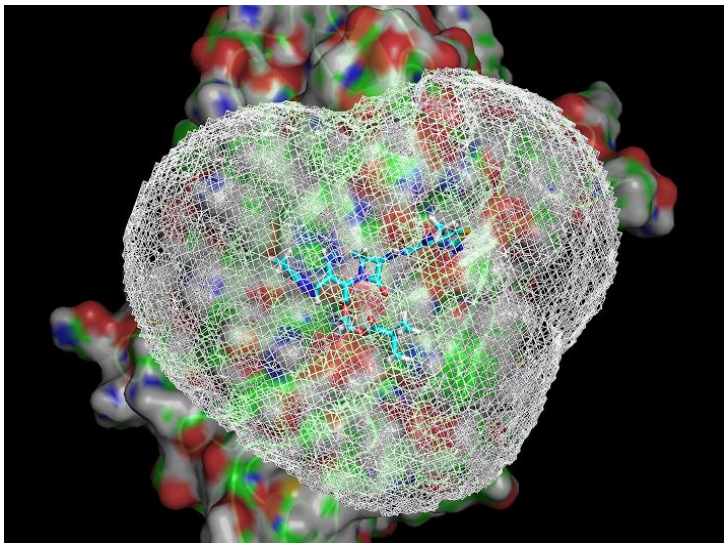

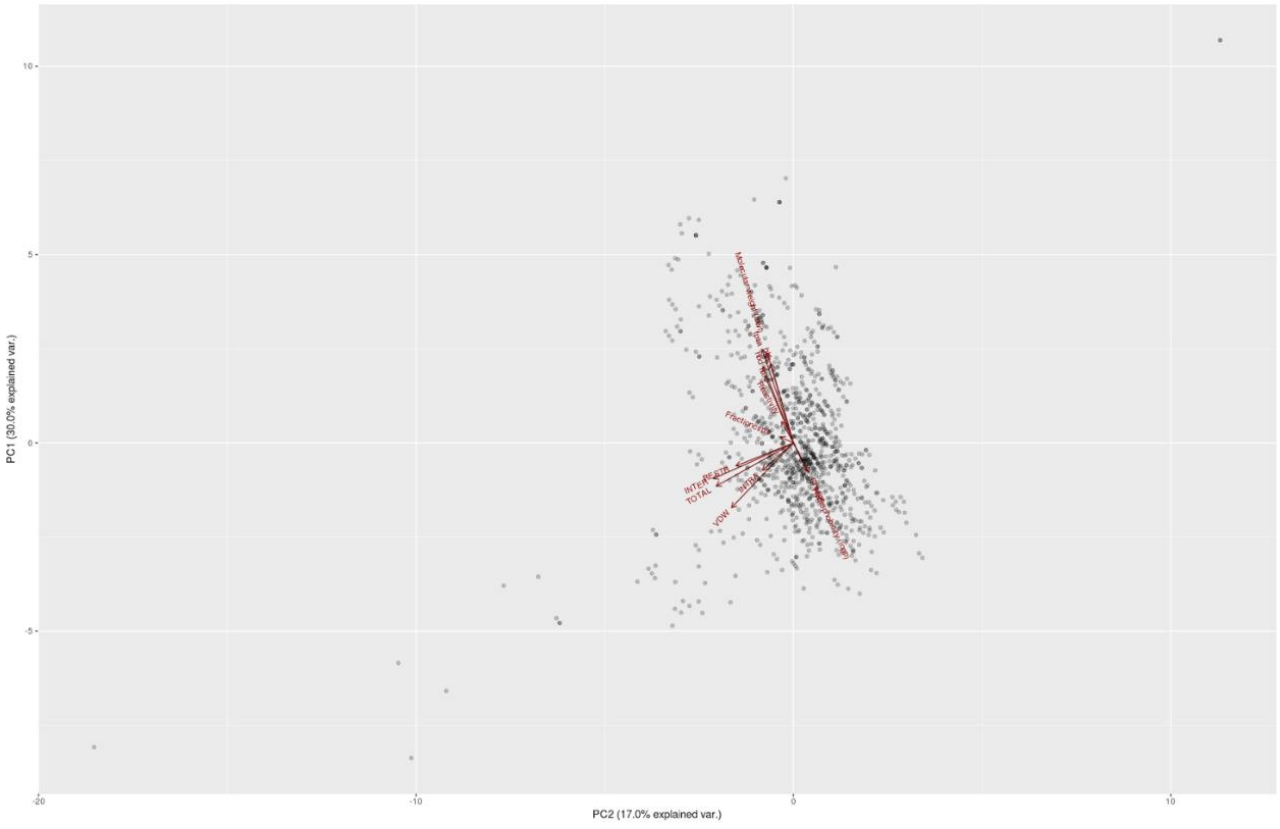

Finally, I aimed to find an optimal candidate for imaging and to introduce possible optimizations based on the computational pipeline based on this computational pipeline I selected.

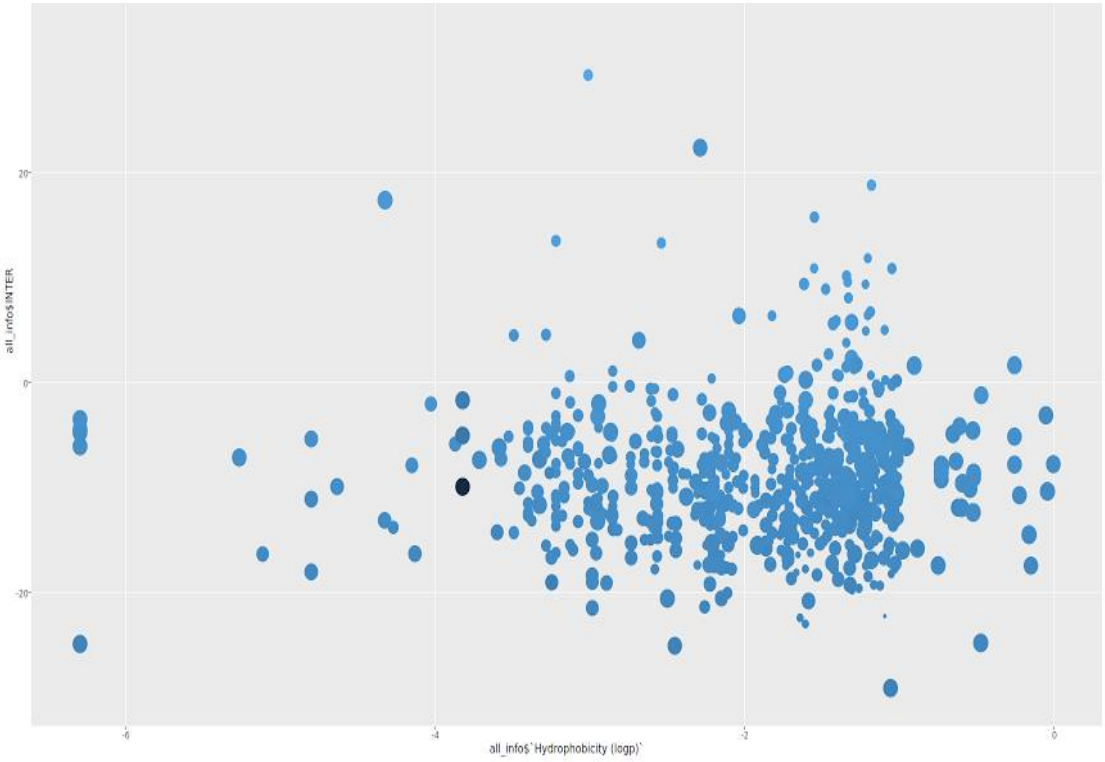
20
0
-20
all_info$INTER
-6
-4
-2
0
all_info$`Hydrophobicity (logp)`

ANNEX III: Publications of this Thesis

Where environment meets cognition: a focus on two developmental intellectual disability disorders.
De Toma I., Manubens-Gil L., Ossowski S., and Dierssen M. Neural Plasticity, 2016

Articles in preparation:
Exploration of the morphospace in a minimal model of local cortical layer II/III: neuromorphological alterations in DS mouse models and their impact on computational capacities. Manubens-Gil L., Garcia-Ojalvo J. and Dierssen M., in preparation.

Environmental enrichment effects on neuromorphological alterations in the tgDyrk1A DS mouse model and its mesoscopic implications on the trisynaptic circuit. Pons-Espinal M.*, Manubens-Gil L.* et al., in preparation (Co-first author).

CLARITY technique optimization through fluorescent protein molecular dynamics and docking simulations. Manubens-Gil L., Swoger J., Sharpe J., Garcia-Ojalvo J. and Dierssen M., in preparation.

Systems-perspective analysis pipeline for whole-organ fluorescence microscopy teravoxel-sized datasets
Manubens-Gil L., García Ojalvo, J. and Dierssen M. in preparation

Multi-scale morphological effects on neuronal network contact topology: Pareto optimality in the tgDyrk1A DS mouse model
Manubens-Gil L., García Ojalvo, J. and Dierssen M.

De Toma I, Manubens-Gil L, Ossowski S, Dierssen M. Where Environment Meets Cognition: A Focus on Two Developmental Intellectual Disability Disorders. Neural Plast. 2016;2016:4235898. DOI: 10.1155/2016/4235898